Spin-Dependent Hadro- and Photoproduction of Heavy Quarks at Next-to-Leading Order of QCD

DISSERTATION
ZUR ERLANGUNG DES DOKTORGRADES
DER NATURWISSENSCHAFTEN (DR. RER. NAT.)
DER FAKULTÄT FÜR PHYSIK
DER UNIVERSITÄT REGENSBURG

vorgelegt von
Johann Riedl
aus Winklarn
2013

Promotionsgesuch eingereicht am: 31. Oktober 2013
Promotionskolloquium am: 17. April 2014
Die Arbeit wurde angeleitet von: Prof. Dr. Andreas Schäfer
Prüfungsausschuss: Prof. Dr. Karsten Rincke
Prof. Dr. Andreas Schäfer
Prof. Dr. Vladimir Braun
Prof. Dr. Thomas Niehaus

Contents

1 Introduction and motivation

The fundamental question of what the world is made of has interested mankind for millennia. Greek philosophers already suggested that the four elements air, water, fire, and soil are the indivisible building blocks of everything. Albeit their imagination turned out to be too simple, their basic idea of indivisible constituents of matter is still being pursued.

With the advent of sophisticated measurement techniques our view of the world has started to improve and ever more details about the structure of matter have been gathered. Since Mendeleev has introduced the table of elements in the 19th century, it has become obvious that the world consists of atoms. Rutherford deduced from the results of his scattering experiments [1] that atoms are not fundamental, but made of electrons and nuclei. After the discovery of the neutron in 1932 [2] it became clear that nuclei consist of protons and neutrons. Later on, starting in the 1960s [3, 4], measurements, where high-energetic leptons were scattered off nuclei [5], have revealed their partonic substructure, quarks and gluons, which are still believed to be point-like. These experiments have established the naive quark model proposed to classify the large amount of hadrons and paved the way to our current understanding of the theory of strong interactions, quantum chromodynamics (QCD). Quarks carry fractional electric charge of $-\frac{1}{3}$ and $\frac{2}{3}$, and each quark flavour is a colour triplet in the fundamental representation of QCD.

Quantum chromodynamics can be unified with the electro-weak theory of Glashow, Salam, and Weinberg in the standard model [6] of particle physics leading to an $SU(3) \times SU(2) \times U(1)$ group structure. The spin-$\frac{1}{2}$ fermions can be grouped into three families, each with two quark flavours, a charged lepton and a neutrino. The strong, electromagnetic, and weak forces between the elementary fermions are mediated by the exchange of spin-1 gluons, photons, and W and Z bosons, respectively.

Up to now there is no consistent quantum theory of gravity, which could be incorporated into the standard model of particle physics. Some precision experiments, like the measurement of the anomalous magnetic moment $g-2$ of the muon [7], and conceptual theoretical problems give further hints that the standard model might be incomplete. Therefore, several extensions have been proposed in the literature, among them string theory [8], supersymmetry [9], and the possibility of a forth family of fundamental fermions [10–16]. We have investigated the latter possibility in [12–14], which is, however, beyond the scope of this thesis. However, the newest results indicate that a forth family is nearly ruled out.

Instead, we focus on the production of heavy charm and bottom quarks belonging to the second and the third family, respectively, in the framework of QCD. A solid

understanding of the theoretical framework for heavy quark production is of utmost importance for several key measurements both ongoing or taking place in the very near future. At the Large Hadron Collider (LHC) at CERN, heavy flavour production by genuine QCD processes is an important background in searches for Higgs bosons within the standard model and beyond as well as for new physics. Moreover, several signatures have been proposed, how production and decay of heavy quarks are modified in the presence of a quark gluon plasma (QGP) [17], which is investigated, e.g., at the Relativistic Heavy Ion Collider (RHIC) at the Brookhaven National Laboratory (BNL) in $Au + Au$ collisions. Furthermore, of topical interest is the production of heavy flavours in longitudinally polarised proton-proton and lepton-hadron collisions, which is the subject of this thesis. At present, it is experimentally studied at RHIC [18, 19] and COMPASS at CERN [20–22]. Together with the theoretical calculations provided here, these experiments should help to improve our understanding of QCD as the theory of strong interactions, and, in particular, how the spin of the proton is carried by quarks and gluons, which is one of the fundamental questions in nucleon physics. In addition, heavy flavour production is part of the physics case for new facilities like GSI-FAIR [23–25] in Germany, J-PARC [26] in Japan, and a possible electron-ion collider (EIC) in the US [27, 28].

In the naive quark-parton model one expects that the spin of the proton is carried entirely by its three constituent quarks. After taking relativistic corrections into account, their contribution is reduced to about 60 percent. This is in striking contrast to all measurements in the last 25 years which found that quark and antiquark spins summed over all flavours provide only about 20 to 30 percent of the proton spin [29–33].

This discrepancy between the parton model and experiments was first dubbed "proton spin crises", but it was quickly realised that the result implies that sizable contributions to the nucleon spin should come from the polarisation of gluons and/or from orbital angular momenta $L_z^{q,g}$ of quarks and gluons. This view is summarised in the proton spin sum rule [34]

$$S_z^p = \frac{1}{2} = \frac{1}{2}\Delta\Sigma + \Delta G + L_z^q + L_z^g, \tag{1.1}$$

where

$$\Delta\Sigma = \int_0^1 dx \sum_{q=u,d,s} [\Delta q(x) + \Delta\bar{q}(x)] \tag{1.2}$$

and

$$\Delta G = \int_0^1 dx \Delta g(x) \tag{1.3}$$

denote the total intrinsic spin contribution of quarks and gluons, respectively [35]. The polarised parton density functions $\Delta q(x), \Delta\bar{q}(x)$, and $\Delta g(x)$ in equations (1.2) and (1.3) are defined as

$$\Delta f(x) = f^+(x) - f^-(x) \tag{1.4}$$

with $f = q, \bar{q}, g$. $f^+(x)$ $[f^-(x)]$ is the probability to find a parton f carrying a fraction x of the momentum of the nucleon and having its spin [anti]aligned with the spin of the nucleon. For simplicity, the dependence of the parton distribution functions on the resolution scale is not explicitly indicated. It will be discussed in detail in chapter 2.

We note that in an interacting field theory the decomposition of the spin in equation (1.1) depends on the gauge and the choice of the reference frame. The sum rule in (1.1) is only valid in the infinite momentum frame and the light-cone gauge, where parton distribution functions are naturally defined [36].

A gauge-invariant decomposition was given in the Ji sum rule [37], where only the total angular momentum J^g enters, which cannot be decomposed any further. This version of the sum rule is, however, relevant for computations within lattice QCD. Only $\Delta\Sigma$ is common to both sum rules.

Currently, the best information on $\Delta\Sigma$ comes from polarised deep inelastic scattering (DIS) experiments performed at different laboratories [32, 33]. They constrain the sum of quark and antiquark densities through measurements of the polarised structure function

$$g_1(x) = \frac{1}{2}\sum_q e_q^2[\Delta q(x) + \Delta\bar{q}(x)] + \mathcal{O}(\alpha_s). \tag{1.5}$$

Similar experiments with an identified hadron in the final state (semi-inclusive DIS) have provided crucial information on the difference between quarks and antiquarks and have tested different assumptions about the flavour structure of the polarised sea. Both inclusive and semi-inclusive DIS give only very limited information on the polarised gluon distribution function $\Delta g(x)$. The latter contributes only indirectly via scaling violations, which are not very pronounced in the kinematic regime covered by the experiments.

To learn about $\Delta g(x)$ one has to consider observables where it contributes dominantly already at the tree-level approximation of QCD. Here, first results on pion and jet production in polarised pp scattering at RHIC [38–46] have led to a significant constraint on the size of Δg in the range $x \in [0.05, 0.2]$. The best way to extract information about parton densities from experimental data is to analyse all available results from DIS, semi-inclusive DIS, and pp scattering simultaneously in a global QCD fit. A first such analysis with longitudinally polarised data was performed by the DSSV group [30, 31]. It turned out that uncertainties are still sizable, in particular for the gluon distribution $\Delta g(x)$ such that reliable results for its first moment ΔG still cannot be obtained. Further experimental probes for $\Delta g(x)$ are urgently needed to reduce extrapolation uncertainties from the small x region.

Among the most promising channels are direct photon and heavy quark production at RHIC [47] and two-hadron and charm production in polarised lepton-nucleon scattering at HERMES [48, 49] and COMPASS [20, 21, 50, 51]. In the latter case data already exist, but could not be included in the DSSV analysis since a proper theoretical framework was not available. For two-hadron photoproduction, some theoretical progress was made, see, e.g. [52]. For polarised heavy quark hadro- and photoproduction flexible Monte Carlo codes up to the second non-trivial (next-to-leading) order in the strong coupling α_s of QCD are presented in this work. These are essential to include current and future data into upcoming global QCD analyses of polarised parton distribution functions.

Our theoretical calculations are performed perturbatively as a power expansion in the strong coupling constant up to $\mathcal{O}(\alpha_s^3)$ and $\mathcal{O}(\alpha_{\rm em}\alpha_s^2)$ for hadro- and photoproduction, respectively. Perturbative calculations for the scattering of quarks and gluons are made possible by the property of asymptotic freedom, which states that the strong interaction becomes weak at short distances, i.e., high momentum transfers. This peculiar energy dependence of α_s is due to the self-interactions of the QCD gauge bosons, which carry a colour charge. Experimentally relevant hadronic cross sections are then obtained as a convolution of the computed hard scattering cross section and non-perturbative functions characterising the parton- and spin-content of hadrons, which is the essence of the factorisation theorem. At typical hadronic scales below 1 GeV, the strong coupling gets large and therefore momentum distributions of quarks

and gluons inside the nucleon can only be calculated with non-perturbative methods such as lattice QCD. This is also related to the phenomenon of confinement, stating that free quarks or gluons can only be observed under extreme conditions as they existed in the early universe and in heavy ion collisions.

Heavy quark production follows rather different underlying QCD hard scattering dynamics than pion and jet production currently used to determine Δg.

For instance, no collinear emission off a heavy quark is allowed due to its mass, in contrast to massless final state particles, where non-perturbative parton-to-hadron fragmentation functions or elaborated jet definitions have to be introduced to absorb divergences associated with particle splittings with zero angle. However, relating theory and experiment for heavy flavour production is not at all an easy task. Experiments usually detect heavy flavours by reconstructing heavy meson decays, e.g., semi-leptonic decay lepton spectra. To avoid unwanted bias from deconvoluting experimental results back to the heavy quark level, all theoretical calculations should be done as close as possible to the observational level. Therefore, we implement in our parton-level Monte Carlo codes also the hadronisation of the produced charm and bottom quarks into D and B mesons and their subsequent decays. Both can be modelled by additional non-perturbative functions extracted from experimental data [53–57].

In the spin-averaged case, next-to-leading order (NLO) calculations for single-inclusive heavy quark hadro- and photoproduction have been available for quite some time [58–61], and partial results at the next-to-next-to-leading order level have been obtained recently [62–70]. In order to calculate also phenomenologically interesting heavy quark correlations, a parton-level Monte Carlo code, which integrates the phase space numerically, was developed in [71, 72]. Hadronisation into heavy mesons and their semileptonic decays were implemented later in [57]. In addition, our work allows the possibility of having longitudinally polarised initial states. This significantly extends previous, largely analytic calculations for spin-dependent heavy flavour production [73–76] which were limited to single-inclusive observables and could not include experimentally relevant acceptance cuts. We note that all order resummations of possibly large logarithms of the ratio of the transverse momentum and the mass of the heavy quark have been considered in the unpolarised case in references [77–82]. For the phenomenological applications in the polarised case studied in this work, resummation effects are expected to be small and hence ignored for the time being.

Another interesting observable related to heavy flavours is the so-called charge asymmetry which describes the difference of cross sections for producing a heavy quark Q or a heavy antiquark $\bar{Q}$ at a certain point in phase space, respectively. This asymmetry probes a subset of NLO radiative corrections and vanishes in tree-level approximation. It was studied in the context of top production in [83–85] in the unpolarised case. We study the corresponding polarised charge asymmetry [86, 87].

This thesis is organised as follows: In chapter 2 we start with briefly outlining the basic principles of QCD. We show how to derive the Feynman rules from the QCD Lagrangian and discuss the framework relevant for perturbative QCD calculations. We introduce the factorisation theorem, discuss the renormalisation procedure, and outline how to deal with collinear and infrared singularities at NLO accuracy. We review the current knowledge about unpolarised and longitudinally polarised parton density functions (PDFs) as well as the status of heavy quark production and hadronisation.

Chapter 3 is devoted to a detailed account of the theoretical framework. We discuss the ingredients of a perturbative QCD calculation at NLO accuracy. Special emphasis is put on the phase space integration where both largely analytical and numerical

methods are introduced. It is shown how experimentally relevant cross sections are obtained from the partonic hard scattering processes, which are presented in detail in chapter 4. Here, we also introduce the charge asymmetry.

In chapter 5 we present our phenomenological studies. We start with a comparison of the analytical and the numerical implementations of the phase space integration to validate our codes. Next, we present expectations for single-inclusive heavy quark distributions and the charge asymmetry for possible future experiments at GSI-FAIR and J-PARC. Then, we turn to hadroproduction at RHIC, where we give detailed results at the decay lepton level for both single-inclusive and correlation observables. We study the sensitivity of the corresponding double spin asymmetries, defined as the ratio of polarised and unpolarised cross sections, to the polarised gluon distribution. Currently available preliminary experimental results [18, 19, 88] are unfortunately not precise enough for a determination of $\Delta g(x)$.

We continue with presenting phenomenological results for photoproduction of charm and compare them to existing results from the COMPASS collaboration [20, 21, 51, 89]. We discuss a possible impact of our next-to-leading order results on the extraction of $\Delta g/g$ performed by COMPASS. We finish with expectations for photoproduction of charm and bottom quarks at a polarised lepton-proton collider currently considered and study the sensitivity of such measurements to the parton content of circularly polarised photons, which is completely unmeasured so far.

We summarise and conclude in chapter 6.

We note that some parts of this thesis, especially the phenomenological results in chapter 5, have already been published in peer-reviewed journals [87, 90, 91].

2

The basics of QCD

Quantum chromodynamics (QCD) describes the interaction caused by the strong force. The particles subjected to it are quarks and gluons. Quarks are fermions of spin 1/2 and can be organised in different families. Three families have been experimentally detected up to now. It has been shown that the existence of more than three families has not been completely excluded; see, e.g., [12] for a review. However, the newest results show that this possibility is rather improbable [15, 16]. Each family contains up- and down-type quarks. Flavours belong to the fundamental representation and contain colour triplets.

The force between the quarks is mediated by gluons, the gauge particles of the strong interaction belonging to the adjoint representation. Gluons carry a colour charge and can interact with themselves due to non-Abelian parts in the Lagrange density. Because of this non-Abelian structure, a closed solution of QCD has not been found yet, but several successful approximative methods have been developed.

In this chapter the basic ideas of QCD are introduced. As in many PhD theses, e.g., [52, 74, 92–94], we will only give a short account of the framework of QCD. Special emphasis is put on perturbative methods which will be used in the following chapters. The literature treating this subject is very large. The interested reader is referred to more detailed textbooks; see, e.g, [95–98].

2.1 The Lagrangian of QCD

The Lagrange density

$$L_{QCD} = L_{matter} + L_{YM} + L_{gauge} + L_{ghost} + L_{\bar{\theta}} \tag{2.1}$$

contains all the rich phenomenology described by quantum chromodynamics. The first two terms are the classical part of the Lagrangian, which is invariant under local gauge transformations of $SU(3)$.

The "matter" part of QCD reads

$$L_{matter} = \sum_{f=1}^{n_f} \bar{\psi}_f (i\gamma^\mu D_\mu - m_f)\psi_f, \tag{2.2}$$

where ψ_f is the Dirac field for a quark of mass m_f; γ^μ are the Dirac matrices, and

$$D_\mu = \partial_\mu - ig_s A^a_\mu T^a \tag{2.3}$$

is the covariant derivative. The Einstein sum convention is implicitly understood for repeated indices. f is the summation index over the different flavours, which differ in their masses. The strong coupling is denoted by g_s, the vectorial gauge field for the gluons by A and the colour matrices by T. They satisfy the commutation relation defining the group $SU(3)$:

$$[T^a, T^b] = if^{abc}T_c, \tag{2.4}$$

where f^{abc}, which is antisymmetric in its indices, is the structure constant of the group. The second term of the Lagrangian (2.1) is the Yang-Mills term. It describes the dynamics of the gluons and reads

$$L_{YM} = -\frac{1}{4}F^2 = -\frac{1}{4}\sum_{a=1}^{8} F^a_{\mu\nu}F^{\mu\nu,a}. \tag{2.5}$$

The last term of the field tensor

$$F^a_{\mu\nu} = \partial_\mu A^a_\nu - \partial_\nu A^a_\mu + g_s f^{abc} A^b_\mu A^c_\nu \tag{2.6}$$

is necessary to assure $SU(3)$ gauge invariance and accounts for the self-interaction of gluons in QCD.

The next step is to quantise the up to now classical Lagrangian. This is not unique and different methods exist for this purpose [99]. To this end, one adds gauge fixing and ghost terms [100] to the Lagrangian, which are for the transverse gauge

$$L_{gauge} = -\frac{1}{2\xi}\sum_{a=1}^{8}(\partial_\mu A^{\mu,a})^2 \tag{2.7}$$

and

$$L_{ghost} = (\partial_\mu \bar{c}_a)(\delta^{ac}\partial^\mu - g_s f^{acb} A^{\mu,b})c_c. \tag{2.8}$$

Here c_a is the scalar anti-commuting so-called Fadeev-Popov ghost field. Physical results do not depend on the details of gauge fixing. The ghost contribution, also called Fadeev-Popov term, assures unitarity and cancels effects by nonphysical polarisations of the gluons.

By fixing the gauge, one explicitly breaks the gauge symmetry of the Lagrangian. As a residual symmetry, the BRST symmetry remains.

We finally mention the term

$$L_{\bar{\theta}} = \bar{\theta}\frac{g^2}{32\pi^2}F^a_{\mu\nu}\tilde{F}^{a\mu\nu}, \tag{2.9}$$

where $\tilde{F}^{a\mu\nu} = \frac{1}{2}\epsilon^{\mu\nu\lambda\rho}F^a_{\lambda\rho}$ with the Levi-Civita tensor $\epsilon^{\mu\nu\lambda\rho}$ is the dual of $F^a_{\mu\nu}$. This term arises from the topology of the vacuum. It does not affect perturbative calculations, because it can be written as the total derivative of a current, i.e., as a surface term in the action. It is important, however, for some non-perturbative observables.

For solving the QCD equations of motion, no completely analytical method has been found up to now due to its non-Abelian structure. Therefore, several approximative and numerical methods have been devised. The mostly used methods are Shifman-Vainshtein-Zakharov (SVZ) and light cone sum rules, the large N_C limit, chiral perturbation theory, lattice QCD and perturbative QCD. Each of these methods has its advantages and shortcomings and is best suited for certain applications. The best approach for solving a certain problem in QCD depends on the nature of the problem.

As we focus in this thesis on scattering experiments characterised by large momentum transfers, we use the framework of perturbative QCD (pQCD). The presence of a hard scale keeps the expansion parameter, the coupling constant α_s, small, and, thus, allows for an expansion in α_s. One has noticed that α_s is not always small, but depends on the energy transfer of a regarded process. The observation that the coupling of QCD decreases at short distances is called asymptotic freedom.

The fact that QCD is a renormalisable quantum field theory has the consequence that g_s has to be defined at a renormalisation scale μ_r and varies with the 4-momentum transfer. Some details of renormalisation will be given in section 2.3 below. Nevertheless, we anticipate here the following important result of renormalisation: The scale evolution of the coupling $\alpha_s(\mu) \equiv \frac{g_s^2(\mu)}{4\pi}$ is predicted by the renormalisation group equation (RGE)

$$\mu \frac{dg_s(\mu)}{d\mu} = \beta[g_s(\mu)] \tag{2.10}$$

where the QCD beta function can be written as a power series

$$\beta(g_s) = -g_s \sum_{n=1}^{\infty} \left(\frac{\alpha_s}{4\pi}\right)^n \beta_n. \tag{2.11}$$

The first two terms have the form

$$\beta_1 = \frac{1}{3}(11N_C - 2n_f) \tag{2.12}$$

and

$$\beta_2 = \frac{1}{3}(102N_c - 38n_f) \tag{2.13}$$

with N_c and n_f being the number of colours and flavours, respectively.

Up to NLO accuracy, one can use

$$\alpha_s(\mu) = \frac{4\pi}{\beta_1 \ln(\mu^2/\Lambda^2)} \left[1 - \frac{\beta_2}{\beta_1^2} \frac{\ln[\ln(\mu^2/\Lambda^2)]}{\ln(\mu^2/\Lambda^2)}\right] \tag{2.14}$$

as an approximation. The fundamental parameter of QCD, Λ, has to be determined from experiment and is of the order $\mathcal{O}(200\text{ MeV})$ for dimensional regularisation.

As a result, perturbative QCD can only be applied for hard scales $\mu \gg \Lambda$.

If the distance between two quarks increases, the momentum transfer decreases and as a consequence the coupling constant $\alpha_s(\mu) = \frac{g_s^2(\mu)}{4\pi}$ will increase as shown in figure 2.1. Confinement is a consequence of this property: it is not possible to separate two quarks. If one tries to do so, due to the increasing coupling at large distances, a new quark-antiquark pair will be created from the vacuum, which will immediately form new hadrons with the separated quarks.

In the case that α_s is small, i.e., at high momentum transfers and short distances, one can express any physical observable, e.g., a cross section $[\Delta]\sigma$ in a power series in α_s with coefficients $[\Delta]A_i$,

$$[\Delta]\sigma = \sum_{i=0}^{\infty} \alpha_s^i [\Delta]A_i, \tag{2.15}$$

which in practise is truncated after a certain order due to the complexity of higher order corrections. We use the notation with the square bracket and the Delta to denote

unpolarised and longitudinally polarised quantities in one equation: without the Δ one gets the equation for the unpolarised and with the Δ for the longitudinally polarised observables.

Though unproven, it is generally assumed that the coefficients of QCD perturbative series are divergent, but the series expansion is asymptotic: A series is called asymptotic, if

$$\left| \Gamma - \sum_{n=0}^{N} \alpha_s^n \Gamma^{(n)} \right| \leq C_{N+1} \alpha_s^{N+1} \tag{2.16}$$

for all integers N.

Even if summed to all orders, a series $\sum_{n=0}^{\infty} \alpha_s^n \Gamma^{(n)}$ does not necessarily define Γ in the limit $\alpha_s \to 0$. However, the generally good agreement of experimental results and theoretical calculations in the framework of perturbative QCD give evidence that pQCD is a helpful tool to describe experimental phenomena.

The qualitative behaviour of observables can often be estimated by leading order calculations. For precise, quantitative calculations, one has to account for higher order corrections, which are sizable. Theoretical calculations depend on unphysical scales if the series is cut off.

Therefore, consider a quantity Γ independent of the scale μ:

$$0 = \mu \frac{\partial}{\partial \mu} \Gamma = \mu \frac{\partial}{\partial \mu} \sum_{n=0}^{\infty} \alpha_s^n \Gamma^{(n)}. \tag{2.17}$$

If the perturbative series is truncated at order N, a scale dependence of the order α_s^{N+1} remains:

$$\mu \frac{\partial}{\partial \mu} \sum_{n=0}^{N} \alpha_s^n \Gamma^{(n)} = -\mu \frac{\partial}{\partial \mu} \sum_{n=N+1}^{\infty} \alpha_s^n \Gamma^{(n)}. \tag{2.18}$$

Generally, a reduction of the scale dependence and hence of the theoretical uncertainties is expected, when higher orders are included in the calculation.

2.2 Outline of the derivation of the Feynman rules

The starting point for the derivation of the so-called Feynman rules used in pQCD calculations is the action

$$S_{QCD} = i \int d^4x L_{QCD}. \tag{2.19}$$

We want to calculate transitions from an initial state $|i\rangle$ to a final state $|f\rangle$. They are mediated by the operator

$$T\{\exp[-iS_{int}]\},$$

where S_{int} is the interaction part of S_{QCD}. In the interaction picture, this operator can be expanded in a series in terms of the coupling and the resulting terms can be decomposed using Wick's theorem. The results can be represented by Feynman diagrams.

The graphical representation of the Feynman diagrams is only a symbolic notation. Each line and each vertex in a Feynman diagram can be translated into a mathematical

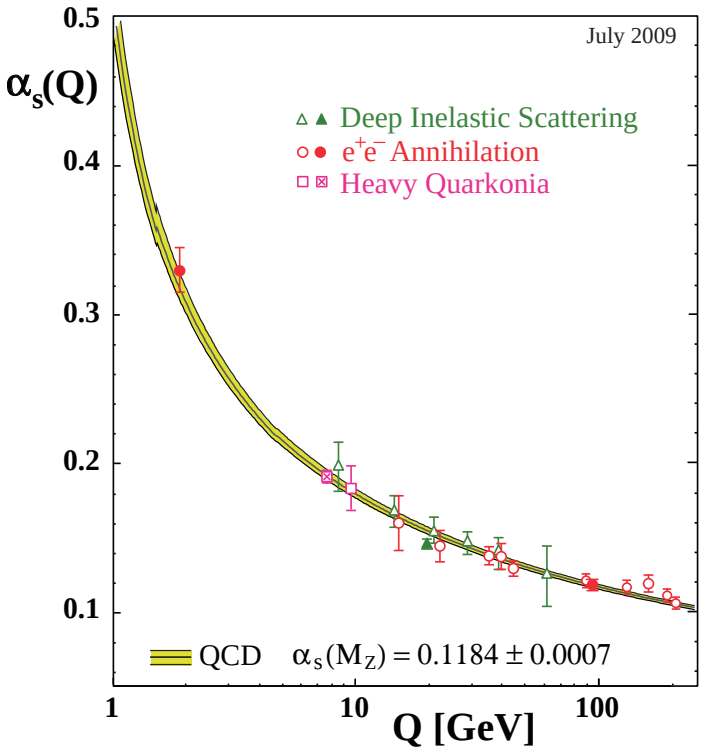

Figure 2.1: The running of the strong coupling constant. Taken from [101].

expression, as given in appendix A. The n point functions can be used to determine Feynman rules. An n point function is the vacuum expectation value of the product of n field operators. The contributions from these n point functions are after the Wick contraction sums and products of the propagators and vertex functions represented by Feynman rules.

2.3 Divergences and renormalisation

Calculations at the lowest order of the perturbative series, the tree level, are free of divergences, and relatively easy to perform, but in general not suitable for quantitative analyses. However, at higher orders, several types of divergences can be found: ultraviolet ones, infrared or soft ones, and collinear ones.

First, one encounters divergences for loop graphs, which come from the behaviour of the integrals at large internal momenta. They are called ultraviolet (UV) divergences and can be eliminated by adding appropriate counterterms to the Lagrangian. A strong motivation for such a renormalisation is that the standard model can only be valid up to the Planck scale because there gravity gets important. At present there is no generally accepted method for the unification of the standard model and gravity. By redefining in an appropriate way the normalisation of the parameters of the Lagrangian, i.e., the mass and the coupling constants, the ultraviolet divergences can systematically be absorbed in each order of perturbation theory. This procedure is called renormalisation. 't Hooft and Veltman have shown that QCD is a renormalisable quantum field theory [102].

From the behaviour of the loop integrals at low energies as well as from the phase space integration of particle momenta in the final state, infrared divergences can appear. Due to the Kinoshita-Lee-Nauenberg and the Bloch-Nordsieck [103] theorem, they cancel in the sum of all contributions up to the considered order. Collinear singularities are discussed below in detail and can be absorbed by the so-called mass factorisation.

In practise, the first step is to isolate the divergences or to make them manifest in a well-defined mathematical procedure. Different methods for this so-called regularisation exist. The most commonly adopted one is dimensional regularisation [102]. In this method, the number of the dimensions of space-time is – with $\varepsilon > 0$ – changed to $4+2\varepsilon$ for the infrared divergences and to $4-2\varepsilon$ for the ultraviolet ones. All these singularities manifest themselves as poles in $1/\varepsilon^p$ with $p \in \{1, 2\}$ in a NLO calculation. Although, in principle, one has to distinguish the ultraviolet and the infrared case, in practise, it is not explicitly necessary. It is sufficient to assume $\varepsilon \neq 0$. After renormalisation and factorisation discussed in section 2.4, all $1/\varepsilon^p$ poles cancel. This property provides a valuable check for the correctness of practical calculations. A further great advantage of dimensional regularisation is that it respects the invariance of the theory under translation, boosts, and gauge transformations.

Let us now take a detailed look at the renormalisation of the Lagrange density. To work directly with the renormalised quantities, one employs a method to replace the existing bare parameters of the theory by their renormalised equivalents. This results in re-writing the Lagrangian as a part containing the renormalised parameters and a part containing the counterterms:

$$L_{QCD} = L^R_{QCD} + L_{counterterms} \tag{2.20}$$

with

$$\begin{aligned} L_{counterterms} &= (Z_2 - 1)\overline{\psi}_R i\partial\!\!\!/ \psi_R - (Z_2 Z_m - 1) m_R \overline{\psi}_R \psi_R \\ &\quad + \frac{1}{2}(Z_3 - 1) A^a_{\mu R} \delta^{ab} [g^{\mu\nu}\partial^\lambda\partial_\lambda - \partial^\mu\partial^\nu] A^b_{\nu R} - (\tilde{Z}_3 - 1)\overline{c}^a_R \delta^{ab} \partial^\lambda \partial_\lambda c^b_R \\ &\quad - (Z_{1F} - 1) g_{sR} \overline{\psi}_R \gamma^\mu T^a \psi_R A^a_{\mu R} - (Z_1 - 1)\frac{1}{2} g_{sR} f^{abc} (\partial_\mu A^a_{\nu R} - \partial_\nu A^a_{\mu R}) A^{b\mu}_R A^{c\nu}_R \\ &\quad - (Z_4 - 1)\frac{1}{4} g^2_{sR} f^{abc} f^{ade} A^b_{\mu R} A^c_{\nu R} A^{d\mu}_R A^{e\nu}_R + (\tilde{Z}_1 - 1) g_{sR} f^{abc} \overline{c}^a_R \partial_\mu (A^{b\mu}_R c^c_R). \end{aligned} \tag{2.21}$$

The subscript R denotes the renormalised quantities. The Z are the multiplicative constants chosen to compensate the divergences. They obey

$$\begin{gathered} \psi = \sqrt{Z_2}\psi_R, \quad A^\mu = \sqrt{Z_3} A^\mu_R, \quad c = \sqrt{\tilde{Z}_3} c_R, \quad g_s = Z_g g_{sR}, \\ \xi = Z_3 \xi_R, \quad m = Z_m m_R, \quad Z_1 = Z_g Z_3^{3/2}, \quad Z_{1F} = Z_g Z_2 Z_3^{1/2}, \\ \tilde{Z}_1 = Z_g \tilde{Z}_3 Z_3^{1/2}, \quad Z_4 = Z_g^2 Z_3^2. \end{gathered} \tag{2.22}$$

From the conservation of the gauge invariance, one can derive the Slavnov-Taylor identities

$$\frac{Z_1}{Z_3} = \frac{\tilde{Z}_1}{\tilde{Z}_3} = \frac{Z_{1F}}{Z_2} = \frac{Z_4}{Z_1}. \tag{2.23}$$

Apart from the divergences the renormalisation constants Z_i can contain arbitrary finite pieces; the actual choice determines the renormalisation scheme. The most common one for QCD is the $\overline{\text{MS}}$ scheme [104], in which the $1/\varepsilon$ poles are subtracted

along with certain finite terms which are characteristic for dimensional regularisation. In practise, the renormalised Lagrange density leads to additional Feynman rules. Adopting them, the UV singularities cancel.

Experimentally, neither free quarks nor free gluons have ever been observed. This phenomenon is called confinement. As the Lagrange density contains only quarks and not hadrons, one has to account for the complications originating from confinement. Due to the factorisation theorem discussed in the next section, the calculation of matrix elements can be split in pQCD in a non-perturbative part describing the long-range interactions, the parton distribution and fragmentation functions, and the perturbatively calculable cross sections on the partonic level. Another class of divergences appears in processes with identified hadrons: collinear singularities result, when the momentum of an emitted particle on an external line becomes parallel to the particle that emitted it. This leads to a diverging propagator. Note that collinear singularities have already been introduced and discussed in detail in [74, 86]. In the next section we will show how a redefinition of the non-perturbative functions can describe this phenomenon.

2.4 Factorisation theorem

We will start with setting the notation for the considered process:

$$H_1(K_1) + H_2(K_2) \to h_1(P_1) + h_2(P_2) + X. \tag{2.24}$$

K_1, K_2 and P_1, P_2 denote here the four-momenta of the incoming and outgoing hadrons, respectively. As the subject of this work is heavy quark production, we can assume the h_i to be heavy quarks, as shown in figure 2.2, or mesons built from them. X contains all particles which are not observed. The reaction, as given in (2.24), corresponds to hadroproduction. In case of photoproduction, one has an incoming lepton or photon instead of one of the incoming hadrons H_1 or H_2. The factorisation theorem states that the hadronic cross section can be obtained through a convolution of the partonic cross sections calculated in perturbative QCD and the non-perturbative parton density functions [105–113]

$$d[\Delta]\sigma(\mu_f) = [\Delta]f_a^{(1)} \otimes [\Delta]f_b^{(2)} \otimes d[\Delta]\sigma_{ab}(\mu_f) + \mathcal{O}\left(\frac{\Lambda}{p_T}\right)^n. \tag{2.25}$$

In this equation the fragmentation functions of the heavy quarks are not included as they are fundamentally different from the ones of light (massless) quarks. The upper index corresponds to the number of the hadron or lepton or photon. The lower index denotes the parton in the parton density functions f and the initially unrenormalised partonic cross section $d[\Delta]\sigma_{ab}$. Recall that the notation with the square bracket gives both the unpolarised (without the Δ) and the longitudinally polarised cross sections (with the Δ) in the same equation.

Here, using the symbols + and − for the two helicities and respecting parity conservation of QCD, $d\sigma^{++} = d\sigma^{--}$ and $d\sigma^{+-} = d\sigma^{-+}$, the unpolarised and longitudinally polarised cross section can be defined by

$$d\sigma = \frac{1}{2}[d\sigma^{++} + d\sigma^{+-}] \tag{2.26}$$

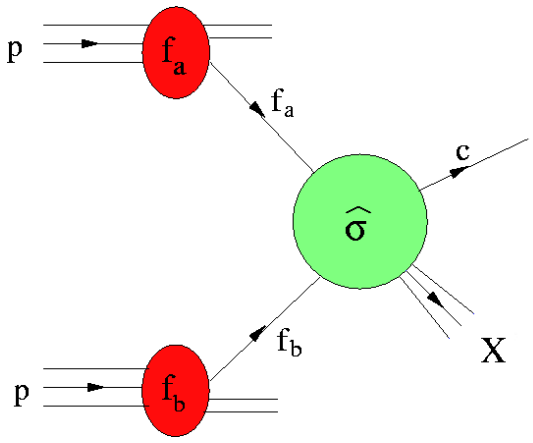

Figure 2.2: Cartoon illustrating factorisation for a generic single inclusive hadroproduction process. For simplicity, the notation is given here for the unpolarised case. The fragmentation functions of the heavy quarks are not shown as they are fundamentally different from the ones of light (massless) quarks.

and

$$d\Delta\sigma = \frac{1}{2}[d\sigma^{++} - d\sigma^{+-}], \tag{2.27}$$

respectively. Analogous definitions hold for the partonic cross sections, which will be denoted by $d[\Delta]\hat{\sigma}$. Defining f_+^+ and f_+^- as the probability to find a parton with helicity $+$ and $-$, respectively, in a hadron with helicity $+$, one defines $f = f_+^+ + f_+^-$ and $\Delta f = f_+^+ - f_+^-$. In the notation adopted here, the $+[-]$ sign denotes positive [negative] helicity.

The factorisation theorem is not exactly valid, but only up to so-called power corrections $\mathcal{O}\left(\frac{\Lambda}{p_T}\right)^n$, which are not discussed further in this work as we consider high p_T processes.

In equation (2.25), the fragmentation (hadronisation) of the heavy quarks into mesons containing a heavy quark is not included because for heavy quarks in the final state, no collinear divergences arise due to their non-vanishing masses and therefore the cross sections with the heavy quark in the final state are finite – contrary to the light particle case. For the light particle case several sets of fragmentation functions have been determined by various groups [114–116]. They serve as an important ingredient in the extraction of polarised parton distribution functions which will be introduced below. In the heavy quark case, for a comparison with experimental observations, it is crucial to include a model for the fragmentation to heavy quark mesons and their subsequent decay. As this procedure is somewhat non-trivial, a detailed discussion of this problem will be given later in section 2.8.

The hadronic cross section has been separated into long and short range parts: The processes which take place at large length scales, i.e., at small momentum transfers, are described by the parton density functions discussed in the next section. The processes proceeding at small length scales, i.e, at large momentum transfers, can be calculated in perturbative QCD.

As it is not possible to control which partons with which momenta from the initial hadrons participate at the partonic process, one has to sum over all possible partons

and to integrate over all kinematically allowed momentum fractions:

$$d[\Delta]\sigma(K_1,K_2) = \sum_{i,j}\int_0^1 dy_1\int_0^1 dy_2[\Delta]f_i^{(1)}(y_1,\mu_f^2)[\Delta]f_j^{(2)}(y_2,\mu_f^2)d[\Delta]\sigma_{ij}(\mu_f^2,\mu_r^2,y_1K_1,y_2K_2). \quad (2.28)$$

Recall that collinear divergences occur, when in a Feynman diagram the momentum of an internal particle gets parallel to an external massless one, because, in this case, the propagator of this internal particle is (quasi) on the mass shell and its denominator diverges. These divergences can be shifted by a redefinition of the bare parton densities into dressed ones, as will be described in detail in the following.

In the modified minimal subtraction ($\overline{\text{MS}}$) scheme [104] used in this work the term $\gamma_E - \ln(4\pi)$, which always occurs in dimensional regularisation, is subtracted together with the ε poles.

Using the splitting functions $[\Delta]P_{ij}(z)$, we define

$$[\Delta]G_{ij}(z,\mu_f^2,\mu_r^2) = \frac{\alpha_s(\mu_r^2)}{2\pi}[\Delta]P_{ij}(z)\left[-\frac{1}{\varepsilon}+\gamma_E-\ln(4\pi)+\ln\frac{\mu_f^2}{\mu_r^2}\right]. \quad (2.29)$$

The splitting functions $[\Delta]P_{ij}(z)$ contribute here up to $\mathcal{O}(\varepsilon^0)$, i.e., without the ε parts. For completeness, the $[\Delta]P_{ij}(z)$ are listed in appendix B. Introducing

$$[\Delta]\Gamma_{ij}(z,\mu_f^2,\mu_r^2) = \delta_{ij}\delta(1-z) + [\Delta]G_{ij}(z,\mu_f^2,\mu_r^2), \quad (2.30)$$

the renormalised parton density functions are given by

$$[\Delta]f_l(x_k,\mu_f^2) = \sum_i\int_0^1 dy_k\int_0^1 dz_k\delta(x_k-y_kz_k)[\Delta]f_i(y_k,\mu_f^2)[\Delta]\Gamma_{li}(z_k,\mu_f^2,\mu_r^2). \quad (2.31)$$

Using

$$d[\Delta]\hat{\sigma}_{ij}^{(0)} = d[\Delta]\sigma_{ij}^{(0)} \quad (2.32)$$

and

$$d[\Delta]\hat{\sigma}_{ij}^{(1)}(\mu_f^2,\mu_r^2) = d[\Delta]\sigma_{ij}^{(1)}(\mu_r^2) - d[\Delta]\sigma_{M,ij}^{(1)}(\mu_f^2,\mu_r^2), \quad (2.33)$$

where

$$d[\Delta]\sigma_{M,ij} = \sum_{l,m}\int_0^1 dz_1\int_0^1 dz_2[[\Delta]G_{li}(z_1,\mu_f^2,\mu_r^2)\delta_{mj}\delta(1-z_2)+ [\Delta]G_{mj}(z_2,\mu_f^2,\mu_r^2)\delta_{li}\delta(1-z_1)]d[\Delta]\sigma_{lm}^{(0)}(z_1k_1,z_2k_2), \quad (2.34)$$

the result for the cross section is:

$$d[\Delta]\sigma(\mu_f^2,\mu_r^2) = \sum_{a,b}[\Delta]f_a^{(1)}(\mu_f^2)\otimes[\Delta]f_b^{(2)}(\mu_f^2)\otimes d[\Delta]\hat{\sigma}(\mu_f^2,\mu_r^2) \quad (2.35)$$

or more explicitly written

$$[\Delta]\sigma(K_1,K_2) = \sum_{a,b}\int_0^1 dx_1\int_0^1 dx_2[\Delta]f_a^{(1)}(x_1,\mu_f^2)[\Delta]f_b^{(2)}(x_2,\mu_f^2)[\Delta]\hat{\sigma}_{ab}(\mu_f^2,\mu_r^2,x_1K_1,x_2K_2). \quad (2.36)$$

The symbol $\otimes$ is used as a shortcut to note a convolution. The $[\Delta]\hat{\sigma}_{ab}$ are finite.

2.5 The parton model and parton distribution functions

Deep-inelastic scattering has provided evidence for the existence of point-like constituents inside hadrons. These constituents are called partons. The term partons comprises both quarks and gluons.

The naive parton model was proposed before the advent of QCD. A fast moving hadron can be thought of as consisting of many collinear point-like constituents, the partons. Later on, the separation of short- and long-distance physics as encoded in the factorisation theorem discussed above has provided the theoretical foundation of the parton model. In pQCD one can calculate partonic hard-scattering cross sections. However, only their hadronic counterparts are experimentally observable. The parton model and the factorisation theorem in particular relate them as stated, e.g., in equation (2.36).

The hadronic cross section can be expressed as a convolution of the non-perturbative parton distribution functions for each hadron with the calculable scattering cross sections $d[\Delta]\hat{\sigma}_{ij}$ of the two partons i and j, as explained in the previous section.

As a consequence of the factorisation theorem, the parton densities $f_i(x, \mu_f^2)$, which describe physics at long distances, are universal, i.e., can be applied in calculations of different hadronic scattering cross sections.

The partonic cross sections that describe the physics at short distances, shall be calculated perturbatively. The scale, at which the separation of short- and long-distance phenomena is done, is set by the factorisation scale μ_f. The actual choice of μ_f is arbitrary and physical cross sections should not depend on μ_f. This leads to a powerful set of renormalisation group equations.

Perturbative QCD does not permit us to calculate size and form of the parton density functions, but their scale evolution is predicted by the DGLAP renormalisation group equations [117–119]. Hence, if one knows the parton density functions at one scale μ_0, they can be predicted at any arbitrary scale $\mu > \mu_0$ with the help of the DGLAP equations.

In the lowest order, they read

$$\frac{d[\Delta]g(x,\mu^2)}{d\ln\mu^2} = \frac{\alpha_s(\mu^2)}{2\pi}\int_x^1 \frac{dy}{y}\left[\sum_q [\Delta]P_{gq}(x/y)[\Delta]q(y,\mu^2) + [\Delta]P_{gg}(x/y)[\Delta]g(y,\mu^2)\right] \tag{2.37}$$

for the gluons and

$$\frac{d[\Delta]q(x,\mu^2)}{d\ln\mu^2} = \frac{\alpha_s(\mu^2)}{2\pi}\int_x^1 \frac{dy}{y}[[\Delta]P_{qq}(x/y)[\Delta]q(y,\mu^2) + [\Delta]P_{qg}(x/y)[\Delta]g(y,\mu^2)] \tag{2.38}$$

for each quark flavour. It is also possible to write these coupled equations in compact matrix form. In the evolution of the quark parton density functions, the first term on the right hand side of equation (2.38) describes the possibility that a quark carrying a momentum fraction x can have been produced by a quark with a larger momentum fraction y having emitted a gluon. Likewise, the second term results from the alternative that a quark with momentum fraction x is produced by a gluon with larger momentum fraction. An analogous interpretation is valid for (2.37), which describes the possibilities to generate a gluon from a quark or a gluon.

The functions $[\Delta]P_{ab}(z)$ are the so-called splitting functions which are calculable in perturbative QCD [117, 120, 121]. They are listed in appendix B. In the case of

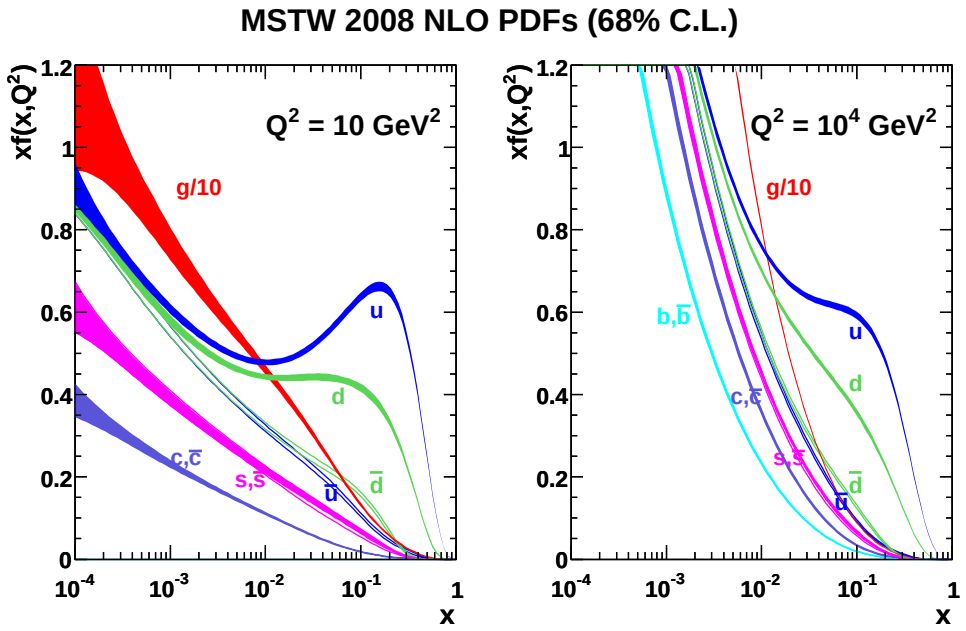

Figure 2.3: The unpolarised parton distributions of MSTW and their uncertainties. Figure taken from [128].

infrared corrections being absent, $[\Delta]P_{ab}(z)$ gives the probability to produce a parton of type a in a collinear splitting of a parton of type b with a fraction z of its longitudinal momentum.

Taking into account also the helicity degree of freedom, unpolarised parton density functions are defined as the sum of the momentum distributions with parallel and antiparallel helicity of the hadron and parton, f_+^+ and f_-^+, respectively. The polarised ones, $\Delta f(x, \mu^2)$, are the difference between these two contributions, see equation (1.4). Parton distribution functions need to be extracted from experiment. A functional form with several fit parameters is assumed. Using all relevant data, where factorisation applies and the partonic cross sections calculated in pQCD, a global fit can be performed. In the unpolarised case, the most recent global fits have been done by the CTEQ and MSTW (former MRST) collaborations [122–127]. The results of the MSTW group are presented in figure 2.3. In the naive parton model, each valence quark carries one third of the total momentum of the proton. In the improved parton model, where it is not anymore assumed that each constituent quark has the same momentum and sea quarks come into play, one can nevertheless identify a peak in the u and d quark distributions around 1/3. The figure shows also the current uncertainty bands. In general, the uncertainty for the gluon distribution is larger than for the valence quarks. Especially, in the limit $x \to 1$ the uncertainties grow for all parton distributions. It is a goal of further experiments, e.g., at the LHC, to pin down parton densities more precisely.

In leading order, the helicity dependent parton distribution functions are subject to the positivity constraint

$$|\Delta f(x, \mu)| < f(x, \mu).$$

Because the interpretation as a probability density is valid only at leading order, this

positivity constraint is – strictly speaking – not correct anymore at NLO. However, if the NLO corrections are not too large, it can be kept as an approximate constraint. Positivity applies of course to physical cross sections, i.e., $|d\Delta\sigma| \leq d\sigma$.

Earlier determinations of helicity dependent parton distribution functions only included DIS data and assumed a flavour symmetric sea [129]. The helicity dependent gluon distribution $\Delta g(x)$ was widely unconstrained, as in DIS processes the gluon does not enter at leading order.

A more recent work (DNS [130]) included semi-inclusive DIS data and resulted in two different sets of parton distribution functions related to different assumptions about fragmentation functions (Kretzer and KKP), which served as an additional non-perturbative input in the semi-inclusive DIS.

The state of the art is a first global fit including DIS, semi-inclusive DIS, and RHIC data [30, 31]. In particular, single-inclusive pion [131] and jet production [132], measured in spin-dependent proton-proton collisions at BNL-RHIC, have started to put significant limits on the amount of gluon polarisation in the nucleon [30]. New, preliminary single and di-jet data from the STAR collaboration [45] show for the first time tantalising hints for a non-zero $\Delta g(x, \mu)$ [46, 133]. Due to the given kinematics, the current probes mainly constrain Δg in the medium-to-large x region, $0.05 \lesssim x \lesssim 0.2$, which is not sufficient to determine its integral (the first moment) reliably.

It results in a rather small Δg in the range of momentum fractions $0.05 \leq x \leq 0.2$ as shown in figure 2.4. This region is mainly constrained by the RHIC data. Beyond this region, Δg is still largely unconstrained. Therefore, the first moment ΔG, defined in equation (1.3), has still large uncertainties. Also improvements for the sea distributions have been achieved. Especially, a node in the Δs distribution and $\Delta\bar{u} > 0$ and $\Delta\bar{d} < 0$ have been found. In figure 2.4 the DSSV results and their error estimates are compared to older sets of parton distribution functions. Recall that all of them, except the DNS2005 sets, have a flavour symmetric sea. Note that from the asymmetry analysis collaboration the AAC03 parton density functions [134] are shown, as these ones will be used in chapter 5. The quark and antiquark distributions of the AAC08 analysis [135] are similar to AAC03. The AAC08 analysis provides two different sets, which, however, are very similar, except for the polarised gluon. One set has a gluon similar to AAC03, the other one – as DSSV – a gluon with a node. However, the absolute values of the AAC08 gluon are much larger than the DSSV gluon. For completeness, we note that also the PDFs of LSS2010 [136] show a moderate gluon, which is within the errors compatible with the analyses of DSSV and DSSV++ [46].

Some experiments have done their own analysis on $\Delta g/g$. In this thesis, we will not discuss the methods used there. We only show the results in comparison to the DSSV values in figure 2.5. Most of the data points agree in the range of the errors with the DSSV fit.

We want to mention that another possible approach is that momenta of the parton density functions can be calculated on the lattice. But, only some low integer momenta are accessible on the lattice at the moment [138]. Δg cannot be calculated in lattice QCD.

2.6 Photonic parton density functions

We will not only discuss heavy quark production in hadron-hadron scattering, but also in lepton-hadron scattering. The latter is measured by COMPASS at CERN and

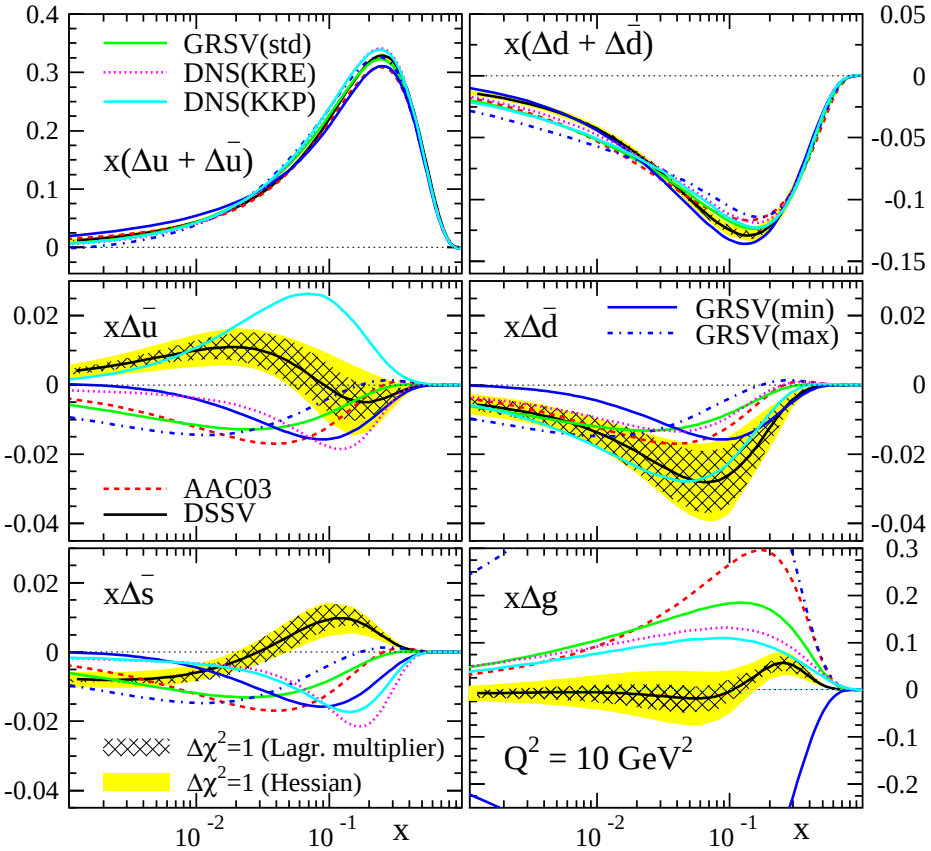

Figure 2.4: The polarised parton distributions from DSSV. The uncertainties are shown as resulting from two different methods applied by the DSSV group: the Lagrange multiplier and the Hessian method. More details about these two methods can be found in [31]. This figure has been adopted from a similar figure in [31]. Not shown are the very new DSSV++ [46] parton distribution functions. The function $\Delta g(x)$ from DSSV++ lies between the functions $\Delta g(x)$ from GRSV(std) and DSSV.

will be pursued in the future at an EIC. In this work, we are mainly concerned with photoproduction, where the photon is quasi-real. Its energy spectrum, i.e., the photons radiated off the lepton, can be described by the Weizsäcker-Williams approximation. This spectrum can be calculated in the framework of quantum electrodynamics (QED). The results for the unpolarised and polarised cases are [139–143]

$$P_{\gamma l} = \frac{\alpha_{em}}{2\pi}\left[\frac{1+(1-y)^2}{y}\ln\frac{Q^2_{\max}(1-y)}{m_l^2 y^2} + 2m_l^2 y\left(\frac{1}{Q^2_{\max}} - \frac{1-y}{m_l^2 y}\right)\right] \tag{2.39}$$

and

$$\Delta P_{\gamma l} = \frac{\alpha_{em}}{2\pi}\left[\frac{1-(1-y)^2}{y}\ln\frac{Q^2_{\max}(1-y)}{m_l^2 y^2} + 2m_l^2 y^2\left(\frac{1}{Q^2_{\max}} - \frac{1-y}{m_l^2 y^2}\right)\right], \tag{2.40}$$

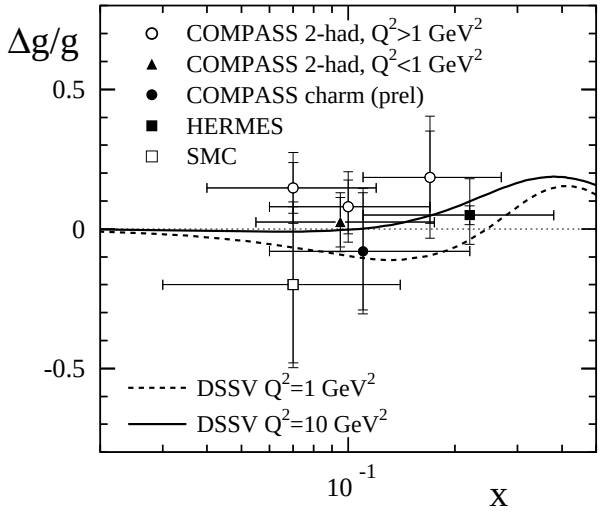

Figure 2.5: Current experimental results on $\Delta g(x)/g(x)$. Some data points are taken from [22, 137].

respectively. The second terms in the square brackets give sizable contributions to the splitting functions for muons due to their large mass. These terms give important contributions to the calculations for COMPASS which has a muon beam.

In heavy quark production, the photon can interact with the hadron either directly by photon-gluon fusion or photon-(anti)quark-scattering in order to produce a heavy quark pair or fluctuate into quarks and gluons which enter the hard scattering process. In the first case, one has $[\Delta]f_\gamma(x,\mu) = \delta(1-x)$. In the second – the resolved – one, the photon parton density functions have to be determined experimentally. In the unpolarised case most of the information on the non-perturbative hadronic structure of photons comes from $\gamma^*\gamma$ DIS in e^+e^- annihilations. These unpolarised photon distribution functions are known as the GRV_γ distributions [144]. As the circularly polarised parton distributions of the photon are completely unknown, only minimum and maximum scenarios as shown in figure 2.6 can be given.

Also for the photon parton density functions, evolution equations similar to the DGLAP equations exist; however, an additional inhomogeneity arises, since the photon can act as its own parton:

$$\frac{d[\Delta]q_\gamma(x,\mu)}{d\ln\mu} = \frac{\alpha_s}{2\pi}([\Delta]k_q(x,\mu) + \{[\Delta]P_{qq}\otimes[\Delta]q_\gamma + [\Delta]P_{qg}\otimes[\Delta]g_\gamma\}), \tag{2.41}$$

$$\frac{d[\Delta]g_\gamma(x,\mu)}{d\ln\mu} = \frac{\alpha_s}{2\pi}([\Delta]k_g(x,\mu) + \{[\Delta]P_{gq}\otimes([\Delta]q_\gamma + [\Delta]\bar{q}_\gamma) + [\Delta]P_{gg}\otimes[\Delta]g_\gamma\}). \tag{2.42}$$

Recall that the symbol $\otimes$ denotes (as usual) a convolution.

As a consequence, the solution of these inhomogeneous evolution equations has a point-like part $[\Delta]f_{\gamma,\,pl}$, which can be calculated perturbatively, and a hadronic contribution

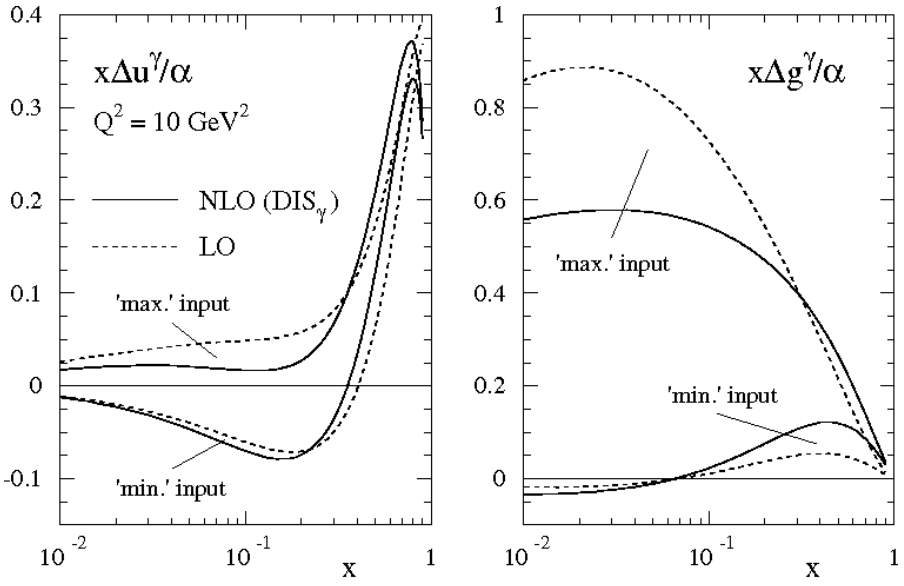

Figure 2.6: The minimum and maximum scenario for the polarised photon parton distribution functions for both LO and NLO at a scale of 10 GeV^2. The left and right panel show the photon parton density functions for the up quark and the gluon, respectively. Figure taken from [145].

$[\Delta]f_{\gamma,\,had}$ which follows from the solution of the according homogeneous equations, see, e.g., [52, 94]. The interested reader is referred to the literature for details.

It follows from the fact that the photonic parton density functions have a point-like and a hadronic component that cross sections with an incoming photon are composed of two parts: the direct and the resolved part:

$$\Delta\sigma = \Delta\sigma_{\mathrm{dir}} + \Delta\sigma_{\mathrm{res}}. \tag{2.43}$$

Experimentally measurable is only the sum of the direct and the resolved part of the cross section, but neither the direct part $\Delta\sigma_{\mathrm{dir}}$ nor the resolved part $\Delta\sigma_{\mathrm{res}}$ alone. Indeed, for certain experimental constellations like charm production at COMPASS, the resolved contribution turns out to be small compared to the direct part, see our results in chapter 5.

Convoluting the photon content of the lepton as given by the Weizsäcker-Williams spectrum, $[\Delta]P_{\gamma l}(y)$, and the photon parton distribution f_γ functions, one gets for the parton density functions in a lepton the master formula

$$[\Delta]f(x_l,\mu_f) = \int_{x_l}^{1} \frac{dy}{y}[\Delta]P_{\gamma l}(y)[\Delta]f_\gamma\left(x_\gamma = \frac{x_l}{y},\mu_f\right), \tag{2.44}$$

which is valid both for the direct and the resolved case. The $[\Delta]f_\gamma$ are of the order of $1/\alpha_s$. This has the consequence that the direct and the resolved contributions enter at the same perturbative order.

2.7 The FONLL formalism for heavy quark production

Up to now we have discussed the parton distribution functions, which are universal for all QCD processes. Now we will turn to some special issues concerning heavy quark production.

A decade ago, the pQCD cross sections undershot the experimental data for bottom production at TeVatron by a factor of roughly 2–3. In [146], it has been pointed out that several ameliorations have led to an improvement of the agreement between theory and experiment.

One improvement is that today not only at least a next-to-leading order formalism is used, but that large next-to-leading logarithms at high transverse momenta are resummed. They become important if the transverse momentum of the produced heavy quark becomes much larger than its mass, as in these cases large logarithms arise to all orders of the perturbative expansion, which are not included in a fixed-order calculation (like at NLO level). This second approach resums all these logarithms at the next-to-leading level of accuracy and is also called the fragmentation function approach: For high p_T the heavy quark arises from a light final state particle by a perturbatively calculable fragmentation function [77] $D_i^{(h)}(z,\mu)$.

The factorised form then reads [78]

$$\frac{Ed^3\sigma}{d^3k} = \sum_i \int \frac{E' d^3\hat{\sigma}_i}{d^3k'}(k',\mu) D_i^{(h)}(z,\mu)\frac{dz}{z^2}. \tag{2.45}$$

The term $\frac{Ed^3\sigma}{d^3k}$ represents the heavy quark cross section at high p_T, which is given as a convolution of the cross section for massless final states $\frac{E' d^3\hat{\sigma}_i}{d^3k'}(k',\mu)$ with the corresponding fragmentation functions $D_i^{(h)}(z,\mu)$. However, this method can not describe the mass dependence of the fixed-order cross section for low p_T.

As a consequence, the fixed-order calculation should be trusted more at low p_T and the fragmentation function method more at high p_T and a matching formalism (like FONLL (Fixed Order Next-to-Leading-Log) [81, 82]) for these two approaches should be used in order to make use of the advantages of both possibilities. Now, the question remains, what low p_T and what high p_T is and at what p_T the matching must be done. We will not discuss this delicate question in this thesis, but refer the reader to the original literature treating this matching [81]. In the original literature the matching between both formalisms is performed roughly when the condition $\sqrt{m^2+p_T^2} \approx 5m$ is fulfilled. Recall that m here denotes the mass of the heavy quark.

In this thesis we will work at the fixed-order-NLO level and not use the FONLL corrections, as we focus on rather small transverse momenta for the polarised cross sections and the spin asymmetry. Furthermore, we study correlations between the produced heavy quark and antiquark and their decay products. A possible future extension of this work could be the calculation of the NLL corrections in the polarised case and the extension of the matching formalism to it.

2.8 Hadronisation and decay of heavy quarks

Heavy quarks can be detected directly by so-called micro-vertex detectors as envisioned for future projects. In current experiments, usually the mesons stemming from the

heavy quarks are detected directly or via their semi-leptonic decays. In the following we will explain the technical framework for this hadronisation and – if experimentally relevant – the subsequent decay of the produced mesons into leptons. The cross section for the charmed mesons can be calculated by a convolution of the cross sections for heavy quarks and the fragmentation $D^{Q\to H_Q}$ of the heavy quark Q into a heavy meson H_Q. This is suitable for experiments reconstructing the heavy quark meson directly, e.g, COMPASS. Other experiments, like RHIC detect presumably the semi-leptonic decay spectrum of the electron. This decay spectrum can be calculated by a convolution of the cross section for the heavy meson and the semi-leptonic decay spectrum $f^{H_Q\to e}$. The resulting formula is schematically given by

$$\frac{Ed^3\sigma(e)}{dp^3} = \frac{E_Q d^3\sigma(Q)}{dp_Q^3} \otimes D^{Q\to H_Q} \otimes f^{H_Q\to e,\mu}. \tag{2.46}$$

$\sigma(Q)$ represents the cross section for the production of heavy quarks. Note that the other two ingredients to equation (2.46) are the fragmentation $D^{Q\to H_Q}$ of the heavy quark Q into a heavy meson H_Q and the semi-leptonic decay $f^{H_Q\to e}$ of H_Q into the experimentally observed electron e (or another lepton). Since m cuts off final-state collinear singularities associated with the heavy quark, its hadronisation $D^{Q\to H_Q}$ is fundamentally different from those for light quarks and gluons. Recall that in the latter case, scale-dependent parton-to-hadron fragmentation functions [114–116] have to be introduced by virtue of the factorisation theorem. The non-perturbative transition $Q \to H_Q$ is described by various phenomenological models (e.g., Peterson [53], Kartvelishvili [54], BCFY [55]) using a scale independent function $D^{Q\to H_Q}$, whose parameters are determined from fits to e^+e^- data [56].

In contrast to fragmentation functions for light quarks and gluons into light mesons [114–116], the non-perturbative functions describing the hadronisation of heavy quarks are very hard, i.e., charm and bottom quarks only lose very little momentum when hadronising. The main effect of the fragmentation functions is to introduce a shift in the normalisation of the heavy meson spectra. It depends mainly on the average momentum fraction z taken by the meson.

The functional form of the fragmentation function and the parameters used in it should correspond to the precise method of the perturbative calculation [146].

However, fixed-order-NLO calculations for e^+e^- do not describe the experimental results. Despite this observation, in [56] a range for the parameters of the fragmentation function is proposed. It was shown that for single-inclusive meson p_T spectra certain Mellin moments are more important than others. To see this, assume that the single-inclusive partonic cross section behaves like $d\hat{\sigma}/dp_T^Q = A(p_T^Q)^{-n}$ near some p_T^Q. Using the Mellin moments, defined as

$$D_N = \int D(z) z^N \frac{dz}{z} \tag{2.47}$$

for any N, one finds [146]

$$\frac{d\sigma}{dp_T} = \int dz dp_T^Q D(z) \frac{A}{(p_T^Q)^n} \delta(p_T - z p_T^Q) = \frac{A}{p_T^n} D_n. \tag{2.48}$$

From this observation it follows that the free parameter in the fragmentation function should be chosen in such a way that the most relevant Mellin moments $N \approx n$ are fitted well. So, especially the lowest moments of the fragmentation functions D_N are important. Here the Kartvelishvili form shows some advantages compared to the Peterson form.

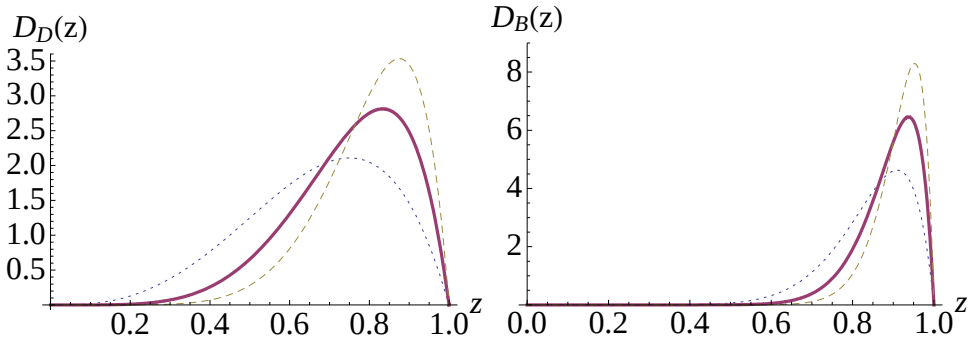

Figure 2.7: The Kartvelishvili form $D_{D,B}(z) \equiv D^{Q\to H_Q}(z) = N_Q(1-z)z^{\alpha_Q}$ with $N_Q = \alpha_Q^2 + 3\alpha_Q + 2$ of the heavy quark fragmentation functions for $c \to D$ and for $b \to B$. The solid line is our default choice with $\alpha = 5$ and $\alpha = 15$, respectively. The dotted and the dashed line correspond to the lowest value ($\alpha = 3$ and $\alpha = 10$) and to the highest value ($\alpha = 7$ and $\alpha = 20$), respectively.

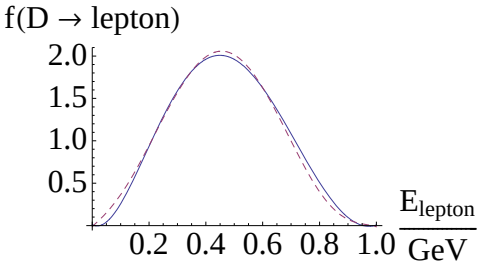

Figure 2.8: The energy distribution of leptons from D meson decays in the c.m.s. of the D meson: our fit (dashed line) and the one of [57] (solid line).

In recent studies of heavy quark production, the FONLL framework is usually used in the unpolarised case. In [57], the fragmentation functions of Kartvelishvili and BCFY are adopted for the hadronisation of bottom and charm, respectively.

Summarising, the details of the shape of $D^{Q\to H_Q}(z)$ have a negligible effect [56]. Moreover, one can expect that ratios of cross sections, like in the experimentally most relevant double-spin asymmetry

$$A_{LL} \equiv \frac{d\Delta\sigma}{d\sigma}, \tag{2.49}$$

are much less affected by the actual choice of $D^{Q\to H_Q}(z)$. We will validate this statement with our results in chapter 5.

Having all this in mind, we use the functional form of Kartvelishvili-Likhoded-Petrov [54] with a single parameter α_Q controlling the hardness of

$$D^{Q\to H_Q}(z) = N_Q z^{\alpha_Q}(1-z)\,, \tag{2.50}$$

where $N_Q = (\alpha_Q+1)(\alpha_Q+2)$ to normalise the integral of $D^{Q\to H_Q}(z)$ to one. We take $\alpha_c = 5$ and $\alpha_b = 15$ from table 4 in reference [56] as the default values in equation (2.50) and vary them in the range $3 \le \alpha_c \le 7$ and $10 \le \alpha_b \le 20$, respectively, to estimate the uncertainties associated with the choice of α_Q. As in reference [57], the fragmentation is numerically performed by rescaling the heavy quark's three-momentum by z at a

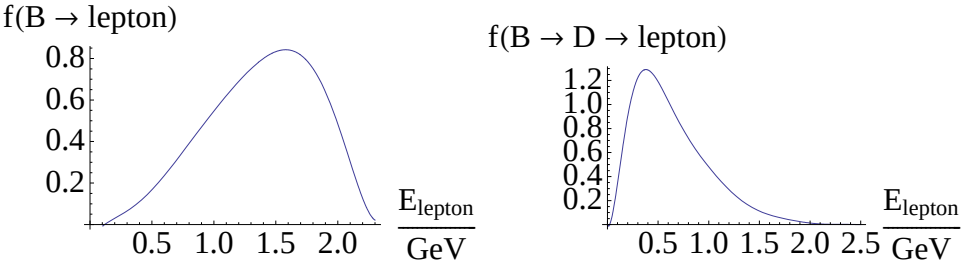

Figure 2.9: The energy distributions for B mesons decaying into leptons directly (left) and via the cascade $B \to D \to$ lepton in the c.m.s. of the B meson.

constant angle in the laboratory frame, i.e., $\vec{p}_{H_Q} = z\vec{p}_Q$. The uncertainty introduced by this particular choice for the "scaling variable" z, which is not uniquely defined for $D^{Q\to H_Q}$, was shown to be not larger than scale and mass uncertainties [147] and will not be considered further.

Finally, in some experiments leptons from meson decays are observed. The decay is described by semi-leptonic decay spectra and branching ratios. The branching ratios can be taken from the PDG values [148]. The spectra for the semi-leptonic decays of the D and B mesons into leptons are controlled by phenomenological functions $f^{H_Q\to e,\mu}$ which need to be extracted from data as well. Here we use the spectra obtained in references [57, 149] based on BaBar and CLEO data [150–152]. Of course, branching ratios drop out of experimentally relevant double-spin asymmetries (2.49).

As mentioned, to describe the decay spectrum, results on the meson level have to be folded with decay spectra [57]. Recall that the resulting formula is schematically given by equation (2.46). The decay functions $f^{H_Q\to\text{lepton}}$ are obtained by phenomenological fits. $f^{H_Q\to\text{lepton}}$ gives the probability that the decay lepton gets a certain energy in the rest frame of the heavy meson. A polynomial ansatz for such a fit can be used. For the D meson decay we have refitted the spectrum given in figure 4 of [152] and obtained a function with a very similar phenomenology as in [57]. However, we used a polynomial ansatz of order 6 and [57] one of order 5. The two results are compared in figure 2.8. In figure 2.9 both the spectra for the direct decay $B \to$ lepton and $B \to D \to$ lepton are shown. We note that further parametrisations for $f^{H_Q\to\text{lepton}}$ are given in [153].

We have thus summarised the framework typically used if decay leptons of heavy mesons are studied. Another possibility is to examine hadronic decay modes of the mesons, as it is done, e.g., by the COMPASS collaboration for the photon-gluon-fusion process. In this case, usually the meson can be reconstructed from its decay products [20, 21], and the functions $f^{H_Q\to\text{lepton}}$ are not necessary.

Recall that we focus in this work on cross sections and spin asymmetries which are in the range of p_T, where resummation effects of large transverse momenta can be safely ignored. Also, threshold resummation effects are beyond the scope of this thesis.

3

Cross sections for heavy quarks at next-to-leading order

In the previous chapter the basic concept of factorisation has been introduced, which is the starting point for any calculation within pQCD. The principle necessity of regularisation and renormalisation has been discussed with special focus on dimensional regularisation. Next, we will provide more insight into the details of the calculation of heavy flavour hadro- and photoproduction which is the basis for the phenomenological applications in chapter 5. After explaining some subtleties of the n dimensional Dirac algebra, we will turn to the partonic matrix elements and the proper procedure for combining virtual one-loop and real emission corrections.

Let us shortly summarise the most important points of a pQCD calculation: The integration and the summation over unobserved final state momenta leads to the phase space formulas discussed in subsection 3.4. The cross section is normalised to the flux of the incoming particles, $1/(2s)$, with s being the partonic centre-of-mass energy squared of the incoming particles. The partonic subprocesses are described by the interaction part of the action, whose decomposition leads to the matrix elements and the Feynman rules for their calculation, see appendix A. In the initial state we regard both unpolarised and longitudinally polarised particles. The polarised cross sections are calculated, the re-calculation of unpolarised cross sections, which are well-known from the literature, at the same time serves as an important check of the correctness of the results. The partonic subprocesses will be discussed in detail in chapter 4.

In this context, different methods for the phase space integration are discussed. A largely analytic approach can provide numerical results with little computational effort. It is restricted, however, to certain, sufficiently simple observables like single-inclusive cross sections. Unfortunately, with this approach it is not possible to include experimental cuts or compute phenomenologically relevant heavy flavour correlations. To do this, we perform the complete phase space integration with numerical methods, which requires to regularise singularities. Therefore, we use the subtraction method introduced in section 3.5. We will compare the results obtained with the analytical and the numerical method later in section 5.1.

3.1 Preliminaries

Recall that the factorisation theorem factorises via $d\sigma = f_a \otimes f_b \otimes d\hat{\sigma}$ and $d\Delta\sigma = \Delta f_a \otimes \Delta f_b \otimes d\Delta\hat{\sigma}$ the cross sections in a long-range non-perturbative and a short-range

perturbative part. Now, we turn to the perturbative part and discuss its ingredients: the matrix elements, the flux factor and the phase space.

Using λ_1 and λ_2 for the helicities of the incoming partons and the projection operators for external lines, which are mentioned in appendix A, the matrix element can be written as

$$|M|^2(\lambda_1, \lambda_2) = |\overline{M}|^2 + \lambda_1\lambda_2\Delta|M|^2. \tag{3.1}$$

Due to parity conservation of QCD there are no terms which are only proportional to either λ_1 or λ_2. Analogously to the unpolarised and longitudinally polarised cross sections, the unpolarised squared matrix element can be written as

$$|\overline{M}|^2 \equiv \frac{1}{2}[|M|^2(++) + |M|^2(+-)] \tag{3.2}$$

and the polarised one as

$$\Delta|M|^2 \equiv \frac{1}{2}[|M|^2(++) - |M|^2(+-)]. \tag{3.3}$$

In general, every partonic cross section can be expressed as a product of the partonic flux, the phase space factor and the squared matrix element:

$$d\hat{\sigma}(\lambda_1, \lambda_2) = \frac{1}{2s}|M(\lambda_1, \lambda_2)|^2 dPS. \tag{3.4}$$

In dPS, each final state particle is assigned the Lorentz-invariant measure $\int \frac{d^n p}{(2\pi)^{n-1}}$ such that for r final particles with masses m_i one has to use the appropriate phase space

$$dPS_{2\to r} = (2\pi)^n \delta^{(n)}(k_1 + k_2 - \sum_{j=1}^{r} p_j) \prod_{i=1}^{r} \frac{d^n p_i}{(2\pi)^{n-1}} \delta(p_i^2 - m_i^2)\Theta(E_i) \tag{3.5}$$

where E_i is the zero component of the four-momentum p_i. Here, two incoming particles with momentum k_1 and k_2 are assumed. .

This leads to

$$d\hat{\sigma}(\lambda_1, \lambda_2) = \sum_{r\in\mathbb{N}} \frac{1}{2s}|M_{2\to r}(\lambda_1, \lambda_2)|^2 dPS_{2\to r}. \tag{3.6}$$

Moreover, in n dimensions, fermions have two spin degrees of freedom as in four dimensions, but massless bosons have $n-2$. In the calculation of unpolarised matrix elements, one averages over the spin degrees of freedom using the factors $\frac{1}{2}$ and $\frac{1}{n-2}$ for fermions and bosons, respectively. As a convention, a factor of $\frac{1}{2}$ is introduced for all incoming partons for the longitudinally polarised case, but this factor does not have the physical meaning of an averaging.

3.2 Extension of the Dirac algebra to n dimensional space time

It has been pointed out in chapter 2 that it is necessary to regularise the various ultraviolet, infrared and collinear singularities first. Throughout this thesis, dimensional regularisation is used. However, in dimensional regularisation, some ambiguities

in the extension of the purely four dimensional objects γ_5 and the Levi-Civita tensor $\epsilon_{\mu\nu\rho\sigma}$ occur. Of several possibilities discussed in the literature, we will use the 't Hooft-Veltman-Breitenlohner-Maison (HVBM) scheme [102, 154], in which the n-dimensional metric is algebraically consistently decomposed into a four-dimensional part $\hat{\hat{g}}_{\mu\nu}$ and a part $\hat{g}_{\mu\nu}$ in $(n-4)$ dimensions.

Furthermore, $\hat{\gamma}_\mu = \hat{g}_{\mu\nu}\gamma^\nu$ and $\hat{\hat{\gamma}}_\mu = \hat{\hat{g}}_{\mu\nu}\gamma^\nu$ are defined [155]. As in four dimensions, one finds

$$\{\gamma^\mu, \gamma^\nu\} = 2g^{\mu\nu}. \tag{3.7}$$

Defining γ^5 via

$$\gamma^5 = i\gamma^0\gamma^1\gamma^2\gamma^3, \tag{3.8}$$

it anti-commutes with γ^μ only for the four dimensional part,

$$\{\hat{\hat{\gamma}}^\mu, \gamma^5\} = 0. \tag{3.9}$$

In the $(n-4)$ dimensional space one has to replace the anticommutator by the commutator:

$$[\hat{\gamma}^\mu, \gamma^5] = 0. \tag{3.10}$$

The entries of $\epsilon^{\mu\nu\rho\sigma}$ are defined as in four dimensions and zero otherwise. γ^5 and $\epsilon^{\mu\nu\rho\sigma}$ enter the calculation of polarised matrix elements via the projection operators for the quark spins and the polarisation sum of the gluons.

In n dimensions also the momenta of external particles get $(n-4)$ dimensional contributions. For incoming and observed final state particles, these contributions vanish. However, at NLO accuracy, there are non-trivial contributions from these so-called hat momenta to the analytic integrals in the n dimensional phase space used for parton-level single-inclusive cross sections, see section 3.4.4.

3.3 Matrix elements

3.3.1 Virtual and real diagrams

In this section the general form of the matrix elements contributing to heavy quark production up to next-to-leading order is discussed. We will focus on the partonic process

$$a(k_1) + b(k_2) \to h_1(p_1) + h_2(p_2) + X. \tag{3.11}$$

The momenta of the unobserved particles are integrated out.

Because we assume that the initial state does not contain any heavy quarks, both a heavy quark Q and a heavy antiquark $\bar{Q}$ in the final state have to be produced in the Feynman diagrams. These two must have the same flavour because they are on the same heavy quark line, which couples only to gluons and hence cannot change the quark flavour in the framework of QCD. Weak interactions are not considered in this work.

To determine the order of the matrix elements, we recall that at each vertex the factor $g = \sqrt{4\pi\alpha_s}$ comes into play, except at the the four-gluon-vertex, which is proportional to g^2. Note that from now on we will write $g = g_s$ when there is no danger of confusion.

Figure 3.1: Sketch of a generic Feynman diagram in leading order.

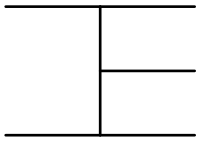

Figure 3.2: Generic Feynman diagram for real emission.

The squared matrix elements at leading order – the lowest order – are called Born contributions and are of order $\mathcal{O}(\alpha_s^2)$ for hadroproduction and $\mathcal{O}(\alpha\alpha_s)$ for photoproduction of heavy quarks. A generic leading order Feynman diagram is sketched in figure 3.1.

In Feynman diagrams of higher order both real and virtual additional particles can be involved, what increases the power of α_s (by one at NLO).

At the next-to-leading order – α_s^3 in the case of hadroproduction and $\alpha\alpha_s^2$ in the case of photoproduction – two basically different types of corrections to leading order cross sections exist: On the one hand, one has to account for the diagrams with still only two particles in the final state, i.e., the heavy quark-antiquark pair and one internal loop, see figure 3.3.

The loop corrections are the second term in the expansion of the $2 \to 2$ matrix elements:

$$[\Delta]M_{2\to 2} = [\Delta]M_B + [\Delta]M_V + \mathcal{O}(\alpha_s^3). \tag{3.12}$$

$[\Delta]M_B$ denotes the Born and $[\Delta]M_V$ the virtual diagrams. One ends up with

$$\begin{aligned} |[\Delta]M_{2\to 2}|^2 &= ([\Delta]M_B + [\Delta]M_V + \mathcal{O}(\alpha_s^3))([\Delta]M_B^* + [\Delta]M_V^* + \mathcal{O}(\alpha_s^3)) = \\ &|[\Delta]M_B|^2 + ([\Delta]M_B[\Delta]M_V^* + [\Delta]M_V[\Delta]M_B^*) + \mathcal{O}(\alpha_s^4) = \\ &|[\Delta]M_B|^2 + 2\mathrm{Re}([\Delta]M_B[\Delta]M_V^*) + \mathcal{O}(\alpha_s^4). \end{aligned} \tag{3.13}$$

As can be seen from equation (3.13), at NLO accuracy only real parts of the interferences of the born diagrams with the one loop diagrams contribute. Equation (3.13) as given here describes hadroproduction; for higher order corrections to photoproduction, $\mathcal{O}(\alpha_s^3)$ and $\mathcal{O}(\alpha_s^4)$ have to be replaced by $\mathcal{O}(\alpha\alpha_s^2)$ and $\mathcal{O}(\alpha\alpha_s^3)$ with the electromagnetic coupling α. Recall that the equation includes both the unpolarised and the longitudinally polarised case as described below equation (3.1).

On the other hand, diagrams for real emission with an additional particle in the final state contribute, as depicted in figure 3.2. These matrix elements are at tree level proportional to g^3 and no loop corrections to them have to be taken into account.

No diagrams with four or more particles in the final states have to be included at NLO accuracy as they are at least of $\mathcal{O}(\alpha_s^4)$ for hadro- and $\mathcal{O}(\alpha\alpha_s^3)$ for photoproduction.

3.3.2 Integration over loop momenta in virtual diagrams

In the virtual diagrams, the momentum associated with the loop is not specified by energy-momentum conservation and has to be integrated over. Virtual diagrams can be classified by the number of propagators in their loop, which is equal to the number of the vertices. Usually, diagrams with four, three, and two internal propagators are called box, vertex, and selfenergy and vacuum polarisation contributions, respectively. A sketch of them can be seen in figure 3.3.

In practical calculations, the integration over the internal loop momentum is done with the help of the Passarino-Veltman decomposition [156].

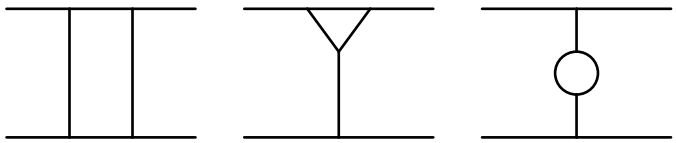

Figure 3.3: A sketch of box, vertex, and selfenergy and vacuum polarisation graphs.

The relevant integrals have the general structure

$$\{B, C, D\}^{\{\mu,\mu\nu,\mu\nu\rho\}} = \int \frac{d^n q}{(2\pi)^n} \frac{\{1, q^\mu, q^\mu q^\nu, q^\mu q^\nu q^\rho\}}{\prod_{j=1}^{i} L_j}. \tag{3.14}$$

Here, q denotes the momentum circulating in the loop.

According to the structure of the propagators, the number of factors q in the numerator is always lower than or equal to the number of the propagators in the loop labelled by i. Since q can take any value, one has to expect infrared and ultraviolet divergences at the lower and upper boundaries, respectively, of the integration $\int d^n q$. The L_j in (3.14) are of the form $L_j = l_j^2 - m_j^2 + i\epsilon$ with l_j being the momentum and m_j the mass on the corresponding internal line. The term $i\epsilon$ preserves causality. This ϵ must not be confused with the ε from dimensional regularisation in $n = 4 - 2\varepsilon$. The choice of the loop momentum q and the Lorentz indices is such that one can write $l_1 = q$, $l_2 = q + q_1$, $l_3 = q + q_1 + q_2$ and $l_4 = q + q_1 + q_2 + q_3$. The q_i are the momenta entering the loop at the vertices. Depending on the number i of the internal propagators the integrals in (3.14) are denoted by capital letters B, C and D for $i = 2$, 3 and 4, respectively. The B, C, and D integrals can be expressed via the following decomposition rules by scalar integrals:

$$\begin{aligned} B^\mu &= q_1^\mu B_1, \\ B^{\mu\nu} &= q_1^\mu q_1^\nu B_{21} + g^{\mu\nu} B_{22}, \end{aligned} \tag{3.15}$$

$$\begin{aligned} C^\mu &= q_1^\mu C_{11} + q_2^\mu C_{12}, \\ C^{\mu\nu} &= q_1^\mu q_1^\nu C_{21} + q_2^\mu q_2^\nu C_{22} + \{q_1 q_2\}^{\mu\nu} C_{23} + g^{\mu\nu} C_{24}, \\ C^{\mu\nu\rho} &= q_1^\mu q_1^\nu q_1^\rho C_{31} + q_2^\mu q_2^\nu q_2^\rho C_{32} + \{q_1 q_1 q_2\}^{\mu\nu\rho} C_{33} + \{q_1 q_2 q_2\}^{\mu\nu\rho} C_{34} \\ &\quad + \{q_1 g\}^{\mu\nu\rho} C_{35} + \{q_2 g\}^{\mu\nu\rho} C_{36}, \end{aligned} \tag{3.16}$$

$$
\begin{aligned}
D^{\mu} &= q_1^{\mu} D_{11} + q_2^{\mu} D_{12} + q_3^{\mu} D_{13}, \\
D^{\mu\nu} &= q_1^{\mu} q_1^{\nu} D_{21} + q_2^{\mu} q_2^{\nu} D_{22} + q_3^{\mu} q_3^{\nu} D_{23} + \{q_1 q_2\}^{\mu\nu} D_{24} + \{q_1 q_3\}^{\mu\nu} D_{25} \\
&\quad + \{q_2 q_3\}^{\mu\nu} D_{26} + g^{\mu\nu} D_{27}, \\
D^{\mu\nu\rho} &= q_1^{\mu} q_1^{\nu} q_1^{\rho} D_{31} + q_2^{\mu} q_2^{\nu} q_2^{\rho} D_{32} + q_3^{\mu} q_3^{\nu} q_3^{\rho} D_{33} + \{q_1 q_1 q_2\}^{\mu\nu\rho} D_{34} + \{q_1 q_1 q_3\}^{\mu\nu\rho} D_{35} \\
&\quad + \{q_1 q_2 q_2\}^{\mu\nu\rho} D_{36} + \{q_1 q_3 q_3\}^{\mu\nu\rho} D_{37} + \{q_2 q_2 q_3\}^{\mu\nu\rho} D_{38} + \{q_2 q_3 q_3\}^{\mu\nu\rho} D_{39} \\
&\quad + \{q_1 q_2 q_3\}^{\mu\nu\rho} D_{310} + \{q_1 g\}^{\mu\nu\rho} D_{311} + \{q_2 g\}^{\mu\nu\rho} D_{312} + \{q_3 g\}^{\mu\nu\rho} D_{313}. \qquad (3.17)
\end{aligned}
$$

$\{\dots\}^{\mu\nu\cdots}$ denotes the sum over all possible permutations of Lorentz indices, such as

$$\{q_1 q_1 q_2\}^{\mu\nu\rho} = q_1^{\mu} q_2^{\nu} q_2^{\rho} + q_1^{\nu} q_1^{\rho} q_2^{\mu} + q_1^{\rho} q_1^{\mu} q_2^{\nu} \qquad (3.18)$$

and

$$\{q_1 g\}^{\mu\nu\rho} = q_1^{\mu} g^{\nu\rho} + q_1^{\nu} g^{\rho\mu} + q_1^{\rho} g^{\mu\nu}. \qquad (3.19)$$

These scalar coefficients B_i, C_i and D_i in equations (3.15) to (3.17) can be deduced from a lengthy decomposition into scalar integrals

$$\{B_0, C_0, D_0\} = \int \frac{d^n q}{(2\pi)^n} \frac{1}{\Pi_{j=1}^{i} L_i}. \qquad (3.20)$$

This is described, e.g., in [74]. These integrals are called n point functions. They can – where required after a suitable transformation of the momenta – be found in [59, 74] and need not to be reproduced here. As, in general, the integrals B_0, C_0 and D_0 diverge in 4 dimensions due to infrared and ultraviolet singularities, they have to be calculated in n dimensions. Only box integrals are finite as is expected from naive power counting.

3.4 Two and three particle phase space

This and the following sections are organised as follows: We will present the relevant calculations for the two methods used: the analytical method and the purely numerical one. For each topic, we will usually start with the analytical case and come to the numerical case afterwards. In this section, we will begin with the phase spaces for the $2 \to 2$ and $2 \to 3$ contributions followed by some remarks on the evaluation of the integrals. The following sections are organised in the same way: section 3.5 discusses how we have handled the singularities in our two calculational methods and section 3.6 illustrates how we can get from the partonic to the hadronic cross sections in each case.

We start with a description of the calculation of the relevant phase space factors $dPS_{2\to r} \equiv dPS_r$ defined in equation (3.4) for the case of heavy quark production. As just mentioned, we will present two different formulations. The first one will be used for the analytical evaluation of the phase space integrals in the calculation of one-particle inclusive cross sections. The other one uses a different set of variables which will be more suited for purely numerical phase space integration with Monte Carlo methods. In the case of dPS_2, relevant for $2 \to 2$ scattering processes, the equivalence of both formulations is obvious. In the $2 \to 3$ case, dPS_3, we derive both results from scratch as a transformation of one result into the other is rather cumbersome.

3.4.1 Two particle phase space

First, let us start with the phase space dPS_2 relevant for the Born and one-loop matrix elements: The momenta of the incoming massless partons a and b are denoted by k_1 and k_2, the ones of the produced heavy quarks C and D by p_1 and p_2:

$$a(k_1) + b(k_2) \to C(p_1) + D(p_2). \tag{3.21}$$

We are free to label $C = Q$ and $D = \bar{Q}$ or vice versa.

In this section, we assume that the heavy (anti)quark D with four-momentum p_2 is detected. The external particles a, b, C and D are on the mass shell, i.e., $k_1^2 = k_2^2 = 0$ and $p_1^2 = p_2^2 = m^2$. Here, m is the mass of the heavy quarks C and D. For the $2 \to 2$ matrix elements we define three modified Mandelstam variables according to:

$$\begin{aligned} s &\equiv (k_1 + k_2)^2 = 2k_1 \cdot k_2, \\ t_1 &\equiv t - m^2 \equiv (k_2 - p_2)^2 - m^2 = -2k_2 \cdot p_2, \\ u_1 &\equiv u - m^2 \equiv (k_1 - p_2)^2 - m^2 = -2k_1 \cdot p_2. \end{aligned} \tag{3.22}$$

Due to four-momentum conservation

$$k_1 + k_2 = p_1 + p_2 \tag{3.23}$$

one finds that

$$u_1 = (k_2 - p_1)^2 - m^2 = -2k_2 \cdot p_1 \tag{3.24}$$

and hence

$$s + t_1 + u_1 = 2k_2 \cdot (k_1 - p_2 - p_1) = -2k_2^2 = 0, \tag{3.25}$$

such that only two of the three invariants in (3.22) are linearly independent. The calculation of the $2 \to 2$ phase space element dPS_2 in (3.4) will be carried out in the centre-of-mass system of the incoming partons (c.m.s.) using $k_1 = \sqrt{s}/2(1, 0, 0, 1, \hat{0})$ and $p_2 = (E_2, 0, |\vec{p_2}| \sin\zeta, |\vec{p_2}| \cos\zeta, \hat{0})$ as parametrisation of the momenta. This is done in n dimensions as in the collinear and soft limits of the $2 \to 3$ contributions, the n dimensional $2 \to 2$ matrix elements and phase space will appear. The parts of the momentum with a hat, the so-called hat momenta, denote the $(n-4)$ dimensional contributions, which here can be ignored as three of the four momenta for $2 \to 2$ scattering, say k_1, k_2 and p_1 can always be orientated in such a way that they have no hat components. Due to momentum conservation, one has also $\hat{p}_2 = 0$. The result for dPS_2 reads in $n = 4 - 2\varepsilon$ dimensions:

$$\begin{aligned} dPS_2 &= \int \frac{d^n p_1}{(2\pi)^{n-1}} \frac{d^n p_2}{(2\pi)^{n-1}} \delta(p_1^2 - m^2)\Theta(E_1)\delta(p_2^2 - m^2)\Theta(E_2)(2\pi)^n \\ &\quad \delta^{(n)}(k_1 + k_2 - p_1 - p_2) \\ &= \frac{1}{(2\pi)^{n-2}} \int d^n p_2 \delta(p_2^2 - m^2)\Theta(E_2)\delta((k_1 + k_2 - p_2)^2 - m^2) \\ &= \frac{\pi^{n/2-1}}{(2\pi)^{n-2}} \frac{\delta(s + t_1 + u_1)}{\Gamma(n/2 - 1)} \int dE_2 (E_2^2 - m^2)^{\frac{n-3}{2}} \Theta(E_2) \int_0^\pi d\zeta \sin^{n-3}\zeta, \end{aligned} \tag{3.26}$$

where $(k_1 + k_2 - p_2)^2 - m^2 = s + t_1 + u_1$, and n dimensional spherical coordinates have been used. After transformation of the integration variables from (E_2, ζ) to (t_1, u_1) one obtains:

$$dPS_2 = \int \frac{2\pi}{s} [(4\pi)^{(2-\varepsilon)}\Gamma(1-\varepsilon)]^{-1} \left(\frac{t_1 u_1 - m^2 s}{s}\right)^{-\varepsilon} \delta(s + t_1 + u_1) dt_1 du_1. \tag{3.27}$$

Including the flux factor $1/(2s)$, the master formula for the differential partonic $2 \to 2$ cross section in equation (3.4) reads

$$\frac{d^2[\Delta]\sigma_{2\to2}}{dt_1 du_1} = F_\varepsilon \delta(s + t_1 + u_1)|[\Delta]M|^2 \tag{3.28}$$

where

$$F_\varepsilon = \frac{\pi}{s^2}[(4\pi)^{(2-\varepsilon)}\Gamma(1-\varepsilon)]^{-1}\left(\frac{t_1 u_1 - m^2 s}{\mu_r^2 s}\right)^{-\varepsilon} \tag{3.29}$$

has been introduced. The factor $\mu_r^{2\varepsilon}$ comes from dimensional regularisation in order to keep the coupling g dimensionless.

The phase space formula in (3.27) can also be expressed by the scattering angle θ_1 of the heavy quark, where θ_1 is defined in the c.m.s. of p_1 and p_2 where the coordinate system is fixed, e.g., by aligning the z axis with the direction of k_1. In the $2 \to 2$ case the c.m.s. of p_1 and p_2 is, of course, equivalent to the c.m.s. of k_1 and k_2. Therefore, we have $\zeta = \theta_1$ here. However, both frames of reference will differ for the case of $2 \to 3$ scattering due to the additional third particle in the final state. In the $2 \to 2$ case, using $\beta = \sqrt{1 - 4m^2/s}$, the phase space (3.26) can be written as

$$dPS_2 = \int \frac{2^{2\varepsilon}}{\Gamma(1-\varepsilon)}\left(\frac{4\pi}{s}\right)^{\varepsilon}\frac{1}{16\pi}\beta^{1-2\varepsilon}\sin^{-2\varepsilon}\theta_1 d\cos\theta_1. \tag{3.30}$$

This expression will be used later for the completely numerical integration based on Monte Carlo methods.

3.4.2 $2 \to 3$ phase space integration used for the analytic case

The real emission contributions M_R depicted in figure 3.2 have a $2 \to 3$ kinematics with an additional massless parton e with four momentum k_3 satisfying $k_3^2 = 0$ in the final state:

$$a(k_1) + b(k_2) \to C(p_1) + D(p_2) + e(k_3). \tag{3.31}$$

Energy-momentum conservation ensures that $k_1 + k_2 = p_1 + p_2 + k_3$. For the $2 \to 3$ kinematics, we define ten invariants,

$$\begin{aligned}
s &\equiv (k_1+k_2)^2 = 2k_1\cdot k_2, & s_3 &\equiv (k_3+p_2)^2 - m^2 = 2k_3\cdot p_2,\\
s_4 &\equiv (k_3+p_1)^2 - m^2 = 2k_3\cdot p_1, & s_5 &\equiv -u_5 \equiv (p_1+p_2)^2 = 2m^2 + 2p_1\cdot p_2\\
t_1 &\equiv (k_2-p_2)^2 - m^2 = -2k_2\cdot p_2, & u_1 &\equiv (k_1-p_2)^2 - m^2 = -2k_1\cdot p_2,\\
t' &\equiv (k_2-k_3)^2 = -2k_2\cdot k_3, & u' &\equiv (k_1-k_3)^2 = -2k_1\cdot k_3,\\
u_6 &\equiv (k_2-p_1)^2 - m^2 = -2k_2\cdot p_1, & u_7 &\equiv (k_1-p_1)^2 - m^2 = -2k_1\cdot p_1.
\end{aligned} \tag{3.32}$$

However, only five of them are linearly independent. Exploiting energy momentum conservation, one can find, e.g., the following relations:

$$\begin{aligned}
s_4 + u' + t' + s_3 &= 0,\\
s_3 + s_5 + u_1 + t_1 &= 0,\\
t' + t_1 + s + u_6 &= 0,\\
u' + u_1 + s + u_7 &= 0,\\
s_4 + s_5 + u_6 + u_7 &= 0,
\end{aligned} \tag{3.33}$$

which considerably simplify the analytical integrations. However, using all ten Mandelstam invariants in the calculations of the matrix elements gives considerably more compact expressions for the unintegrated matrix elements than reducing the result to 5 Mandelstam variables.

The $2 \to 3$ phase space dPS_3 is defined by

$$dPS_3 = \int \frac{d^n k_3}{(2\pi)^{n-1}} \frac{d^n p_1}{(2\pi)^{n-1}} \frac{d^n p_2}{(2\pi)^{n-1}} (2\pi)^n \delta^{(n)}(k_1+k_2-k_3-p_1-p_2)\delta(k_3^2)\delta(p_1^2-m^2)$$
$$\delta(p_2^2-m^2)\Theta(E_1)\Theta(E_2)\Theta(E_3). \quad (3.34)$$

This Lorentz invariant expression serves as the starting point for any explicit evaluation of the phase space whatever set of variables one wants to use.

First, we will derive an expression best suited for an analytical evaluation of the phase space integrals relevant for single-inclusive heavy flavour production. Introducing $r = p_1 + k_3$ and using $r^2 = (p_1 + k_3)^2 = s_4 + m^2$, the $2 \to 3$ phase space can be split into a $2 \to 2$ (I) one and a $1 \to 2$ (II) contribution:

$$dPS_3 = \frac{1}{(2\pi)^{2n-3}} \int ds_4$$
$$\underbrace{\int d^n p_2 \int d^n r \delta(p_2^2-m^2)\delta(r^2-s_4-m^2)\delta^{(n)}(k_1+k_2-p_2-r)}_{I}$$
$$\underbrace{\int d^n k_3 d^n p_1 \delta(k_3^2)\delta(p_1^2-m^2)\delta^{(n)}(r-p_1-k_3))}_{II}\Theta(E_1)\Theta(E_2)\Theta(E_3). \quad (3.35)$$

The two parts can be calculated separately. In the $2 \to 2$ part, the delta function can be evaluated by integrating over p_2, giving

$$I = \int d^n r \delta((k_1+k_2-r)^2-m^2)\delta(r^2-s_4-m^2). \quad (3.36)$$

Parametrising the auxiliary momentum as

$$r = (r_0, r_\parallel = r\cos\theta, r_\perp^{n-2}), \quad (3.37)$$

(the subscripts $\parallel$ and $\perp$ stand for components parallel and perpendicular with respect to k_2.) and performing the $(n-3)$ dimensional angular integration, one obtains

$$I = \int dr_0 dr_\perp^{(n-2)} dr_\parallel \delta(s+r^2-2r_0\sqrt{s}-m^2)\delta(r_0^2-r_\perp^2-r_\parallel^2-s_4-m^2) =$$
$$\int \frac{\pi^{\frac{n-3}{2}}}{\Gamma(\frac{n-2}{2})} dr_0 d\cos\theta (r_0^2-r_\parallel^2-s_4-m^2)^{\frac{n-4}{2}} \sqrt{r_0^2-s_4-m^2}\,\delta(s+r^2-2r_0\sqrt{s}-m^2). \quad (3.38)$$

After integration over r_0 and some algebraic manipulations, one arrives at

$$I = \frac{\pi^{\frac{n-2}{2}}}{\Gamma(\frac{n-2}{2})} \frac{1}{2\sqrt{s}} \int d\cos\theta \left[\frac{(s-s_4)^2}{4s} - m^2\right]^{\frac{n-3}{2}} [\sin\theta]^{n-4}. \quad (3.39)$$

The $1 \to 2$ part of the phase space gives after the integration over the n-dimensional delta distribution

$$II = \int d^n p_1 \delta(r-p_1)^2 \delta(p_1^2-m^2). \quad (3.40)$$

The remaining integrations are done in the c.m.s. of p_1 and k_3 with $\vec{r} = 0$. With the parametrisation $p_1 = (p_{1,0}, p_{1,\perp}, p_{1,\parallel}, \hat{p}_1) = (p_{1,0}, p_{1,\perp}, (p_{1,\parallel})_1, (p_{1,\parallel})_2, \hat{p}_1)$ one can integrate over the delta function and the angles. The result is

$$II = \int \frac{\pi^{\frac{n-4}{2}}}{\Gamma(\frac{n-4}{2})} \frac{1}{2\sqrt{s_4+m^2}} (\hat{p}_1^2)^{\frac{n-6}{2}} d\hat{p}_1^2 d^2 p_{1,\parallel} \frac{1}{\sqrt{\frac{(s_4+2m^2)^2}{4(s_4+m^2)} - (p_{1,\parallel})^2 - \hat{p}_1^2 - m^2}}. \tag{3.41}$$

Writing $p_{1,\parallel}$ as

$$(p_{1,\parallel})_1 = -\omega_3 \sin\gamma_1 \cos\gamma_2 \text{ and } (p_{1,\parallel})_2 = -\omega_3 \cos\gamma_1 \tag{3.42}$$

with $\omega_3 = \frac{s_4}{2\sqrt{s_4+m^2}}$ (cf. equation (3.77) below), the remaining integrations can be transformed to $d\gamma_1 d\gamma_2$ ones:

$$II = \frac{\pi^{\frac{n-4}{2}}}{\Gamma(\frac{n-4}{2})} \frac{s_4^2}{8(s_4+m^2)^{3/2}} \int_0^\pi d\gamma_1 \int_0^\pi d\gamma_2 \sin^2\gamma_1 \sin\gamma_2 \int_0^{\hat{p}^2_{1,\max}} (\hat{p}_1^2)^{\frac{n-6}{2}} d\hat{p}_1^2 \frac{1}{\sqrt{\frac{s_4^2}{4(s_4+m^2)} \sin^2\gamma_1 \sin^2\gamma_2 - \hat{p}_1^2}}, \tag{3.43}$$

where

$$\hat{p}^2_{1,\max} = \frac{s_4^2}{4(s_4+m^2)} \sin^2\gamma_1 \sin^2\gamma_2 \tag{3.44}$$

denotes the upper limit of the integration over the hat momentum $\hat{p}_1$. Defining

$$x = \frac{\hat{p}_1^2}{\hat{p}^2_{1,\max}} = \frac{4(s_4+m^2)\hat{p}_1^2}{s_4^2 \sin^2\gamma_1 \sin^2\gamma_2} \tag{3.45}$$

and using

$$d\hat{p}_1^2 = \frac{s_4^2 \sin^2\gamma_1 \sin^2\gamma_2}{4(s_4+m^2)} dx, \tag{3.46}$$

the $d\hat{p}_1^2$ integration can be transformed into a dx integration.

Collecting now all parts of the $2 \to 3$ phase space and the factor $\mu_r^{2\varepsilon}$ from dimensional regularisation, one arrives after some algebraic manipulations at

$$\begin{aligned} dPS_3 &= \int ds_4 d\cos\theta \frac{\sqrt{(s-s_4)^2 - 4m^2 s}}{2} \frac{1}{s} \left(\frac{1}{4\pi}\right)^n \frac{1}{\Gamma(n-3)} \left(\frac{t_1 u_1 - s m^2}{\mu_r^2 s}\right)^{\frac{n}{2}-2} \\ &\quad \frac{s_4^{n-3}}{(s_4+m^2)^{\frac{n}{2}-1}} \int_0^\pi d\gamma_1 \int_0^\pi d\gamma_2 \sin^{n-3}\gamma_1 \sin^{n-4}\gamma_2 \frac{1}{B(\frac{1}{2}, \frac{n-4}{2})} \int_0^1 dx \frac{x^{\frac{n-6}{2}}}{\sqrt{1-x}} \\ &= \int dt_1 du_1 \frac{1}{s} \left(\frac{1}{4\pi}\right)^n \frac{1}{\Gamma(n-3)} \left(\frac{t_1 u_1 - s m^2}{\mu_r^2 s}\right)^{\frac{n}{2}-2} \\ &\quad \frac{s_4^{n-3}}{(s_4+m^2)^{\frac{n}{2}-1}} \int_0^\pi d\gamma_1 \int_0^\pi d\gamma_2 \sin^{n-3}\gamma_1 \sin^{n-4}\gamma_2 \frac{1}{B(\frac{1}{2}, \frac{n-4}{2})} \int_0^1 dx \frac{x^{\frac{n-6}{2}}}{\sqrt{1-x}} \end{aligned} \tag{3.47}$$

with

$$s_4 = s + t_1 + u_1 \tag{3.48}$$

and

$$\cos\theta = \frac{t_1 - s_4 + \frac{s_4+s}{2}}{\sqrt{s}\sqrt{\frac{(s-s_4)^2}{4s} - m^2}}. \tag{3.49}$$

$B(a,b)$ denotes the Euler-Beta function.

Helicity dependent matrix elements $\Delta|M|^2$ may depend on $\hat{p}_1$. In such a case,

$$\frac{1}{B(\frac{1}{2},\frac{n-4}{2})}\int_0^1 dx \frac{x^{\frac{n-6}{2}}}{\sqrt{1-x}}\hat{p}_1^2 = (n-4)\frac{s_4^2\sin^2\gamma_1\sin^2\gamma_2}{4(s_4+m^2)} \tag{3.50}$$

has to be used for the $\hat{p}_1^2$ integration.

In the unpolarised case, all hat momenta drop out.

If a term in the matrix element is independent of $\hat{p}_1^2$, like in the spin-averaged case, one finds:

$$\frac{1}{B(\frac{1}{2},\frac{n-4}{2})}\int_0^1 dx \frac{x^{\frac{n-6}{2}}}{\sqrt{1-x}} = 1. \tag{3.51}$$

We finally note that the integrals over γ_1, γ_2 and x are done analytically. The other integrals over t_1 and u_1 or s_4 and $\cos\theta$ are calculated numerically or used to display differential partonic cross sections. More details can be found in [86]. In section 3.6.1 is shown how the additional integrations over the x_1 and x_2 from the parton distribution functions are treated.

3.4.3 $2 \to 3$ phase space for the Monte Carlo subtraction method

Now, we will turn to the phase space calculation as used in the purely numerical code. In the method presented above, the $1 \to 2$ part of the phase space (3.35) contains the particles with momenta p_1 and k_3. This was indeed an arbitrary but the most useful choice for analytical evaluations of phase space integrals appearing in single-inclusive observables. There, the particle with momentum p_2 was observed and the particle with p_1 was integrated out. In principle, each combination of two of the three final state particles can be taken for the $1 \to 2$ phase space. For a totally numerical integration, it is more suitable to define the $1 \to 2$ phase space by the heavy quark and the heavy antiquark [81, 82]. This is a symmetric choice and advantageous particularly for heavy quark correlations.

A possible parametrisation of the momenta in the centre-of-mass frame of the $Q\bar{Q}$ system is given by

$$k_1 = k_1^0(1,0,0,1), \tag{3.52}$$

$$k_2 = k_2^0(1,0,\sin\psi,\cos\psi), \tag{3.53}$$

$$k_3 = k_3^0(1,0,\sin\psi',\cos\psi'), \tag{3.54}$$

$$p_1 = \frac{1}{2}\sqrt{s_5}(1,\beta_x\sin\theta_2\sin\theta_1,\beta_x\cos\theta_2\sin\theta_1,\beta_x\cos\theta_1), \tag{3.55}$$

$$p_2 = \frac{1}{2}\sqrt{s_5}(1,-\beta_x\sin\theta_2\sin\theta_1,-\beta_x\cos\theta_2\sin\theta_1,-\beta_x\cos\theta_1), \tag{3.56}$$

where

$$k_1^0 = \frac{s+u'}{2\sqrt{s_5}}, \tag{3.57}$$

$$k_2^0 = \frac{s+t'}{2\sqrt{s_5}}, \tag{3.58}$$

$$k_3^0 = -\frac{t'+u'}{2\sqrt{s_5}}, \tag{3.59}$$

$$\cos\psi = 1 - \frac{s}{2k_1^0 k_2^0} \text{ with } \sin\psi > 0, \tag{3.60}$$

$$\cos\psi' = 1 + \frac{u'}{2k_1^0 k_3^0} \text{ with } \sin\psi > 0, \tag{3.61}$$

$$\beta_x = \sqrt{1 - \frac{4m^2}{sx}} \text{ with } x = \frac{s_5}{s}. \tag{3.62}$$

The variable x gives the invariant mass of the $Q\bar{Q}$ system scaled by the partonic c.m.s. energy squared, i.e., $4m^2/s \leq x \leq 1$. Introducing furthermore y as the cosine of the angle between $\vec{k}_1$ and $\vec{k}_3$ in the centre-of-mass system of the incoming partons, one can express the matrix elements in terms of the five independent Mandelstam variables: s, $t' = -\frac{1}{2}s(1-x)(1+y)$, $u' = -\frac{1}{2}s(1-x)(1-y)$, $u_7 = -\frac{s+u'}{2}(1-\beta_x\cos\theta_1)$ and $t_1 = -\frac{s+t'}{2}(1+\beta_x\cos\theta_1\sin\theta_1\sin\psi + \beta_x\cos\theta_1\cos\psi)$. Therefore, it is convenient to express the three-particle phase space also in these variables. In the following, we will present the necessary steps.

As previously, we start with

$$\begin{aligned} dPS_3 = \int \frac{d^n p_1}{(2\pi)^{n-1}} \frac{d^n p_2}{(2\pi)^{n-1}} \frac{d^n k_3}{(2\pi)^{n-1}} (2\pi)^n \\ \delta^{(n)}(k_1 + k_2 - p_1 - p_2 - k_3)\delta(k_3^2)\delta(p_1^2 - m^2)\delta(p_2^2 - m^2)\Theta(E_1)\Theta(E_2)\Theta(E_3) \\ = (2\pi)^{-2n+3} \int d^n p_1 \delta(p_1^2 - m^2)\delta(p_2^2 - m^2)\Theta(E_1)\Theta(E_2)\cdot \\ \int d^n k_3 \delta(k_3^2)\Theta(E_3) \end{aligned} \tag{3.63}$$

and evaluate dPS_3 in the c.m.s. of p_1 and p_2. The first step is to rearrange the order of the integration (for the sake of brevity, we will not write out the Theta functions in the phase space integrals anymore) as

$$dPS_3 = (2\pi)^{-2n+3} \int d^n k_3 \delta(k_3^2) \underbrace{\int d^n p_1 \delta(p_1^2 - m^2)\delta[(k_1 + k_2 - p_1 - k_3)^2 - m^2]}_{I_1}. \tag{3.64}$$

Now, we write

$$\begin{aligned} I_1 = \int dp_1 \delta(p_1^2 - m^2)\delta[(k_1 + k_2 - p_1 - k_3)^2 - m^2] = \\ \int dE_1 d|\vec{p}_1| d\Omega_1 \delta(p_1^2 - m^2)\delta[(k_1 + k_2 - p_1 - k_3)^2 - m^2] = \\ \int dE_1 d|\vec{p}_1| d\Omega_1 \delta[E_1^2 - |\vec{p}_1|^2 - m^2]\delta[(k_1 + k_2 - p_1 - k_3)^2 - m^2] = \\ \int dE_1 \frac{1}{2|\vec{p}_1|} d\Omega_1 \delta[(k_1 + k_2 - p_1 - k_3)^2 - m^2] = \\ \int dE_1 \frac{1}{2|\vec{p}_1|} d\Omega_1 \delta([k_1 + k_2 - k_3]^2 + p_1^2 - m^2 - 2p_1(k_1 + k_2 - k_3)) = \\ \int dE_1 \frac{1}{2|\vec{p}_1|} d\Omega_1 \delta([k_1 + k_2 - k_3]^2 + p_1^2 - m^2 - 2E_1(k_1 + k_2 - k_3)^0). \end{aligned} \tag{3.65}$$

We use $d\Omega_1$ as given in (3.66) as a short notation for the angular part of the integration of dp_1. dE_1 represents the integration over the time-like component and $d|\vec{p}_1|$

the integration over the absolute value. Using the parametrisation (3.55) for p_1, one obtains $|\vec{p}_1| = \frac{1}{2}\beta_x\sqrt{s_5}$ and $(k_1+k_2-k_3)^0 = (p_1+p_2)^0 = \sqrt{s_5}$ in the c.m.s. of p_1 and p_2. So, we can write

$$\begin{aligned} I_1 &= \int \frac{1}{2\beta_x s_5} d\Omega_1 = \int \frac{1}{2\beta_x s_5} |\vec{p}_1|^{n-2} d\theta_1 \sin^{n-3}\theta_1 \sin^{n-4}\theta_2 d\theta_2 2\pi \prod_{j=1}^{n-5} \sin^j \tilde{\theta}_j d\tilde{\theta}_j \\ &= \int \frac{1}{s_5\beta_x} (\frac{1}{2}\beta_x\sqrt{s_5})^{n-2} d\theta_1 d\theta_2 \sin^{n-3}\theta_1 \sin^{n-4}\theta_2 \pi^{\frac{n-3}{2}} \frac{1}{\Gamma(\frac{n-3}{2})}. \end{aligned} \tag{3.66}$$

Now we can present the phase space as

$$dPS_3 = (2\pi)^{-2n+3} \int dk_3 \delta(k_3^2) I_1. \tag{3.67}$$

We have already chosen a c.m.s. (the one of p_1 and p_2); at this point we can make, however, an integral transformation, which transforms the k_3 integration into the c.m.s. of k_1 and k_2. Lorentz invariance tells us that we will not get any Jacobian which differs from unity for this integral transformation.

The remaining integration over the phase space of the light final state particle yields:

$$\int d^n k_3 \delta(k_3^2) = \int dE_3 d^{n-1} k_3 \delta(E_3^2 - |\vec{k}_3|^2) = \int \frac{1}{2|\vec{k}_3|} d^{n-1} k_3. \tag{3.68}$$

Next, we will use spherical coordinates in n dimensions in order to accomplish the angular integration:

$$\begin{aligned} &\int \frac{1}{2|\vec{k}_3|} d|\vec{k}_3| |\vec{k}_3|^{n-2} \sin^{n-3}\alpha_1 \sin^{n-4}\alpha_2 \cdots \sin\alpha_{n-3} d\alpha_1 \cdots d\alpha_{n-2} \\ &\quad = \int d|\vec{k}_3| d\cos\alpha_1 \sin^{n-4}\alpha_1 |\vec{k}_3|^{n-3} \pi^{1+\frac{n-4}{2}} \frac{1}{\Gamma(\frac{n-2}{2})}, \end{aligned} \tag{3.69}$$

where k_3 is parametrised by

$$k_3 = (E_3, |\vec{k}_3| \underbrace{\cos\alpha_1}_{y}, |\vec{k}_3| \sin\alpha_1 \cos\alpha_2, \dots)$$

in the c.m.s. of k_1 and k_2, in which one can write

$$1 - x = \frac{s - s_5}{s} = \frac{-u' - t'}{s} = \frac{2k_3 \cdot (k_1 + k_2)}{s} = \frac{2E_3}{\sqrt{s}} = \frac{2|\vec{k}_3|}{\sqrt{s}} \tag{3.70}$$

and

$$s = (k_1 + k_2)^2 = [(k_1 + k_2)^0]^2. \tag{3.71}$$

This leads to the relations $|k_3| = \frac{\sqrt{s}}{2}(1-x)$ and $d|k_3| = -\frac{\sqrt{s}}{2}dx$. Furthermore, defining $y = \cos\alpha_1$ implies that $\sin\alpha_1 = \sqrt{1-\cos^2\alpha_1} = \sqrt{1-y^2}$ and $\sin^{n-4}\alpha_1 = (1-y^2)^{\frac{n-4}{2}}$.

Thus, the transformation yields

$$\begin{aligned} &\int dx \left(-\frac{\sqrt{s}}{2}\right) dy (1-y^2)^{\frac{n-4}{2}} \left(\frac{\sqrt{s}}{2}\right)^{n-3} (1-x)^{n-3} \pi^{\frac{n}{2}-1} \frac{1}{\Gamma(\frac{n-2}{2})} \\ &\quad = \int dx dy (1-y^2)^{\frac{n-4}{2}} (1-x)^{n-3} \left(\frac{\sqrt{s}}{2}\right)^{n-2} \frac{\pi^{\frac{n}{2}-1}}{\Gamma(\frac{n-2}{2})}. \end{aligned} \tag{3.72}$$

In the last step, the minus sign was absorbed into the integration limits.

We combine the two parts (3.66) and (3.72) in order to get the final result

$$\begin{aligned}
dPS_3 = &\int dxdyd\theta_1 d\theta_2 \sin^{n-3}\theta_1 \sin^{n-4} d\theta_2 (1-y^2)^{\frac{n-4}{2}} (1-x)^{n-3} \cdot \\
&2^{(2-n)\cdot 2} \pi^{\frac{2n-5}{2}} \frac{1}{\Gamma(\frac{n-2}{2})\Gamma(\frac{n-3}{2})} s^{n-2-1} \beta_x^{n-2-1} x^{\frac{n-2}{2}-1} (2\pi)^{3-2n} \\
= &\int dxdyd\theta_1 d\theta_2 \sin^{n-3}\theta_1 \sin^{n-4} d\theta_2 (1-y^2)^{\frac{n-4}{2}} (1-x)^{n-3} \cdot \\
&2^{4-2n} \pi^{n-\frac{5}{2}} \frac{1}{\Gamma(\frac{n-2}{2})\Gamma(\frac{n-3}{2})} s^{n-3} \beta_x^{n-3} x^{\frac{n}{2}-2} (2\pi)^{3-2n} = \\
= &\int dxdyd\theta_1 d\theta_2 \sin^{n-3}\theta_1 \sin^{n-4} d\theta_2 (1-y^2)^{\frac{n-4}{2}} (1-x)^{n-3} \cdot \\
&2^{3-3n} \pi^{-n} \frac{1}{\Gamma(n-3)} s^{n-3} \beta_x^{n-3} x^{\frac{n}{2}-2},
\end{aligned} \tag{3.73}$$

where the identity

$$\Gamma\left(\frac{n-2}{2}\right)\Gamma\left(\frac{n-3}{2}\right) = 2^{4-n}\sqrt{\pi}\Gamma(n-3) \tag{3.74}$$

was used.

Expression (3.73) will be used in all completely numerical calculations which will be presented in chapter 5.

3.4.4 Analytical calculation of phase space integrals

Now we will turn to the details of the integrals which are done analytically. We will start with the case of the analytical calculation. After the integration of the phase space element dPS_3, see equation (3.47), has been re-written in terms of γ_1, γ_2, and two Mandelstam variables, one can perform the angular integration in the c.m.s. of p_1 and k_3; therefore, all momenta have to be parametrised in this frame. The orientation, i.e., the z axis of the coordinate system is not determined by the parametrisation of $p_{1,\parallel}$ in (3.42). Here, two possibilities are used: in set 1 the z axis is chosen parallel to $\vec{k}_2$. This leads to the parametrisation of the momenta in the c.m.s. of the two unobserved particles:

$$\begin{aligned}
k_1 &= (\omega_1, 0, |\vec{p}|\sin\tau, |\vec{p}|\cos\tau - \omega_2, \hat{0}), \\
k_2 &= (\omega_2, 0, 0, \omega_2, \hat{0}), \\
k_3 &= (\omega_3, k_3^x, \omega_3 \sin\gamma_1 \cos\gamma_2, \omega_3 \cos\gamma_1, \hat{k}_3), \\
p_1 &= (E_1, p_1^x, -\omega_3 \sin\gamma_1 \cos\gamma_2, -\omega_3 \cos\gamma_1, \hat{p}_1), \\
p_2 &= (E_2, 0, |\vec{p}|\sin\tau, |\vec{p}|\cos\tau, \hat{0}).
\end{aligned} \tag{3.75}$$

If, as in set 2, the z axis is parallel to $\vec{k}_1$, the parametrisation reads:

$$\begin{aligned}
k_1 &= (\omega_1, 0, 0, \omega_1, \hat{0}),\\
k_2 &= (\omega_2, 0, |\vec{p}|\sin\tau, |\vec{p}|\cos\tau - \omega_1, \hat{0}),\\
k_3 &= (\omega_3, k_3^x, \omega_3 \sin\gamma_1\cos\gamma_2, \omega_3\cos\gamma_1, \hat{k}_3),\\
p_1 &= (E_1, p_1^x, -\omega_3\sin\gamma_1\cos\gamma_2, -\omega_3\cos\gamma_1, \hat{p}_1),\\
p_2 &= (E_2, 0, |\vec{p}|\sin\tau, |\vec{p}|\cos\tau, \hat{0}).
\end{aligned} \tag{3.76}$$

As we work in the c.m.s. of k_3 and p_1, the $(n-4)$ dimensional hat components are constrained to $\hat{p}_1 = -\hat{k}_3$ due to momentum conservation. The x components fulfil $k_3^x = -p_1^x$. The ω_i, E_i, and $\cos\tau$ can be re-expressed by the Mandelstam variables s, t_1, u_1, and s_4, satisfying $s_4 - s - t_1 - u_1 = 0$ [59].

In set 1, one obtains:

$$\begin{gathered}
\omega_1 = \frac{s+u_1}{2\sqrt{s_4+m^2}}, \qquad \omega_2 = \frac{s+t_1}{2\sqrt{s_4+m^2}}, \qquad \omega_3 = \frac{s_4}{2\sqrt{s_4+m^2}},\\
E_1 = \frac{s_4+2m^2}{2\sqrt{s_4+m^2}}, \qquad E_2 = -\frac{t_1+u_1+2m^2}{2\sqrt{s_4+m^2}},\\
|\vec{p}| = \frac{\sqrt{(t_1+u_1)^2-4m^2 s}}{2\sqrt{s_4+m^2}}, \qquad \cos\tau = \frac{t_1 s_4 - s(u_1+2m^2)}{(s+t_1)\sqrt{(t_1+u_1)^2-4m^2 s}}.
\end{gathered} \tag{3.77}$$

In set 2, the same relations hold, except for

$$\cos\tau = \frac{u_1 s_4 - s(t_1+2m^2)}{(s+u_1)\sqrt{(t_1+u_1)^2-4m^2 s}}. \tag{3.78}$$

For a detailed derivation, see also appendix A of [75]. All Mandelstam variables can be expressed with the help of the parametrisations given in (3.75) and (3.76) as

$$A + B\cos\gamma_1 + C\sin\gamma_1\cos\gamma_2, \tag{3.79}$$

where A, B, and C are functions of the external kinematic variables s, t_1, u_1 and m. These expressions can be classified further into three different categories:

- $A \neq 0, B = C = 0$ (category 1)
- $A \neq 0, B \neq 0, C = 0$ (category 2) and
- $A \neq 0, B \neq 0, C \neq 0$ (category 3).

s, t_1, u_1, and s_4 always belong to category 1. In set 1, t' and u_6 are in category 2, and s_3, s_5, u', and u_7 in category 3. In set 2, u' and u_7 are in category 2, and s_3, s_5, t', and u_6 in category 3. It can be shown that the matrix element $|[\Delta]M|^2$, which contains only integer powers of Mandelstam variables, can be written as

$$|[\Delta]M|^2 = \sum_i (v_1)_i (v_2^{-k})_i (v_3^{-l})_i \tag{3.80}$$

with i being a summation index. Practically, this can be achieved by extensive partional fractioning and the relations listed in (3.33). A detailed discussion of this procedure can be found in [74] and does not need to be repeated here. The v_2, v_3 are (sums of) Mandelstam variables of category 2 and 3, respectively, where $k, l \in \mathbb{Z}$; $(v_1)_i$ is for each i an expression of Mandelstam variables of category 1.

This decomposition is not unique. It can be done by parametrising all summands in one specific set, which is helpful for an automated procedure – although it gives longer results [74]. Due to the additivity of the phase space integral, in

$$\int \sum_i (v_1)_i (v_2^{-k})_i (v_3^{-l})_i = \sum_i \int (v_1)_i (v_2^{-k})_i (v_3^{-l})_i \tag{3.81}$$

not all summands have to be parametrised in the same set, i.e., both sets can be mixed. This is very useful when the integration of short matrix elements is done by hand, like, e.g., in the soft limit. By mixing both sets, one can avoid that $(v_2)_i$ and $(v_3)_i$ are sums of Mandelstam variables.

Writing $v_2 = a + b\cos\gamma_1$ and $v_3 = A + B\cos\gamma_1 + C\sin\gamma_1\cos\gamma_2$, the angular integration can be expressed by

$$I_\varepsilon^{(k,l)} = \int d\Omega_\varepsilon (a + b\cos\gamma_1)^{-k} (A + B\cos\gamma_1 + C\sin\gamma_1\cos\gamma_2)^{-l} \tag{3.82}$$

with

$$\int d\Omega_\varepsilon = \int_0^\pi d\gamma_1 \int_0^\pi d\gamma_2 \sin^{1-2\varepsilon}\gamma_1 \sin^{-2\varepsilon}\gamma_2 \tag{3.83}$$

and $k, l \in \mathbb{Z}$. These integrals can be sorted into four groups

(a) $I_0^{(k,l)}$: $a^2 \neq b^2$ and $A^2 \neq B^2 + C^2$;

(b) $I_a^{(k,l)}$: $a^2 = b^2$ and $A^2 \neq B^2 + C^2$;

(c) $I_A^{(k,l)}$: $a^2 \neq b^2$ and $A^2 = B^2 + C^2$;

(d) $I_{aA}^{(k,l)}$: $a^2 = b^2$ and $A^2 = B^2 + C^2$,

and can be done analytically.

A detailed description and a tabulation of the results can be found in [59, 73, 74]. The needed expressions are found by insertion of a, b, A, B, and C. All I_0 integrals are finite, the other ones can have poles. These singularities have their origin in collinear splittings. Only in combination with an additional infrared singularity in the case $s_4 \to 0$ double poles in $1/\varepsilon^2$ can occur. The singularities in $\frac{1}{\varepsilon}|_{\text{collinear}} \frac{1}{\varepsilon}|_{\text{infrared}}$ are cancelled by the according contributions in the virtual matrix elements.

Furthermore, in the polarised matrix elements, there are terms proportional to $\hat{p}_1^2$. They do not lead to infrared divergences. After having carried out the integration in (3.50), the parts integrated over the hat momentum are finite in the limit $s_4 \to 0$.

The lowest power coming from the propagators in the matrix element can be of the order s_4^{-2}, which is compensated by s_4^2 in (3.50). In [73, 74], it is shown that from the terms containing hat momenta, only those contribute, which are proportional to $1/(t')^2$ or $1/(u')^2$.

The techniques outlined in this section allow one to compute all phase space integrals for single-inclusive heavy quark observables analytically. This was described in detail in [58, 59, 73–76, 86]. In these works, also the integrated results for the soft cross sections are explicitly listed.

In the purely numerical case, all integrations will be done numerically except for the soft case, see below in section 3.5.2, where the integrals listed in appendix B1 are used.

3.5 Different methods for the Monte Carlo integration

Next, we want to introduce Monte Carlo integration techniques, which provide more flexibility by performing all phase space integrations numerically. These methods are essential for computing heavy quark correlations or implementing experimental cuts.

The principal idea of the various Monte Carlo integration methods can be exemplified [157, 158] on the basis of the following integral:

$$I = \lim_{\varepsilon \to 0^+} \left\{ \int_0^1 \frac{dx}{x} x^\varepsilon F(x) - \frac{1}{\varepsilon} F(0) \right\}. \tag{3.84}$$

In our case, $F(x)$ will be a known but complicated function related to a two-to-three body matrix element. The term $-\frac{1}{\varepsilon}F(0)$ results from the remaining singularities of the virtual contributions and the mass factorisation. Recall that in the phase space integration of the real emission matrix elements squared, one encounters infrared and collinear singularities. These singularities cancel, however, in combination with the virtual matrix elements and the mass factorisation counterterms due to the Bloch-Nordsieck and Kinoshita-Lee-Nauenberg theorems [103, 159–161] and the factorisation theorem, respectively.

The two most common schemes for numerical integration techniques are the subtraction and the phase space slicing method. In the subtraction method one adds and subtracts $F(0)$ under the integral sign, i.e.,

$$\begin{aligned} I &= \lim_{\varepsilon \to 0^+} \left\{ \int_0^1 \frac{dx}{x} x^\varepsilon [F(x) - F(0) + F(0)] - \frac{1}{\varepsilon} F(0) \right\} \\ &= \int_0^1 \frac{dx}{x} [F(x) - F(0)]. \end{aligned} \tag{3.85}$$

This yields a finite and numerically calculable result. Up to now, no approximations have been made. However, in practical calculations due to limited machine precision, the integral must be cut off, which is, however, not a problem in practise.

In the phase space slicing method, the integration region is divided into two parts $0 < x < \delta$ and $\delta < x < 1$ by introducing a small arbitrary parameter δ. A MacLaurin expansion of $F(x)$ yields

$$\begin{aligned} I &= \lim_{\varepsilon \to 0^+} \left\{ \int_0^\delta \frac{dx}{x} x^\varepsilon F(x) + \int_\delta^1 \frac{dx}{x} x^\varepsilon F(x) - \frac{1}{\varepsilon} F(0) \right\} \\ &= \int_\delta^1 \frac{dx}{x} F(x) + F(0) \ln \delta + \mathcal{O}(\delta). \end{aligned} \tag{3.86}$$

In the following, we will – in analogy to previous works [71, 72, 74] – adopt the phase space slicing method once in our analytical approach and the subtraction method twice in our purely numerical method. We will show this in the following subsections. We will always start with the term corresponding to $\int_0^1 \frac{dx}{x} x^\varepsilon F(x)$ from our introductory example. The term corresponding to $-\frac{1}{\varepsilon}F(0)$ from the introductory example is stemming from soft and collinear singularities and will be added later and is therefore not shown in the following.

3.5.1 The phase space slicing method in the analytical approach

In this work, the phase space slicing method is used to deal with infrared singularities in the analytic approach. The infrared divergences appear in the limit $s_4 \to 0$, i.e., when the $2 \to 3$ kinematics is effectively reduced to a $2 \to 2$ one. Therefore, we rewrite one of the remaining integrations in the $2 \to 3$ phase space (3.47) to ds_4 for partonic cross sections.

The δ cut-off introduced in (3.86) in the previous section is adopted here for the variable s_4. The term corresponding to $\frac{1}{\varepsilon}F(0)$ in (3.84) is not considered here. It stems from the remaining $1/\varepsilon$ poles of the virtual matrix element.

Let us consider a function $H(s_4)$ with an infrared singularity of the form $s_4^{-1+2\varepsilon}S(s_4)$ and a finite part $F(s_4)$, $H(s_4) = s_4^{-1-2\varepsilon}S(s_4) + F(s_4)$ where both $S(s_4)$ and $F(s_4)$ are finite in the limit $s_4 \to 0$. The function $H(s_4)$ corresponds now to the function $F(x)$ from our introductory example. Then, the result is [73–75]:

$$\int_0^{s_4^{\max}} ds_4 H(s_4) = \int_0^{s_4^{\max}} ds_4 [s_4^{-1-2\varepsilon}S(s_4) + F(s_4)] = \int_0^{\Delta} ds_4 \left[\frac{\Delta^{-2\varepsilon}}{-2\varepsilon} S(s_4)\delta(s_4) + \{S(s_4) - S(0)\}s_4^{-1-2\varepsilon} + F(s_4)\right] + \int_{\Delta}^{s_4^{\max}} ds_4 H(s_4), \tag{3.87}$$

where $s_4^{\max}$ is the upper limit allowed by kinematics. The Δ is a small parameter which has the same function as the δ from the introductory example in (3.86).

If Δ is small enough, one can neglect the term $\{S(s_4) - S(0)\}s_4^{-1-2\varepsilon} + F(s_4)$ in the first integral, and (3.87) can be approximated by:

$$\begin{aligned}\int_0^{s_4^{\max}} ds_4 H(s_4) &\approx \int_0^{s_4^{\max}} ds_4 \left[\frac{\Delta^{-2\varepsilon}}{-2\varepsilon}\delta(s_4)S(s_4) + \Theta(s_4 - \Delta)H(s_4)\right] \\ &= \int_0^{s_4^{\max}} ds_4 \left[\frac{\Delta^{-2\varepsilon}}{-2\varepsilon}\delta(s_4)S(0) + \Theta(s_4 - \Delta)H(s_4)\right].\end{aligned} \tag{3.88}$$

The soft pole contribution can be evaluated analytically with Born kinematics due to the factor $\delta(s_4)$. The term $\Delta^{-2\varepsilon}$ has to be expanded in a series. The term, stemming from the 0th order of this expansion, cancels later with the poles from the virtual corrections.

The $\ln\delta$ term in (3.86) can be recovered by expanding $\Delta^{-2\varepsilon}$ in ε. Due to the specific structures of the matrix elements, we find also $1/\varepsilon^2$ terms, and hence terms proportional to $(\ln\Delta)^2$. As in the phase space formula (3.47) the factor $s_4^{1-2\varepsilon}$ is already present, it is sufficient to determine in the matrix elements only those parts which are proportional to $1/s_4^2$ after angular integration over γ_1 and γ_2. Therefore, we express all the Mandelstam variables by s_4, t_1, s, γ_1, and γ_2. This can be done by re-writing the variables $\omega_1, \omega_2, \omega_3, \cos\tau, |\vec{p}|$ in the two different sets – as shown in equation (3.77) – to the Mandelstam variables s, t_1, u_1 and s_4.

The soft parts $S(0)$ in (3.87) can be obtained by either a direct expansion of the full matrix element or by applying the eikonal approximation to it. Then, the 0th orders of the expansion in powers of s_4 of

$$s_3 = s_4\underline{s_3}, \qquad t' = s_4\underline{t'}, \qquad \text{and} \qquad u' = s_4\underline{u'} \tag{3.89}$$

vanish. In the other Mandelstam variables

$$s_5 = s + s_4\underline{s_5}, \qquad u_6 = u_1 + s_4\underline{u_6}, \qquad u_7 = t_1 + s_4\underline{u_7}, \tag{3.90}$$

one finds $\mathcal{O}(s_4^0) \neq 0$. The underlined quantities represent the so-called reduced Mandelstam variables [74], which are defined by equation (3.90). In the limit $s_4 \to 0$, they are finite, non-vanishing functions of m^2 and the $2 \to 2$ Mandelstam variables in equation (3.22). Having introduced the reduced Mandelstam variables, the expansion of the matrix element in powers of s_4 can be done. To determine $S(0)$, we first eliminate the terms which have two of the subleading Mandelstam variables in (3.89) in the denominator. Afterwards, we factor out a factor $1/s_4^2$ from these terms and take the limit $s_4 \to 0$ in the remaining part before we perform the angular integration and arrive at the soft cross section, which has to be added to the virtual diagrams.

3.5.2 Subtraction method for the fully numerical code

Next, we discuss the application of the subtraction method to the numerical calculation. It is necessary to isolate the singularities in the calculation of the real contributions to the cross section. In this section we will, therefore, introduce a set of useful distributions.

We start with calculating a typical integral which exhibits a soft singularity in the limit $x \to 1$. In the following, we use $h(x)$ instead of $F(x)$ from the introductory example to this section. However, the singularity is now at $x = 1$ and not at $x = 0$ as in the introductory example. Furthermore, a Taylor expansion simplifies our calculation considerably. We get:

$$\begin{aligned}
\int_{\tilde{\rho}}^1 h(x)(1-x)^{-1-2\varepsilon}dx &= \int_{\tilde{\rho}}^1 \frac{h(x)}{(1-x)^{1+2\varepsilon}}dx = \int_{\tilde{\rho}}^1 \frac{h(1)}{(1-x)^{1+2\varepsilon}}dx + \int_{\tilde{\rho}}^1 \frac{h(x)-h(1)}{(1-x)^{1+2\varepsilon}}dx \\
&\overset{\text{Taylor}}{=} \int_{\tilde{\rho}}^1 \frac{h(1)}{(1-x)^{1+2\varepsilon}}dx + \int_{\tilde{\rho}}^1 (h(x)-h(1))\left[\frac{1}{1-x} - \frac{2\log(1-x)\varepsilon}{1-x} + \mathcal{O}(\varepsilon^2)\right]dx \\
&= \int_{\tilde{\rho}}^1 \left\{h(x)\frac{(1-\tilde{\rho})^{-2\varepsilon}}{-2\varepsilon}\delta(1-x) + (h(x)-h(1))\left[\frac{1}{1-x} - \frac{2\log(1-x)\varepsilon}{1-x} + \mathcal{O}(\varepsilon^2)\right]\right\}dx.
\end{aligned} \tag{3.91}$$

Here, $h(x)$ is an arbitrary test function, which is finite in the limit $x \to 1$. Leaving out the integral sign, we can write this in short form as a distribution:

$$(1-x)^{-1-2\varepsilon} = -\frac{\tilde{\beta}^{-4\varepsilon}}{2\varepsilon}\delta(1-x) + \left(\frac{1}{1-x}\right)_{\tilde{\rho}} - 2\varepsilon\left(\frac{\log(1-x)}{1-x}\right)_{\tilde{\rho}} \tag{3.92}$$

in which we have defined

$$\begin{aligned}
\int_{\tilde{\rho}}^1 h(x)\left(\frac{1}{1-x}\right)_{\tilde{\rho}}dx &= \int_{\tilde{\rho}}^1 \frac{h(x)-h(1)}{1-x}dx, \\
\int_{\tilde{\rho}}^1 h(x)\left(\frac{\log(1-x)}{1-x}\right)_{\tilde{\rho}}dx &= \int_{\tilde{\rho}}^1 [h(x)-h(1)]\frac{\log(1-x)}{1-x}dx
\end{aligned} \tag{3.93}$$

with an arbitrary parameter $\tilde{\rho} \in]\rho, 1[$ and $\tilde{\beta} = \sqrt{1-\tilde{\rho}}$.

Note again that the first term in the last line of equation (3.91) cancels in the sum with the virtual corrections.

In our final phase space formula (3.73) with the variables x and y from section 3.4.3, the limit $x \to 1$ corresponds to the infrared singularities. The collinear singularities occur for $|y| \to 1$.

Therefore, similar distributions in y can be introduced, which regulate collinear regions of phase space characterised by $y \to \pm 1$.

Compared to our introductory example, we now use $h(y)$ instead of $F(x)$ and the singularities are at $y = 1$ and $y = -1$. We start with the case $y = 1$.

The relevant integral has the form

$$\int_{1-w}^{1} h(y) \frac{1}{(1-y^2)^{1+\varepsilon}} dy = \int_{1-w}^{1} \frac{1}{2} \left(\frac{1}{1-y} + \frac{1}{1+y} \right) \frac{h(y)}{(1-y^2)^{\varepsilon}} dy, \tag{3.94}$$

where $h(y)$ is now sufficiently regular in the limit $y \to \pm 1$. Concentrating on the first term in the round brackets on the r.h.s. of (3.94), which is singular, one obtains

$$\begin{aligned}
&\int_{1-w}^{1} \frac{1}{2} \left(\frac{1}{1-y} \right) \frac{h(y)}{(1-y^2)^{\varepsilon}} dy = \\
&\int_{1-w}^{1} \frac{1}{2(1+y)^{\varepsilon}} h(y) \frac{1}{(1-y)^{1+\varepsilon}} dy = \frac{w^{-\varepsilon}}{-\varepsilon} \frac{h(1)}{2^{1+\varepsilon}} + \int_{1-w}^{1} \frac{1}{(1-y)^{1+\varepsilon}} \left[\frac{h(y)}{2(1+y)^{\varepsilon}} - \frac{h(1)}{2^{1+\varepsilon}} \right] dy \\
&\qquad = \frac{-(2w)^{-\varepsilon}}{2\varepsilon} h(1) + \int_{1-w}^{1} \frac{1}{2(1-y)} [h(y) - h(1)] dy + \mathcal{O}(\varepsilon) \\
&\quad = \int_{1-w}^{1} \left\{ \frac{-(2w)^{-\varepsilon}}{2\varepsilon} h(y) \delta(1-y) + \frac{1}{2(1-y)} [h(y) - h(1)] \right\} dy + \mathcal{O}(\varepsilon).
\end{aligned} \tag{3.95}$$

Here, $w \in]-1; 1[$ is an arbitrary parameter, too.

In principle, the results for these integrals and the cross sections calculated using them are independent of the actual choice of $\tilde{\rho}$ and w in the given intervals, but extreme choices may lead to a bad convergence of the numerical results. See also below.

Hence, the result for (3.94) reads

$$\begin{aligned}
&\int_{1-w}^{1} h(y) \frac{1}{(1-y^2)^{1+\varepsilon}} dy = \\
&\quad \int_{1-w}^{1} \left\{ -\frac{(2w)^{-\varepsilon}}{2\varepsilon} h(y) \delta(1-y) + \frac{1}{2(1-y)} [h(y) - h(1)] + \frac{h(y)}{2(1+y)} \right\} dy + \mathcal{O}(\varepsilon).
\end{aligned} \tag{3.96}$$

Analogously, for the case $y \to -1$, in which the relevant integration limits read $\int_{-1}^{-1+w}$, one finds

$$\begin{aligned}
&\int_{-1}^{1+w} h(y) \frac{1}{(1-y^2)^{1+\varepsilon}} dy = \\
&\int_{-1}^{1+w} \left\{ -\frac{(2w)^{-\varepsilon}}{2\varepsilon} h(y) \delta(y+1) + \frac{1}{2(1+y)} [h(y) - h(-1)] + \frac{h(y)}{2(1-y)} \right\} dy + \mathcal{O}(\varepsilon).
\end{aligned} \tag{3.97}$$

We will merge these two cases and define the following distribution:

$$(1-y^2)^{-1-\varepsilon} = -[\delta[(1+y)+\delta(1-y)]\frac{(2w)^{-\varepsilon}}{2\varepsilon} + \frac{1}{2}\left[\left(\frac{1}{1-y}\right)_w + \left(\frac{1}{1+y}\right)_w\right] + \mathcal{O}(\varepsilon), \tag{3.98}$$

where

$$\int_{1-w}^{1} h(y)\left(\frac{1}{1-y}\right)_w dy = \int_{1-w}^{1} \frac{h(y)-h(1)}{1-y}dy,$$

$$\int_{-1}^{-1+w} h(y)\left(\frac{1}{1+y}\right)_w dy = \int_{-1}^{-1+w} \frac{h(y)-h(-1)}{1+y}dy.$$

In the following, we will insert these distributions into the phase-space formula (3.73) and show how these distributions are used to regulate the infrared and the collinear singularities of the real matrix element.

As no hat momenta contribute here, it can be shown that no double poles in t' and u' appear in the real matrix element.

Thus, the function

$$[\Delta]f(x,y,\theta_1,\theta_2) = 4t'u'[\Delta]M^{(real)}(s,t',u',t_1,u_1)$$

is regular for $y=\pm 1$ and $x=1$.

Here, the flux factor $\frac{1}{2s}$ is included in $[\Delta]M^{(real)}(s,t',u',t_1,u_1)$.

After expressing t' and u' by s, x, and y one gets

$$[\Delta]M^{(real)}(s,t',u',t_1,u_1) = \frac{[\Delta]f(x,y,\theta_1,\theta_2)}{s^2(1-x)^2(1-y^2)}. \tag{3.99}$$

The factors in the denominator of (3.99) can now be combined with the corresponding factors from the phase space formula (3.73). Introducing the prefactor

$$\mathcal{F} = \frac{(4\pi)^{2\varepsilon-2}2^{2\varepsilon}}{32\pi^2\Gamma(1-2\varepsilon)}, \tag{3.100}$$

the result for the $2\to 3$ cross section is

$$\begin{aligned} d[\Delta]\sigma_r = \mathcal{F}\cdot(sx)^{-\varepsilon}\beta_x^{1-2\varepsilon}\sin^{-2\varepsilon}\theta_1 d\cos\theta_1 dx s^{-1-\varepsilon}dy \\ \sin^{-2\varepsilon}\theta_2 d\theta_2 (1-x)^{-1-2\varepsilon}(1-y^2)^{-1-\varepsilon}[\Delta]f(x,y,\theta_1,\theta_2). \end{aligned} \tag{3.101}$$

To proceed, one can use the expansions (3.92) and (3.98) above to regulate the singular limits $x\to 1$ and $y\to\pm 1$.

First, expanding $(1-x)^{-1-2\varepsilon}$, one obtains

$$\begin{aligned} d[\Delta]\sigma_r = d[\Delta]\sigma^s + dxdyd\theta_1 d\theta_2 \sin^{1-2\varepsilon}\theta_1 \sin^{-2\varepsilon}\theta_2 (1-y^2)^{-\varepsilon} \\ \left[\left(\frac{1}{1-x}\right)_{\tilde{\rho}} - 2\varepsilon\left(\frac{\log(1-x)}{1-x}\right)_{\tilde{\rho}}\right]\mathcal{F}s^{-1-2\varepsilon}x^{-\varepsilon}\beta_x^{1-2\varepsilon}[\Delta]f(x,y,\theta_1,\theta_2), \end{aligned} \tag{3.102}$$

where the soft part reads with $\tilde{\beta} = \sqrt{1-\tilde{\rho}}$:

$$d[\Delta]\sigma^s = dxdyd\theta_1 d\theta_2 \sin^{1-2\varepsilon}\theta_1 \sin^{-2\varepsilon}\theta_2 (1-y^2)^{-1-\varepsilon} \left[-\frac{\tilde{\beta}^{-\varepsilon}}{2\varepsilon}\delta(1-x)\right] \mathcal{F} s^{-1-2\varepsilon}\beta^{1-2\varepsilon}[\Delta]f(x,y,\theta_1,\theta_2). \quad (3.103)$$

This can be explicitly integrated over x, y and θ_2 in order to obtain

$$d[\Delta]\sigma^s = -(4\pi)^{\varepsilon-2}\frac{\Gamma(1-\varepsilon)}{\Gamma(1-2\varepsilon)} dPS_2 \frac{1}{4\pi\varepsilon} s^{-1-\varepsilon}\tilde{\beta}^{-4\varepsilon}[\Delta]f^s(\theta_1) \quad (3.104)$$

where dPS_2 is the two particle phase space given in (3.30).

The function $[\Delta]f^s(\theta_1)$ can be obtained by a Taylor expansion of $[\Delta]f(x,y,\theta_1,\theta_2)$ and integration over x, y and θ_2 using the integrals tabulated in appendix B1.

Expanding also $(1-y^2)^{-1-\varepsilon}$, the decomposition

$$d[\Delta]\sigma_r = d[\Delta]\sigma^s + d[\Delta]\sigma^{c+} + d[\Delta]\sigma^{c-} + d[\Delta]\sigma^f \quad (3.105)$$

is obtained. Here, the collinear parts read

$$d[\Delta]\sigma^{c\pm} = -\mathcal{F}\cdot(sx)^{-\varepsilon}\beta_x^{1-2\varepsilon}\sin^{-2\varepsilon}\theta_1 d\cos\theta_1 dx s^{-1-\varepsilon}dy \sin^{-2\varepsilon}\theta_2 d\theta_2 \cdot \left[\left(\frac{1}{1-x}\right)_{\tilde{\rho}} - 2\varepsilon\left(\frac{\log(1-x)}{1-x}\right)_{\tilde{\rho}}\right]\delta(1\mp y)\frac{(2w)^{-\varepsilon}}{2\varepsilon}[\Delta]f(x,y,\theta_1,\theta_2). \quad (3.106)$$

The remaining finite part without any singularities reads

$$d[\Delta]\sigma^f = dxdyd\theta_1 d\theta_2 \sin^{1-2\varepsilon}\theta_1 \sin^{-2\varepsilon}\theta_2 \frac{1}{2}\left[\left(\frac{1}{1-y}\right)_w + \left(\frac{1}{1+y}\right)_w\right] \left[\left(\frac{1}{1-x}\right)_{\tilde{\rho}} - 2\varepsilon\left(\frac{\log(1-x)}{1-x}\right)_{\tilde{\rho}}\right]\mathcal{F} s^{-1-2\varepsilon}x^{-\varepsilon}\beta_x^{1-2\varepsilon}[\Delta]f(x,y,\theta_1,\theta_2). \quad (3.107)$$

In the limit $\varepsilon \to 0$ one obtains

$$d[\Delta]\sigma^f = dxdyd\theta_1 d\theta_2 \sin\theta_1 \frac{1}{2}\left[\left(\frac{1}{1-y}\right)_w + \left(\frac{1}{1+y}\right)_w\right]\left[\left(\frac{1}{1-x}\right)_{\tilde{\rho}}\right] \quad (3.108)$$

$$\mathcal{F}_0 s^{-1}\beta_x[\Delta]f(x,y,\theta_1,\theta_2), \quad (3.109)$$

where $\mathcal{F}_0 = \lim_{\varepsilon\to 0}\mathcal{F} = \frac{1}{512\pi^4}$.

The range of integration goes from ρ to 1 for x and from -1 to $+1$ for y.

We split these integrals $I_{x,y}$ as follows: we have

$$\int_\rho^1 I_x dx = \int_\rho^{\tilde{\rho}} I_x dx + \int_{\tilde{\rho}}^1 I_x dx \quad (3.110)$$

for the x integration and similarly

$$\int_{-1}^{+1} I_y dy = \int_{-1}^{-1+w} I_y dy + \int_{-1+w}^{1-w} I_y dy + \int_{1-w}^{1} I_y dy \quad (3.111)$$

for the y integration.

Recall that in principle, the parameters $\tilde{\rho} \in]0,1[$ and $w \in]0,2[$ are arbitrary. Due to the additivity of integrals, the result does theoretically not depend on them. For the x integration the first part is not singular and can be evaluated directly without resorting to the distributions introduced above. The second part is evaluated using equation (3.92). The part in the middle of the y integral is evaluated directly because it is not singular. In the first term $\int_{-1}^{-1+w} I_y dy$ the denominator in $1+y$ is singular for $y \to -1$. Analogously, in the 3rd term $\int_{1-w}^{1} I_y dy$ the denominator part in $1-y$ gets singular for $y \to 1$. In both cases we have to use the expansion given in equation (3.98). We emphasise again that the individual terms on the right hand sides of (3.110) and (3.111) are not independent of $\tilde{\rho}$ and w, but only the sum on the right hand sides.

Summarising these results, we get

$$\begin{aligned} d[\Delta]\sigma^f = \frac{1}{1024\pi^4} \int_\rho^1 \int_{-1}^{+1} dy \frac{d\cos\theta_1 \theta_2 dy dx}{s(1-x)} \cdot \\ \left\{ \beta_x \left[\frac{2[\Delta]f(x,y)}{1-y^2} - \frac{[\Delta]f(x,1)}{1-y}\Theta(y-1+w) - \frac{[\Delta]f(x,-1)}{1+y}\Theta(-y-1+w) \right] \right. \\ -\beta \left[\frac{[\Delta]f(1,y)}{(1-y)^2}\Theta(x-\tilde{\rho}) - \frac{[\Delta]f(1,1)}{1-y}\Theta(y-1+w)\theta(x-\tilde{\rho}) \right. \\ \left. \left. - \frac{[\Delta]f(1,-1)}{1+y}\Theta(-y-1+w)\Theta(x-\tilde{\rho}) \right] \right\}. \end{aligned}$$

Note that although in principle the choices of $\tilde{\rho}$ and w are arbitrary, some choices are, however, more useful than others in the numerical implementation of this formula.

If $x \approx 1$ and $|y| \approx 1$, the numerical calculation of $f(x,y)$ gets less exact due to rounding errors following from limited machine precision of the computer. In these limits it is more efficient to use analytical series expansions of $f(x,y)$ for $x \approx 1$ and $|y| \approx 1$, respectively.

The remaining singularities in $d[\Delta]\sigma^s$ and $d[\Delta]\sigma^{c\pm}$ are shifted into the parton density functions as described in section 2.4. Furthermore, for the collinear terms we get after mass factorisation schematically [72]

$$\begin{aligned} d\hat{\sigma}^{c\pm} = \int_\rho^1 dx \frac{\beta_x \alpha_s}{32\pi^2} \left\{ \left[\left(\log\frac{s}{\mu_f^2} + \log\frac{w}{2} \right) + 2\log(1-x) \right] [\Delta]\tilde{P}_0(x) - [\Delta]\tilde{P}_1(x) \right\} \cdot \\ \cdot [\Delta]M_{born}(x\,s, q_{2,1}). \end{aligned} \quad (3.112)$$

The hard terms $[\Delta]\tilde{P}(x) = [\Delta]\tilde{P}_0(x) + \varepsilon[\Delta]\tilde{P}_1(x)$ of the splitting functions are listed in appendix B. The soft terms can be obtained from the literature by replacing the plus distribution by our ρ distribution what leads to additional logarithmic terms.

The soft parts of the splitting functions lead to effective $2 \to 2$ kinematics and are subtracted from $d[\Delta]\sigma^s$ as described in [71]. This gives $d[\Delta]\hat{\sigma}^s$.

3.6 From partonic to hadronic cross sections

As mentioned in chapter 2, relevant for the experiments are not the partonic cross sections, but only their hadronic counterparts. Due to the factorisation theorem the

partonic cross sections have to be convoluted with the parton density functions. Furthermore, dependent on the final state, the fragmentation of the heavy quarks and the subsequent decays of the D and B mesons have to be included. We will now sketch how the two additional integrals resulting from factorisation are implemented in our two types of codes.

3.6.1 The largely analytical case

All studies based on the analytical code remain on the single-inclusive heavy quark or antiquark level. Denoting this process by

$$H_1(K_1) + H_2(K_2) \to h(p_2) + X \tag{3.113}$$

for hadroproduction (photoproduction goes analogously), the hadronic kinematic invariants read

$$\begin{aligned} S &\equiv (K_1 + K_2)^2, \\ T_1 &\equiv (K_2 - p_2)^2 - m^2, \\ U_1 &\equiv (K_1 - p_1)^2 - m^2. \end{aligned} \tag{3.114}$$

Using $k_i = x_i K_i$, their partonic counterparts can be expressed as

$$\begin{aligned} s &= (x_1 K_1 + x_2 K_2)^2 = x_1 x_2 S, \\ t_1 &= (x_2 K_2 - p_2)^2 - m^2 = x_2 T_1, \\ u_1 &= (x_1 K_1 - p_1)^2 - m^2 = x_1 U_1. \end{aligned} \tag{3.115}$$

For the phase space slicing method, the condition $\Delta \leq s_4$ reads

$$\Delta \leq s_4 = s + t_1 + u_1 = x_1 x_2 S + x_2 T_1 + x_1 U_1. \tag{3.116}$$

Assuming the x_2 integration to be the inner one, the lower limit depends on x_1 and the hadronic Mandelstam variables given above:

$$x_2 \geq x_2^{\min}(\Delta) = \frac{\Delta - x_1 U_1}{x_1 S + T_1}, \text{ where } x_1 \geq x_1^{\min} = -\frac{T_1}{S + U_1}. \tag{3.117}$$

Summarising, the hadronic cross section can be denoted by

$$\frac{d^2[\Delta]\sigma(K_1, K_2)}{dT_1 dU_1} = \sum_{l,m} \int_{x_1^{\min}}^1 dx_1 \int_{x_2^{\min}}^1 dx_2 x_1[\Delta] f_l^{(1)}(x_1, \mu_f^2) x_2[\Delta] f_m^{(2)}(x_2, \mu_f^2) \cdot \frac{d^2[\Delta]\hat{\sigma}_{lm}(x_1 K_1, x_2 K_2)}{dt_1 du_1}. \tag{3.118}$$

The parts containing a $\delta(s_4)$ function can be transformed into a delta function in x_2:

$$\delta(s_4) = \delta(x_1 x_2 S + x_2 T_1 + x_1 U_1) = \delta(x_2(x_1 S + T_1) + x_1 U_1) = \frac{\delta(x_2 - x_2^{\min}(0))}{x_1 S + T_1}. \tag{3.119}$$

For these processes, which have a $2 \to 2$ kinematics, one finally obtains

$$\frac{d^2[\Delta]\sigma}{dT_1 dU_1} = \sum_{l,m} \int_{x_1^{\min}}^1 dx_1 \frac{1}{x_1 S + T_1} x_1[\Delta] f_l^{(1)}(x_1, \mu_f^2) x_2^{\min}(0)[\Delta] f_m^{(2)}(x_2^{\min}(0), \mu_f^2) \cdot \frac{d^2[\Delta]\hat{\sigma}_{lm}(x_1 K_1, x_2^{\min}(0) K_2)}{dt_1 du_1}. \quad (3.120)$$

Also for the real emission the x_2 integration can be transformed to a s_4 one:

$$\frac{d^2[\Delta]\sigma}{dT_1 dU_1} = \sum_{l,m} \int_{x_1^{\min}}^1 dx_1 \int_\Delta^{s_4^{\max}} ds_4 \frac{1}{x_1 S + T_1} x_1[\Delta] f_l^{(1)}(x_1, \mu_f^2) x_2'[\Delta] f_m^{(2)}(x_2', \mu_f^2) \cdot \frac{d^2[\Delta]\hat{\sigma}_{lm}(x_1 K_1, x_2' K_2)}{dt_1 du_1}. \quad (3.121)$$

Here,

$$x_2' = \frac{s_4 - x_1 U_1}{x_1 S + T_1} \quad \text{and} \quad s_4^{\max} = x_1 S + T_1 + x_1 U_1. \quad (3.122)$$

As the Mandelstam variables T_1 and U_1 are not directly measured, we will recall their connection to the experimental quantities rapidity y and transverse momentum p_T. In the c.m.s. of the incoming hadrons, the four-momentum of the detected heavy quark shall be denoted by $(E, p_L, \vec{p}_T)$ with E its energy and p_L and $\vec{p}_T$ its longitudinal and transverse momentum. One can express the transverse mass m_T and the rapidity y by T_1 and U_1:

$$m_T^2 = m^2 + p_T^2 = \frac{T_1 U_1}{S} \quad (3.123)$$

and

$$y = \operatorname{arctanh} \frac{p_L}{E} = \frac{1}{2} \log \frac{U_1}{T_1}. \quad (3.124)$$

Using the Jacobian

$$dT_1 dU_1 = S dm_T^2 dy \quad (3.125)$$

and changing the integration limits accordingly, one can express the total cross section as

$$\int_{\frac{S}{2}(1-\beta_S)}^{\frac{S}{2}(1+\beta_S)} d(-T_1) \int_{-\frac{m^2 S}{T_1}}^{S+T_1} d(-U_1) = S \int_{m^2}^{S/4} dm_T^2 \int_{-\operatorname{arcosh} \frac{\sqrt{S}}{2m_T}}^{\operatorname{arcosh} \frac{\sqrt{S}}{2m_T}} dy = S \int_{-\frac{1}{2} \ln \frac{1+\beta_S}{1-\beta_S}}^{\frac{1}{2} \ln \frac{1+\beta_S}{1-\beta_S}} dy \int_{m^2}^{\frac{S}{4 \cosh^2 y}} dm_T^2. \quad (3.126)$$

This integral can also be transformed into various other phenomenologically interesting variables. For further discussions the reader is referred to [74] and [86].

In addition, we note the relation between pseudorapidity η and rapidity y, which differ for massive particles [86]:

$$\tanh(\eta) = \cos\theta_H = \frac{\sqrt{\frac{m_T^2}{1-\tanh^2 y}} \tanh y}{\sqrt{\frac{m_T^2}{1-\tanh^2 y} - m^2}}. \quad (3.127)$$

3.6.2 The fully numerical case

In the fully numerical case, all phase space integrations and the convolutions with the parton distribution functions are performed with Monte Carlo methods using the VEGAS algorithm [162, 163] supplemented with a histogramming routine. With the choice of the integration variables x_1, x_2, x, y, θ_1 and θ_2 all observables of interest can be calculated. The relation to the Mandelstam variables is given in section 3.4.3 above. Using these Mandelstam variables, the momentum/momenta of the heavy quark(s) in the c.m.s. of the incoming particles can be calculated and transformed to the laboratory system. Afterwards, cuts can be applied to these momenta and to observables defined through them. The remaining events are subsequently sorted into histograms. Several histograms can be made at the same time, as long as they use the same sets of input variables (e.g., renormalisation and factorisation scales, mass, c.m.s. energy, free parameter of the heavy quark to meson fragmentation function). In the limit of a very small bin size the limit of differential cross sections is reached. How closely this limit can be reached, is, of course, a practical issue.

The equation implemented in the program reads

$$\begin{aligned} d[\Delta]\sigma^Q &= \sum_{a,b} \int dx_1 dx_2 [\Delta] f_a(x_1, \mu_f) [\Delta] f_b(x_2, \mu_f)\, \mathcal{S} \\ &\times \quad d[\Delta]\hat{\sigma}_{ab}(x_1, x_2, S, m, p_1, p_2, \mu_f, \mu_r). \end{aligned} \tag{3.128}$$

Practically, this means that one has two additional integrations ($dx_1 dx_2$) compared to the calculation in section 3.5.2, which are also done numerically like for the phase space variables x, y, θ_1 and θ_2. Furthermore, in equation (3.128), the "measurement function" $\mathcal{S}$ is used to define the observable one is interested in. It can be simply implemented by a multiplication with the calculated cross section values. One can think of $\mathcal{S}$ as being a set of step functions implementing the experimental cuts imposed on the final-state particles and selecting a certain bin in a histogram. In this case, the implementation in the numerical code is possible simply using an IF-loop.

Charm and bottom quarks are currently detected only indirectly at RHIC, mainly through the semi-leptonic decays of the produced heavy D and B mesons. At COMPASS the produced D mesons are reconstructed via their hadronic decays into kaons and pions. Thus, the cross section (2.36) at the heavy quark-level is not yet sufficient for comparing theory with experimental results. One needs to convolute the parton-level results for $d\Delta\sigma^Q$ with additional phenomenological fragmentation functions $D^{Q\to H_Q}$ and, where necessary, $f^{H_Q\to e,\mu}$ describing the hadronisation into a heavy meson H_Q and the semi-leptonic decay of H_Q into the observed lepton, respectively. This was described in section 2.8. Our flexible parton-level Monte Carlo program not only performs the phase-space integrations for arbitrary $\mathcal{S}$ for any infrared safe observable but, if applicable, also accounts for the semi-leptonic decays of the heavy quark pair into electrons and muons. We specify our choice for $D^{Q\to H_Q}$ and $f^{H_Q\to e,\mu}$ in chapter 5.

4

Partonic subprocesses and contributing Feynman diagrams

The previous chapter has been devoted to general technical aspects of the calculation like the treatment of phase space integrals and the decomposition of the matrix elements into soft, collinear, and finite contributions. Next, the partonic subprocesses will be discussed. Starting from the relevant Feynman diagrams, the way to obtain the matrix elements squared in terms of Mandelstam variables will be briefly recalled. We will present the leading order results in detail and sketch the next-to-leading order calculations. Similar results can be found in [58, 59, 73–75].

4.1 Hadroproduction of heavy quarks

4.1.1 The leading order contributions

For quark-antiquark annihilation

$$q(k_1) + \bar{q}(k_2) \to Q_k(p_1) + \bar{Q}_l(p_2) \tag{4.1}$$

only one Feynman diagram, $M_{q\bar{q}}^{\mathrm{LO}}$, shown in figure 4.1, contributes at leading order. The momenta are labelled by $k_{1,2}$ and by $p_{1,2}$.

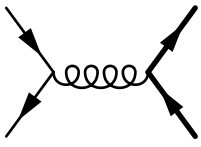

Figure 4.1: Feynman diagram for quark-antiquark annihilation at leading order.

Applying the Feynman rules given in the appendix, one obtains for the scattering amplitude

$$iM_{q\bar{q}}^{\mathrm{LO}} = \bar{v}(k_2) ig\gamma_\mu T^a u(k_1) \frac{-i}{s} ig\bar{u}(p_1)\gamma^\mu T^a v(p_2). \tag{4.2}$$

Including the factor $\frac{1}{4N_C^2}$ for the averaging over spins and colours of the incoming partons, the result for the helicity-dependent matrix element squared reads

$$|M_{q\bar{q}}^{\mathrm{LO}}|^2(\lambda_1,\lambda_2) = \overline{|M|^2} + \lambda_1\lambda_2\Delta|M|^2 = \mathrm{Tr}(\not{k}_2(1-\lambda_1\gamma_5)\gamma_\mu\not{k}_1(1+\lambda_2\gamma_5)\gamma_\nu) \\ \mathrm{Tr}((\not{p}_2 - m)\gamma^\nu(\not{p}_1 + m)\gamma^\mu)g^4\frac{1}{s^2}\,\mathrm{Tr}(T^aT^b)\,\mathrm{Tr}(T^aT^b)\frac{1}{4N_C^2}. \quad (4.3)$$

Here Tr is used as shorthand notation for trace. In the following, the averaging over spins and colours of the incoming partons will always be included in the matrix element squared if not stated otherwise.

The calculation of the traces of gamma matrices has been done with the package Tracer [164] in Mathematica [165]; furthermore, the HVBM scheme [102, 154] for γ_5 and the Levi-Civita tensor in $n = 4 - 2\varepsilon$ dimensions, see section 3.1, has been adopted if applicable. FeynCalc [166] was useful to evaluate complicated colour traces in Mathematica.

We obtain from equation (4.3)

$$|[\Delta]M_{q\bar{q}}^{\mathrm{LO}}|^2 = \frac{C_F}{N_C}g^4[\Delta]A_{\mathrm{QED}} + \mathcal{O}(\varepsilon^3) \quad (4.4)$$

with

$$A_{\mathrm{QED}} = \frac{t_1^2+u_1^2}{s^2} + \frac{2m^2}{s} - \varepsilon \quad (4.5)$$

and

$$\Delta A_{\mathrm{QED}} = -\frac{t_1^2+u_1^2}{s^2} - \frac{2m^2}{s} - \varepsilon. \quad (4.6)$$

For gluon-gluon fusion,

$$g(k_1) + g(k_2) \to Q(p_1) + \bar{Q}(p_2) \quad (4.7)$$

one has to consider the three diagrams, $M_{gg,1}^{\mathrm{LO}}$, $M_{gg,2}^{\mathrm{LO}}$, and $M_{gg,3}^{\mathrm{LO}}$ shown in figure 4.2. If

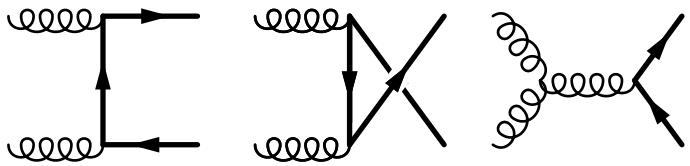

Figure 4.2: Feynman diagrams for gluon-gluon fusion in leading order.

the calculation of the unpolarised matrix elements is done using $\sum_\lambda \epsilon^\mu(q,\lambda)\epsilon^{\nu *}(q,\lambda) = -\frac{1}{2}g_{\mu\nu}$ for the sum of gluon polarisations, one has to include additional ghost contributions, $M_{gg,4}^{\mathrm{LO}}$ and $M_{gg,5}^{\mathrm{LO}}$, as depicted in figure 4.3. They give additional contributions, which eliminate the unphysical longitudinal degrees of freedom of the gluon in the Feynman gauge. A detailed discussion can be found in [74].

One ends up with

$$|\overline{M}_{gg}^{\mathrm{LO}}|^2 = (\overline{M}_{gg,1}^{\mathrm{LO}} + \overline{M}_{gg,2}^{\mathrm{LO}} + \overline{M}_{gg,3}^{\mathrm{LO}})(\overline{M}_{gg,1}^{\mathrm{LO}} + \overline{M}_{gg,2}^{\mathrm{LO}} + \overline{M}_{gg,3}^{\mathrm{LO}})^* + |\overline{M}_{gg,4}^{\mathrm{LO}}|^2 + |\overline{M}_{gg,5}^{\mathrm{LO}}|^2 \quad (4.8)$$

and

$$|\Delta M_{gg}^{\mathrm{LO}}|^2 = (\Delta M_{gg,1}^{\mathrm{LO}} + \Delta M_{gg,2}^{\mathrm{LO}} + \Delta M_{gg,3}^{\mathrm{LO}})(\Delta M_{gg,1}^{\mathrm{LO}} + \Delta M_{gg,2}^{\mathrm{LO}} + \Delta M_{gg,3}^{\mathrm{LO}})^*. \quad (4.9)$$

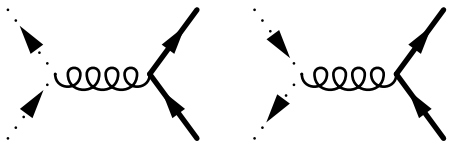

Figure 4.3: Leading order ghost contributions for unpolarised gluon-gluon fusion.

In terms of kinematic invariants, the result reads [73, 74]:

$$|[\Delta]M_{gg}^{\mathrm{LO}}|^2 = g^4 \frac{1}{2(N_C^2-1)} \left[2C_F - 2C_A \frac{t_1 u_1}{s^2}\right] [\Delta]E_\varepsilon^2 [\Delta]B_{\mathrm{QED}} + \mathcal{O}(\varepsilon^3) \tag{4.10}$$

with

$$B_{\mathrm{QED}} = \frac{t_1}{u_1} + \frac{u_1}{t_1} + \frac{4m^2 s}{t_1 u_1}\left(1 - \frac{m^2 s}{t_1 u_1}\right) - 2\varepsilon\left(\frac{s^2}{t_1 u_1} - 1\right) + \varepsilon^2 \frac{s^2}{t_1 u_1} \tag{4.11}$$

and $E_\varepsilon = \frac{1}{1-\varepsilon}$. In the longitudinally polarised case, E_ε has to be replaced by $\Delta E_\varepsilon = 1$ as it originates in the unpolarised case from the averaging over the $n-2$ spin degrees of freedom. The corresponding matrix element is given by

$$\Delta B_{\mathrm{QED}} = \left(\frac{t_1}{u_1} + \frac{u_1}{t_1}\right)\left(\frac{2m^2 s}{t_1 u_1} - 1\right). \tag{4.12}$$

The LO differential cross section is given via equation (3.28). At leading order accuracy no singularities occur and the limit $\varepsilon \to 0$ can be taken. The $\mathcal{O}(\varepsilon)$ contributions in equations (4.5), (4.6), (4.11) and (4.12) are relevant for the soft and collinear regions of phase space at NLO accuracy. Therefore, we have presented them up to order $\mathcal{O}(\varepsilon^2)$. In LO, the phase space integration can be performed completely analytically. With the abbreviation

$$\beta = \sqrt{1 - \frac{4m^2}{s}} \tag{4.13}$$

the results for the total partonic cross sections read

$$\hat{\sigma}_{q\bar{q}}(s, m^2, \mu_r^2) = \frac{8\pi\alpha_s^2(\mu_r^2)}{27 s^2}\beta(2m^2 + s) = -\Delta\hat{\sigma}_{q\bar{q}}(s, m^2, \mu_r^2) \tag{4.14}$$

due to helicity conservation. For gluon-gluon fusion, one obtains

$$\hat{\sigma}_{gg}(s, m^2, \mu_r^2) = \frac{\pi\alpha_s^2(\mu_r^2)}{48 s^2}\left[\frac{16(m^4 + 4m^2 s + s^2)}{s}\ln\left(\frac{1+\beta}{1-\beta}\right) - 4\beta(31m^2 + 7s^2)\right] \tag{4.15}$$

and

$$\Delta\hat{\sigma}_{gg}(s, m^2, \mu_r^2) = \frac{\pi\alpha_s^2(\mu_r^2)}{16 s^2}\left[20\beta(m^2 + s) + \frac{8}{3}(9m^2 + 2s)\ln\left(\frac{1-\beta}{1+\beta}\right)\right]. \tag{4.16}$$

We note that one way to visualise the total partonic cross sections is to present them in terms of scaling functions, which can be defined by

$$[\Delta]\hat{\sigma}_{lm}^{(0)}(s, m^2, \mu_r^2) = \frac{\alpha_s^2(\mu_r^2)}{m^2}[\Delta]f_{lm}^{(0)}(\eta) \tag{4.17}$$

with

$$\eta \equiv \frac{s}{4m^2} - 1 = \frac{\beta^2}{1-\beta^2}. \tag{4.18}$$

η measures the distance from the partonic threshold for $Q\bar{Q}$ production, i.e., $s = 4m^2$. This definition can be straightforwardly extended to NLO, as was extensively discussed in the literature [73, 74, 86] and will be shown in equation (4.24).

4.1.2 Hadroproduction of heavy quarks at next-to-leading order

At next-to-leading order, virtual and real corrections to the leading order processes have to be considered. One additional process not present at leading order occurs at next-to-leading order: the gluon-(anti)quark scattering.

The five real diagrams for quark-antiquark annihilation

$$q(k_1) + \bar{q}(k_2) \to Q(p_1) + \bar{Q}(p_2) + g(k_3) \tag{4.19}$$

are shown in figure 4.4.

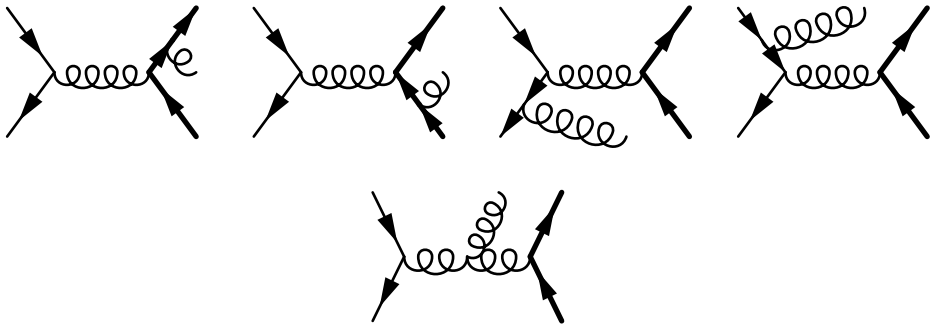

Figure 4.4: Real emission contributions to quark-antiquark annihilation at NLO.

The virtual one loop corrections to

$$q(k_1) + \bar{q}(k_2) \to Q(p_1) + \bar{Q}(p_2) \tag{4.20}$$

are sketched in figure 4.5.

In the literature the matrix elements for quark-antiquark annihilation have been decomposed into several contributions with different colour structure [58] in order to relate them to analogous QED processes. Such a decomposition can be helpful in order not to lose the overview. However, we will not repeat this discussion here, as in principle such a decomposition is completely arbitrary and not of any physical relevance.

Next, we will discuss the NLO corrections to gluon-gluon fusion, the second process already contributing at LO. Gluon-gluon fusion at NLO,

$$g(k_1) + g(k_2) \to Q(p_1) + \bar{Q}(p_2) + g(k_3) \tag{4.21}$$

has many contributing Feynman diagrams which considerably complicates the calculations. The real emission corrections are shown in figure 4.6, and the virtual contributions are depicted in figure 4.7.

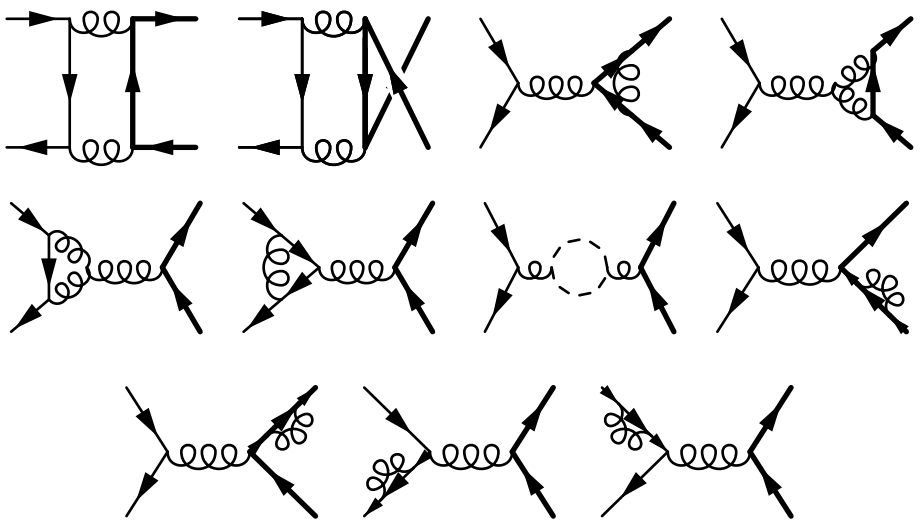

Figure 4.5: Virtual diagrams for quark-antiquark annihilation. The dashed loop represents a gluon, a ghost or a quark-antiquark loop.

In the unpolarised case, additional ghost graphs have to be included to cancel unphysical degrees of freedom, see the discussion in section 4.1.1 above. The ghost contributions are obtained by the following procedure: in all diagrams with a three gluon vertex two external gluons are replaced by a ghost line. Both directions of momentum flow need to be taken into account, see figure 4.3.

Gluon-(anti)quark scattering,

$$g(k_1) + \bar{q}(k_2) \to Q(p_1) + \bar{Q}(p_2) + \bar{q}(k_3) \tag{4.22}$$

is a genuine NLO process to which the five Feynman diagrams shown in figure 4.8 contribute.

In the unpolarised case, the matrix elements $\overline{M}_{g\bar{q}}$ can be obtained from $\overline{M}_{q\bar{q}}$ by crossing of the momenta k_1 and k_3. However, a factor (-1) for the exchange of a fermion in the initial state with a boson in the final state has to be taken into account. This crossing does not work in the polarised case, because we have already summed over the helicities of the final-state partons. The Feynman diagrams of gluon-quark fusion

$$g(k_1) + q(k_2) \to Q(p_1) + \bar{Q}(p_2) + q(k_3) \tag{4.23}$$

can be derived from the Feynman diagrams of gluon-antiquark fusion, which are depicted in figure 4.8, by inverting the direction of momentum on the light quark line. As there is no leading order process for gluon-(anti)quark scattering, there are no virtual corrections.

The scaling functions at NLO are defined via

$$[\Delta]\hat{\sigma}_{lm}(s, m^2, \mu_f^2, \mu_r^2) = \int_{s/2(1-\beta)}^{s/2(1+\beta)} d(-t_1) \int_{-\frac{m^2 s}{t_1}}^{s+t_1} d(-u_1) \frac{d^2[\Delta]\hat{\sigma}_{lm}}{dt_1 du_1} = \frac{\alpha_s^2(\mu_r^2)}{m^2} \cdot$$
$$\left\{ [\Delta] f_{lm}^{(0)}(\eta) + 4\pi\alpha_s(\mu_r) \left[[\Delta] f_{lm}^{(1)}(\eta) + [\Delta] \bar{f}_{lm}^{(1)}(\eta) \ln \frac{\mu_f^2}{m^2} + \frac{\beta_1}{8\pi^2} [\Delta] f_{lm}^{(0)}(\eta) \ln \frac{\mu_r^2}{\mu_f^2} \right] \right\}, \tag{4.24}$$

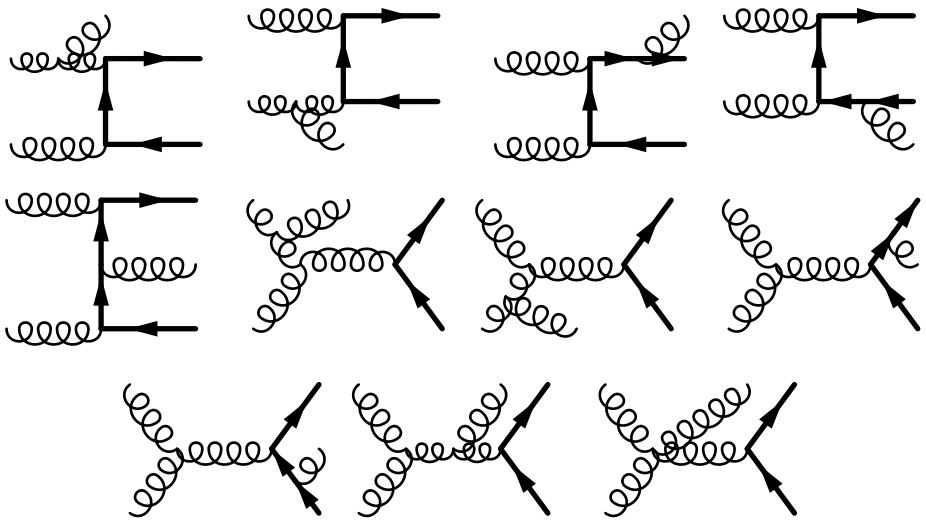

Figure 4.6: Real Feynman diagrams for gluon-gluon fusion. The rest of the diagrams can be obtained by inverting the arrows on the heavy quark lines in the first five diagrams.

where β_1 has been defined in equation (2.12) and η in equation (4.18).

A detailed discussion of the scaling functions including several plots can be found in [73, 74, 86]. Therefore, we refrain from showing them here.

4.1.3 The charge asymmetry

At LO approximation the processes (4.1) and (4.7) relevant for heavy flavour production do not discriminate between a produced heavy quark Q and a heavy antiquark $\bar{Q}$. Hence, at any given point (p_T, y) in phase-space the yields $\frac{d\sigma}{dp_T}$ and $\frac{d\sigma}{dy}$ for Q and $\bar{Q}$ are identical.

Radiative corrections change this picture and give rise to charge asymmetries

$$A_C \equiv \frac{d\sigma^Q - d\sigma^{\bar{Q}}}{d\sigma^Q + d\sigma^{\bar{Q}}}. \tag{4.25}$$

Any measurement of A_C will directly probe and perhaps improve our understanding of QCD dynamics beyond the LO. For a long time, this higher-order effect has received relatively little attention [83, 84, 86, 167–170] but was measured for the first time in case of top production at CDF [171]. At the TeVatron, the top quark charge asymmetry was larger than predicted [172–175]. At the LHC, the charge asymmetry for top quarks amounts to a few percent and agrees with theoretical calculations [83, 84, 86] with large experimental uncertainties [176–178]. We will explore the prospects of accessing A_C in pp and $\bar{p}p$ collisions at J-PARC and GSI-FAIR, respectively in section 5.2.3 below. Due to the relatively low c.m.s. energies available there, we have to limit ourselves to charm quark production. Given that longitudinally polarised beams and targets are a viable option, we also explore for these experiments the polarised charge asymmetry,

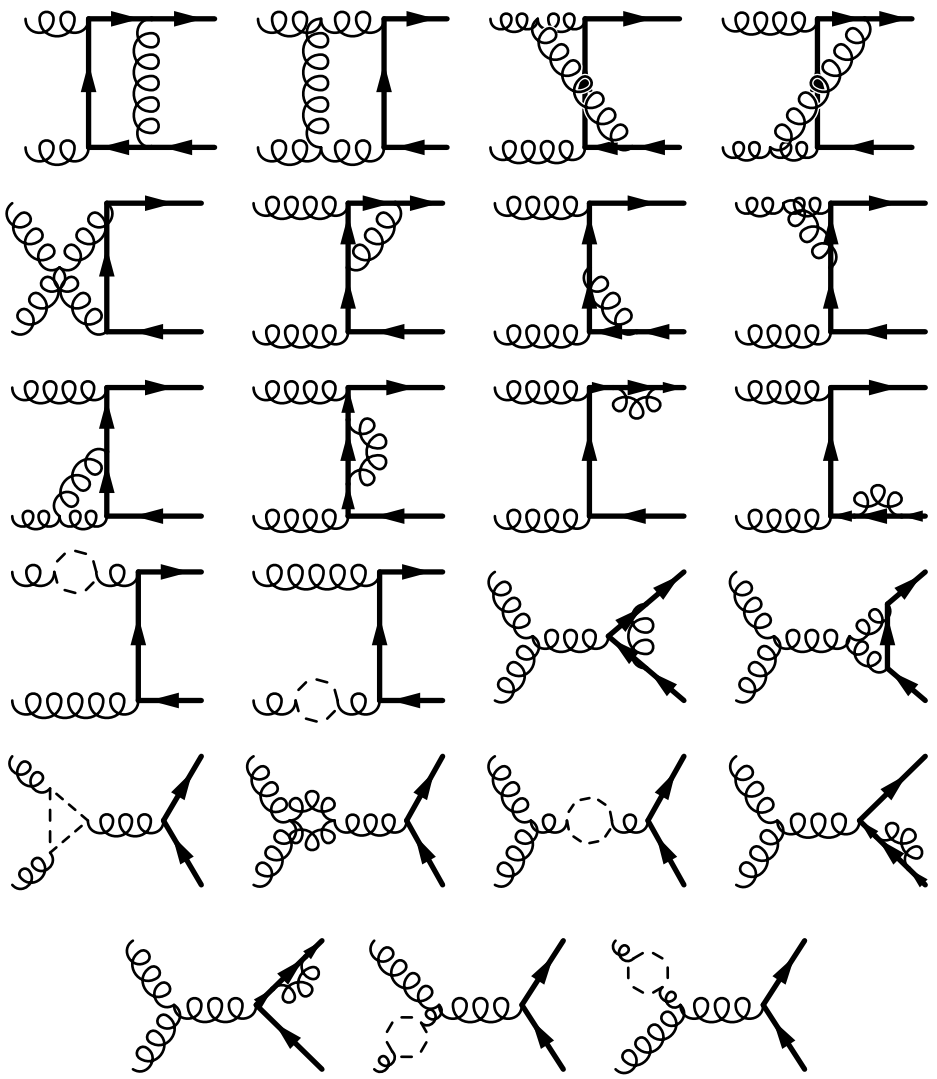

Figure 4.7: Virtual diagrams for the gluon-gluon fusion process. Additional virtual diagrams can be obtained by inverting the arrows on the heavy quark lines in the diagrams 1, 2, and 5 to 14. The dashed loops represent here gluon, ghost and quark loops as in the quark-antiquark case.

which we define as in equation (4.25) with the cross sections $d\sigma^{Q[\bar{Q}]}$ replaced by their polarised counterparts $d\Delta\sigma^{Q[\bar{Q}]}$. The results are presented in chapter 5.

At NLO the charge asymmetry receives only a very limited number of contributions. Instead of making use of the results available in the literature [58–60, 71, 73, 179], we chose to re-calculate the numerator of A_C from scratch in both the unpolarised and polarised case. The origin of A_C resides in the Abelian (QED) part of the higher order processes and is related to the interference between amplitudes which acquire different signs under the exchange of Q and $\bar{Q}$. The gluon-gluon fusion process in (4.7) is evidently charge symmetric also beyond LO and does not contribute to A_C. Also non-Abelian amplitudes involving the triple-gluon vertex depend only on $Q + \bar{Q}$ and lead to contributions which are symmetric under exchanging Q and $\bar{Q}$. Upon close

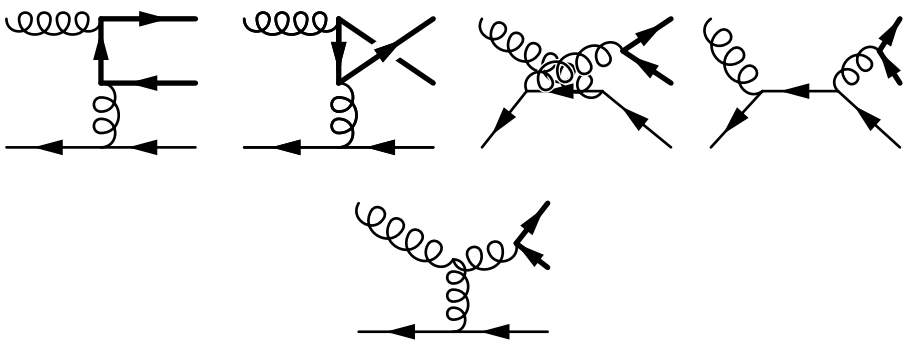

Figure 4.8: Feynman diagrams for gluon-antiquark scattering at $\mathcal{O}(\alpha_s^3)$.

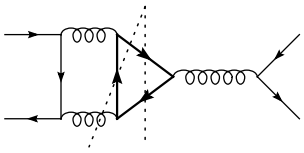

Figure 4.9: Sample $q\bar{q}$ cut diagram contributing to A_C.

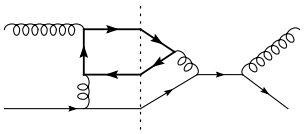

Figure 4.10: Sample gq cut diagram contributing to A_C.

examination of the remaining amplitudes for the $q\bar{q}$ and gq $[g\bar{q}]$ initiated subprocesses at NLO, one finds that only such "cut diagrams" contribute which have three vertices on both the heavy and light quark line, as explained below. In case of the virtual loop corrections to the LO $q\bar{q}$ process, only the interference of the box diagrams with the Born amplitude contributes. Examples of cut diagrams relevant for the computation of A_C and ΔA_C are depicted in Figs. 4.9 and 4.10.

This observation can be readily understood. To this end, let us write the partonic subprocess cross section $d\hat{\sigma}_{ab\to QX}$ as the sum of the interference contributions labelled by the indices i, j

$$d\hat{\sigma}_{ab\to QX} = K_{ab} \sum_{ij} \mathcal{M}_i \mathcal{M}_j^* \Big|_{ab\to QX}. \tag{4.26}$$

For simplicity, pre-factors such as the spin and colour averages are mapped into K_{ab}. Phase-space integration for all unobserved partons is implicitly understood in (4.26). Expressions similar to (4.26) hold for polarised partonic cross sections $d\Delta\hat{\sigma}_{ab\to QX}$ as well as for $ab \to \bar{Q}X$. For the numerator of A_C we have to examine the difference

$$\Delta_{ij} = \mathcal{M}_i \mathcal{M}_j^* \Big|_{ab\to QX} - \mathcal{M}_i \mathcal{M}_j^* \Big|_{ab\to \bar{Q}X} \tag{4.27}$$

for all i, j. By interchanging Q and $\bar{Q}$, the Dirac structure relevant for $\mathcal{M}_i \mathcal{M}_j^*$ changes sign for an odd number of propagators in the heavy quark trace and otherwise remains

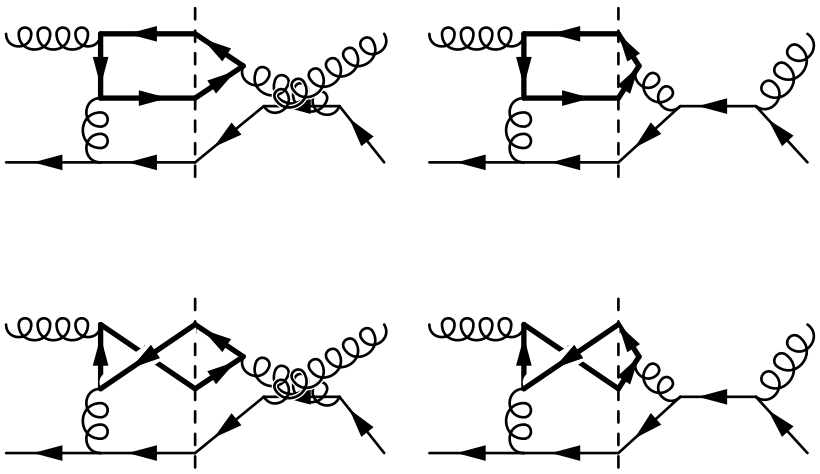

Figure 4.11: Examples of interference diagrams contributing to the charge asymmetry in the gluon-antiquark case.

the same. The colour structure is invariant, except for $\mathrm{Tr}[T_k T_l T_m] = (d_{klm} + i f_{klm})/4$ which contains a symmetric and an anti-symmetric piece, $d_{klm} = d_{mlk}$ and $f_{klm} = -f_{mlk}$, respectively.

Combining everything, only those cut diagrams with three vertices on both the heavy and the light quark line, cf. figure 4.11, contribute to A_C, and one finds [84]

$$\Delta_{ij} = \frac{1}{8}(d_{klm})^2 \widetilde{\mathcal{M}_i \mathcal{M}_j^*}\Big|_{ab\to QX} = \frac{5}{3}\widetilde{\mathcal{M}_i \mathcal{M}_j^*}\Big|_{ab\to QX}, \tag{4.28}$$

with $(d_{klm})^2 = 40/3$. A more detailed calculation can be found in [86]. $\widetilde{\mathcal{M}_i \mathcal{M}_j^*}$ denotes the interference of the two amplitudes except for the factor related to the QCD colour structure, and is the same (up to prefactors) as for the corresponding QED processes [180–182], e.g, $e^+e^- \to \mu^+\mu^-\gamma$. Let us mention that there is a similar effect in the QCD scale evolution of parton densities at next-to-next-to-leading order (NNLO) also proportional to $(d_{klm})^2$ and leading to a strange quark asymmetry $s(x) \neq \bar{s}(x)$ [183].

All contributions to the numerator of A_C at $\mathcal{O}(\alpha_s^3)$ are free of ultraviolet as well as collinear singularities as a consequence of the symmetry of the LO processes (4.1) and (4.7) under exchanging Q and $\bar{Q}$. Infrared (IR) singularities appear in both real gluon emission and virtual loop corrections to the LO $q\bar{q}$ process and cancel in their sum. Effectively this implies that the NLO matrix elements only contain the charge asymmetry at LO approximation. As in [58–60, 71, 73, 179] and described in the previous chapter, we use dimensional regularisation to deal with IR poles in intermediate steps of the calculation. In [84] a small gluon energy E^g_{cut} was used to cut off IR singularities. While the charge asymmetry also appears in the limit $m \to 0$, it vanishes for the total heavy quark cross section as a consequence of charge conjugation invariance.

Similar considerations as the ones which have led to the charge asymmetry result in the following useful relations:

$$|M(gq \to Q\bar{Q}q)|^2 = |M(g\bar{q} \to \bar{Q}Q\bar{q})|^2, \tag{4.29}$$

$$|M(gq \to \bar{Q}Qq)|^2 = |M(g\bar{q} \to Q\bar{Q}\bar{q})|^2, \tag{4.30}$$

and hence

$$\begin{aligned} |M(gq \to Q\bar{Q}q)|^2 - |M(g\bar{q} \to Q\bar{Q}\bar{q})|^2 &= |M(gq \to Q\bar{Q}q)|^2 - |M(gq \to \bar{Q}Qq)|^2 \\ &= |M(g\bar{q} \to \bar{Q}Q\bar{q})|^2 - |M(g\bar{q} \to Q\bar{Q}\bar{q})|^2. \end{aligned} \tag{4.31}$$

4.2 Photoproduction of heavy quarks

4.2.1 Decomposition in direct and resolved part

Heavy quarks can also be produced in photoproduction processes, e.g., in photon-proton scattering, where the photon has a small virtuality Q^2. In case of photoproduction, where a quasi-real photon is exchanged, one has to include not only the direct contributions, but also the so called "resolved" contributions, where the photon fluctuates into a vector meson of the same quantum numbers before the hard scattering with partons in the proton takes place.

Speaking in more detail, the photon can either interact directly with an other parton from the proton or it can fluctuate into quarks and gluons, which then interact with the other parton from the proton as described in section 2.6. The direct and resolved part can formally be derived using the factorisation theorem. We emphasise that only the sum of the direct and the resolved part is of physical relevance. However, at certain experimental kinematics, e.g., at COMPASS, the resolved part can be very small and therefore negligible compared to other uncertainties. In section 5.4 below, a detailed discussion of the phenomenological importance of the two parts can be found.

In the direct part, the parton distribution function of the photon interacting directly with the proton is formally a delta function $\delta(1-x)$ and as a consequence, cross sections can be calculated by a convolution of the parton distribution functions of the second parton (a gluon or (anti)quark) in, e.g., the proton with the perturbatively calculable partonic cross sections $[\Delta]\hat{\sigma}_{\gamma g \to Q\bar{Q}(X)}$ and $[\Delta]\hat{\sigma}_{\gamma q \to Q\bar{Q}(X)}$, respectively. For this purpose, the matrix elements shown in the following subsection have to be used. Note that formally the convolution with the parton distribution function of the photon vanishes due to the delta function:

$$\begin{aligned} d\sigma = \int dx_1 dx_2 f_\gamma f_{g,q} d\hat{\sigma}_{\gamma g, \gamma q \to Q\bar{Q}(X)} = \\ \int dx_1 dx_2 \delta(1-x_1) f_{g,q} d\hat{\sigma}_{\gamma g, \gamma q \to Q\bar{Q}(X)} = \int dx_2 f_{g,q} d\hat{\sigma}_{\gamma g, \gamma q \to Q\bar{Q}(X)}. \end{aligned} \tag{4.32}$$

For the so called resolved part, the photonic parton distribution functions shown in section 2.6 and the matrix elements for hadroproduction discussed in the previous sections come into play, as the partonic subprocesses are in this case the same as in hadroproduction. As this was extensively discussed in [52, 94] for massless final states and the calculation proceeds analogously to the case of hadroproduction, we refrain here from a more detailed discussion. Formally, compared to hadroproduction, one only has to replace the parton distribution functions for the hadron by the parton distribution functions for finding a gluon/(anti)quark in a photon.

Moreover, the incoming photon can result from a lepton. In this case the photonic cross sections have to be convolved with the Weizsäcker-Williams spectrum as shown in section 2.6.

If the virtuality Q of the photon is of $\mathcal{O}(1\,\mathrm{GeV})$ or higher, resolved processes are sufficiently suppressed, but the additional momentum scale Q greatly complicates the calculations of phase-space and loop integrals. This case, where, in contrast to photoproduction, Q^2 is large, is called electroproduction and is not considered in this thesis. However, it can be relevant for a future electron-hadron collider.

4.2.2 Details for the direct part

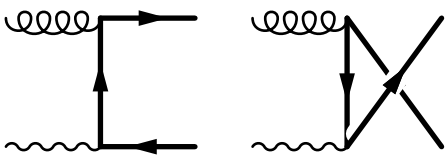

Figure 4.12: Leading order diagrams for photoproduction of a $Q\bar{Q}$ pair.

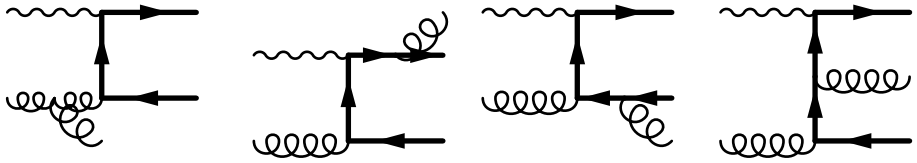

Figure 4.13: Real emission contributions to photon-gluon fusion at NLO. Additional diagrams are obtained by inverting the propagator arrows on the heavy quark lines.

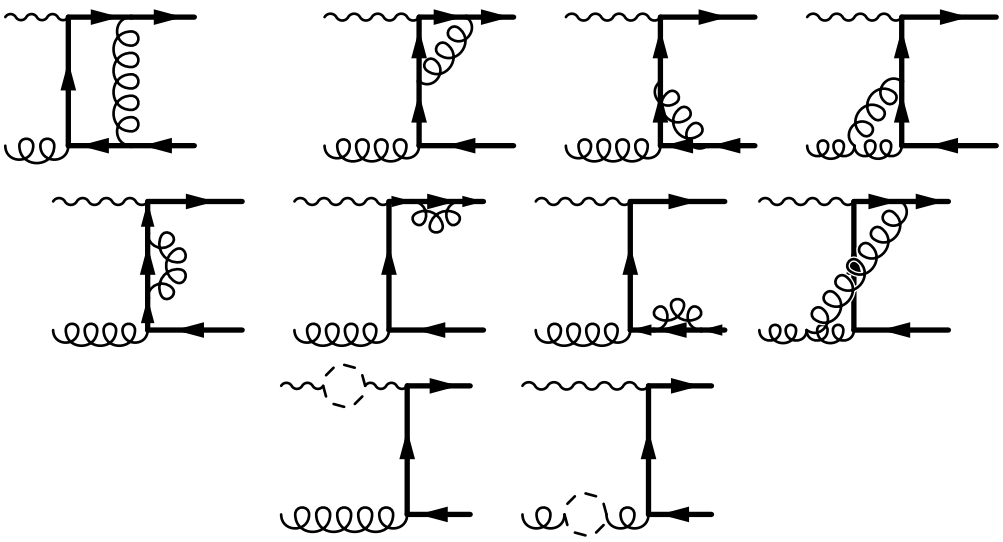

Figure 4.14: Virtual contributions to photon-gluon fusion. Additional virtual diagrams can be obtained by inverting the arrows on the heavy quark lines in all but the last three diagrams. The dashed lines represent ghost and quark loops and on the external gluon line also a gluon loop.

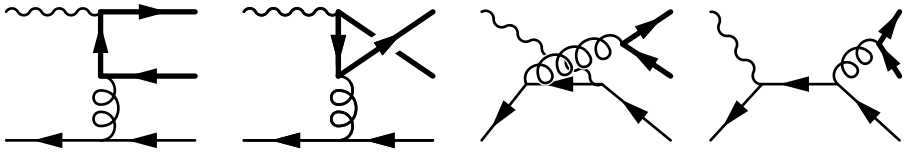

Figure 4.15: Feynman diagrams for photon-antiquark fusion.

Here, we show the additional matrix elements for the direct case. At leading order only photon-gluon fusion contributes, as shown in figure 4.12. At next-to-leading order, there are the usual $\mathcal{O}(\alpha_s^2)$ real-emission and one-loop corrections to the photon-gluon process depicted in figures 4.13 and 4.14, respectively.

In addition, there is the genuine NLO process of photon-(anti)quark scattering. The Feynman diagrams can be found in figure 4.15.

The leading order result for the differential cross section for the direct part can be found in equation (2.20) in reference [74]. As for hadroproduction, the partonic results can also be displayed in the form of scaling functions as was extensively discussed in [74–76]. The interested reader is referred to these works.

5 Phenomenological Results

Up to now, all theoretical ingredients to our calculations have been introduced. This section is devoted to a presentation of our results for the experiments best suited to studies on polarised heavy quark production. After having shown the agreement of the results for $d\sigma/dp_T$ obtained using the analytical and the numerical version of phase space integration, we continue with phenomenological applications to various experiments [184]. We start with results for GSI-FAIR-PAX in Germany and J-PARC in Japan obtained with the analytical code on the partonic level [87] and continue with results for RHIC (Relativistic Heavy Ion Collider) at the BNL (Brookhaven National Laboratory) obtained with the numerical code and including also hadronisation and decay of the heavy quarks [90, 185]. Afterwards we will turn to photoproduction. We will apply our numerical code to the COMPASS experiment situated at CERN (Organisation Européenne pour la Recherche Nucléaire) [91, 184] and give an outlook on heavy quark production at a future electron-ion collider. Note that most of the results presented in this section have already been published in peer-reviewed journals [87, 90, 91]. In part, this chapter is identical to these publications.

5.1 Comparison of the analytic and the Monte Carlo approach

In the analytic method, over the whole phase space of one parton of the heavy quark pair is integrated. Thus, only one-particle inclusive cross sections of one heavy final state particle can be predicted. No cuts can be posed to the particle whose phase space is integrated out. In contrast, with the Monte Carlo integration method, a lot of correlations between the heavy quark and the heavy antiquark can be studied. Furthermore, the great advantage of the purely numerical method is the possibility of demanding cuts on both heavy particles. Also, fragmentation and decay functions can be added easily for both heavy particles. With the histogram technique, it is possible to create histograms in various variables in the same run. However, the sampling routine of the VEGAS integration program [162, 163] chooses the most integration points, where the largest contributions to the integral stem from. As a consequence, histograms often show large fluctuations where the entries are small. In general, more integration points are necessary for the Monte Carlo method than for the analytic approach, what results in a longer CPU calculation time of the Monte Carlo technique. On the other side, the Monte Carlo program can produce histograms in several variables simultaneously. However, if one is only interested in selective inclusive cross

sections without any measurement functions, it may be faster and hence better to use the program with the analytically integrated matrix elements.

In the possible ranges, we can compare the results of the analytical and the Monte Carlo code to demonstrate the agreement between both. This provides a valuable check for the correctness of both calculations, as both start independently from the matrix element level. However, the comparison is only possible on the heavy quark level and for single-inclusive variables as in the current version of the analytical code the hadronisation and the decay of the resulting meson into leptons are not implemented. Here, we present the results for $d\sigma/dp_T^c$ for hadroproduction and photoproduction. All comparisons are done using the mass $m = 1.35$ GeV and the scale $\mu_f = \mu_r = 5m$ so that also contributions of the logarithms of the scales are sizable. In each figure, the comparison for the unpolarised case can be seen on the left, and for the polarised case on the right.

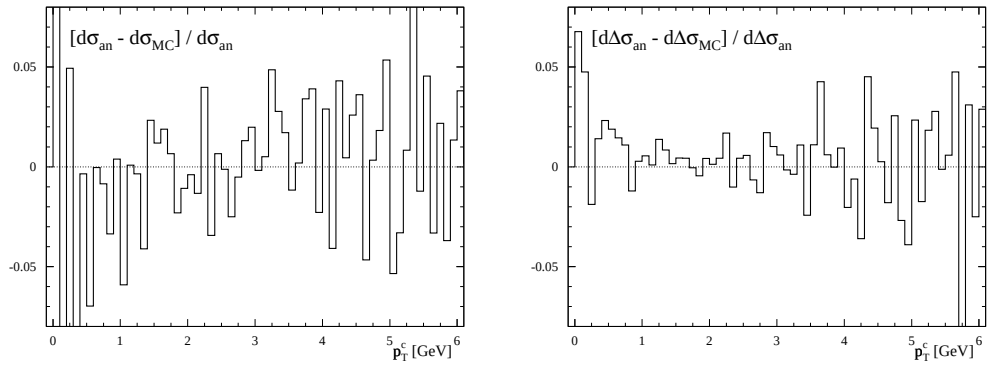

Figure 5.1: Comparison of the results of our Monte Carlo code, $d[\Delta]\sigma_{\mathrm{MC}}$, with the analytical calculation, $d[\Delta]\sigma_{\mathrm{an}}$, for single-inclusive charm hadroproduction as a function of transverse momentum p_T^c and integrated over all rapidities. The left panel shows the comparison for the unpolarised case, the right panel for the polarised one.

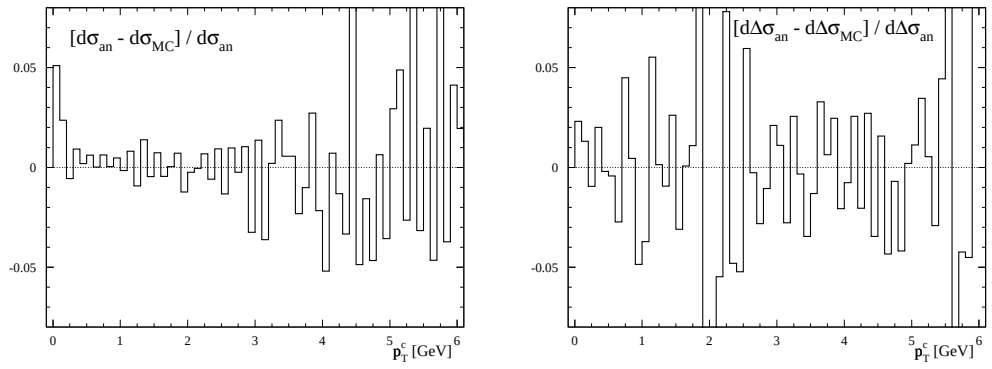

Figure 5.2: Comparison of the results of our Monte Carlo code, $d[\Delta]\sigma_{\mathrm{MC}}$, with the analytical calculation, $d[\Delta]\sigma_{\mathrm{an}}$, for single-inclusive charm photoproduction as a function of transverse momentum p_T^c and integrated over all rapidities. The left panel shows the comparison for the unpolarised case, the right panel for the polarised one.

In figure 5.1 the comparison is shown for hadroproduction. As incoming hadrons two protons with a c.m.s. energy of 200 GeV, the c.m.s. energy of RHIC, are used. In figure 5.2 the same is done for the direct part of photoproduction. A photon with a sharp energy of 160 GeV, the c.m.s. energy of COMPASS, is assumed to collide with a fixed-target proton. The aim of these plots is merely to show the accordance of both calculations. Therefore, we decided against doing the convolution with the Weizsäcker-Williams spectrum for the photon, as it would be necessary for COMPASS. Also for comparison purposes, the scale was taken at the somewhat unphysical value of $\mu = 5m$.

As the small bin size of 0.1 GeV in p_T is chosen, one can still see the numerical fluctuations of the Monte Carlo code. Within the statistical fluctuations a good agreement of both codes can be observed. The statistical fluctuations could be improved further by taking more integration points and iterations of the VEGAS routine [162, 163], what, however, would result in a longer calculation time.

5.2 Results with the analytical code for J-PARC and GSI-FAIR-PAX

Charm production has been studied in several experiments. The experimental results or extrapolations for charm production in pp collisions at c.m.s. energies below $\sqrt{S} = 50\,\text{GeV}$ gathered so far are shown in figure 5.3.

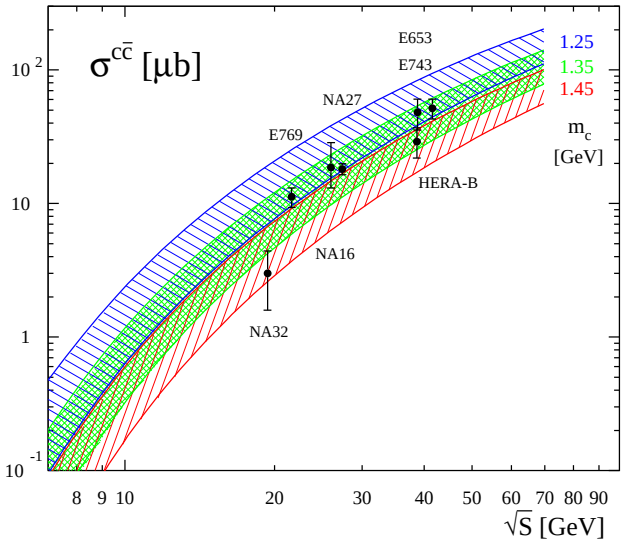

Figure 5.3: Experimental results [186] for the total charm production cross section at fixed-target energies compared to NLO pQCD calculations for three different values of the charm quark mass m_c. In each case, the shaded band indicates the theoretical uncertainties from varying $\mu = \mu_r = \mu_f$ in the range $m_c \leq \mu \leq 2m_c$.

Figure 5.3 shows the available data [186] compared to our calculations at NLO accuracy for the total cross section using different values of the charm quark mass and scales $\mu = \mu_f = \mu_r$. As can be seen, uncertainties from small variations of m_c are as important

as scale ambiguities, and both combined can lead to almost an order of magnitude change in the total charm yield at $\sqrt{S} \simeq 10 \div 20\,\text{GeV}$. From figure 5.3 one can also infer that the theoretical uncertainties become somewhat less pronounced with increasing c.m.s. energy.

Although most experimental results can be described with the same choice of m_c and scale μ, there is a clear need for further precise measurements, in particular closer to threshold, below the result of NA32, which does not line up easily with other experiments. GSI-FAIR and J-PARC, to which we shall turn now, will be able to explore this energy range in future.

Here, we will focus on a detailed phenomenological study of the prospects of open charm production in $\bar{p}p$ and pp collisions at the heavy quark level at the (future) GSI-FAIR [24] and J-PARC [26] facilities, respectively. In doing so, we will neglect the hadronisation of the heavy quarks. For GSI-FAIR we consider the so-called "collider option" as proposed by the PAX collaboration [25], using a 15 GeV antiproton and a 3.5 GeV proton beam, with the plan of having both beams also longitudinally or transversely polarised. The main goal of the PAX experiment would be a determination of the so far unknown "transversity" parton densities by analysing the transversely polarised Drell-Yan process. This measurement would gain substantially from a polarised antiproton beam due to the dominance of the lowest order (LO) quark-antiquark annihilation channel. At the J-PARC facility in Japan a 50 GeV proton beam and a solid-state target are used. The possibility of having both beam and target polarised is a conceivable option for future upgrades currently being scrutinised. At GSI-FAIR [J-PARC] the available $\bar{p}p$ [pp] c.m.s. energy will be $\sqrt{S} \simeq 14.5\,[10]\,\text{GeV}$. We will make some reasonable assumptions for the relevant acceptances as stated below in section 5.2.1. We will demonstrate that measurements of open charm at these facilities have the potential to further our understanding of the underlying QCD dynamics at moderate c.m.s. energies, which are so far little explored.

5.2.1 Phenomenological inputs and experimental cuts

The part of the future GSI-FAIR accelerator complex amenable to pQCD studies is an asymmetric proton-antiproton collider option proposed by the PAX collaboration [25] with maximum beam energies for protons and antiprotons of 3.5 GeV and 15 GeV, respectively, resulting in a c.m.s. energy of about $\sqrt{S} = 14.5\,\text{GeV}$. Studies of methods to polarise both beams either longitudinally or transversely are currently pursued [25]. The PAX detector will have nearly full azimuthal acceptance and a polar angle coverage from 5 to 130 degrees is envisioned [25, 187].

The proton accelerator at J-PARC, which will reach up to 50 GeV beam energy, has been finalised, and the hadron physics programme started at a c.m.s. energy of about $\sqrt{S} = 10\,\text{GeV}$ with both beam and target being unpolarised. We also consider longitudinally polarised collisions, which will be a conceivable upgrade of the J-PARC facility in the future [26]. Since little is known about the experimental set-up at this stage, we assume a forward spectrometer geometry with a 200 mrad acceptance, similar to the one used by the COMPASS experiment at CERN.

Since not all details of charm detection in these experiments are available yet, we will perform all our calculations on the charm quark level, i.e., we do – in contrast to our phenomenological studies for RHIC, see section 5.3 – not attempt to model the hadronisation of charm quarks into charmed mesons and their subsequent decays here. We only present inclusive cross sections having used the analytical code. For the

PAX experiment, however, identification of open charm events most likely proceeds through the detection of decay muons for which a minimal momentum of $p_\mu = 1\,\mathrm{GeV}$ is required [25, 187]. Therefore we impose a similar cut on the laboratory momentum of the primary charm quark in all our calculations for GSI-FAIR.

In all unpolarised calculations at LO and NLO accuracy we use the CTEQ6L1 and CTEQ6M parton distribution functions [124] and the corresponding LO and NLO values for the strong coupling, respectively. Unless stated otherwise, the GRSV "standard" set of helicity-dependent parton densities [129] is used in the computation of polarised cross sections and the charge and spin asymmetries. Since $m_c = 1.35\,\mathrm{GeV}$ provides a good description of most of the data shown in figure 5.3, this is our default choice for the charm quark mass.

5.2.2 Expectations for charm production cross sections

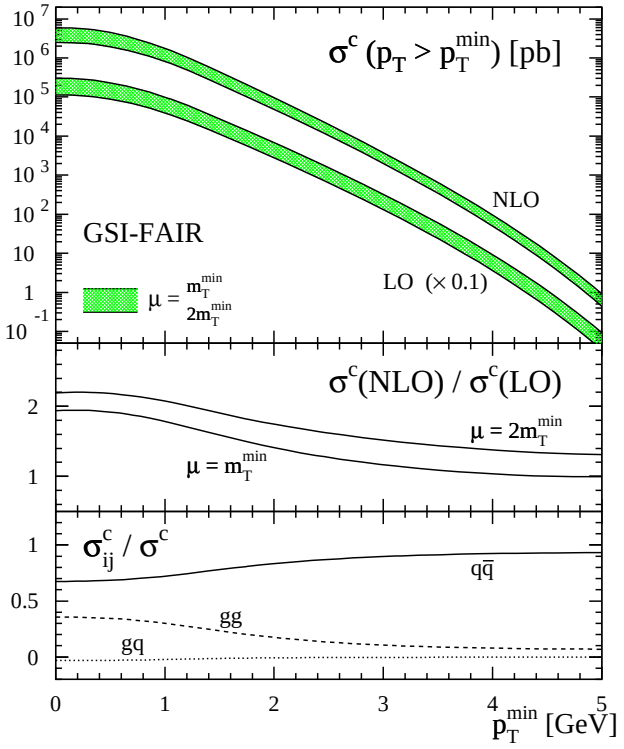

Figure 5.4: Upper panel: LO and NLO unpolarised charm cross section at GSI-FAIR, integrated over $p_T > p_T^{\min}$ and the angular acceptance $5^\circ \leq \theta_c \leq 130^\circ$, using $m_c = 1.35\,\mathrm{GeV}$. The shaded bands indicate the uncertainties from varying $\mu = \mu_r = \mu_f$ in the range $m_T^{\min} \leq \mu \leq 2m_T^{\min}$; middle panel: ratio of the NLO and LO cross sections ("K-factor"); lower panel: fractional contribution of the different partonic channels σ_{ij}^c to the NLO cross section σ^c for $\mu = \sqrt{2}m_T^{\min}$.

Figure 5.4 shows our expectations for the unpolarised charm production cross section at GSI-FAIR at LO and NLO accuracy, integrated over transverse momentum $p_T > p_T^{\min}$ and the angular acceptance of $5^\circ \leq \theta_c \leq 130^\circ$ for PAX. The shaded bands indicate the

theoretical uncertainties when the factorisation and renormalisation scales are varied simultaneously in the range $m_T^{\min} \leq \mu_f = \mu_r \leq 2m_T^{\min}$. Also shown in figure 5.4 are the "K-factors", the ratios of the NLO and LO cross sections, for two choices of scales $\mu_f = \mu_r$ and the fractional contributions of the different partonic channels σ_{ij}^c to the NLO cross section.

Besides the sizable dependence on the scales $\mu_{f,r}$, there is also a similar uncertainty due to the choice of m_c in the region $p_T^{\min} \lesssim 1\,\text{GeV}$, in line with the observations for the total charm yields in figure 5.3. For $p_T^{\min} \gtrsim 2\,\text{GeV}$, however, varying m_c in the range $1.25\,\text{GeV} \leq m_c \leq 1.45\,\text{GeV}$ has – similar to the polarised case discussed below – a negligible impact on the cross section shown in the upper panel of figure 5.4. It is worth noticing that there is only a rather marginal reduction in the scale ambiguity when going from the LO to the NLO approximation. This is not unexpected for experiments with limited c.m.s. energies, and similar observations have been made for single-inclusive hadron production [188]. From the lower panel of figure 5.4 one can infer that the quark-antiquark annihilation subprocess is the most important contribution to the cross section. This can be readily understood since quarks and antiquarks are both "valence" partons in the proton and antiproton, respectively, and from the fact that one probes fairly large momentum fractions $x_{1,2} \gtrsim 0.1$. The genuine NLO quark-gluon subprocess is negligible in the entire p_T range shown.

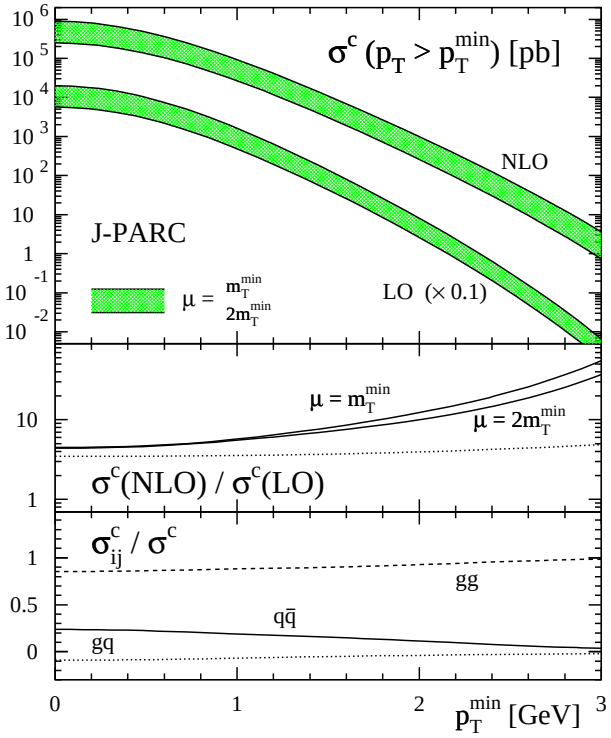

Figure 5.5: Same as in Figure 5.4, but now for J-PARC kinematics.

The corresponding results for J-PARC are summarised in figure 5.5. There are striking differences compared to the results for GSI-FAIR shown in the previous figure. The dependence of the charm cross section on unphysical scales $\mu_{f,r}$ is even larger here

and does not improve when NLO corrections are included. This can be taken as a strong indication that higher order terms in the perturbative series are very important. Hopefully, a resummation of the leading terms to all orders in α_s will tame the scale ambiguities. Secondly, the size of the NLO corrections compared to the LO term, displayed in the middle panel of figure 5.5, seems to be beyond control. Most of the pathological behaviour of the K-factor at large $p_T^{\min}$ can be attributed to the differences in the LO and NLO gluon distributions at large $x_{1,2}$, where they are basically unconstrained by data [124]. If one uses NLO parton densities in the calculation of the LO cross section, the K-factor does not show such a sharp rise, though it remains large (dotted curve in figure 5.5). Despite the rather large $x_{1,2}$ values probed at J-PARC, and contrarily to what happens in $\bar{p}p$ collisions at GSI-FAIR, the gluon-gluon fusion subprocess is by far the dominant mechanism to produce charm quarks. We also note that varying m_c in the range $1.25\,\text{GeV} \leq m_c \leq 1.45\,\text{GeV}$ has a somewhat bigger impact on the cross sections displayed in the upper panel of figure 5.5 than in case of GSI-FAIR due to the smaller c.m.s. energy.

Figures 5.4 and 5.5 already demonstrate the potential of future low energy $\bar{p}p$ and pp experiments in further constraining quark and gluon distributions, respectively, in the medium-to-large x region, difficult to access at high energy colliders. They also show, however, that the quantitative reliability of the pQCD framework can not be taken for granted in this energy regime. Applications of pQCD have to be carefully scrutinised by comparing the theoretical expectations with data.

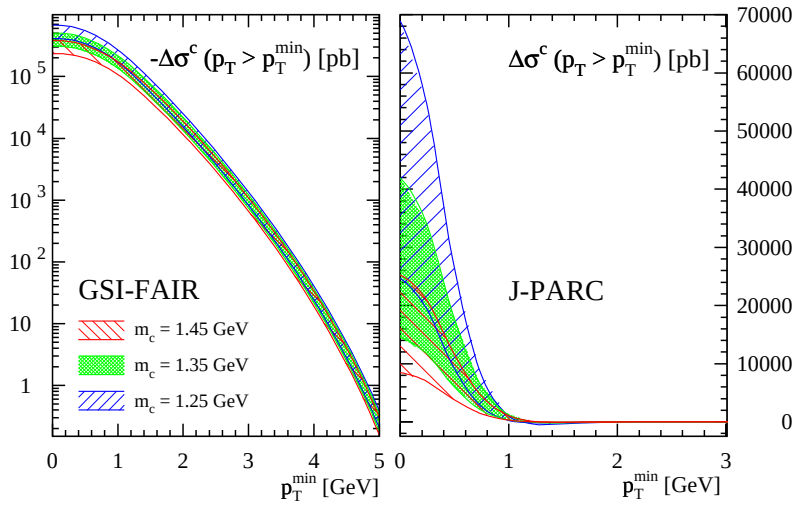

Figure 5.6: Expectations for the longitudinally polarised cross section for charm production at GSI-FAIR (left panel) and J-PARC (right panel), using the GRSV "standard" set [129]. Note that the results on the left hand side are for $-\Delta\sigma$. The scale uncertainty is shown for three different choices of m_c, varying $\mu = \mu_r = \mu_f$ in the range $m_T^{\min} \leq \mu \leq 2m_T^{\min}$.

Figure 5.6 shows the corresponding longitudinally polarised cross sections at NLO accuracy for GSI-FAIR and J-PARC, respectively. Instead of giving also the LO results [the K-factors are smaller than in the unpolarised case, between 1.5 and 2 (2 and 4) for GSI-FAIR (J-PARC)], we chose to display the dependence of the polarised cross sections on m_c. Since J-PARC can cover only a smaller range in p_T than GSI-FAIR due to the smaller $\sqrt{S}$, the mass effects are more important here. The fractional contributions of the different subprocesses are very similar to those shown in figure 5.4

for GSI-FAIR and dependent strongly on the size of the polarised gluon distribution in case of J-PARC, as can be expected already from the lower panel of figure 5.5. We note that at J-PARC kinematics, the polarised cross section exhibits a node at $p_T^{\min} \simeq 1\,\text{GeV}$ if the GRSV "standard" parton densities are used in the calculation.

5.2.3 The unpolarised and polarised charge asymmetry

We now turn to a detailed discussion of the charge asymmetry A_C defined in equation (4.25) in section 4.1.3. We show expectations for the size of the effect and discuss the theoretical uncertainties due to variations of $\mu_{f,r}$ and m_c. All results are presented as a function of the c.m.s. rapidity y of the heavy (anti)quark, which is related to the rapidity in the laboratory frame y_{lab} by a simple additive boost. Positive rapidities refer to the direction from which the antiproton and proton beam at GSI-FAIR and J-PARC comes to the collision point, respectively. Note that rapidity y and pseudo-rapidity η are not the same for massive particles. Recall that the relation between y and the scattering angle θ_c of the heavy quark depends on both p_T and m_c as given in equation (3.127):

$$\cos\theta_c = \left(\sqrt{\frac{m_T^2}{1-\tanh^2 y}}\tanh y\right) \Big/ \sqrt{\frac{m_T^2}{1-\tanh^2 y} - m_c^2}$$

while $\cos\theta_c = \tanh\eta$. Therefore, angular cuts imposed upon the heavy quarks by the experiments do not translate into simple, p_T independent cuts for rapidity-dependent differential cross sections.

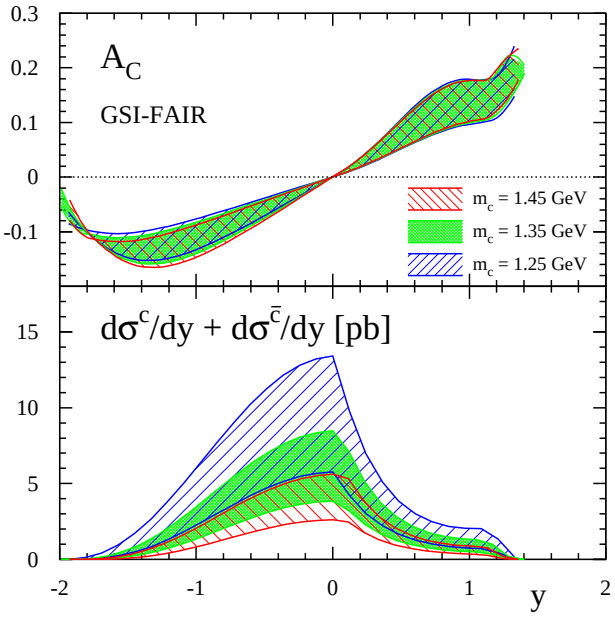

Figure 5.7: The unpolarised charge asymmetry A_C (upper panel) and the NLO c.m.s. rapidity-dependent differential charm plus anti-charm cross section $d\sigma^c/dy + d\sigma^{\bar{c}}/dy$ (lower panel) for GSI-FAIR. The scale uncertainty is shown for three different choices of m_c, varying $\mu = \mu_r = \mu_f$ in the range $m_c \leq \mu \leq 2m_c$.

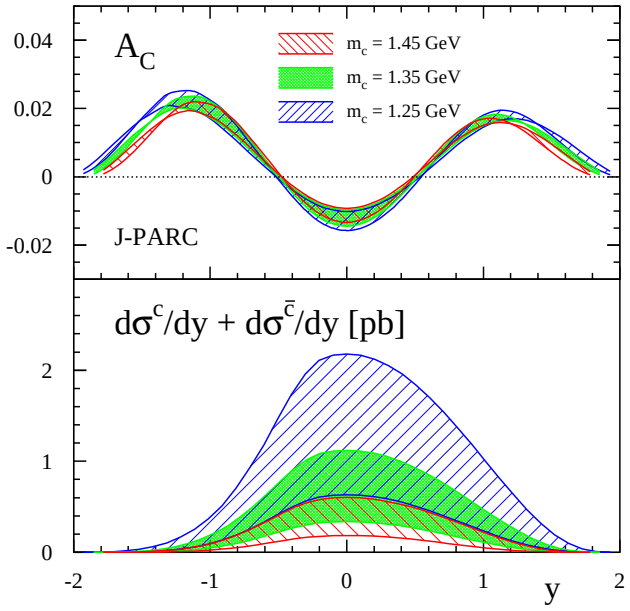

Figure 5.8: Same as in figure 5.7 but for J-PARC kinematics.

The upper panels of figures 5.7 and 5.8 show our expectations for the unpolarised charge asymmetry A_C at $\mathcal{O}(\alpha_s^3)$ for charm quarks at GSI-FAIR and J-PARC, respectively, using the phenomenological inputs and experimental acceptance cuts specified in section 5.2.1. The results for A_C are largely independent of the choice for the charm quark mass m_c, in contrast to the sizable mass dependence observed for the NLO c.m.s. rapidity-dependent differential cross sections for the sum of charm and anti-charm production (lower panels), which enters in the denominator of A_C in equation (4.25).

Note that the c.m.s. rapidity y and the experimentally relevant rapidity y_{lab} in the laboratory frame are simply related by $y_{lab} = y - 0.737$ and $y_{lab} = y - 2.334$ for GSI-FAIR and J-PARC, respectively. The scale $\mu_{f,r}$ dependence partially cancels in A_C, as can be seen by comparing the upper and lower panels of figures 5.7 and 5.8. A residual dependence on $\mu_{f,r}$ is not surprising since the numerator of A_C at $\mathcal{O}(\alpha_s^3)$ is effectively a LO approximation. It vanishes as $\mathcal{O}(\alpha_s^2)$ and is free of collinear singularities. Also note that the sharp drop of $d\sigma^c/dy + d\sigma^{\bar{c}}/dy$ in the lower panel of figure 5.7 is due to the cut imposed on the momentum of the heavy (anti)quark, $p_{lab} > 1\,\text{GeV}$.

Figure 5.9 shows our results for the longitudinally polarised charge asymmetry ΔA_C defined as in equation (4.25), but with all cross sections $d\sigma$ replaced by their helicity dependent counterparts $d\Delta\sigma$. Again, the scale uncertainty is shown for three different choices of m_c, varying $\mu = \mu_r = \mu_f$ in the range $m_c \leq \mu \leq 2m_c$. All results are obtained with the GRSV "standard" set [129] of spin-dependent parton densities. As in the unpolarised case, the mass dependence largely drops out in ΔA_C, in particular for GSI-FAIR, but a residual scale $\mu_{f,r}$ ambiguity remains.

Since the mass and scale dependence of $d\Delta\sigma^c/dy + d\Delta\sigma^{\bar{c}}/dy$ is qualitatively very similar to the corresponding unpolarised cases shown in the lower panels of figures 5.7 and

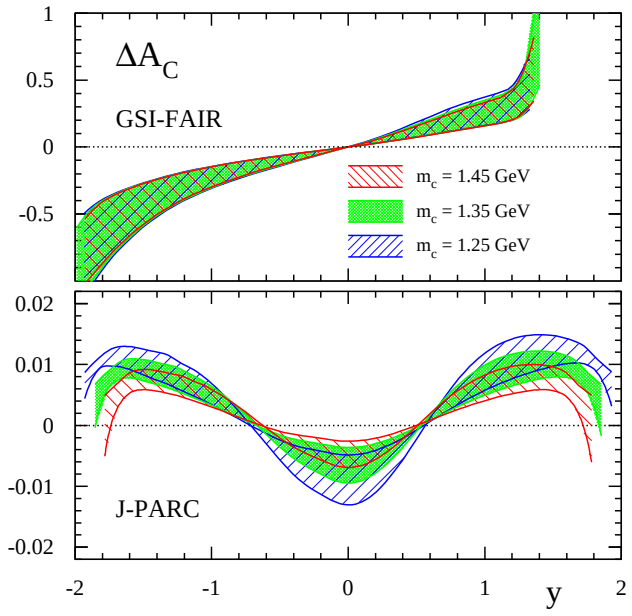

Figure 5.9: Same as in the upper panels of figures 5.7 and 5.8 but now for the polarised charge asymmetry ΔA_C.

5.8, we refrain from giving these results here. Instead, we shall discuss the significant dependence of both numerator and denominator of ΔA_c on the choice of a particular set of polarised parton densities.

Figure 5.10 shows the numerator and the denominator of the polarised charge asymmetry ΔA_C at J-PARC, obtained with different sets of polarised parton densities. Apart from our default set, GRSV "standard", we also use the sets of AAC [134] and DNS [130]. The latter is based on an analysis using also data from polarised semi-inclusive deep-inelastic scattering. Two different choices of parton-to-hadron fragmentation functions have been made in the DNS analysis, and the two resulting sets, labelled as DNS (KRE) and DNS (KKP) in figure 5.10, differ mainly in the sea quark content, in particular, $\Delta\bar{u}$, which has opposite sign in both sets. The positive polarisation of $\Delta\bar{u}$ in DNS (KKP), unlike in all other sets of spin-dependent parton densities, is responsible for the opposite sign of $d\Delta\sigma^c/dy \pm d\Delta\sigma^{\bar{c}}/dy$ obtained with DNS (KKP). In the denominator of ΔA_C, gluon-gluon fusion does not drop out and can make a significant contribution depending on the amount of gluon polarisation Δg. The set with the largest Δg, AAC, gives the largest cross section. The other three sets have relatively small gluon distributions and quark-antiquark annihilation is equally important. On the other hand, different sets of polarised parton densities have only very limited impact on the results for $d\Delta\sigma^c/dy \pm d\Delta\sigma^{\bar{c}}/dy$ and ΔA_C for GSI-FAIR. This can be expected, since in $\bar{p}p$ collisions at small $\sqrt{S}$ one predominantly probes the fairly well constrained valence quark distributions, and uncertainties in the polarised sea-quark and gluon densities do not matter much.

Finally, we note that *without* taking into account any experimental cuts, A_C and ΔA_C are anti-symmetric functions in the c.m.s. rapidity for $\bar{p}p$ collisions, as can be

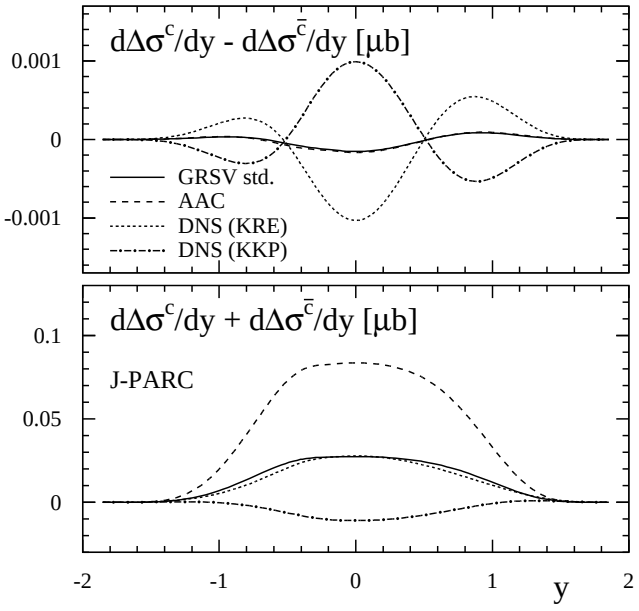

Figure 5.10: Numerator (upper panel) and denominator (lower panel) of the polarised charge asymmetry ΔA_C at J-PARC, calculated with different sets of polarised parton densities.

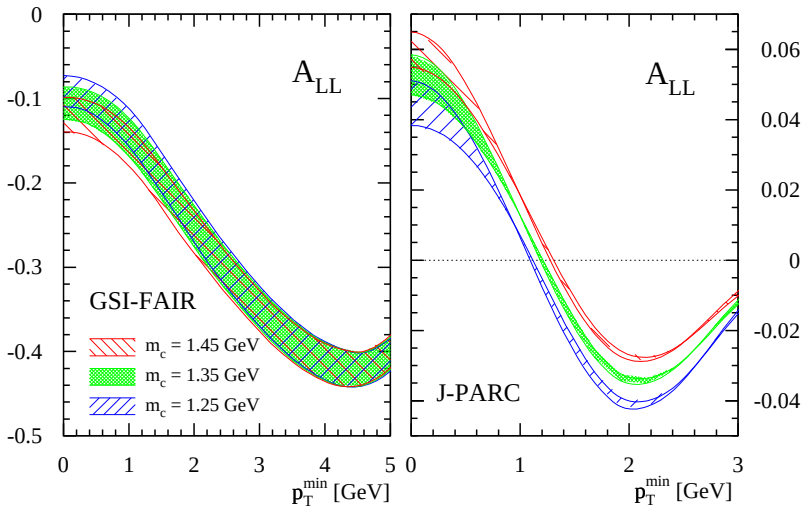

Figure 5.11: The integrated double-spin asymmetry A_{LL} as function of $p_T^{\min}$ at NLO accuracy for GSI-FAIR (left panel) and J-PARC (right panel) using the GRSV "standard" distributions and the same experimental cuts as before. The scale uncertainty is shown for three different choices of m_c, varying $\mu = \mu_r = \mu_f$ in the range $m_T^{\min} \leq \mu \leq 2m_T^{\min}$.

anticipated from figures 5.7 – 5.9 (which, however, do include certain acceptance cuts).

Similarly, A_C and ΔA_C are symmetric in c.m.s. rapidity for pp experiments. This is a consequence of the anti-symmetric and symmetric initial states $\bar{p}p$ and pp, respectively. The charge asymmetry on the partonic level for the dominant $q\bar{q}$ subprocess implies that Q is preferentially emitted into the direction of q and $\bar{Q}$ into the direction of $\bar{q}$. As was explained in [83, 84], in pp collisions one then finds an excess of centrally produced $\bar{Q}$, while Q dominates at large absolute rapidities. This is also what we observe for J-PARC in figures 5.8 and 5.9. The size of A_C and ΔA_C for pp collisions at J-PARC is significantly smaller than for $\bar{p}p$ collisions at GSI-FAIR, simply because of the fact that for the relevant $q\bar{q}$ subprocess both partons are valence quarks in $\bar{p}p$, greatly enhancing its relative contribution. When integrated over rapidity and without any kinematical restrictions, A_C and ΔA_C vanish, and the total yields of charm and anti-charm quarks are the same.

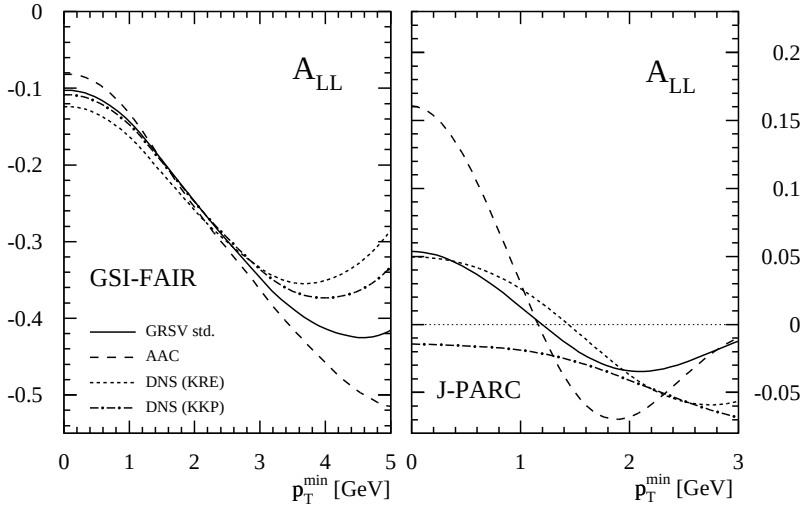

Figure 5.12: As in figure 5.11 but now comparing the results obtained with different sets of polarised parton densities using $m_c = 1.35\,\text{GeV}$ and $\mu_f = \mu_r = \sqrt{2}m_T^{\min}$.

5.2.4 Expectation for longitudinal spin asymmetries

Experiments usually present their spin-dependent measurements in terms of spin-asymmetries rather than polarised cross sections. The double-spin asymmetry A_{LL}, defined in equation (2.49), has the advantage that many experimental uncertainties cancel in the ratio, in particular, it is not required to determine the absolute normalisation of the helicity dependent cross sections. Also, theoretical uncertainties may cancel to some extent in A_{LL}. However, before exploiting this, one has to make sure that pQCD is applicable in the relevant kinematical regime by comparing, for instance, the unpolarised cross section with data.

Figure 5.11 shows the integrated double-spin asymmetry A_{LL} as function of $p_T^{\min}$ at NLO accuracy for GSI-FAIR (left panel) and J-PARC (right panel), using the GRSV "standard" distributions and the same experimental cuts as for the underlying cross sections shown in figures 5.4 – 5.6. As usual, the scale uncertainty is shown for three different choices of m_c, varying $\mu = \mu_r = \mu_f$ in the range $m_T^{\min} \leq \mu \leq 2m_T^{\min}$. As can be seen, there is still a significant scale ambiguity and, in case of J-PARC, also

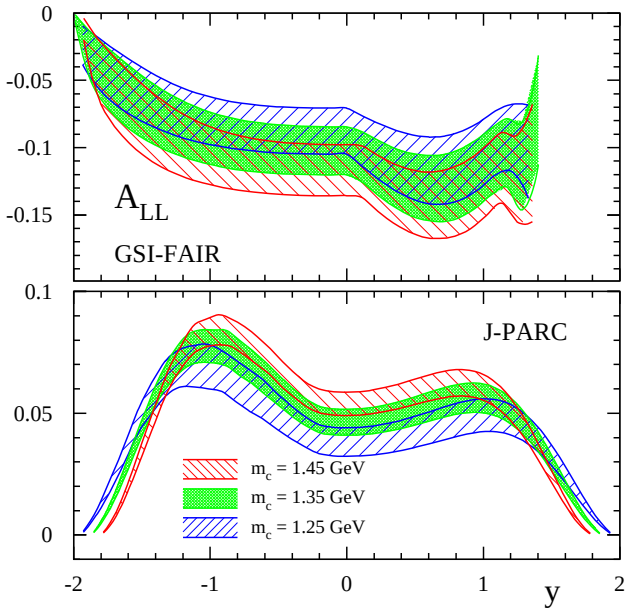

Figure 5.13: As in figure 5.11 but now as function of the c.m.s. rapidity y. The scales $\mu_{f,r}$ are varied in the range $m_c \leq \mu_f = \mu_r \leq 2m_c$.

a dependence on m_c. We refrain from showing LO results, but we note that because NLO corrections tend to be larger in the unpolarised case, as discussed above, A_{LL} is typically reduced by a factor of about two when NLO corrections are included, which is, therefore, absolutely necessary.

The sensitivity of A_{LL} to different sets of polarised parton distributions is studied in figure 5.12. As expected, the differences are small for GSI-FAIR which mainly probes the fairly well known valence distributions. Only at large $p_T^{\min}$, which corresponds to currently unexplored momentum fractions $x_{1,2} \to 1$, some differences are noticeable. At J-PARC, expectations for A_{LL} depend much more on the choice of spin-dependent parton densities, in line with the observations already made in the lower panel of figure 5.10.

Finally, in figure 5.13 we present the spin asymmetry as a function of the c.m.s. rapidity y and integrated over transverse momentum. The behaviour of A_{LL} for GSI-FAIR in the upper panel for positive y is driven by the cut on the charm momentum $p_{lab} > 1\,\text{GeV}$. Both mass and scale uncertainties do not cancel and remain significant.

In this section, we have performed a detailed study of the physics opportunities with open charm production at low c.m.s. energy $\bar{p}p$ and pp collisions at GSI-FAIR and J-PARC, respectively, including unpolarised and polarised cross sections and charge and spin asymmetries. All calculations are done at $\mathcal{O}(\alpha_s^3)$ accuracy, and theoretical uncertainties due to the choice of scales $\mu_{f,r}$ and the charm mass m_c are discussed in detail. In general, they turn out to be significant with exception of the mass dependence of the charge asymmetries A_C and ΔA_C.

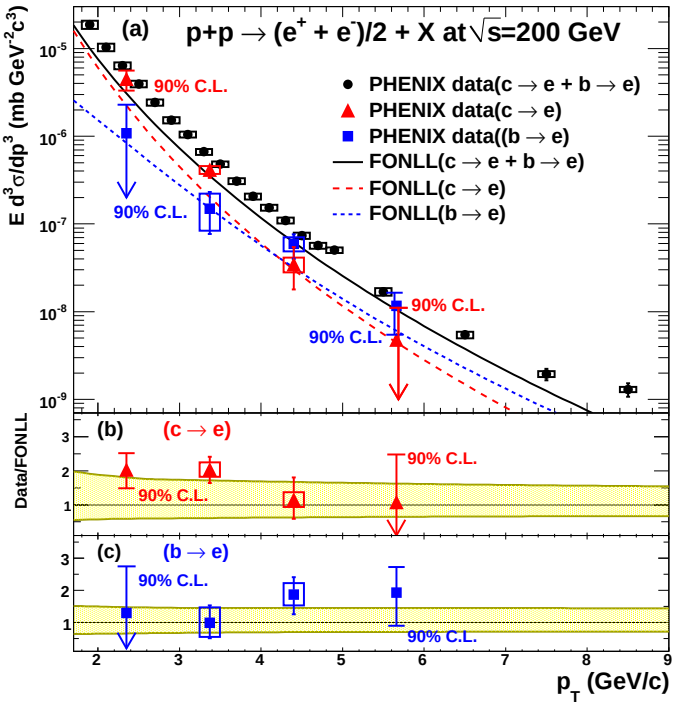

Figure 5.14: Example for an unpolarised measurement at RHIC, as presented in [189]: (a): Invariant cross sections of electrons from charm and bottom with the result of the FONLL calculation [57]. (b) and (c): The ratios of data points over the FONLL prediction as a function of electron p_{T} for charm and bottom. The shaded area shows the uncertainty of the FONLL prediction. Note that figure 12 of reference [88] also shows these results.

5.3 Results for hadroproduction at RHIC using the Monte Carlo code

At RHIC polarised pp collisions as well as heavy ion collisions are studied. The polarised pp studies aim at constraining the gluon polarisation in the proton. For this purpose, several types of final states are scrutinised. Current results from RHIC on jet and pion production have been included in the DSSV analysis of polarised PDFs. Further restrictions can come from prompt photon production and from heavy quark production. For the latter, the expectations are presented in this thesis at the NLO level on the basis of the current knowledge of polarised PDFs.

Here, we use our purely numerical method as it allows to include detailed acceptance cuts.

5.3.1 Preliminaries

We now turn to a detailed phenomenological study of heavy flavour hadroproduction in longitudinally polarised pp collisions and semi-leptonic decays of produced mesons at RHIC. For comparison and to compute experimentally relevant double-spin asym-

metries, defined as

$$A_{LL} \equiv \frac{d\Delta\sigma}{d\sigma},$$

we also present results for the corresponding unpolarised quantities. We study the impact of the NLO QCD corrections on the polarised and unpolarised cross sections and quantify the theoretical uncertainties by comparing results for different choices for the unphysical factorisation and renormalisation scales, heavy quark masses, and parameters describing the hadronisation of the heavy quarks.

We concentrate on observables of immediate relevance for the RHIC spin programme with collisions of longitudinally polarised protons at a c.m.s. energy of $\sqrt{S} = 200\,\text{GeV}$. These are single-inclusive transverse momentum distributions of electrons and muons from semi-leptonic decays of charm and bottom quarks, and, in particular, invariant mass spectra for two leptons observed in coincidence. Such measurements have been already carried out in spin-averaged pp collisions at RHIC [88, 189–196] and are intended to be performed with longitudinally polarised beams once sufficient statistics has been accumulated [18, 88]. The current status of the measurement of unpolarised cross sections and theory is presented in figure 5.14, where the experimental values are compared to the FONLL calculation described in section 2.7.

We note that the leptons can stem from both charm and bottom quark decays which usually cannot be separated experimentally until displaced vertex detector upgrades have been installed. Therefore, our results always refer to the sum of charm and bottom production, their hadronisation into D and B mesons, including $c \to D$, $b \to B$, and "cascade" $b \to B \to D$ contributions, and the subsequent semi-leptonic decays of the heavy mesons into the observed leptons. We assume that electrons and muons are detected at central and forward rapidities $|\eta_e| \leq 0.35$ and $1.2 \leq |\eta_\mu| \leq 2.2$, respectively, which corresponds to the acceptance of the PHENIX experiment [18, 189–192].

The fragmentation of the heavy quarks and the following semi-leptonic decay is modelled by phenomenological functions as described in section 2.8.

We note that we do *not* normalise our cross sections with the appropriate branching ratios for $D \to e$, $B \to e$, etc., which are all close to 10% [148]. Of course, branching ratios drop out of experimentally relevant double-spin asymmetries (2.49).

The main motivation to study heavy flavour production with polarised beams at RHIC is the expected sensitivity to the helicity-dependent gluon density through the tree-level gluon-gluon fusion process, $gg \to Q\bar{Q}$, which is known to be dominant for unpolarised collisions up to the largest values of the heavy quark's transverse momentum currently accessible at RHIC [58–60] (see also our results in section 5.3.3 below).

We will show, however, that the fractional contribution of gluon-gluon fusion to the spin-dependent cross section depends crucially on the assumed set of polarised parton densities. Our default choice is the DSSV set [30, 31], obtained in a global QCD analysis of newer spin-dependent data, including those from RHIC on single-inclusive pion and jet production [39, 40, 42, 44, 197–199]. Due to the smallness of $\Delta g(x)$ in the DSSV set and its sign change near $x \simeq 0.1$ [30, 31], the $q\bar{q}$ annihilation subprocess, $q\bar{q} \to Q\bar{Q}$, turns out to be the dominant mechanism for charm and bottom production in polarised pp collisions at RHIC, contrary to expectations based on unpolarised results. For comparison and to study the sensitivity to $\Delta g(x)$, we adopt also two alternative sets of spin-dependent parton densities, GRSV(std) [129] and DNS(KRE) [130], both characterised by a positive gluon polarisation of moderate size and already used in section 5.2. In general, the effects of gluon polarisations on double-spin asymmetries for leptons from heavy flavour decays calculated using results of current QCD fits

[30, 31, 129, 130] all turn out to be small, often well below the one percent level, making their measurement very challenging. This is in particular true for single-inclusive lepton observables.

In the computation of the NLO unpolarised cross sections in (2.49), which proceeds along the methods outlined in chapter 3 (for more details, see also reference [71]) we use the NLO CTEQ6M parton densities [124] and values for the strong coupling α_s. Since the DSSV analysis [30, 31] does not provide a LO set of spin-dependent parton distributions, our LO results always refer to the Born part of the full NLO calculation, i.e., they are computed with NLO parton densities and values for α_s. Strictly speaking this is, of course, inconsistent as it introduces some unwanted scheme dependence into a tree-level quantity. Nevertheless, the LO results should give a faithful estimate of the relevance of NLO corrections. As will be demonstrated below, they turn out to be sizable and rather different for unpolarised and polarised cross sections such that they do not cancel in experimentally relevant double-spin asymmetries.

We take $m_c = 1.35\,\text{GeV}$ and $m_b = 4.75\,\text{GeV}$ as reference values for the charm and bottom quark mass and vary them in the range $1.2\,\text{GeV} \leq m_c \leq 1.5\,\text{GeV}$ and $4.5\,\text{GeV} \leq m_b \leq 5.0\,\text{GeV}$, respectively, to estimate the resulting mass uncertainties. For the factorisation and renormalisation scale we take $\mu_f = \mu_r = \xi(m_Q^2 + [(p_T^Q)^2 + (p_T^{\bar{Q}})^2]/2)^{1/2}$ as the central value with $\xi = 1$. As usual, the sensitivity of the cross section to missing higher order corrections is estimated by varying μ_f and μ_r simultaneously in the range $1/2 \leq \xi \leq 2$. Following the procedure used for unpolarised charm and bottom production at RHIC in reference [57], we also vary μ_f and μ_r independently in the same range of ξ and combine the ensuing uncertainty with the one stemming from variations of $m_{c,b}$ in quadrature. Unless stated otherwise, we use the central values for μ_f, μ_r, $m_{c,b}$, and $\alpha_{c,b}$ given above.

5.3.2 Heavy flavour cross sections and correlations

We begin our detailed numerical studies with a discussion of unpolarised and polarised cross sections for various decay lepton distributions accessible at RHIC.

Figure 5.15 shows the single-inclusive transverse momentum spectrum of electrons from charm and bottom decays in LO and NLO accuracy, integrated over the angular acceptance of the PHENIX detector, i.e., $|\eta_e| \leq 0.35$ [189–192]. Similar results are obtained for the STAR experiment [193–195] with its larger acceptance for electrons at central rapidities, $|\eta_e| < 0.8$, and are not discussed here in detail. Only the results for A_{LL} for single electrons at STAR will be presented in section 5.3.4 below. The transverse momentum p_T^e is limited to a region which should be accessible with luminosities envisaged in longitudinally polarised pp collisions at RHIC. Photon conversion, $\gamma \to e^+e^-$, and Dalitz decays, $\pi^0 \to \gamma e^+e^-$, are the dominant sources of electron background for such measurements and may require an additional cut $p_T^e > 1\,\text{GeV}$ [189–195]. Recall that the branching ratios of about 10% are not included in the cross sections shown in figure 5.15.

The solid lines are obtained with the default values of the heavy quark masses, scales, parameters, and parton densities stated in the previous subsection. The shaded bands indicate the theoretical uncertainty from varying the factorisation and renormalisation scale simultaneously in the range $1/2 \leq \xi \leq 2$ discussed above. Note that the LO results are rescaled by a factor of 0.1, and all polarised cross sections are multiplied by -1 to display them on a logarithmic scale. The bottom panel of figure 5.15 gives

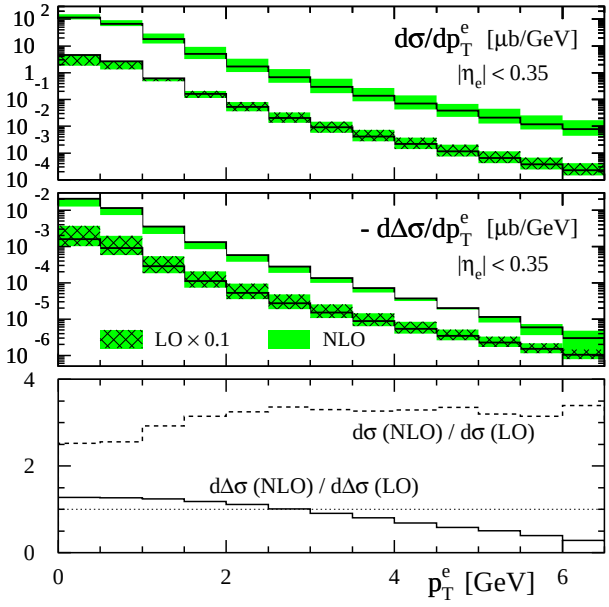

Figure 5.15: Scale dependence of the single-inclusive transverse momentum spectrum of electrons from heavy quark decays at central rapidities $|\eta_e| \leq 0.35$ in unpolarised (upper panel) and polarised (middle panel) pp collisions at RHIC. All scales are varied simultaneously, i.e., $\mu_f = \mu_r = \xi(m_Q^2 + [(p_T^Q)^2 + (p_T^{\bar{Q}})^2]/2)^{1/2}$, in the range $1/2 \leq \xi \leq 2$ (shaded bands). The solid lines correspond to the default choice $\xi = 1$. Note that the LO results are rescaled by a factor 0.1, and all polarised cross sections are multiplied by -1. The lower panel shows the ratio of NLO to LO polarised and unpolarised cross sections (K-factor).

the resulting unpolarised and polarised "K-factors", defined as usual by the ratio

$$K \equiv \frac{d[\Delta]\sigma^{\mathrm{NLO}}}{d[\Delta]\sigma^{\mathrm{LO}}} \ . \tag{5.1}$$

One notices that the NLO corrections are sizable in the unpolarised case, $K \simeq 3$, but moderate for polarised pp collisions, except for the region $p_T^e \gtrsim 5\,\mathrm{GeV}$, where the cross section starts to develop a node and perturbative corrections are artificially enhanced.

Less pronounced NLO corrections for polarised cross sections are a rather generic feature and have been observed already for other hadronic processes such as single-inclusive pion [131, 200] and jet [132] production. To some extent this behaviour can be traced back to the less singular scale evolution of polarised parton densities at small momentum fractions x [120, 121, 201], such that the partonic threshold region, which is the source of large logarithmic corrections associated with the emission of soft gluons, is less emphasised in the convolution (2.25) than in the unpolarised case. Specifically for heavy flavour production, it was noticed in [73] that large NLO corrections to the gluon-gluon fusion process related to amplitudes with a gluon exchange in the t-channel are independent of the helicities of the interacting gluons and hence do not contribute to the polarised cross section. Substantially different K-factors for unpolarised and polarised cross sections immediately imply that Born level estimates for double-spin asymmetries (2.49) can serve only as very rough estimates but are insufficient for

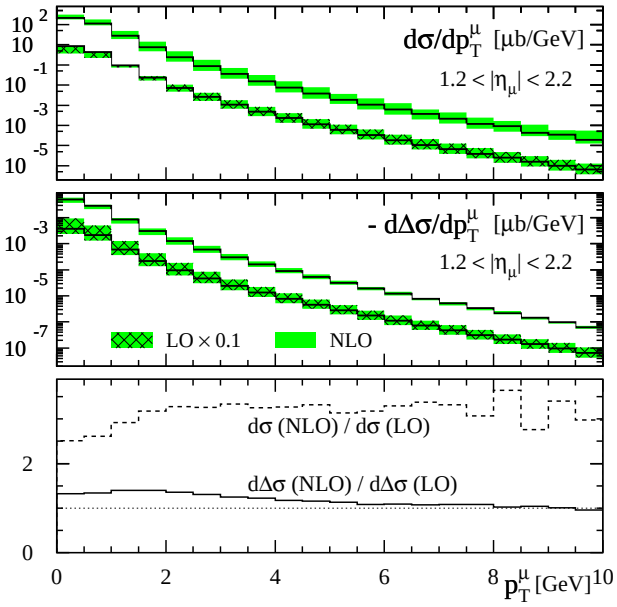

Figure 5.16: Same as in figure 5.15 but for the single-inclusive transverse momentum spectrum of muons from heavy quark decays at forward rapidities $1.2 \leq |\eta_\mu| \leq 2.2$.

any quantitative analysis such as a global QCD extraction of spin-dependent parton densities.

As can be inferred from figure 5.15, theoretical ambiguities due to the choice of μ_r and μ_f in (2.36) are reduced in the polarised but not in the unpolarised case. Along with the observation of large QCD corrections, this indicates the need for next-to-next-to-leading order corrections for the unpolarised cross section to better control the dependence on μ_f and μ_r. We note that substantial progress in this direction has been made recently [62–70], mainly to allow for precision studies of the large amount of top quarks (expected to be) produced at the CERN-LHC. In addition, fixed order calculations need to be amended by all-order resummations if $\ln p_T^Q/m_Q$ becomes large. This was achieved in [78, 79, 81] and described in a nutshell in section 2.7, but is not really relevant for our discussions here since we are mainly interested in the region where $p_T^Q \sim m_Q$. We postpone a discussion of theoretical uncertainties due to the choice of m_Q and α_Q in equation (2.50), as well as the effect of varying μ_r and μ_f independently, until the end of this subsection.

The single-inclusive transverse momentum spectrum of muons from heavy quark decays is shown in figure 5.16 in LO and NLO accuracy. The pseudorapidity η_μ of the muon is integrated in the range $1.2 \leq |\eta_\mu| \leq 2.2$ corresponding to the angular acceptance of the PHENIX experiment. All observations made in figure 5.15 regarding the relevance of NLO corrections, the behaviour of the K-factor, and the dependence on $\mu_{f,r}$ apply also here. The polarised K-factor stays even closer to one than in figure 5.15 as $d\Delta\sigma/dp_T^\mu$ develops no node in the p_T^μ range shown.

Glancing at the relative sizes of the unpolarised and polarised single-inclusive transverse momentum spectra for electrons and muons shown in figure 5.15 and 5.16, re-

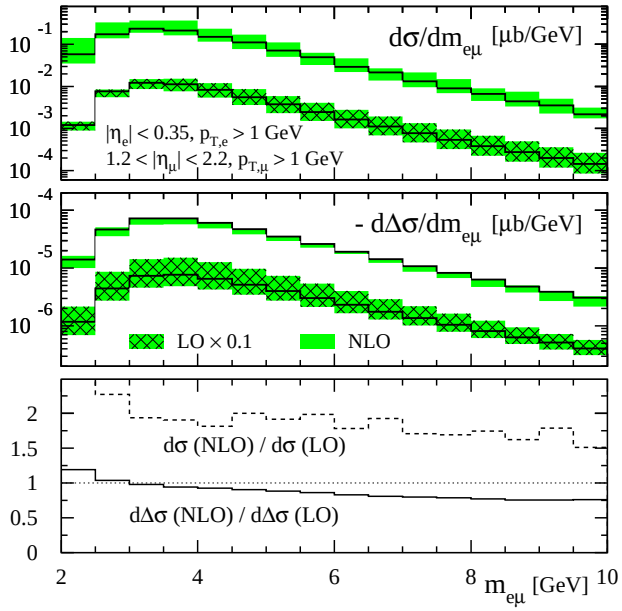

Figure 5.17: Same as in figure 5.15 but for the invariant mass spectrum of electron-muon correlations from heavy quark decays. Electrons are detected at central rapidities, $|\eta_e| \leq 0.35$, and muons are detected at forward rapidities, $1.2 \leq |\eta_\mu| \leq 2.2$. The transverse momenta of both electrons and muons are required to be larger than 1 GeV.

spectively, it becomes immediately obvious that the corresponding double-spin asymmetries A_{LL}^e and A_{LL}^μ, which we turn to in subsection 5.3.4, are very small if the up-to-date DSSV parton densities [30, 31] are used. Expected asymmetries of the order of a few tenths of a percent are extremely challenging experimentally as systematic uncertainties, like the one from the determination of the relative beam luminosities at RHIC, are of similar size [202]. At higher $p_T^{e,\mu}$, where double-spin asymmetries are largest, the single-inclusive cross sections in figures 5.15 and 5.16 have dropped already by several orders of magnitude from their peak values, and measurements require substantial integrated luminosities.

More promising appear to be observables where both the heavy quark and the heavy antiquark decay semi-leptonically and both leptons are observed in coincidence. This is also where our numerical phase space integration and the flexible Monte Carlo code for polarised heavy flavour hadroproduction introduced in chapter 3 become truly essential. Particle correlations are hard, and often impossible, to compute at NLO with largely analytical methods, see, e.g., [203].

Figure 5.17 shows our results for the invariant mass spectrum of electron-muon correlations from semi-leptonic decays of D and B mesons within the angular acceptance of the PHENIX detector, i.e., $|\eta_e| \leq 0.35$ and $1.2 \leq |\eta_\mu| \leq 2.2$. The invariant mass of two particles a and b is generally defined as $m_{ab} = \sqrt{(p_a + p_b)^\mu (p_a + p_b)_\mu}$. In addition, we require a minimum transverse momentum for both leptons of 1 GeV as required also by experiment. As in figures 5.15 and 5.16, results shown as solid lines are obtained with the default choice of parameters. Again, shaded bands indicate the theoretical

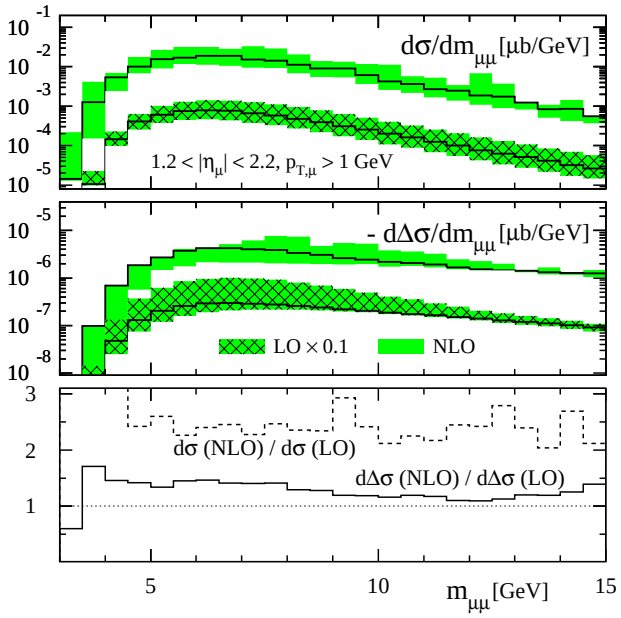

Figure 5.18: Same as in figure 5.15 but for the invariant mass spectrum of muon-muon correlations from heavy quark decays. Both muons are detected at forward rapidities, $1.2 \leq |\eta_\mu| \leq 2.2$, but in different hemispheres. The transverse momentum of each muon is required to be larger than 1 GeV.

uncertainty from varying the factorisation and renormalisation scales simultaneously in the range $1/2 \leq \xi \leq 2$.

The K-factor, shown in the lower panel of figure 5.17, is smaller than the ones found for the single-inclusive observables in figures 5.15 and 5.16 in the unpolarised case. Still, NLO corrections differ considerably for the unpolarised and polarised invariant mass spectra. Again, the corrections are such that the corresponding double-spin asymmetry is reduced at NLO accuracy. The scale uncertainty is significantly smaller for the spin-dependent cross section with NLO corrections included. The improvement in the helicity-averaged case is much less pronounced.

Compared to the single-inclusive results in figures 5.15 and 5.16, the cross sections obtained for the electron-muon invariant mass spectrum are smaller but $d(\Delta)\sigma/dm_{e\mu}$ drops much less with increasing $m_{e\mu}$ than $d(\Delta)\sigma/dp_T^{e\mu}$ with increasing p_T^e or p_T^μ, which makes measurements of $A_{LL}^{e\mu}$ at comparatively large values of $m_{e\mu}$ feasible. We do not consider here correlations with back-to-back electrons at central rapidities since electron-muon correlations are phenomenologically more interesting due to their asymmetric kinematics with respect to rapidity, probing the interacting partons at different momentum fractions x as will be demonstrated below.

The corresponding invariant mass spectrum for two muons from D and B meson decays observed in coincidence is shown in figure 5.18. Both muons are required to have $1.2 \leq |\eta_\mu| \leq 2.2$ and $p_T^\mu > 1\,\text{GeV}$, with one muon detected at forward (positive) and one muon detected at backward (negative) pseudorapidities. Again, the cross sections $d[\Delta]\sigma$ decrease rather slowly with increasing invariant mass $m_{\mu\mu}$. This observable is

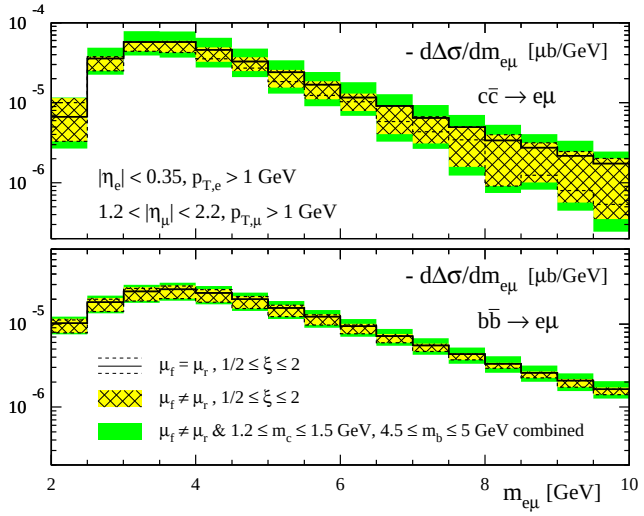

Figure 5.19: Scale and mass uncertainties for the polarised invariant mass spectrum of electron-muon correlations at NLO accuracy, using the same cuts as in figure 5.17. The upper and lower panel shows the contribution from $c\bar{c}$ and $b\bar{b}$ decays, respectively, multiplied by -1. The dashed lines indicate the range of uncertainties for $\mu_f = \mu_r$, $1/2 \leq \xi \leq 2$, and central values of $m_{c,b}$ as in figure 5.17. The solid curves are for $\xi = 1$. The effect of varying μ_f and μ_r independently in the same range of ξ for fixed $m_c = 1.35\,\text{GeV}$, $m_b = 4.75\,\text{GeV}$ and for $1.35\,\text{GeV} \leq m_c \leq 1.5\,\text{GeV}$, $4.5\,\text{GeV} \leq m_b \leq 5.0\,\text{GeV}$ is illustrated by hatched and solid bands, respectively. In the latter case, scale and mass uncertainties are combined in quadrature (see text).

very demanding in terms of required Monte Carlo statistics as can be seen by the still fairly pronounced fluctuations, most noticeable in the unpolarised K-factor. The general trend and features of the cross sections are, however, reliable. As before, NLO corrections are more significant in the unpolarised case, where $K \simeq 2$. Unfortunately, the reduction of the theoretical ambiguities related to the choice of $\mu_{f,r}$ is only marginal at NLO.

We now turn to a more detailed discussion of theoretical uncertainties for the observables discussed in this section, taking the phenomenologically interesting invariant mass spectrum for electron-muon correlations presented in figure 5.17 as an example. Qualitatively very similar results are obtained for the other cross sections given in figures 5.15, 5.16, and 5.18 and hence not shown here.

The impact of varying μ_f and μ_r independently is shown in figure 5.19 for the electron-muon invariant mass spectrum in polarised pp collisions at NLO accuracy. Since we are also interested in variations of $m_{c,b}$, the contribution from $c\bar{c}$ and $b\bar{b}$ decays are shown in separate panels and add up to $-d\Delta\sigma/dm_{e\mu}$ discussed in figure 5.17. Following reference [57], we compute our results for seven different settings of scales $\mu_{f,r} = \xi_{f,r}(m_Q^2 + [(p_T^Q)^2 + (p_T^{\bar{Q}})^2]/2)^{1/2}$, using $(\xi_f, \xi_r) = \{(1,1),(2,2),(1/2,1/2),(1,1/2),(2,1),(1/2,1),(1,2)\}$ and keeping m_Q fixed to their central values $m_c = 1.35\,\text{GeV}$ and $m_b = 4.75\,\text{GeV}$. The envelope of all resulting curves defines the scale uncertainty and is shown as hatched bands in figure 5.19. For comparison, the dashed lines indicate the range of uncertainties for the standard choice $\mu_f = \mu_r$ used in figure 5.17. As can be seen,

taking $\mu_f \neq \mu_r$ does not significantly enlarge the scale ambiguities for the polarised cross section, in particular, for the contribution from bottom quarks shown in the lower panel.

The solid bands in figure 5.19 take also variations of m_c and m_b into account. The recipe we follow here is again similar to the one used for estimating theoretical uncertainties for unpolarised heavy flavour production [57, 147]. In practise, we add scale and mass uncertainties in quadrature, and the envelope of all results is defined by $C + [(M_\mu^+ - C)^2 + (M_{m_Q}^+ - C)^2]^{1/2}$ and $C - [(C - M_\mu^-)^2 + (C - M_{m_Q}^-)^2]^{1/2}$. Here, C denotes the results obtained for central values of scales and masses. M_μ^+ (M_μ^-) are the maximum (minimum) cross sections computed for $\mu_f \neq \mu_r$, $m_c = 1.35\,\text{GeV}$, and $m_b = 4.75\,\text{GeV}$, as depicted by the hatched bands. Correspondingly, $M_{m_Q}^+$ ($M_{m_Q}^-$) denote the maximum (minimum) cross sections for $\xi_{f,r} = 1$ and varying m_c and m_b in the range $1.35\,\text{GeV} \leq m_c \leq 1.5\,\text{GeV}$ and $4.5\,\text{GeV} \leq m_b \leq 5.0\,\text{GeV}$, respectively. In general, the combined uncertainties are much smaller for $b\bar{b}$ than for $c\bar{c}$ production and decays, which is not too surprising. In both cases, variations of m_Q add noticeably to the theoretical uncertainties.

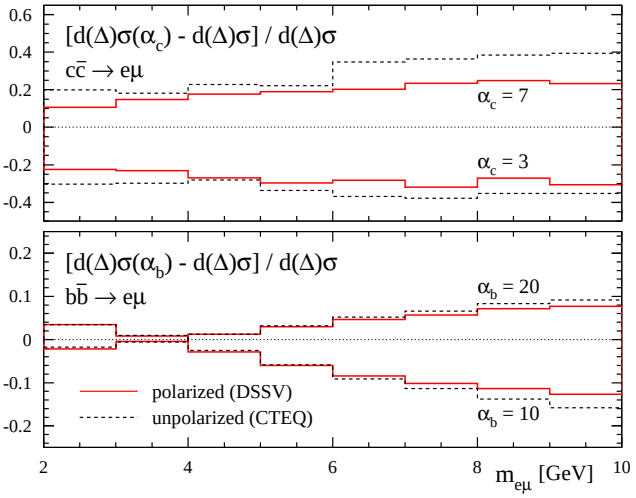

Figure 5.20: Dependence of the polarised (solid lines) and unpolarised (dashed lines) invariant mass spectra for electron-muon correlations at NLO accuracy on the choice of fragmentation parameters α_c (upper panel) and α_b (lower panel) defined in equation (2.50). Displayed are the relative deviations for $c\bar{c}$ and $b\bar{b}$ decays using $\alpha_c = 3, 7$ and $\alpha_b = 10, 20$ with respect to the cross sections obtained for our default values $\alpha_c = 5$ and $\alpha_b = 15$ [56], respectively. μ_f, μ_r, and heavy quark masses are taken at their central values, and the same experimental cuts as in figure 5.17 are adopted.

The dependence of the cross sections on the choice of α_Q in the non-perturbative function $D^{Q\to H_Q}(z)$ describing the hadronisation of the heavy quarks into D and B mesons, see equation (2.50), is illustrated in figure 5.20. Again, we take the invariant mass spectrum for electron-muon correlations as a representative example. We vary α_c and α_b in the range [56] $3 \leq \alpha_c \leq 7$ and $10 \leq \alpha_b \leq 20$, respectively, and show the impact on the invariant mass spectrum as relative uncertainty with respect to the results obtained for the central values $\alpha_c = 5$ and $\alpha_b = 15$ used in figure 5.17.

It turns out that polarised and unpolarised invariant mass spectra are affected very much in the same way by variations of $\alpha_{c,b}$. For charm production and taking $3 \leq \alpha_c \leq 7$, it roughly amounts to a shift in the normalisation of the cross sections by $\pm 20 \div 30\%$. The impact of varying α_b on the contribution to $d[\Delta]\sigma/dm_{e\mu}$ from bottom decays is significantly smaller, up to about $\pm 10\%$ deviations from the results for $\alpha_b = 15$, but is less uniform with $m_{e\mu}$. These observations have the important implication that theoretical uncertainties associated with the actual choice of $\alpha_{c,b}$ drop out to a large extent for experimentally relevant double spin asymmetries A_{LL} discussed in section 5.3.4 below.

5.3.3 Subprocess, charm, and bottom fractions

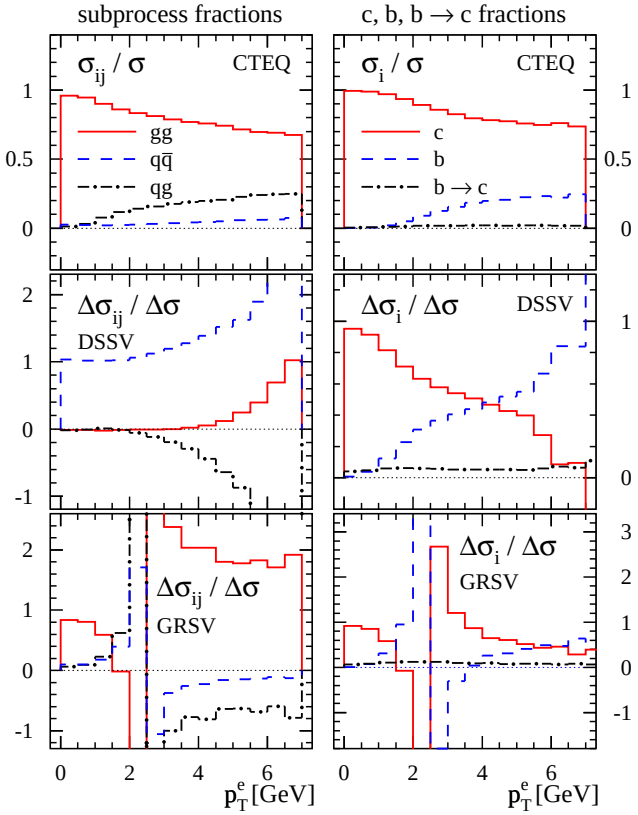

Figure 5.21: Fractional amount of different partonic subprocesses at NLO accuracy (left column) and of charm, bottom, and cascade ($b \to c$) decays (right column) contributing to the single-inclusive transverse momentum spectrum of electrons shown in figure 5.15. Results are shown for unpolarised (upper row) and polarised (middle and lower rows) pp collisions at RHIC using the CTEQ6 [124], DSSV [30, 31], and GRSV [129] set of parton densities, respectively.

We now take a detailed look at the fractional contributions of the different partonic hard scattering processes to the cross sections shown in figures 5.15 – 5.18. This will help to understand the dependence of the double-spin asymmetries on different sets of polarised parton densities, to be discussed in the next subsection. Since charm and

bottom decays both contribute to the lepton spectra, we additionally present their fractional contributions. This includes also the "cascade" decay $b \to c \to e, \mu$ which is modelled following the procedure discussed in [57]. It is found to be negligible for all observables we are interested in.

The left-hand-side of figure 5.21 shows the contributions of the three different subprocesses at NLO accuracy, with gg, $q\bar{q}$, and qg initial-states, to the single-inclusive decay electron spectra shown in figure 5.15. In the unpolarised case (upper panel), gluon-gluon fusion is the by far dominant subprocess for heavy flavour production at RHIC energies, with $q\bar{q}$ annihilation becoming somewhat more relevant at larger values of transverse momentum p_T^e. Interestingly enough, the genuine NLO, i.e., α_s suppressed, qg scattering process also contributes very significantly at larger p_T^e, even exceeding the $q\bar{q}$ annihilation cross section. This observation can be linked to the abundance of gluons at all momentum fractions x [124], such that the partonic flux relevant for qg scattering, i.e., $q(x_1, \mu_f)g(x_2, \mu_f)$, is much larger than the corresponding flux for $q\bar{q}$ annihilation, in particular, at the medium-to-large momentum fractions $x_{1,2}$ relevant for RHIC. This compensates for the $\mathcal{O}(\alpha_s)$ suppression in the qg hard scattering channel. In $p\bar{p}$ scattering, e.g., at the TeVatron, where antiquarks are "valence" quarks in the antiproton beam, this is different, and the $q\bar{q}$ flux is much enhanced. A similar observation concerning the relevance of the $q\bar{q}$ annihilation channel was made also for fixed-target experiments in section 5.2, where it is expected to contribute very significantly to charm hadroproduction in proposed $p\bar{p}$ collisions at the GSI-FAIR facility, but not in pp scattering of similar c.m.s. energy planned at J-PARC.

In general, the situation is much more involved in the polarised case, where both hard scattering cross sections and parton densities are not positive definite and can contribute with either sign, depending on the kinematics relevant for a particular process. In the vicinity of nodes, large cancellations are to be expected. As we shall demonstrate below, depending on the chosen set of polarised parton densities, the subprocess fractions can differ considerably from each other and from gluon-gluon fusion dominance found in the unpolarised case.

The middle panel of figure 5.21 shows our results for the polarised subprocess fractions obtained with the DSSV set [30, 31], our default choice of parton densities used in figures 5.15 – 5.18. At small p_T^e, the cross section is entirely dominated by $q\bar{q}$ annihilation, contrary to the unpolarised case. Towards larger p_T^e, both gg and qg processes contribute significantly but with opposite sign, leading to strong cancellations. This happens, however, in a kinematic region close to a sign change of the cross section at $p_T^e \simeq 7\,\text{GeV}$.

A rather different pattern of fractional subprocess contributions can be found in the bottom panel of figure 5.21, where the GRSV(std) [129] parton densities were used. Note that the cross section has a sign change now already near $p_T^e = 2\,\text{GeV}$, which explains the complicated behaviour of the ratios in this region and makes it very awkward to display them properly. Like in the unpolarised case, gluon-gluon fusion is the most important contribution to the cross section. At larger p_T^e, $q\bar{q}$ and qg subprocesses become more relevant, both contributing with the opposite sign compared to gg scattering, leading again to fairly significant cancellations.

The gross features of the results in figure 5.21 obtained with DSSV and GRSV parton densities can be readily understood by comparing the size and sign of the individual quark, antiquark, and gluon densities in both sets, see, e.g., figure 2.4 in section 2.5. Since the decay electrons stem from heavy (anti)quarks produced at central rapidities, the interacting partons have very similar momentum fractions, i.e., $x_1 \simeq x_2$. Therefore,

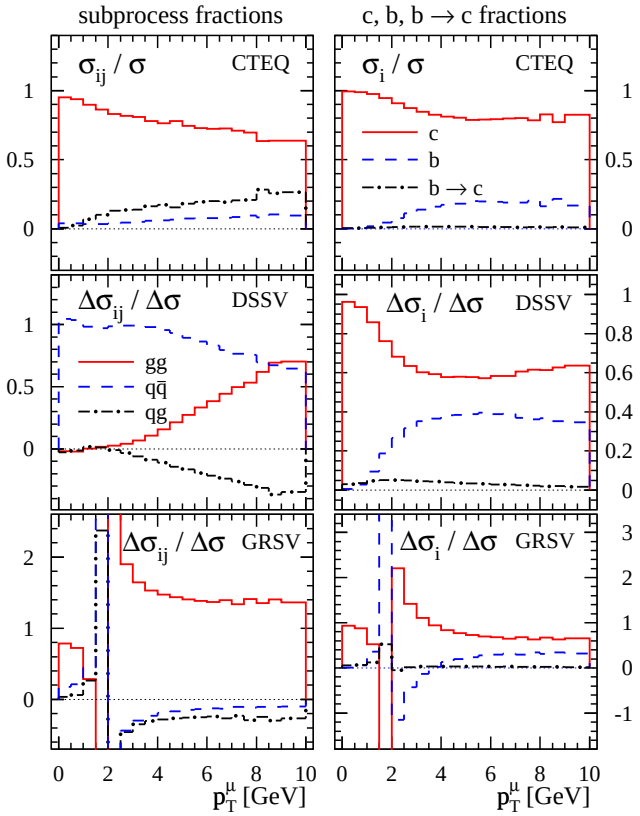

Figure 5.22: Same as in figure 5.21 but now for the single-inclusive transverse momentum spectrum of muons shown in figure 5.16.

$\Delta g(x_1)\Delta g(x_2) > 0$, irrespective of the node in the DSSV gluon distribution, and the sign of the gg contribution follows the sign of the hard scattering cross section, which changes from positive at small p_T to negative at larger p_T values.

Due to helicity conservation, $d\Delta\hat{\sigma}_{q\bar{q}} = -d\hat{\sigma}_{q\bar{q}} < 0$ [73], the sign of the $q\bar{q}$ contribution depends on the individual parton densities for each quark and antiquark flavour. All sets of polarised parton densities have $\Delta u(x) > 0$ and $\Delta d(x) < 0$, resembling the features of the naive quark model. The GRSV(std) set [129] assumes an $SU(3)$ symmetric sea, with all antiquark polarisations being negative, such that for the dominant u-quarks one has $\Delta u(x_1)\Delta\bar{u}(x_2) < 0$, resulting in a net positive contribution to the cross section. This is exactly the opposite in the DSSV set [30, 31], where $\Delta u(x_1)\Delta\bar{u}(x_2) > 0$, unless x_2 gets very large. The genuine NLO qg subprocess cross section, as well as the sum of all quark and antiquark polarisations, $\Delta\Sigma = \sum_q[\Delta q + \Delta\bar{q}]$, are both positive, such that the sign of the qg contribution depends on the sign of $\Delta g(x)$ in the relevant region of x, which turns out to be positive for both GRSV(std) and DSSV. Overall, the fractional contributions of the individual subprocesses to the single-inclusive decay electron spectrum are essentially controlled by the modulus of the polarised gluon density, $|\Delta g(x)|$, which is much larger for the GRSV(std) set, i.e., $|\Delta g(x)|_{GRSV} \gg |\Delta g(x)|_{DSSV}$. The bigger the gluon density, the closer the result is to what we have found in the unpolarised case. It turns out that even for the moderate gluon polarisation of the GRSV(std) set, the gluon-gluon channel prevails for all p_T^e

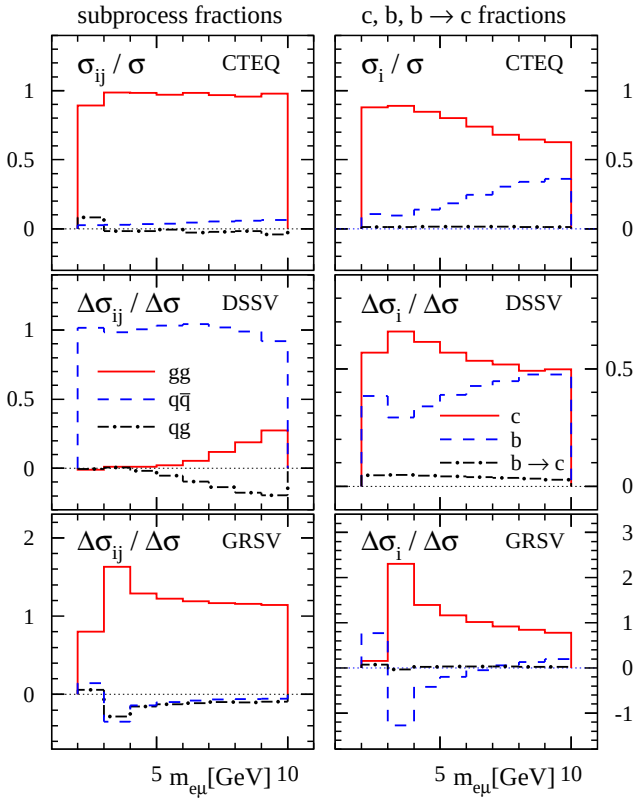

Figure 5.23: Same as in figure 5.21 but now for the invariant mass spectrum of electron-muon correlations shown in figure 5.17.

values shown in figure 5.21.

The right-hand-side of figure 5.21 shows the fractional contributions of the charm, bottom, and "cascade" $b \to c$ decays to the single-inclusive transverse momentum spectrum of electrons. For $p_T^e \lesssim 2\,\mathrm{GeV}$, almost all electrons originate from charm decays, but above the bottom contribution catches up, yielding about 25% at $p_T^e = 6\,\mathrm{GeV}$ in the unpolarised case shown in the upper panel of figure 5.21. Eventually, at somewhat larger values of p_T^e, it becomes dominant, as was shown in [57].

As for the subprocess fractions, the corresponding results in the polarised case depend on the choice of parton densities, and cancellations and possible sign changes of the individual hard scattering subprocesses $d\Delta\hat{\sigma}_{ab}$ further complicate their interpretation. The only feature common to both the unpolarised and the polarised inclusive electron spectra is the smallness of the $b \to c \to e$ cascade decay contribution. The results obtained with the DSSV set (middle panel) show a very sizable bottom contribution, exceeding the $c \to e$ decay above $p_T^e \simeq 4\,\mathrm{GeV}$. However, this is due to a sign change of the $c \to e$ cross section at $p_T^e \simeq 7\,\mathrm{GeV}$, and above, $c \to e$ and $b \to e$ contribute on equal footing. Choosing the GRSV(std) distributions instead (lower panel), both the $c \to e$ and the $b \to e$ cross sections change from positive to negative at 2 and 4 GeV, respectively, with $b \to e$ starting to be the dominant contribution above $p_T^e \sim 6\,\mathrm{GeV}$.

The fractional contributions of the different partonic hard scattering processes (left-

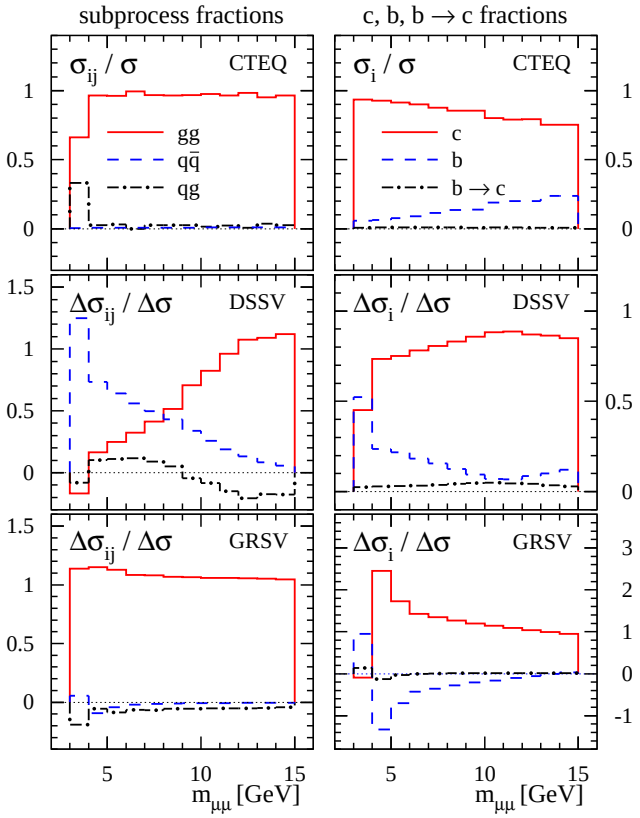

Figure 5.24: Same as in figure 5.23 but now for the invariant mass spectrum of muon-muon correlations shown in figure 5.18.

hand-side) and heavy flavour decays (right-hand-side) to the single-inclusive muon cross section shown in figure 5.16 are given in figure 5.22. The results are qualitatively very similar to the ones depicted in figure 5.21 and discussed above. Again, the polarised subprocess fractions very much depend on the choice of parton densities, and the interpretation is obscured by sign changes and large cancellations among the different contributions. Compared to the single-inclusive electron spectrum at central rapidities, bottom decays contribute less to the muon transverse momentum spectrum at $1.2 \leq |\eta_\mu| \leq 2.2$, even up to $p_T^\mu = 10\,\text{GeV}$. Its contribution is rather flat with respect to p_T^μ and amounts to about 40% (20%) in the (un)polarised case.

Corresponding results for the electron-muon and muon-muon invariant mass distributions, shown in figures 5.17 and 5.18, can be found in figures 5.23 and 5.24, respectively. As before, subprocess fractions can be found on the left-hand-side and contributions from different heavy flavour decays on the right-hand-side of the plots. Note that in all panels of figures 5.23 and 5.24, the bin corresponding to the smallest invariant mass only has a small number of entries due to the cuts $p_T^{e,\mu} > 1\,\text{GeV}$, and the numerical results for that bin should be taken with caution. In general, cancellations among different subprocesses are less pronounced than in figures 5.21 and 5.22, except for small invariant masses, say, below 4 GeV, where a sign change in the polarised cross section occurs.

As compared to single-inclusive decay lepton observables, gluon-gluon fusion is even

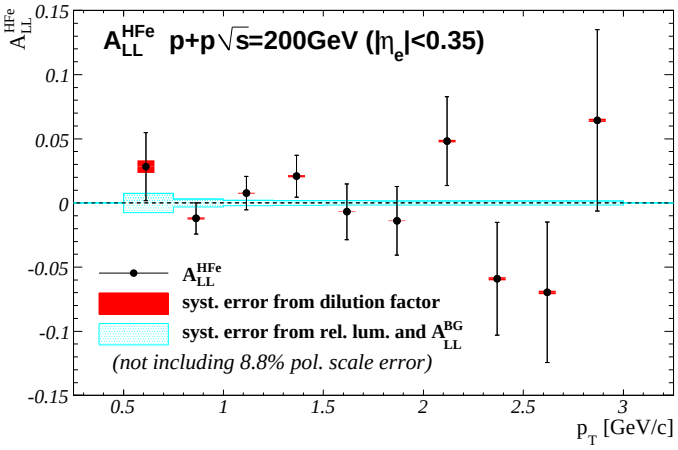

Figure 5.25: Double-spin asymmetry of the heavy flavour electron production. The red error bands represent scaling systematic uncertainties from the dilution factor and the blue error bands represent offset systematic uncertainties from relative luminosity and the background spin asymmetry. Figure taken from [88].

more dominant for electron-muon and muon-muon correlations, with both $q\bar{q}$ and qg subprocesses being negligible in the unpolarised case (upper row). This is also the case for the polarised cross section if the GRSV (std) parton distribution is chosen. For the DSSV set, $q\bar{q}$ annihilation remains dominant for electron-muon correlations, but gluon-gluon fusion contributes significantly to muon-muon correlations for $m_{\mu\mu} \gtrsim 10\,\mathrm{GeV}$. As will be shown in the next subsection, back-to-back muon-muon correlations with $1.2 \leq |\eta_\mu| \leq 2.2$ probe on average fairly large momentum fractions, $\langle x \rangle \gtrsim 0.1$, where the DSSV $\Delta g(x)$ is positive and larger than the sea quark polarisations, such that $d\Delta\hat{\sigma}_{gg} > d\Delta\hat{\sigma}_{q\bar{q}}$. Since the DSSV $\Delta\bar{u}(x)$ turns negative at large x, there are additional cancellations among the different quark flavours in the $q\bar{q}$ annihilation channel, as $\Delta u(x_1)\Delta\bar{u}(x_2) < 0$ and $\Delta d(x_1)\Delta\bar{d}(x_2) > 0$.

As in figures 5.21 and 5.22, the contribution from the cascade $b \to c \to e, \mu$ decay is found to be negligible for lepton-lepton correlations. In particular, the muons in back-to-back correlations originate mainly from charm decays, as can be seen on the right-hand-side of figure 5.24. At the same invariant lepton-lepton mass, bottom quark decays contribute more significantly to electron-muon correlations than to muon-muon correlations for $m_{e\mu}, m_{\mu\mu} > 5\,\mathrm{GeV}$.

5.3.4 Double-spin asymmetries

The quantities of actual interest in experiments exploiting polarised beams and targets are the double-spin asymmetries

$$A_{LL} \equiv \frac{d\Delta\sigma}{d\sigma}$$

defined in (2.49). Experimental normalisation uncertainties conveniently cancel to a large extent in the ratio (2.49). In general, this does not happen for higher order QCD corrections or the various sources of theoretical ambiguities as we shall demonstrate below. Nevertheless, it is often erroneously assumed that LO estimates for A_{LL} give faithful results which can be used in quantitative QCD analyses.

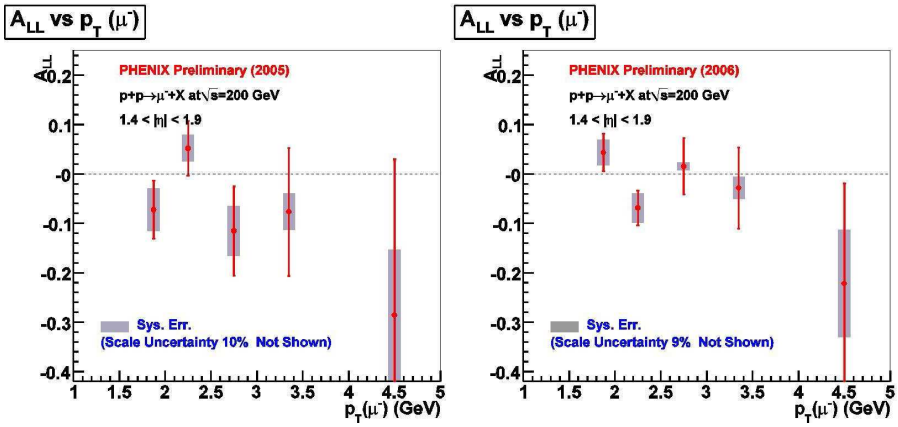

Figure 5.26: Experimental status in the determination of A_{LL} at RHIC. Double spin asymmetry A_{LL} for μ^- from heavy flavour decay as a function of p_T from $p+p$ runs in 2005 and 2006, with averaged polarisation 50 % and 60 %, respectively. Taken from [18].

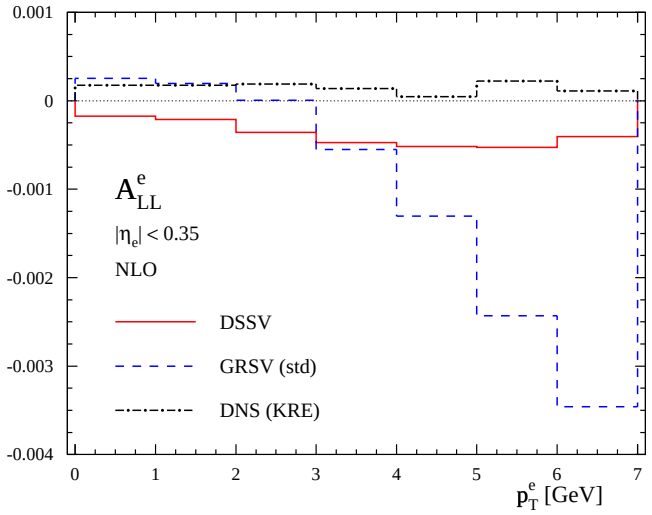

Figure 5.27: Double-spin asymmetry A^e_{LL} for single-inclusive electrons from charm and bottom decays at RHIC, computed at NLO accuracy for three different sets of polarised parton densities: DSSV [30, 31] (solid line), GRSV(std) [129] (dashed line), and DNS(KRE) [130] (dot-dashed line). Electrons are restricted to central rapidities $|\eta_e| \leq 0.35$.

Figures 5.25 and 5.26 give the current status of the determination of double spin asymmetries in single-inclusive processes at RHIC. The error bars are still large. In the following, we will show that we expect only very low values of A_{LL}. As a consequence, it is unfortunately presently still not possible to constrain Δg from our calculations below, as our predictions for all used PDF sets are smaller than the errors of the experimental results.

We start, however, by giving expectations for various double-spin asymmetries at NLO

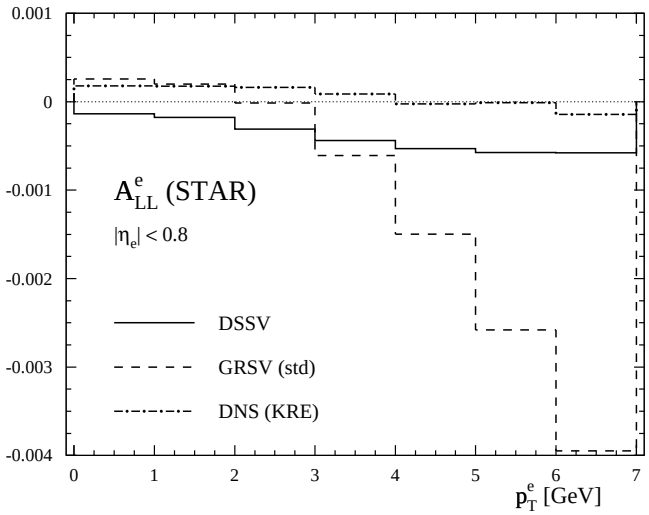

Figure 5.28: Expectation for A_{LL} at STAR. Double-spin asymmetry A_{LL}^e for single-inclusive electrons from charm and bottom decays at RHIC, computed at NLO accuracy for three different sets of polarised parton densities: DSSV [30, 31] (solid line), GRSV(std) [129] (dashed line), and DNS(KRE) [130] (dot-dashed line). Electrons are restricted to central rapidities $|\eta_e| \leq 0.8$.

accuracy in figures 5.27 – 5.31, based on the polarised and unpolarised cross sections for decay lepton transverse momentum and invariant mass distributions, presented in figures 5.15 – 5.18. Apart from our default choice of DSSV polarised parton densities [30, 31], which leads to very small asymmetries throughout, we adopt again also two alternative sets, GRSV(std) [129] and DNS(KRE) [130], both, unlike DSSV, characterised by a positive gluon polarisation of moderate size and an almost $SU(3)$ symmetric sea. We refrain from using outdated models with a large, but strongly disfavoured gluon polarisation in the x range already probed by RHIC pp and fixed target data [20, 39, 40, 42, 44, 48–50, 197–199, 204].

Figures 5.27 and 5.28 present our results for the kinematics of the PHENIX and the STAR detector, respectively. With the exception of the double-spin asymmetry A_{LL}^e for single-inclusive electrons from charm and bottom decays shown in figures 5.27 and 5.28, differences in the results obtained with GRSV(std) and DNS(KRE) parton distributions are readily explained by the slightly larger $\Delta g(x)$ in the GRSV set. For A_{LL}^e the results based on the DNS(KRE) set are strongly affected by cancellations between the gg subprocess on the one hand, and the $q\bar{q}$, qg processes on the other hand, leading to an essentially zero spin asymmetry in the p_T^e range shown. Cancellations among the different subprocesses contributing with different sign are less pronounced for the GRSV set, see the lower left panel of figure 5.21, due to a significantly less negative $\Delta\bar{u}$ density at $x \simeq 0.1$. Cancellations in conjunction with the smallness of A_{LL}^e for all p_T^e make this observable not really suited for studies of the nucleon's spin structure.

The double-spin asymmetry A_{LL}^μ for single-inclusive decay muons at $1.2 \leq |\eta_\mu| \leq 2.2$, presented in figure 5.29, shows a much better correlation of the size of $\Delta g(x)$ and A_{LL}^μ. As was demonstrated in figure 5.22, cancellations among the different subprocesses

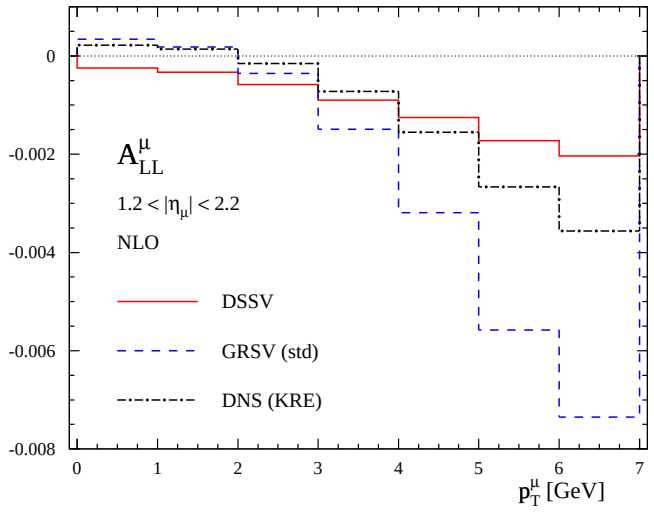

Figure 5.29: Same as in figure 5.27 but for the single-inclusive muon spectrum at forward rapidities $1.2 \leq |\eta_\mu| \leq 2.2$.

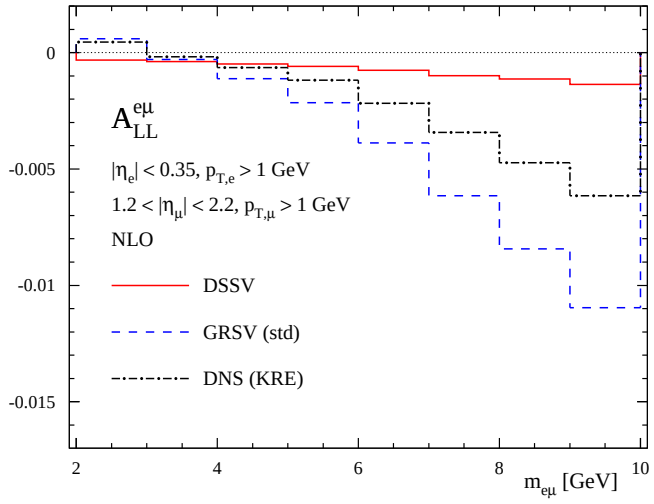

Figure 5.30: Same as in figure 5.27 but for the invariant mass spectrum for electron-muon correlations. Electrons and muons are restricted to $|\eta_e| \leq 0.35$ and $1.2 \leq |\eta_\mu| \leq 2.2$, respectively. In addition, we demand $p_T^e \geq 1\,\text{GeV}$.

are less pronounced than for A_{LL}^e. For the same value of transverse momentum, the obtained spin asymmetries are about a factor of two larger for $A_{LL}^{\mu}(p_T^{\mu})$ than for $A_{LL}^e(p_T^e)$ but still significantly smaller than in projections based on very large positive, but outdated gluon polarisation like GRSV(max) [129], see, e.g., figure 3 in reference [18]. Nevertheless, with sufficient statistics accumulated, spin asymmetries of $\mathcal{O}(0.5\%)$ should be measurable.

The best suited observables related to heavy flavour hadroproduction in longitudinally

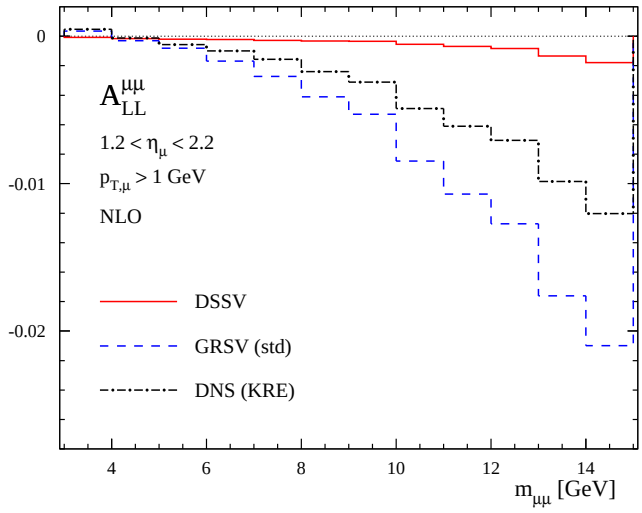

Figure 5.31: Same as in figure 5.27 but for the invariant mass spectrum for muon-muon correlations. The muons are restricted to forward rapidities $1.2 \leq |\eta_\mu| \leq 2.2$ and have to be in opposite hemispheres. In addition, we demand $p_T^\mu \geq 1\,\text{GeV}$.

polarised pp collisions at RHIC are double spin asymmetries for invariant mass spectra of electron-muon and muon-muon correlations shown in figures 5.30 and 5.31, respectively. At small invariant mass, the corresponding cross sections are smaller than for single-inclusive transverse momentum distributions at similar values of $p_T^{e,\mu}$, but fall off much more slowly with increasing invariant mass, cf. figures 5.15 – 5.18. This should allow for measurements of $A_{LL}^{e\mu}$ and $A_{LL}^{\mu\mu}$ up to $m_{e\mu,\mu\mu} = 10 \div 15\,\text{GeV}$ where spin asymmetries can be up to the $1 \div 2\,\%$ level for the GRSV(std) and DNS(KRE) parton densities. In addition, the size of $A_{LL}^{e\mu,\mu\mu}$ and $\Delta g(x)$ in the relevant range of momentum fractions x, see below, are nicely correlated. In the absence of shifted vertex detectors at the RHIC experiments, $A_{LL}^{\mu\mu}$ is the observable with the cleanest sample of charm decays for all $m_{\mu\mu}$ shown in figure 5.31 and irrespective of the set of polarised parton densities used in the calculations, cf. figure 5.24.

Figure 5.32 clearly illustrates the inadequacy of computing double-spin asymmetries with LO estimates of heavy flavour cross sections. Depicted is the K-factor, i.e., $A_{LL}(NLO)/A_{LL}(LO)$, for all double-spin asymmetries presented in figures 5.27 – 5.31, computed in each case using the DSSV polarised and CTEQ6 unpolarised parton densities. Other sets of polarised parton densities yield qualitatively very similar results. On average, LO estimates for A_{LL} are about a factor of two larger than corresponding calculations at NLO accuracy and depend, in case of the single-inclusive observables A_{LL}^e and A_{LL}^μ, strongly on $p_T^{e,\mu}$. This reflects the difference of K-factors for the polarised and unpolarised cross sections found in figures 5.15 – 5.18 and invalidates any approximation based on constant K-factors or the idea that higher order QCD corrections cancel in A_{LL}.

As was already illustrated in figure 5.20, theoretical uncertainties associated with the actual choice of the parameters $\alpha_{c,b}$ in the non-perturbative function $D^{Q\to H_Q}(z)$ given in equation (2.50) cancel to a large extent in double-spin asymmetries. Unfortunately, this is not the case for ambiguities related to the choice of scales $\mu_{f,r}$. As a representative example, we show in figure 5.33 the dependence of the double-

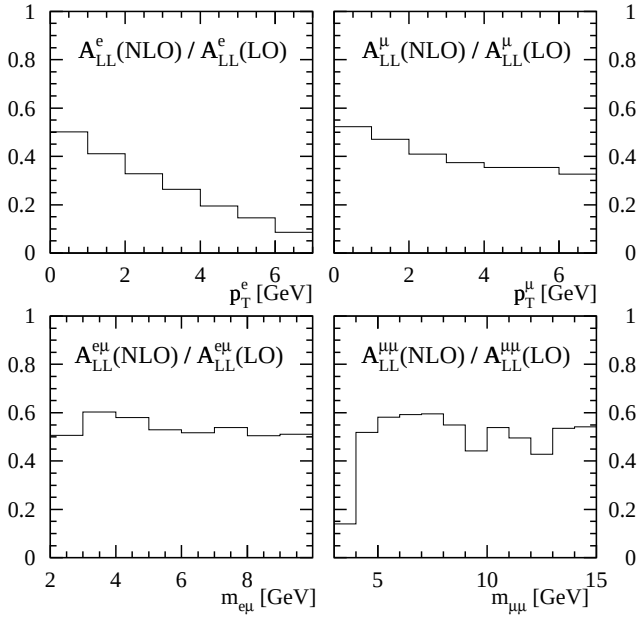

Figure 5.32: Impact of NLO QCD corrections on the double-spin asymmetries shown in figures 5.27 – 5.31. Depicted is the K-factor, i.e., $A_{LL}(NLO)/A_{LL}(LO)$, computed in each case using the DSSV polarised and CTEQ6 unpolarised parton densities.

spin asymmetry $A_{LL}^{e\mu}$ for electron-muon correlations on variations of $\mu_{f,r}$. The shaded band in the upper panel of figure 5.33 illustrates the uncertainty on $A_{LL}^{e\mu}$ if $\mu_f = \mu_r = \xi(m_Q^2 + [(p_T^Q)^2 + (p_T^{\bar{Q}})^2]/2)^{1/2}$ are varied simultaneously in the range $1/2 \leq \xi \leq 2$. The lower panel gives the relative deviation of $A_{LL}^{e\mu}$ for $\xi = 1/2,\ 2$ with respect to the result obtained for our default value $\xi = 1$. The scale uncertainties are quite substantial and not uniform with the invariant mass $m_{e\mu}$. Nevertheless, the asymmetries obtained with the DSSV parton densities are still much smaller than for sets with larger gluon polarisations, like DNS(KRE) or GRSV(std), as can be inferred by comparison with the results given in figure 5.30.

As we have discussed in section 5.3.2, the dependence of unpolarised heavy flavour cross sections on variations of $\mu_{f,r}$ is in general more pronounced than in the polarised case, see figure 5.17 for electron-muon correlations. This can cause sizable ambiguities also for ratios of cross sections, like double-spin asymmetries. Qualitatively similar effects as in figure 5.33 are found for the other double-spin asymmetries discussed in this subsection. We refrain from varying μ_f and μ_r independently, which increases the uncertainties only slightly for the specific observables and kinematics we are interested in, cf. figure 5.19. We proceed likewise for variations of the heavy quark masses $m_{c,b}$, which, in principle, need to be considered as well, see figure 5.19.

Finally, we estimate the range of momentum fractions x at which the (un)polarised parton densities in equation (2.25) are predominantly probed for the different single-inclusive and lepton-lepton correlation observables discussed in this section. Figure 5.34 shows the corresponding cross sections differential in x. In each case, we have integrated over the angular acceptance for detecting electrons and/or muons with the PHENIX experiment at RHIC as well as all transverse momenta of the decay leptons.

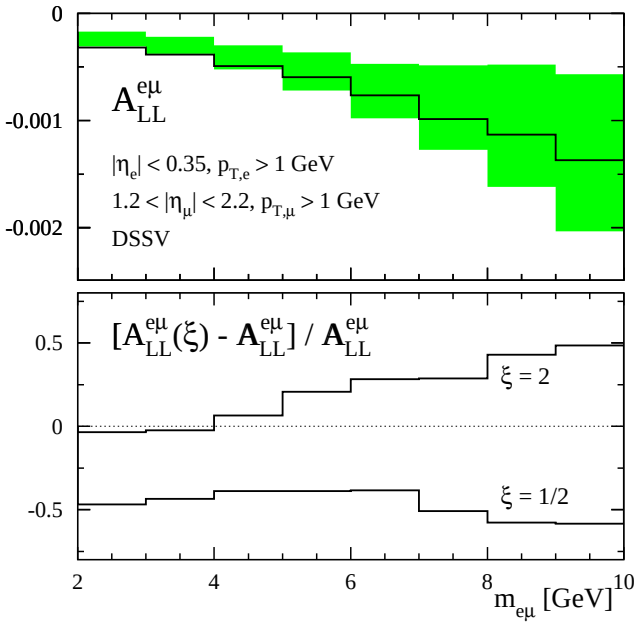

Figure 5.33: Impact of variations of the scales $\mu_f = \mu_r = \xi(m_Q^2 + [(p_T^Q)^2 + (p_T^{\bar{Q}})^2]/2)^{1/2}$ on the double-spin asymmetry $A_{LL}^{e\mu}$ for electron-muon correlations at NLO accuracy. The upper panel shows $A_{LL}^{e\mu}$ computed with the DSSV parton densities for $\xi = 1$ (solid line) and in the range $1/2 \leq \xi \leq 2$ (shaded band). The lower panel gives the relative deviation of $A_{LL}^{e\mu}$ for $\xi = 1/2$, 2 with respect to the result obtained for our default value $\xi = 1$.

As before, an additional cut $p_T^{e,\mu} > 1\,\text{GeV}$ is imposed for lepton-lepton correlations. All x distributions are normalised to the respective integrated cross section $(\Delta)\sigma_{int}$.

Since small transverse momenta probe also the smallest possible x values, figure 5.34 gives a rough idea of the lowest possible momentum fractions accessible in heavy quark hadroproduction at RHIC with a c.m.s. energy of $\sqrt{S} = 200\,\text{GeV}$. As can be seen, single-inclusive observables, shown in the panels on the left, receive contributions from x values as low as 10^{-3}, but the majority of events has $\langle x \rangle \simeq 0.01$. Both, electron-muon and muon-muon correlations, displayed on the right-hand-side of figure 5.34, probe on average larger values of x. In particular, the latter observable can be used to study parton densities at $\langle x \rangle \simeq 0.1$ or higher. The entire suite of possible observables related to heavy flavour hadroproduction at RHIC can cover a wide range in x and has the potential to provide new information on the spin structure of the nucleon and the application of perturbative QCD in polarised hard scattering processes.

However, heavy flavour production at RHIC cannot compete with the statistical precision achievable for more abundant probes of the nucleon's spin structure, like pions and jets [39, 40, 42, 44, 197–199], which are already used in global fits [30, 31]. Nevertheless, measurements of double-spin asymmetries related to heavy flavour production will be crucial for further testing and establishing the all important concept of factorisation and universality for helicity-dependent scattering processes and parton densities, respectively. The underlying dynamics of the partonic scattering processes, i.e., $gg \to Q\bar{Q}$ and $q\bar{q} \to Q\bar{Q}$, is significantly different from the multitude of QCD

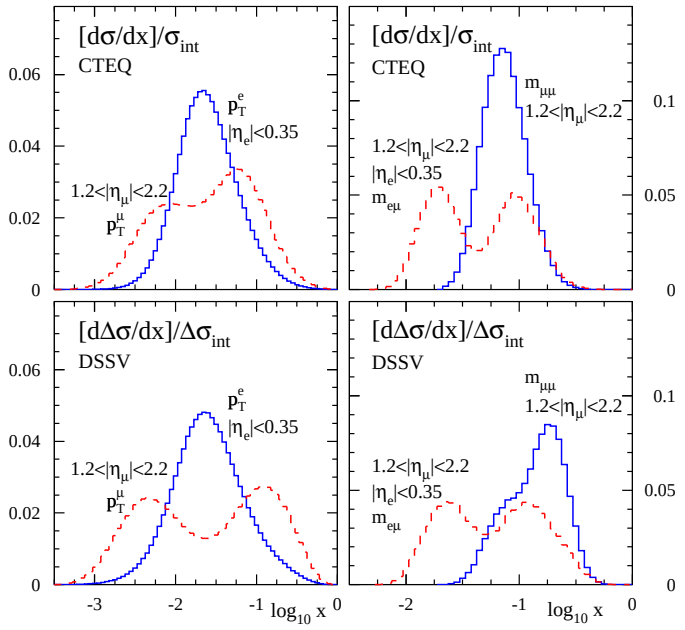

Figure 5.34: Typical range of momentum fractions x at which the parton densities in equation (2.25) are probed for the integrated unpolarised (upper row) and polarised (lower row) cross sections for leptons from heavy flavour decays at RHIC shown in figures 5.15 – 5.18. The left panels show the results for the single-inclusive electron (solid lines) and muon (dashed lines) cross sections. Results for the electron-muon (dashed lines) and muon-muon (solid lines) correlations are presented in the right panels.

processes driving the production of light hadrons [131, 200] or jets [132].

5.4 Results for photoproduction using the Monte Carlo code

Having described studies for hadroproduction in detail in the previous section, we turn now to photoproduction of heavy quarks.

As described in chapters 2 and 4, photoproduction cross sections are composed of the direct part and the resolved part. In the direct part, the gluon enters at leading order directly via the only subprocess, photon-gluon fusion. The subprocess of photon-(anti)quark fusion, which first contributes at NLO, attains usually only a small subprocess fraction at NLO, see below. As a consequence, the direct part is largely influenced by the parton distribution function of the gluon. In kinematic regions, where the resolved part is small, e.g., at COMPASS energies, the photoproduction of heavy quarks is, therefore, very sensitive to Δg.

As discussed in section 4.2, the matrix elements for the resolved part are the same as for hadroproduction and can be taken from there.

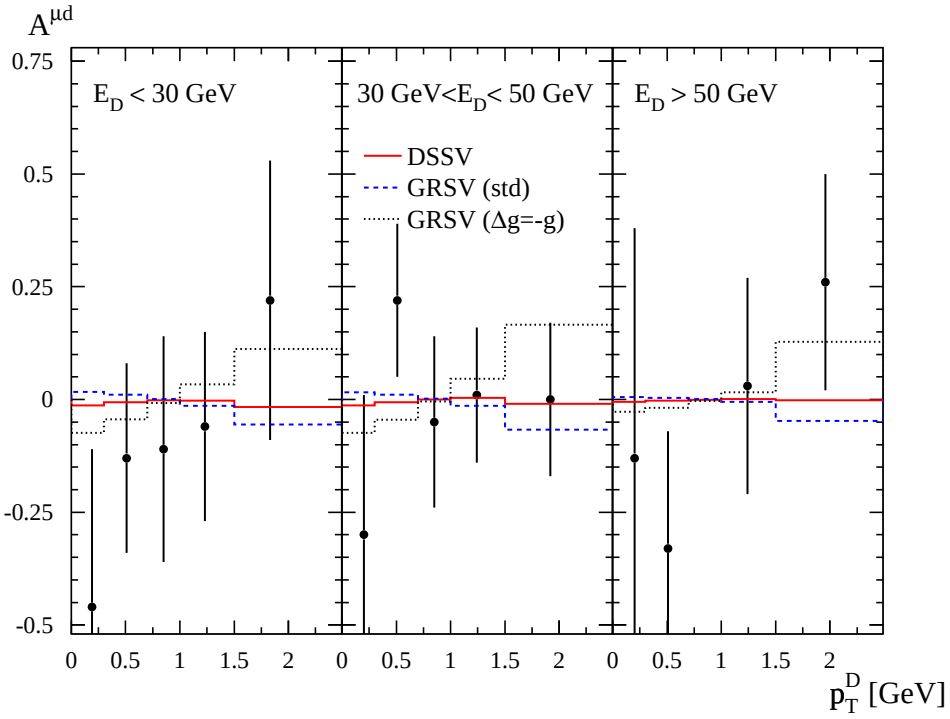

Figure 5.35: Predictions for the double-spin asymmetry for D meson photoproduction at COMPASS at NLO accuracy for three different sets of helicity PDFs and in three bins of E_D compared to data. Note that in the bottom panel one of the data points is outside the range shown for A_{LL}. The points with the error bars represent the experimental values of the COMPASS collaboration.

5.4.1 Results for COMPASS

The COMPASS experiment situated at the CERN scatters a variable energy muon beam with $\langle E_\mu \rangle = 160$ GeV off a fixed target. Until 2006 this was a ^{6}LiD solid state target, which was changed in 2007 to a NH_3 gas target. We focus on the first case, where the deuterium acted as the scattering partner of the muon. The resulting centre-of-mass energy is $\sqrt{S} \approx 18$ GeV. The spectrometer has an opening angle of 180 mrad. COMPASS detects the charm quark by hadronic decay channels of the produced D mesons into kaons and pions.

The COMPASS collaboration has done a leading order analysis, see, e.g. [205, 206] for details, itself and published the results thereof in [20] and [21]; in the latter, they have for the first time also published their results for the asymmetries on the level of the D meson. Details of a NLO analysis, which uses some additional assumptions and was performed by the COMPASS collaboration itself, can be found in [51, 207, 208]. In this thesis we will present our results at NLO without these additional assumptions. As the COMPASS experiment reconstructs the D mesons via their decay channels, we convolute our partonic results with a fragmentation function for heavy quarks. As in the charm case for RHIC, see section 5.3 above, we take again the Kartvelishvili-Likhoded-Petrov form introduced in section 2.8 [54],

$$D^{Q\to H_Q}(z) = N_Q z^{\alpha_Q}(1-z)\,, \tag{5.2}$$

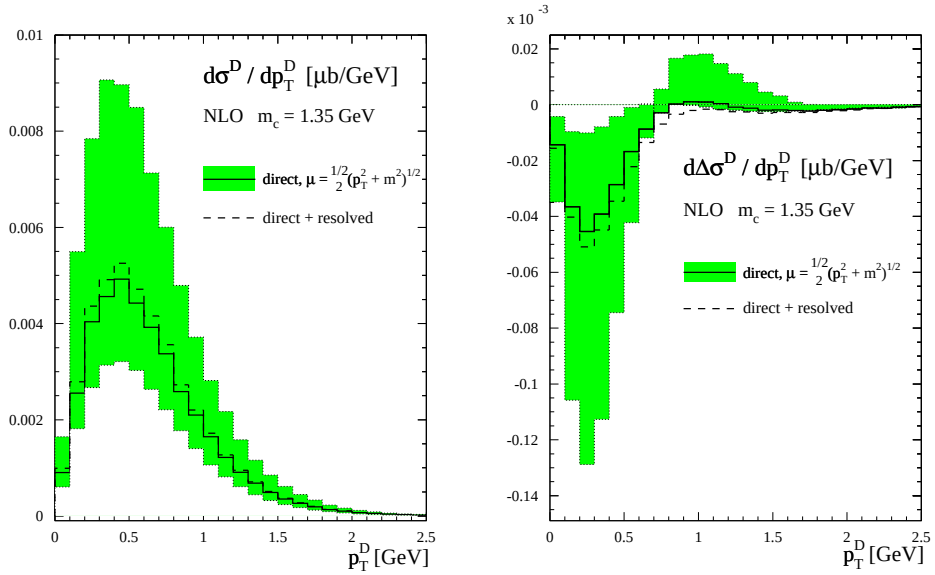

Figure 5.36: Scale dependence of the single-inclusive transverse momentum spectrum of D mesons at NLO with $E_D < 30\,\text{GeV}$ for the dominant direct photon contribution in unpolarised (**left-hand side**) and polarised (**right-hand side**) muon-deuterium collisions at COMPASS kinematics; see text. Factorisation and renormalisation scales are varied simultaneously in the range $\mu = \xi(p_T^2+m_c^2)^{1/2}, 1/2 \leq \xi \leq 2$; the solid line refers to $\xi = 1$. In both panels, the dashed line shows the result for the sum of direct and resolved photon cross sections for $\xi = 1$.

where $N_Q = (\alpha_Q + 1)(\alpha_Q + 2)$ to normalise the integral of $D^{Q\to H_Q}(z)$ to one. Our default choice is $\alpha = 5$. Only for studying the hadronisation effects, we will vary α from 3 to 7.

We start by showing our most important result for COMPASS: In figure 5.35 we compare our NLO results for A_{LL} obtained with the three polarised parton density functions DSSV, GRSV(std) and GRSV(min) with the experimental values of COMPASS for $A^{\mu d\to D}$. The most positive scenario compatible with other experiments uses the GRSV(std) set, and the most negative one GRSV(min). GRSV(max) has been excluded for some years and is not used here. The best global fit to Δg is currently DSSV. The set GRSV(min), also denoted as GRSV($\Delta g = -g$), is characterised by a very large and negative gluon density based on setting $\Delta g(x,\mu_0) = -g(x,\mu_0)$ at some low bound-state like input scale μ_0 [129] for the evolution. We note that current data suggest that GRSV(min) is very improbable. As the published values from [21] are somewhat outdated, we have taken the values of [207, 208], which were also presented by Franco at the conference CHARM2012 and which have been published in [51]. A weighted average is performed to combine the results for the three decay channels $D \to K\pi$, $D \to K\pi\pi$, and $D \to K\pi\pi\pi$ listed there. We adopt the photon polarisation dilution factors tabulated there to convert the data for A_{LL} given in the photon-nucleon system into the double-spin asymmetries for muon-nucleon scattering computed with our Monte Carlo code.

The collinear emission of a quasi-real photon with low virtuality Q and momentum fraction y off a muon with mass m_μ is given by the Weizsäcker-Williams (WW) equivalent photon spectrum [139–143] given in equations (2.39) and (2.40). The upper limit $Q_{\max}$

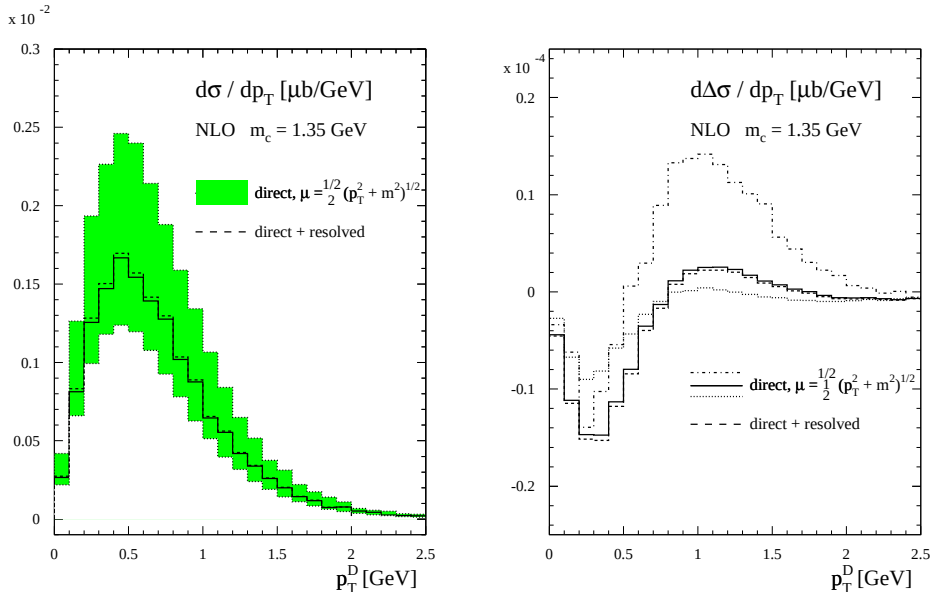

Figure 5.37: The scale uncertainty and the contribution of the resolved part to the unpolarised (left panel) and to the polarised (right panel) DSSV cross sections for 30 GeV$<$ E_D $<$ 50 GeV.

is determined by experimental conditions. For COMPASS we take $Q^2_{\max} = 0.5\,\mathrm{GeV}^2$ and, in addition, restrict the fraction y of the muon's momentum taken by the quasi-real photon to the range $0.1 \leq y \leq 0.9$.

To estimate the range of validity of the WW approximation (2.40), we follow the studies performed in the unpolarised case in references [141] and [209] and compare the exact deep-inelastic cross section [210] and the charm photoproduction cross section,

$$\begin{aligned} d\Delta\sigma^Q &\equiv \frac{1}{2}\left[d\sigma^Q_{++} - d\sigma^Q_{+-}\right] \\ &= \sum_{a,b}\int dx_a dx_b \Delta f^l_a(x_a,\mu_f)\Delta f^p_b(x_b,\mu_f)\,\mathcal{S} \\ &\times \; d\Delta\hat{\sigma}_{ab}(x_a,x_b,S,m_Q,k_1,k_2,\mu_f,\mu_r)\,, \end{aligned} \tag{5.3}$$

at LO accuracy for COMPASS kinematics. We find that deviations from the exact LO result are at the level of 5, 7, and 10% for $Q^2_{\max} = 0.2, 0.5$, and $0.8\,\mathrm{GeV}^2$ in equation (2.40), respectively. As in the unpolarised case [141, 209, 211], for the WW approximation to work, the upper limit $Q^2_{\max}$ in (2.40) must be set to a value sufficiently smaller than the typical energy scale characterising the production process, in our case m_c.

We also use the cut on $z > 0.2$ described in [21, 51]. z is here the fraction of the energy of the virtual photon carried by the D^0 meson candidate. COMPASS published their values in bins in E_D and p_T. Therefore, we have chosen to show three plots, where in each plot the cross section differential in the transverse momentum is presented under the given restrictions on E_D and z. I.e., in the left, middle and right plot, the energy of the produced D meson is only allowed in $E_D < 30$ GeV, 30 GeV $< E_D <$ 50 GeV and $E_D > 50$ GeV, respectively. In all plots, the experimental values with their error bars are also shown. Unfortunately, especially due to the low branching ratios $D \to K + X$,

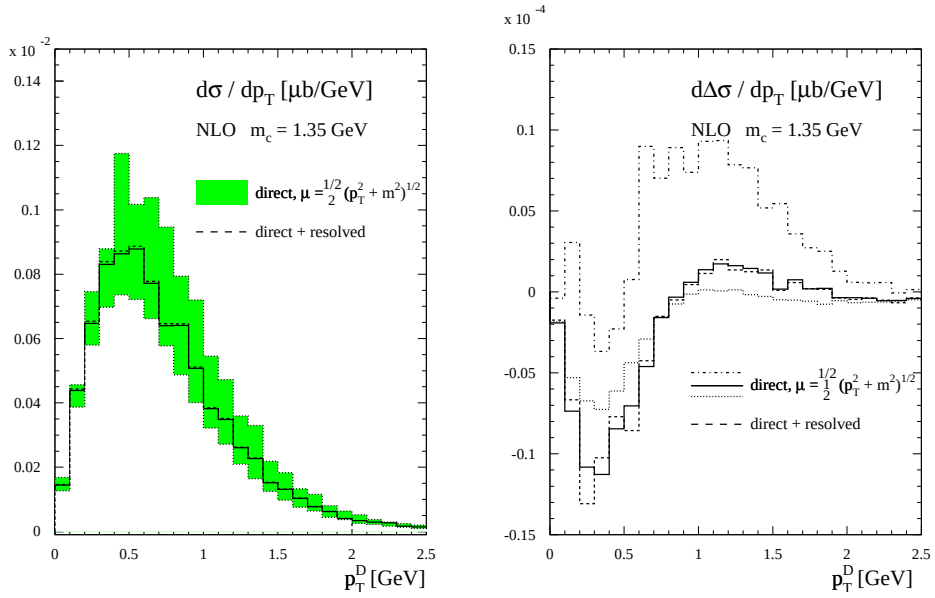

Figure 5.38: The scale uncertainty and the contribution of the resolved part to the unpolarised (left panel) and to the polarised (right panel) DSSV cross sections for $E_D > 50$ GeV.

the experimental statistical errors turn out to be large. So, for each plot, we have five experimental data points. Note that in the third plot one data point is out of the plot range.

As a consequence of the experimental setup, the error bars are usually larger than the differences in A_{LL} between our three sets used for the parton distributions – although we have varied them in a wide range (DSSV, GRSV(std), GRSV(min)). We find that all results are compatible with data within the experimental precision. Clearly, present experimental uncertainties are too large to discriminate between different spin-dependent gluon densities. But, if one wants to read tea leaves with our results, one could perhaps say the following: A positive Δg (like GRSV(std)) seems to be disfavoured by our calculation. The left and the right panel seem to favour GRSV(min), the middle one DSSV. Altogether this might suggest a negative Δg in the range in which the COMPASS experiment is sensitive to it. We will show below that this is mostly the case for $0.03 < x < 0.2$. But more on the impact of the COMPASS results on Δg can only be said after an upcoming global PDF analysis including the COMPASS results.

Next, we want to study by which partonic channels our results are mostly triggered. Figure 5.36 presents the direct leading order and next-to-leading order calculation and points out how important the resolved contributions are. It shows also the scale ambiguity from varying $\mu_{f,r} = \xi(p_T^2 + m_c^2)^{1/2}$ simultaneously in the range $1/2 \leq \xi \leq 2$ for the dominant direct photon contribution ($a = \gamma$) only. The solid lines denote our default choice of scales, $\xi = 1$. Since the published COMPASS data [21, 51] are divided into three bins in the energy E_D of the produced D meson, $E_D < 30\,\text{GeV}$, $30 \leq E_D \leq 50\,\text{GeV}$, and $E_D > 50\,\text{GeV}$, we impose the cut $E_D < 30\,\text{GeV}$ in figure 5.36. Results for the other two bins in E_D are very similar and shown in figures 5.37 and 5.38.

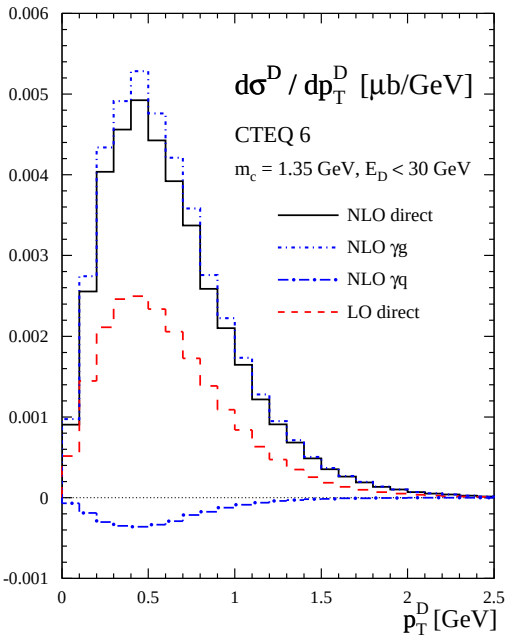

Figure 5.39: Contributions of the individual γg and γq initiated subprocesses to the direct photoproduction cross section at NLO for $\xi = 1$ and $E_D < 30\,\text{GeV}$ (solid line). Also shown is the LO result (dashed line).

In the left panels we present the unpolarised case (CTEQ6) and in the right panels the polarised case (DSSV). The green bands in figure 5.36 show the scale dependence of the direct cross sections when we vary the scale factor between $\xi = 0.5$ and $\xi = 2$, where $\mu = \xi(m_c^2 + p_{T,c}^2)$. For $\xi = 1$ not only the direct result is displayed, but also the full result consisting of the direct and the resolved part. One can clearly see that the resolved part only gives a very small contribution, much smaller than the scale uncertainty. Here, we assume the charm mass to be known exactly. Additionally, one could introduce an uncertainty resulting from varying the charm mass as we have done for RHIC (see section 5.3). This would obviously further enlarge the theoretical uncertainty; also an independent variation of μ_f and μ_r would inflate theoretical errors. In the other two ranges of E_D the relative contribution of the resolved part is equal to or smaller than in the case $E_D < 30$ GeV, see figures 5.37 and 5.38. Because of the special functional form of the DSSV parton distribution functions, the curve for $\xi = 1$ is in the polarised case (DSSV) not always between the curves $\xi = 0.5$ and $\xi = 2$. Therefore, we do not show coloured bands, but only the three lines for $\xi = 0.5$, $\xi = 1$ and $\xi = 2$.

As a consequence, for the extraction of the gluon polarisation from open charm production, it is a justifiable approximation to neglect the resolved part as it should not much influence the values of A_{LL}. The additional error is much smaller than scale uncertainties. Also, in an experimental analysis, the uncertainty introduced by leaving out the resolved part can by far be compensated by the fact that numerical codes using only the direct part are much less computer-time consuming.

Let us turn to the subprocesses and the impact of a next-to-leading order calculation

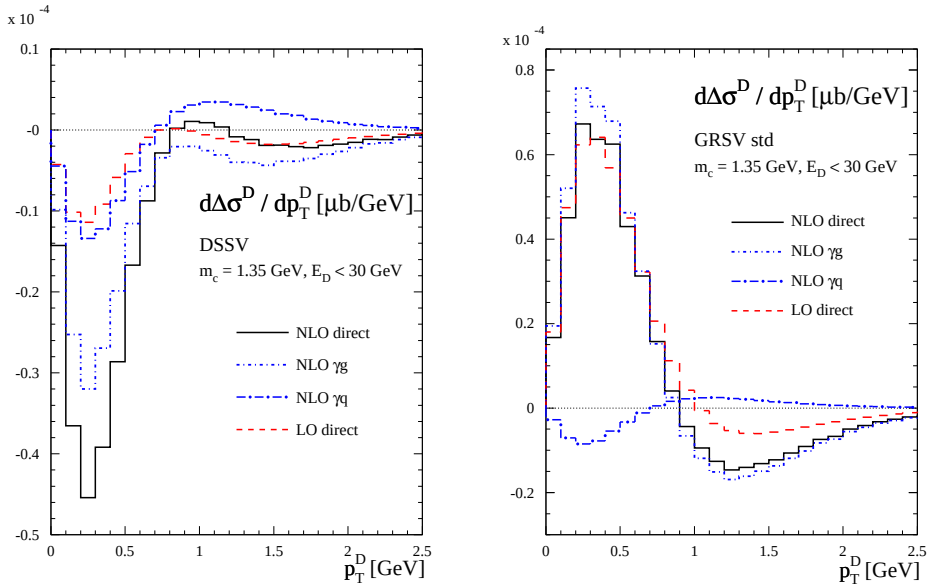

Figure 5.40: As in figure 5.39 but now for the spin-dependent photoproduction cross section for two different choices of helicity PDFs: DSSV [30] (**left-hand side**) and GRSV "standard" [129] (**right-hand side**).

compared to a leading order one. We focus only on the direct part as we have just shown that the resolved part is negligible. Figure 5.39 shows this effect for the unpolarised case and figure 5.40 for the polarised cross sections using DSSV and GRSV(std) parton distribution functions. We choose $E_D < 30\,\text{GeV}$. Results for the other two bins in E_D are very similar and hence not shown. Each of the figures shows the leading order term, which consists only of the one subprocess γg, and the next-to-leading order term containing two types of subprocesses: photon-gluon fusion and photon-(anti)quark scattering. Everywhere, the effects induced by next-to-leading order could not be ignored. And the changes from adding this order are not always the same. As expected, the photon-gluon fusion mechanism, which is already present at LO, gives the main contribution to the unpolarised cross section. The genuine NLO photon-quark channel yields a negative but small correction. The NLO result for the D meson production cross section is roughly a factor of two larger than the corresponding estimate at LO as can be gathered from comparing the dashed and solid lines in figure 5.39.

One notices that the results in figure 5.40 obtained with the DSSV and GRSV(std) sets differ in sign and magnitude of the cross section, which is readily explained by the very different gluon densities in both sets. The positive definite $\Delta g(x, \mu_f)$ of GRSV(std) leads to a similar decomposition into γg and γq subprocesses as was observed in the unpolarised case in figure 5.39. Again, the cross section is strongly dominated by photon-gluon fusion, and the γq channel only yields a small correction. In contrast, the oscillating $\Delta g(x, \mu_f)$ of the DSSV set of helicity PDFs leads to a negative $d\Delta\sigma^D$. Since the DSSV gluon is much smaller in size than the one of GRSV(std), the genuine NLO photon-quark contribution, which is numerically very similar in both PDF sets, is more important and yields more than a quarter of the cross section at small p_T^D. Another important observation concerns the relevance of NLO corrections which appears to be very different for the DSSV and GRSV(std) helicity PDFs. This implies that higher

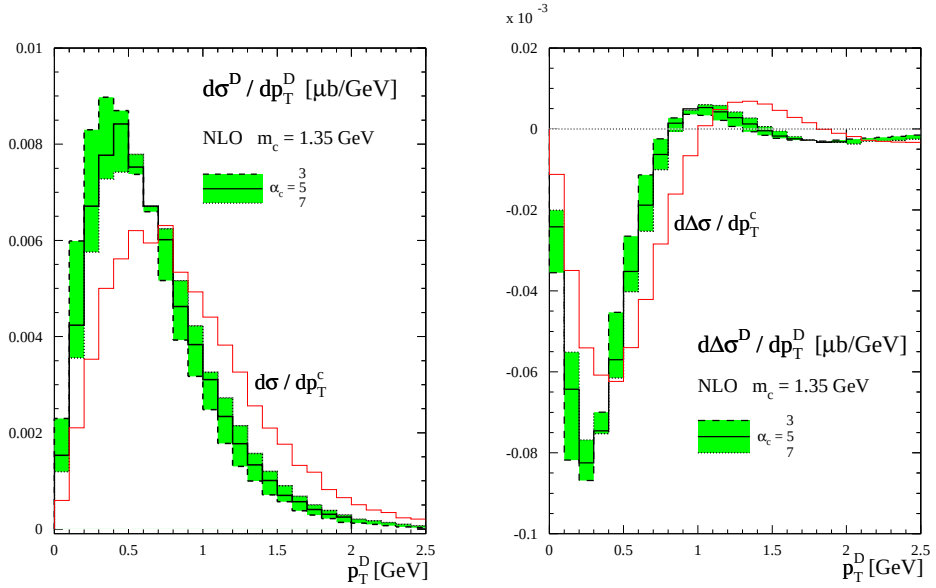

Figure 5.41: As in figure 5.36, but now for variations of the parameter α_c in the fragmentation function (2.50) for the direct cross section computed with $\xi = 1$. No cuts on the D meson or charm quark are imposed; see text. Also shown are the results on the charm quark level, $d(\Delta)\sigma/dp_T^c$.

order QCD effects do *not* cancel in the experimentally relevant double-spin asymmetry,

$$A_{LL} \equiv \frac{d\Delta\sigma^D}{d\sigma^D},$$

defined in (2.49) which we shall discuss in more detail below. Clearly, for a reliable quantitative analysis of charm photoproduction in terms of polarised PDFs, preferably as part of a global QCD fit, it is indispensable to properly include NLO corrections.

In other words, if one wants to conclude from the measured cross section, the Δg value can be under- or overestimated when only the LO approximation is used. From our figures one can especially see that it is not possible to give a K-factor for A_{LL} which is independent from the used set of parton distribution functions. Hence, a full next-to-leading order analysis of the COMPASS results is very important. A leading order analysis can only give a very rough estimate and is not suitable for detailed analyses.

In figure 5.41 the effect of the hadronisation is studied. Therefore, the cross section is shown differential in the transverse momentum of the charm quark and the D meson. The hadronisation from the charm quark to the D meson is simulated by the Kartvelishvili-Likhoded-Petrov function in which the parameter α is varied from 3 to 7 as pointed out in section 5.3 concerning our results for RHIC. In this figure no data from the integrated-out-phase-space-region is excluded – no cuts are imposed for the D meson in order to allow a better comparability between the charm and the D meson spectrum which are both presented. The left figure is for the unpolarised cross sections and the right one for the polarised ones using DSSV. In both cases the characteristic curves for p_T are shifted to smaller momenta through the hadronisation process. And an additional uncertainty from α is introduced. We show the direct photon contribution for $\xi = 1$. Compared to the factorisation scale ambiguities, the dependence of our results on α_c is fairly moderate for both the unpolarised and the

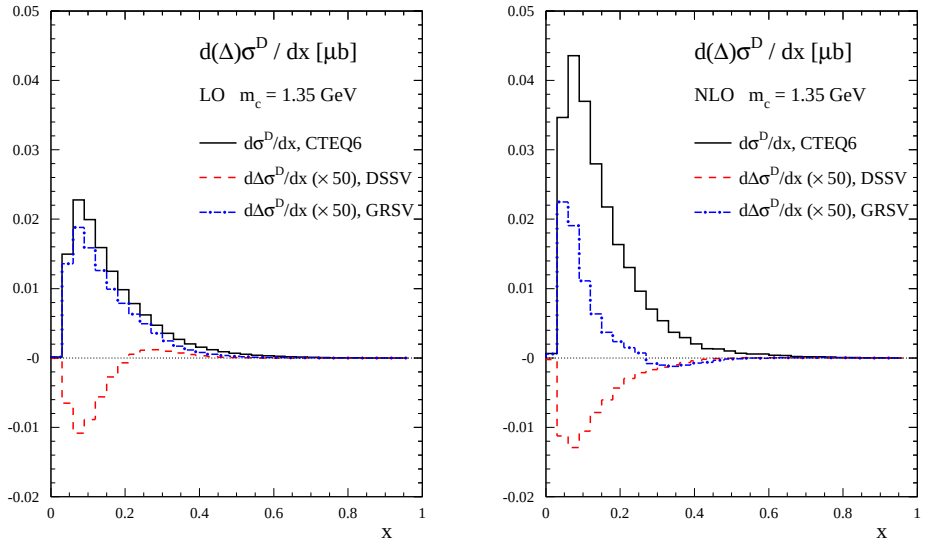

Figure 5.42: Distribution $d(\Delta)\sigma^D/dx$ in the momentum fraction x probed in the PDFs at NLO (**left-hand side**) and LO (**right-hand side**) accuracy for both the unpolarised and polarised direct photon contribution, integrated over phase-space and without imposing cuts. Note that the polarised results are scaled by a factor of 50 for better visibility.

polarised cross sections. A similar observation was made in the case of hadroproduction [90], see section 5.3. Since charm quarks lose only very little of their momentum during hadronisation, i.e., $D^{Q\to H_Q}(z)$ is peaked at fairly large values of z, see section 2.8, the convolution

$$\frac{Ed^3\sigma(e)}{dp^3} = \frac{E_Q d^3\sigma(Q)}{dp_Q^3} \otimes D^{Q\to H_Q} \tag{5.4}$$

introduces only a rather small shift in the transverse momentum spectrum of the charm quarks. This can be inferred from the curves labelled $d(\Delta)\sigma/dp_T^c$ in figure 5.41.

The additional uncertainty caused by the fragmentation processes could have been avoided if micro-vertex detectors could have been used at COMPASS – we also suggest their use to future experiments if technically feasible and possible with the experimental setup.

Another interesting question concerns the range of momentum fractions x predominantly probed in the PDFs by the COMPASS data. Due to the dominance of the photon-gluon fusion process, charm photoproduction will mainly lead to a constraint on the gluon distribution, which is the prime motivation for such measurements. The x distribution in LO and NLO, for both the unpolarised and polarised direct photon contribution to the cross section is explored in figure 5.42. No cuts are imposed in this calculation and the D meson spectrum is integrated over the entire phase space. Note that for the sake of visibility the curves for the polarised case are multiplied by a factor of 50. As has to be expected from the fact that the PDFs enter the cross section through a convolution, a broad range of x values is sampled. It turns out, however, that the mean value of x, where the distribution $d(\Delta)\sigma^D/dx$ is peaked, is fairly independent not only of the order in perturbation theory, LO or NLO, but to

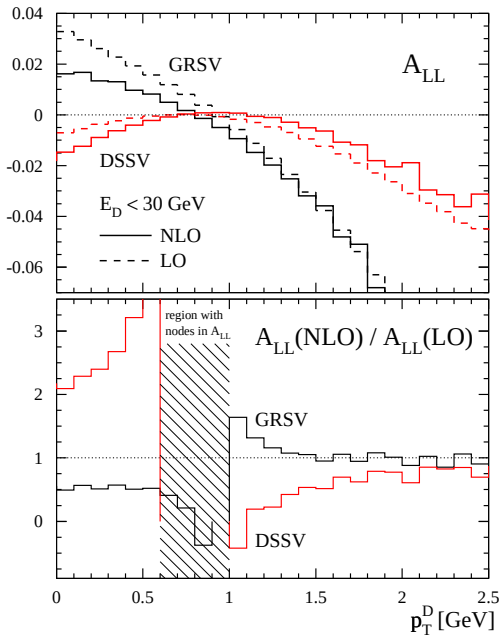

Figure 5.43: **Upper panel**: double spin asymmetry in LO and NLO for D meson photoproduction at COMPASS kinematics for the DSSV and GRSV sets of helicity PDFs; as in figures 5.36 and 5.39 a cut $E_D < 30\,\text{GeV}$ is imposed; **lower panel**: the corresponding ratio of the NLO and LO results. The region where A_{LL} changes sign and the ratio becomes meaningless is indicated by the shaded band.

a large extent also of the chosen set of polarised or unpolarised PDFs. We roughly estimate the average momentum fraction to be $\langle x \rangle \simeq 0.08$ with an error of about $^{+0.12}_{-0.03}$.

Our results differ from estimates of $\langle x \rangle$ by the COMPASS collaboration [51, 207, 208], where NLO results have been obtained based on some parton shower Monte Carlo to approximate the phase space for the NLO matrix elements of reference [76], which are presented in section 4.2 of this thesis. Significant differences between $\langle x \rangle$ estimated in LO and NLO are found in this way. While their LO result for $\langle x \rangle$ agrees with our estimate of about 0.08, their NLO results are $\langle x \rangle = 0.28^{+0.19}_{-0.10}$ [207, 208] and $\langle x \rangle = 0.20$ [51]. It is not yet clear how these results can be compared to our full NLO calculation. We also note that once data on photoproduction processes are implemented in global QCD analyses of helicity PDFs, information on $\langle x \rangle$, though useful, is no longer required or relevant as the fits automatically impose the constraints from data for any given functional form assumed for the $\Delta f(x, \mu_f)$.

Next, we return to the experimentally measured double-spin asymmetry, defined in equation (2.49), which was analysed at LO accuracy and under certain simplifying assumptions in terms of the mean gluon polarisation $\Delta g(\langle x \rangle, \mu_f)/g(\langle x \rangle, \mu_f)$ by the COMPASS collaboration [21]. NLO estimates are also available with the hybrid method outlined above [51, 207, 208].

At the start of this section, we have already presented our results for A_{LL} in figure 5.35, where we have, however, adopted the bin size to the bin size of the experimental values. In figure 5.43 we show A_{LL} for the two sets DSSV and GRSV(std) of helicity

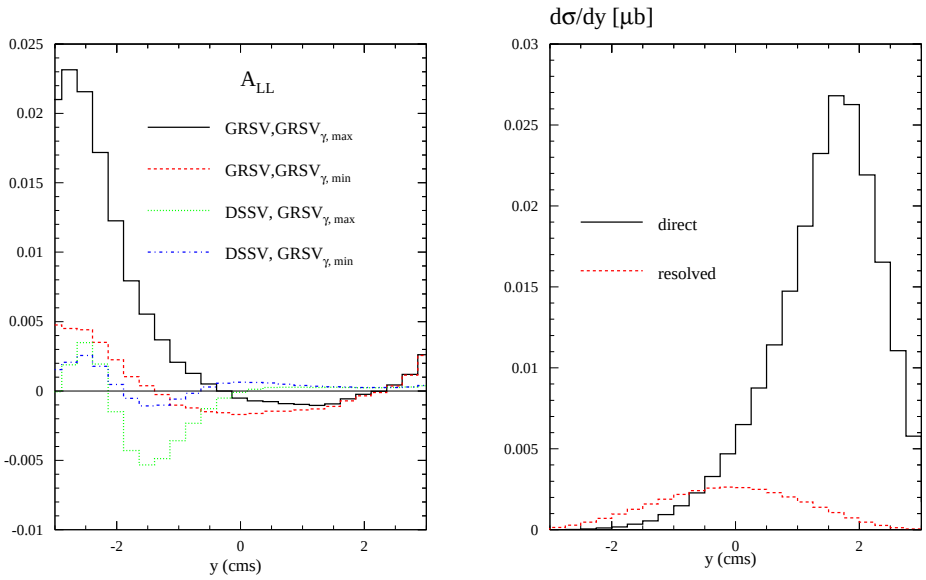

Figure 5.44: Left Plot: A_{LL} for the eRHIC scenario described in the text for different polarised parton distribution functions. Right Plot: direct and resolved contribution to the unpolarised cross section.

PDFs by computing the ratio of the cross sections shown in figures 5.36, 5.39 and 5.40 for $E_D < 30\,\text{GeV}$. Note that we have presented the results in figure 5.36 with a smaller bin size than in figure 5.43. To resolve the differences in A_{LL} obtained with the DSSV and GRSV PDFs, which mainly stem from Δg, an experimental precision of at least $\delta A_{LL} \simeq 0.02$ needs to be achieved.

We also compare NLO and LO estimates of A_{LL} for both sets of helicity PDFs in the lower panel of figure 5.43 and find rather different patterns depending on p_T^D. At small p_T^D, the NLO A_{LL} is about a factor of two larger than the LO estimate for the DSSV set whereas a reduction by roughly the same amount is found with the GRSV PDFs. This illustrates that any approximations for the spin asymmetry, either to assume a cancellation of NLO corrections or a constant pattern independent of the choice of PDFs, are not justified and should not be used for analysing data. Again, only a global analysis will lead to consistent results. Qualitatively very similar results have been obtained for other cuts on the energy E_D of the observed D meson, $30 \leq E_D \leq 50\,\text{GeV}$ and $E_D > 50\,\text{GeV}$.

With our method we have established the basic framework to include the open charm measurement of COMPASS in one of the next global QCD analyses of polarised parton density functions. Therefore, we refrain here from presenting a special value for $\Delta g/g$. Anyway, this would only be a rough estimate as this ratio is not constant. Only a global fit can give a reliable result.

5.4.2 Outlook to a possible future collider: eRHIC

eRHIC [27, 46] is proposed as a successor project of RHIC. At eRHIC, electrons shall be collided with a 250 GeV proton beam [212] or a correspondingly less energetic beam of nuclei. For the electrons different energy scenarios (e.g., 4 GeV, 10 GeV and 20 GeV)

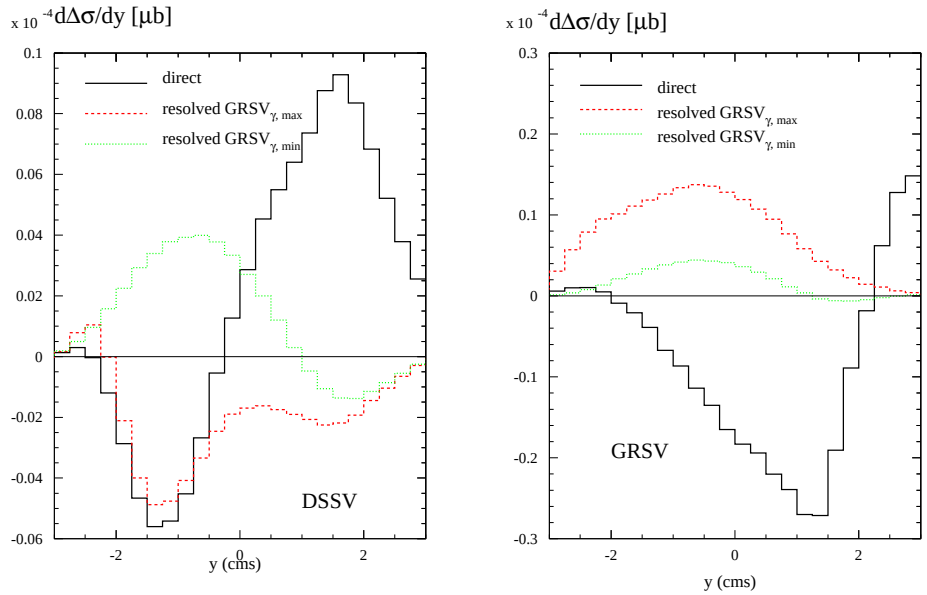

Figure 5.45: The polarised cross section for eRHIC using different models for the polarised and for the photon parton distributions.

are proposed. We have, therefore, performed a first exploratory study in which we focus on rapidity differential cross sections and give here the preliminary results. We show in our plots the cross sections differential in the rapidity of a detected D meson in the c.m.s. of the incoming particles. It is related to the rapidity in the laboratory frame by a simple additional constant. We focus on the case of 4 GeV electrons and charm production. For simplicity we have chosen the scale to be $\mu^2 = m^2 + \frac{p_{T,1}^2 + p_{T,2}^2}{2}$ in our plots. $p_{T,1}$ and $p_{T,2}$ denote here the transverse momenta of the produced heavy charm and anticharm, respectively. The electron flies into the positive direction. Furthermore we choose $Q^2_{max} = 0.01$ GeV^2. On the l.h.s. of figure 5.44 we present the results of our calculation for the spin asymmetry A_{LL} for four models of polarised parton distribution functions. For the proton, we use the DSSV and the GRSV(std) models. The polarised quark and gluon content of the photon is obtained by the GRSV$_\gamma$ sets in its maximum and minimum scenarios. Already from this figure one can see that the resolved part comes largely into play at eRHIC. For the unpolarised parton distribution functions, we have used CTEQ6M. To study the contributions of the direct and resolved part in more detail, we focused on the direct and resolved part separately. The r.h.s. of figure 5.44 shows the unpolarised contributions. Although generally the resolved contribution is less important than the direct part, our figure indicates that kinematical regions can be found in which the resolved part dominates already for the unpolarised case.

Figure 5.45 shows the resolved and the direct contributions to the polarised cross section using the same models for the parton distributions as in the left part of figure 5.44. Here the importance of the resolved part gets obvious. It is in most kinematic regions in the order of the direct part. This figure shows also the sensitivity of the resolved part to the chosen set of GRSV$_\gamma$. As a consequence, A_{LL} is also sensitive to the polarised hadronic content of the photon. This might give a possibility of constraining in future the hadronic component of polarised photons. A calculation with only the direct part would not be meaningful. Although not shown here, for higher electron energies as well as for bottom production, our results indicate that the

resolved part becomes still more important for these scenarios.

Summarising, especially in the polarised case, where we use the DSSV and GRSV(std) parton density functions, the resolved part turns out to give sizable corrections for eRHIC, whereas in the COMPASS case the resolved photon part was nearly negligible over the whole kinematic range. We will not discuss eRHIC any further as not all experimental details for eRHIC are clear at the moment. More calculations for eRHIC will come up, when the eRHIC project gets more concrete and when also more details of the detection possibilities of the charm and/or bottom quarks are clarified: it could be that the quarks are detected directly with micro-vertex detectors or the mesons produced during hadronisation can be seen – or, like currently at RHIC and COMPASS – their decay particles.

Altogether we emphasise again that the smallness of the resolved part at COMPASS is only due to the relatively small energy of that experiment. At experiments at higher c.m.s. energies the resolved part cannot be neglected anymore.

6

Summary and conclusions

Heavy flavour hadroproduction is important for spin physics. The partonic hard scattering processes differ from their counterparts for light hadron and jet production utilised in global QCD analyses so far. Existing and upcoming measurements of heavy flavour production, e.g., at CERN-COMPASS and BNL-RHIC further our current understanding of factorisation in the presence of spin and test the notion of universality for helicity dependent parton densities.

In this thesis, we have studied heavy quark hadro- and photoproduction in detail and examined the possibilities of using heavy quark production for the extraction of the polarised parton distribution functions. All calculations are performed at $\mathcal{O}(\alpha_s^3)$ and $\mathcal{O}(\alpha\alpha_s^2)$ accuracy, respectively, and theoretical uncertainties due to the choice of scales $\mu_{f,r}$ and the heavy quark mass m_Q have been discussed in detail. Based on our theoretical results we have presented detailed phenomenological studies for the existing PHENIX and STAR experiments at BNL-RHIC and the COMPASS experiment at CERN. Predictions have been made for possible future experiments at a low-energy antiproton-proton collider at GSI-FAIR, a proton-proton collider at J-PARC and an upcoming high-energy electron-ion collider (EIC).

The most important results of this thesis can be summarised as follows:

After the introduction we have reviewed the ingredients of a perturbative QCD calculation and discussed their application to the production of heavy quarks. Especially, the differences between the hadronisation for heavy and light quarks have been pointed out, and the phenomenological parametrisations used in our numerical studies have been introduced.

Next, we have described the necessary steps and ingredients to arrive at a cross section for heavy quark production at next-to-leading order accuracy. We have devised two different methods for the evaluation of the relevant phase-space integrations. For single-inclusive distributions, such as transverse momentum spectra of a produced heavy quark, all angular integrals can be performed with largely analytical methods. However, studies of phenomenologically interesting heavy quark correlations, the implementation of experimental acceptance cuts as well as the hadronisation of the produced heavy quarks require control over all final-state partons and hence need a numerical implementation for phase-space integrations. The development of flexible parton-level Monte Carlo programs for polarised heavy quark hadro- and photoproduction is the main result of this thesis. These programs allow one to compute any infrared-safe heavy flavour distribution or correlation at NLO accuracy in longitudinally polarised collisions, including experimental acceptance cuts as well as the details

of hadronisation and subsequent decay of the heavy quarks. Details of the computation of the relevant partonic subprocesses at leading and next-to-leading order both for hadro- and photoproduction can be found in chapter 4.

Finally, in chapter 5, our various phenomenological results have been presented and discussed elaborately and compared to the experimental results available at the moment. A comparison of the results obtained with the analytical and the numerical methods of phase space integration is presented in section 5.1. In the range of statistical fluctuations, the analytical and the numerical methods agree very well. As both program sets have been developed independently of each other, this serves as an important cross check for the correctness of both implementations.

Eventually, sections 5.2 to 5.4 are devoted to a detailed presentation and discussion of various phenomenological results obtained with our numerical programs. First we performed a study of the physics opportunities with open charm production at low c.m.s. energy $\bar{p}p$ and pp collisions at GSI-FAIR and J-PARC, respectively, including unpolarised and polarised cross sections and charge and spin asymmetries. The charge asymmetry vanishes at $\mathcal{O}(\alpha_s^2)$ and hence is a clear probe of non-trivial QCD dynamics beyond tree-level. In general, theoretical uncertainties turn out to be significant at low c.m.s. energies, except for the mass dependence of the charge asymmetries A_C and ΔA_C.

Using our Monte Carlo program, we have moreover performed a comprehensive phenomenological study of various observables at RHIC where heavy quarks are identified through their semi-leptonic decays into electrons or muons. In general, we expect the double spin asymmetry A_{LL} to be very small – especially if only one of the final heavy quarks is observed. We find that decay lepton correlations are particularly suited probes for the spin structure of the nucleon, and experimentally relevant double-spin asymmetries of about one percent can be expected.

Phenomenological studies of photoproduction of heavy quarks at COMPASS have shown that the spin asymmetry A_{LL} at NLO differs significantly from LO estimates. The resolved photon contribution turns out to be negligible at COMPASS.

Our flexible Monte-Carlo code for polarised hadro- and photoproduction of heavy quarks will be very useful to estimate and eventually analyse various observables for future experiments such as an electron-ion collider. Some of these studies are potentially relevant for the detector design, i.e., for optimising the sensitivity to detect heavy flavours in regions of phase space where most of the heavy quarks are produced. A brief outlook on photoproduction at an EIC has been given at the end of chapter 5. Here, resolved photons contribute more significantly than at fixed target kinematics.

Avenues for future research are the extension of the Monte Carlo code to electroproduction of heavy flavours where the virtuality Q^2 of the exchanged photon significantly complicates the calculations. Results in the polarised case are so far only available at LO accuracy of QCD. In addition, the inclusion of resummations of potentially large threshold logarithms to all orders might be relevant for reliable analyses at fixed target kinematics. Future measurements of heavy quark observables both at colliders and at fixed target experiments will for sure further our knowledge of the nucleon structure. In particular, the helicity gluon density and the Monte Carlo program developed in this thesis will be an important tool in phenomenological studies.

A

Feynman rules

In this part the Feynman rules for the calculation of matrix elements iM are summed up [213]. Quark, gluon and ghost lines are represented by solid, curled and dotted lines, respectively. The colour indices are i, j for quarks and a, b, c, d for gluons and ghosts. Flavour and spinor indices are not noted explicitly.

For external lines the rules are (the momentum flows in each case from left to right):

incoming lines

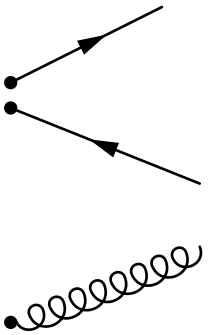

$u(p,h)$

$\bar{v}(p,h)$

$\epsilon_\mu(q,\lambda)$

outgoing lines

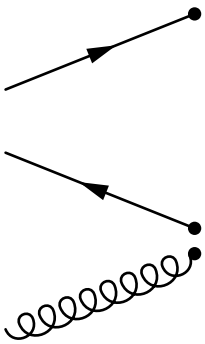

$\bar{u}(p,h)$

$v(p,h)$

$\epsilon^*_\mu(q,\lambda)$

$u(p,h)$ and $v(p,h)$ are the spinors of quarks and antiquarks, respectively, with momentum p and helicity h; $\epsilon_\mu(p,\lambda)$ is the polarisation vector of the gluon.

The propagators read

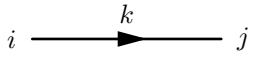

$$i\delta_{ij}\frac{\not{k}+m}{k^2-m^2+i\epsilon}$$

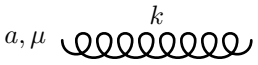

$$\frac{-i\delta_{ab}}{k^2+i\epsilon}\left[g_{\mu\nu}-(1-\xi)\frac{k_\mu k_\nu}{k^2}\right]$$

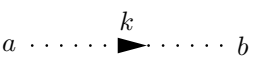

$$\frac{-i\delta_{ab}}{k^2+i\epsilon}$$

k is the momentum of the appropriate particle; the short notation $\not{k} = k_\mu \gamma^\mu$ is used. The parameter ξ in the gluon propagator is gauge dependent; in this thesis the Feynman gauge with $\xi = 1$ is used.

The Lagrangian gives the following rules for the vertices:

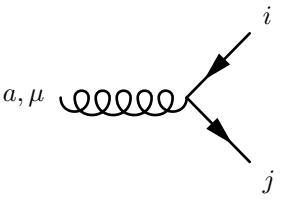

$$-ig\gamma_\mu T^a_{ij}$$

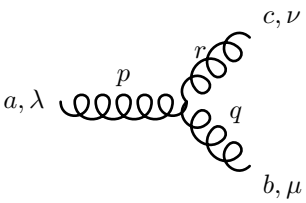

$$-gf^{abc}[(p-q)_\nu g_{\lambda\mu} + (q-r)_\lambda g_{\mu\nu} + (r-p)_\mu g_{\nu\lambda}]$$

(the momenta p, q and r are outgoing)

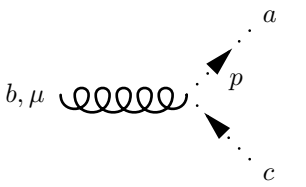

$$gf^{abc}p_\mu$$

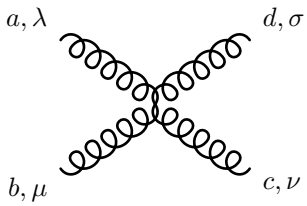

$$-ig^2 f^{abe} f^{cde}(g_{\lambda\nu}g_{\mu\sigma} - g_{\lambda\sigma}g_{\mu\nu})$$
$$-ig^2 f^{ace} f^{bde}(g_{\lambda\mu}g_{\nu\sigma} - g_{\lambda\sigma}g_{\mu\nu})$$
$$-ig^2 f^{ade} f^{cbe}(g_{\lambda\nu}g_{\mu\sigma} - g_{\lambda\mu}g_{\sigma\nu})$$

Furthermore, for a closed fermion and ghost loop the matrix element has to be multiplied by (-1) .

In each closed loop, one integrates over the undetermined momentum with the measure

$$\int \frac{d^n k}{(2\pi)^n}.$$

For possible permutations one has to include the appropriate symmetry factor.

To calculate cross sections, $|M|^2 = MM^*$ is needed. Here, one gets products of projection operators for particles with definite helicity, which can be rewritten by:

$$u(p,\lambda)\bar{u}(p,\lambda) = \frac{1}{2}(\not{p} + m)(1 - \gamma_5 \lambda), \tag{A.1}$$

$$v(p,\lambda)\bar{v}(p,\lambda) = \frac{1}{2}(\not{p} - m)(1 + \gamma_5 \lambda), \tag{A.2}$$

$$\epsilon^\mu(q,\lambda)\epsilon^{\nu *}(q,\lambda) = \frac{1}{2}\left[-g_{\mu\nu} + \frac{q^\mu r^\nu + q^\nu r^\mu}{q\cdot r} + i\lambda\epsilon^{\mu\nu\sigma\kappa}\frac{q_\sigma r_\kappa}{q\cdot r}\right], \tag{A.3}$$

where r is an arbitrary momentum satisfying $r^2 = 0$ and $q \cdot r \neq 0$. Additional Feynman rules for photons can be found in [52].

B

Detailed Results of the expansion for $x \to 1$ and $y \to \pm 1$

Here, we give some detailed results for the hadro- and photoproduction of heavy quarks in the limits mentioned in the title of this appendix. The results for hadro- and photoproduction are also listed in [71] and in [72], respectively for the unpolarised case. The polarised case can be obtained by replacing there the unpolarised matrix elements and splitting functions with their polarised counterparts. For completeness, some formulas already given in chapters 3 and 4 are repeated.

B.1 Case $x \to 1$

In the case $x \to 1$ one encounters the soft limit. The flux factor $1/(2s)$ is included in the matrix element. We start with the soft part for hadroproduction:

$$|[\Delta]M^s_{gg}|^2_R = \frac{1}{2s}[\Delta]E_\varepsilon^2 g^6 \frac{1}{2(N_C^2-1)}[(2C_F)^2[\Delta]D^{\rm soft}_{\rm QED} + C_A^2[\Delta]D^{\rm soft}_{\rm OQ} + [\Delta]D^{\rm soft}_{\rm KQ}]. \quad \text{(B.1)}$$

Here is

$$[\Delta]D^{\rm soft}_{\rm QED} = -2\left[\frac{m^2}{s_4^2} + \frac{m^2}{s_3^2} + \frac{2m^2-s}{s_3 s_4}\right][\Delta]B_{\rm QED}, \quad \text{(B.2)}$$

$$[\Delta]D^{\rm soft}_{\rm OQ} = 2\left[\frac{2m^2-s}{s_3 s_4} + \frac{t_1^2+u_1^2}{st'u'} + \frac{2m^2 t_1 u_1}{s^2}\left(\frac{1}{s_4^2}+\frac{1}{s_3^2}\right) + \frac{t_1^2 u_1}{s^2}\left(\frac{1}{t's_4}+\frac{1}{s_3 u'}\right) + \frac{t_1 u_1^2}{s^2}\left(\frac{1}{s_4 u'}+\frac{1}{s_3 t'}\right)\right][\Delta]B_{\rm QED}, \quad \text{(B.3)}$$

$$[\Delta]D^{\rm soft}_{\rm KQ} = -2\left[\frac{2(m^2-s)}{s_3 s_4}\left(1+\frac{t_1 u_1}{s^2}\right) + \frac{2m^2 t_1 u_1}{s^2}\left(\frac{1}{s_4^2}+\frac{1}{s_3^2}\right) + t_1\left(\frac{1}{s_4 u'}+\frac{1}{s_3 t'}\right) + u_1\left(\frac{1}{t's_4}+\frac{1}{s_3 u'}\right)\right][\Delta]B_{\rm QED}, \quad \text{(B.4)}$$

$$|[\Delta]M^{\rm LO}_{gg}|^2 = \frac{1}{2s}g^4\frac{1}{2(N_C^2-1)}\left[2C_F - 2C_A\frac{t_1 u_1}{s^2}\right][\Delta]E_\varepsilon^2[\Delta]B_{\rm QED} + \mathcal{O}(\varepsilon^3) \quad \text{(B.5)}$$

with

$$B_{\mathrm{QED}} = \frac{t_1}{u_1} + \frac{u_1}{t_1} + \frac{4m^2 s}{t_1 u_1}\left(1 - \frac{m^2 s}{t_1 u_1}\right) - 2\varepsilon\left(\frac{s^2}{t_1 u_1} - 1\right) + \varepsilon^2 \frac{s^2}{t_1 u_1} \tag{B.6}$$

and

$$\Delta B_{\mathrm{QED}} = \left(\frac{t_1}{u_1} + \frac{u_1}{t_1}\right)\left(\frac{2m^2 s}{t_1 u_1} - 1\right). \tag{B.7}$$

In the $q\bar{q}$ case we get:

$$|[\Delta] M^s_{q\bar{q}}|^2_R = \frac{1}{2s} g^6 \frac{C_F}{4N_C} [2C_F [\Delta] O^{\mathrm{soft}}_{\mathrm{QED}} + C_A [\Delta] O^{\mathrm{soft}}_{\mathrm{OK}}] \tag{B.8}$$

with

$$[\Delta] O^{\mathrm{soft}}_{\mathrm{QED}} = 8\left[\frac{s}{t'u'} + \frac{2t_1}{t's_3} + \frac{2t_1}{u's_4} - \frac{2u_1}{t's_4} - \frac{2u_1}{u's_3} + \frac{s - 2m^2}{s_3 s_4} - \frac{m^2}{s_3^2} - \frac{m^2}{s_4^2}\right][\Delta] A_{\mathrm{QED}} \tag{B.9}$$

and

$$[\Delta] O^{\mathrm{soft}}_{\mathrm{OK}} = 8\left[-\frac{s}{t'u'} - \frac{t_1}{t's_3} - \frac{t_1}{u's_4} + \frac{2u_1}{t's_4} + \frac{2u_1}{u's_3} - \frac{s - 2m^2}{s_3 s_4}\right][\Delta] A_{\mathrm{QED}} \tag{B.10}$$

with

$$A_{\mathrm{QED}} = \frac{t_1^2 + u_1^2}{s^2} + \frac{2m^2}{s} - \varepsilon \tag{B.11}$$

and

$$\Delta A_{\mathrm{QED}} = -\frac{t_1^2 + u_1^2}{s^2} - \frac{2m^2}{s} - \varepsilon. \tag{B.12}$$

Now, we will give the soft result for photoproduction. As in LO only photon–gluon fusion is possible, there is only this process which can get soft:

$$|[\Delta] M^s_{\gamma g}|^2_R = \frac{1}{2s} E_\varepsilon^2 g^4 e^2 [2C_F [\Delta] S^{\mathrm{soft}}_{\mathrm{QED}} + C_A [\Delta] S^{\mathrm{soft}}_{\mathrm{OK}}] \tag{B.13}$$

with

$$S^{\mathrm{soft}}_{\mathrm{QED}} = \left[-2m^2\left(\frac{1}{s_4^2} + \frac{1}{s_3^2}\right) - \frac{2(2m^2 - s)}{s_3 s_4}\right][\Delta] B_{\mathrm{QED}} \tag{B.14}$$

and

$$S^{\mathrm{soft}}_{\mathrm{OK}} = \left[\frac{2}{t'}\left(\frac{t_1}{s_3} + \frac{u_1}{s_4}\right) + \frac{2(2m^2 - s)}{s_3 s_4}\right][\Delta] B_{\mathrm{QED}}. \tag{B.15}$$

The integrals used for the integration of the soft phase space are defined by

$$I(vw) = \int dy d\theta_2 (1 - y^2)^{-1-\varepsilon} \sin^{-2\varepsilon} \theta_2 4t'u'(vw)\big|_{x=1}. \tag{B.16}$$

The results of them are

$$I\left(\frac{2s}{t'u'}\right) = -\frac{8\pi s}{\varepsilon}, \tag{B.17}$$

$$I\left(\frac{2u_7}{s_4u'}\right) = 4\pi s\left(-\frac{1}{2}\varepsilon\log^2\left(\frac{\beta+1}{1-\beta}\right) + \log\left(-\frac{t_1}{m^2}\right) + \log\left(-\frac{t_1}{s}\right)\right.$$
$$-2\varepsilon\log\left(-\frac{2t_1}{(1-\beta)s}\right)\log\left(-\frac{2t_1}{(\beta+1)s}\right) - 2\varepsilon\mathrm{Li}_2\left(\frac{2t_1}{(1-\beta)s}+1\right) -$$
$$\left.2\varepsilon\mathrm{Li}_2\left(\frac{2t_1}{(\beta+1)s}+1\right) - \frac{1}{\varepsilon}\right), \quad \text{(B.18)}$$

$$I\left(\frac{2u_6}{t's_4}\right) = 4\pi s\left(-\frac{1}{2}\varepsilon\log^2\left(\frac{\beta+1}{1-\beta}\right) + \log\left(-\frac{u_1}{m^2}\right) + \log\left(-\frac{u_1}{s}\right)\right.$$
$$-2\varepsilon\log\left(-\frac{2u_1}{(1-\beta)s}\right)\log\left(-\frac{2u_1}{(\beta+1)s}\right) - 2\varepsilon\mathrm{Li}_2\left(\frac{2u_1}{(1-\beta)s}+1\right)$$
$$\left.-2\varepsilon\mathrm{Li}_2\left(\frac{2u_1}{(\beta+1)s}+1\right) - \frac{1}{\varepsilon}\right), \quad \text{(B.19)}$$

$$I\left(\frac{2u_1}{u's_3}\right) = I\left(\frac{2u_6}{t's_4}\right), \quad \text{(B.20)}$$

$$I\left(\frac{t_1}{t's_3}\right) = I\left(\frac{2u_7}{s_4u'}\right), \quad \text{(B.21)}$$

$$I\left(\frac{4m^2}{s_4^2}\right) = 8\pi s\left(\frac{\varepsilon\log\left(\frac{\beta+1}{1-\beta}\right)}{\beta}+1\right), \quad \text{(B.22)}$$

$$I\left(\frac{4m^2}{s_3^2}\right) = I\left(\frac{4m^2}{s_4^2}\right), \quad \text{(B.23)}$$

$$I\left(\frac{2(s_5-2m^2)}{s_4s_3}\right) = \frac{8\pi s}{\beta}\left(1-\frac{2m^2}{s}\right)s\left(\log\left(\frac{\beta+1}{1-\beta}\right)+\varepsilon\left(\mathrm{Li}_2\left(\frac{2\beta}{\beta+1}\right)-\mathrm{Li}_2\left(-\frac{2\beta}{1-\beta}\right)\right)\right). \quad \text{(B.24)}$$

Note that Li_2 denotes the dilogarithmic function.

B.2 Case $y \to \pm 1$

We start again with hadroproduction: The limits $y \to \pm 1$ give

$$\lim_{y\to\pm1}[\Delta]M^{(real)}(s,t_k,u_k,q_1,q_2) = \lim_{y\to\pm1}\frac{[\Delta]f(x,y=\pm1,\theta_1,\theta_2)}{s^2(1-x)^2(1-y^2)} =$$
$$\frac{[\Delta]f_1^{c\pm}(x,y=\pm1,\theta_1,\theta_2)}{s^2(1-x)^2(1-y^2)} + \frac{[\Delta]f_2^{c\pm}(x,y=\pm1,\theta_1,\theta_2)}{s^2(1-x)^2(1-y^2)} \quad \text{(B.25)}$$

with

$$\frac{[\Delta]f_{gg,1}^{c+}(x,y=+1,\theta_1,\theta_2)}{s^2(1-x)^2(1-y^2)} = -\frac{2g^2}{u'}[\Delta]M_{gg}^b(xk_1,k_2,p_1)[\Delta]\tilde{P}_{gg}(x) \quad \text{(B.26)}$$

and

$$\frac{f_{gg,2}^{c+}(x,y=1,\theta_1,\theta_2)}{s^2(1-x)^2(1-y^2)} = \frac{g^6}{8s(1-\varepsilon)^2}\cdot$$
$$\frac{16m^2\left(\cos^2(\theta_1)-1\right)\left(2(\varepsilon-1)\cos^2(\theta_2)+1\right)\beta_x^2\left(9\cos^2(\theta_1)\beta_x^2+7\right)}{s^2x^2(1-y)\left(\cos^2(\theta_1)\beta_x^2-1\right)^2} \quad \text{(B.27)}$$

and

$$\frac{\Delta f^{c+}_{gg,2}(x, y = \pm 1, \theta_1, \theta_2)}{s^2(1-x)^2(1-y^2)} = 0. \tag{B.28}$$

In the polarised case the second part gives zero and the first part shows up with the same structure. For $d\sigma^{c-}$ one gets the analogous expressions after an interchange of the momenta, i.e., y has to be changed to $-y$. Furthermore, one gets

$$[\Delta] f^{(c-)}_{gq} = 8g^2 s(1-x)[\Delta] M^{(b)}_{qq}(k_1, xk_2, p_1)[\Delta]\tilde{P}_{qg}(x), \tag{B.29}$$

$$[\Delta] f^{(c+)}_{qg,1} = 8g^2 s(1-x)[\Delta] M^{(b)}_{gg}(xk_1, k_2, p_1)[\Delta]\tilde{P}_{gq}(x) \tag{B.30}$$

and

$$\frac{f^{c+}_{qg,2}(x, y = 1, \theta_1, \theta_2)}{s^2(1-x)^2(1-y^2)} = \frac{g^6}{18s(1-\varepsilon)} \cdot \frac{16m^2 \left(\cos^2(\theta_1) - 1\right) \left(2(\varepsilon - 1)\cos^2(\theta_2) + 1\right) \beta_x^2 \left(9\cos^2(\theta_1)\beta_x^2 + 7\right)}{s^2 x^2 (1-y) \left(\cos^2(\theta_1)\beta_x^2 - 1\right)^2} \tag{B.31}$$

and

$$\frac{\Delta f^{c\pm}_{qg,2}(x, y = \pm 1, \theta_1, \theta_2)}{s^2(1-x)^2(1-y^2)} = 0. \tag{B.32}$$

Note that in the polarised case the contribution $\Delta f^{c\pm}_{xx,2}$ vanishes always. In the $q\bar{q}$ case one has:

$$[\Delta] f^{(c+)}_{q\bar{q}} = 8g^2 s(1-x)[\Delta] M^{(b)}_{q\bar{q}}(xk_1, k_2, p_1)[\Delta]\tilde{P}_{qq}(x) \tag{B.33}$$

and

$$[\Delta] f^{(c-)}_{q\bar{q}} = 8g^2 s(1-x)[\Delta] M^{(b)}_{q\bar{q}}(k_1, xk_2, p_1)[\Delta]\tilde{P}_{qq}(x) \tag{B.34}$$

where the splitting functions are given by [117, 201]

$$P_{qq}(z) = C_F \left[\frac{2}{[1-z]_+} - 1 - z - \varepsilon(1-z) + \frac{3+\varepsilon}{2}\delta(1-z) \right], \tag{B.35}$$

$$P_{gq}(z) = C_F \frac{1 + (1-z)^2)}{z} - \varepsilon C_F z, \tag{B.36}$$

$$P_{qg}(z) = \frac{1}{2}\left[z^2 + (1-z)^2\right] - \varepsilon z(1-z), \tag{B.37}$$

$$P_{gg}(z) = 2C_A \left[\frac{z}{[1-z]_+} + \frac{1-z}{z} + z(1-z) \right] + \frac{\beta_0}{2}\delta(1-z). \tag{B.38}$$

In the polarised case one has [120, 121]

$$\Delta P_{qq}(z) = C_F \left[\frac{2}{[1-z]_+} - 1 - z + 3\varepsilon(1-z) + \frac{3+\varepsilon}{2}\delta(1-z) \right], \tag{B.39}$$

$$\Delta P_{qg}(z) = \frac{1}{2}\left[2z - 1 - 2\varepsilon(1-z)\right], \tag{B.40}$$

$$\Delta P_{gq}(z) = C_F \left[2 - z + 2\varepsilon(1-z)\right], \tag{B.41}$$

$$\Delta P_{gg}(z) = 2C_A \left[\frac{1}{[1-z]_+} - 2z + 1 + 2\varepsilon(1-z) \right] + \left(\frac{\beta_0}{2} + \frac{N_C}{6}\varepsilon \right)\delta(1-z). \tag{B.42}$$

Note that for our purposes the usual plus distribution has to be rewritten to the rho distribution defined in chapter 3. Note that in this notation $\beta_0 = \beta_1$.

The singularities remaining after the angle integration over θ_1 and θ_2 are cured by mass factorisation.

Now, we turn to photoproduction of heavy quarks. We give only some short additional remarks as the procedure is very similar to hadroproduction. We note again that non vanishing-parts of $f^{c\pm}_{xx,2}$ only occur in the unpolarised case, e.g.,

$$\frac{f^{c-}_{\gamma g,2}(x, y=-1, \theta_1, \theta_2)}{s^2(1-x)^2(1-y^2)} = \frac{g^4 e_Q^2}{s(1-\varepsilon)^2} \cdot \frac{(-192(-1+\cos^2(\theta_1))(-1+\cos^2(\theta_2)(2+\varepsilon))m^2(4m^2-sx))}{(sx^2(sx+\cos^2(\theta_1)(4m^2-sx))^2(1+y))}. \quad \text{(B.43)}$$

They can be obtained by an expansion of the full matrix element in y.

Furthermore, we get

$$f^{c+}_{\gamma q} = 32\pi\alpha_{em} e_q^2 s(1-x)[\Delta]\tilde{P}_{q\gamma}(x)[\Delta]M^{(b)}_{q\bar{q}}(xk_1, k_2, p_1) \quad \text{(B.44)}$$

and

$$f^{c-}_{\gamma q,1} = 32\pi\alpha_s s(1-x)[\Delta]\tilde{P}_{gq}(x)[\Delta]M^{(b)}_{\gamma g}(k_1, xk_2, p_1); \quad \text{(B.45)}$$

in the unpolarised case only $f^{c-}_{\gamma q,2}$ does not vanish and is identical to $f^{c-}_{\gamma g,2}$ after the multiplication with C_F/C_A,

where

$$[\Delta]P_{q\gamma}(x) = [\Delta]\frac{N_c}{2}P_{qg}(z). \quad \text{(B.46)}$$

Finally, we mention that

$$\Delta P_{qq}(x) = \Delta P_{\bar{q}\bar{q}}(x) = P_{qq}(x) + P^{\mathrm{HVBM}}(x) \quad \text{(B.47)}$$

with [120]

$$P^{\mathrm{HVBM}}(x) = -2C_F(n-4)(1-x). \quad \text{(B.48)}$$

The term with the index HVBM is needed in order to cure the helicity violation introduced by the HVBM scheme [102, 154].

It occurs at the qqg vertex due to the commuting γ_5 parts in the extra $n-4$ dimensions. These unphysical remnants of the HVBM scheme can be subtracted with the poles. With this method, helicitiy conservation can be restored.

Due to helicity conservation, the longitudinally polarised cross section for quark-antiquark annihilation processes is the negative of its unpolarised counterpart:

$$\frac{\sigma_{q\bar{q}}}{\Delta\sigma_{q\bar{q}}} = -1. \quad \text{(B.49)}$$

Furthermore, we have used

$$C_F = \frac{4}{3},\ N_C = 3,\ T_f = T_R n_f = \frac{1}{2}n_f,\ \beta_1 = \frac{11}{3}N_C - \frac{4}{3}T_f\ . \quad \text{(B.50)}$$

Bibliography

[1] E. Rutherford, *The scattering of α and β particles by matter and the structure of the atom*, Phil. Mag. **21** (1911) 669–688.

[2] J. Chadwick, *Possible existence of a neutron*, Nature **129** (1932) 312.

[3] M. Breidenbach *et al.*, *Observed Behavior of Highly Inelastic Electron-Proton Scattering*, Phys. Rev. Lett. **23** (1969) 935–939.

[4] E. D. Bloom *et al.*, *High-Energy Inelastic e p Scattering at 6-Degrees and 10-Degrees*, Phys. Rev. Lett. **23** (1969) 930–934.

[5] J. I. Friedman and H. W. Kendall, *Deep inelastic electron scattering*, Ann. Rev. Nucl. Part. Sci. **22** (1972) 203–254.

[6] S. F. Novaes, *Standard model: An Introduction*, `arXiv:hep-ph/0001283`.

[7] M. Passera, W. J. Marciano, and A. Sirlin, *The muon $g-2$ discrepancy: errors or new physics?*, AIP Conf. Proc. **1078** (2009) 378–381, `arXiv:0809.4062`.

[8] J. Louis, T. Mohaupt, and S. Theisen, *String theory: An overview*, Lect. Notes Phys. **721** (2007) 289–323.

[9] M. M. Nojiri *et al.*, *Physics Beyond the Standard Model: Supersymmetry*, `arXiv:0802.3672`.

[10] T. Yanir, *Phenomenological constraints on extended quark sectors*, JHEP **06** (2002) 044, `arXiv:hep-ph/0205073`.

[11] M. S. Chanowitz, *Bounding CKM Mixing with a Fourth Family*, Phys. Rev. **D79** (2009) 113008, `arXiv:0904.3570`.

[12] M. Bobrowski, A. Lenz, J. Riedl, and J. Rohrwild, *How much space is left for a new family of fermions?*, Phys. Rev. **D79** (2009) 113006, `arXiv:0902.4883`.

[13] M. Bobrowski, A. Lenz, J. Riedl, and J. Rohrwild, *$D-\bar{D}$ mixing in the framework of the HQE revisited*, `arXiv:0904.3971`.

[14] M. Bobrowski, A. Lenz, J. Riedl, and J. Rohrwild, *How Large Can the SM Contribution to CP Violation in $D^0-\bar{D}^0$ Mixing Be?*, JHEP **1003** (2010) 009, `arXiv:1002.4794`.

[15] O. Eberhardt, G. Herbert, H. Lacker, A. Lenz, A. Menzel, *et al.*, *Impact of a Higgs boson at a mass of 126 GeV on the standard model with three and four fermion generations*, Phys. Rev. Lett. **109** (2012) 241802, `arXiv:1209.1101`.

[16] A. Lenz, *Constraints on a fourth generation of fermions from Higgs Boson searches*, Adv. High Energy Phys. **2013** (2013) 910275.

[17] A. Frawley *et al.*, *Heavy Flavor Working Group Report of RHIC II Science Workshop*, `http://www.bnl.gov/physics/rhicIIscience`.

[18] PHENIX Collaboration, X. Wang, *Longitudinal Double Spin Asymmetries in Heavy Flavor Production in Polarized $p+p$ Collisions at $\sqrt{s}=200$ GeV*, AIP Conference Proceedings **1149** (2008) 393, Proceedings of the 18th Spin Physics Symposium.

[19] R. Hans, *Probing the spin structure of the proton via heavy flavor and hyperon measurements at PHENIX*, J. Phys. G: Nucl. Part. Phys. **36** (2009) 064045.

[20] COMPASS Collaboration, M. Alekseev *et al.*, *Direct Measurement of the Gluon Polarisation in the Nucleon via Charmed Meson Production*, `arXiv:0802.3023`.

[21] COMPASS Collaboration, M. Alekseev *et al.*, *Gluon polarisation in the nucleon and longitudinal double spin asymmetries from open charm muoproduction*, Phys. Lett. **B676** (2009) 31–38, `arXiv:0904.3209`.

[22] COMPASS Collaboration, C. Adolph *et al.*, *Measurement of the Cross Section for High-p_T Hadron Production in Scattering of 160 GeV/c Muons off Nucleons*, `arXiv:1207.2022`.

[23] GSI-PAX Collaboration, P. Lenisa, and F. Rathmann (spokesperson) *et al.*, Technical Proposal, `hep-ex/0505054`, see also: F. Rathmann and P. Lenisa, in *Proceedings of the 16th International Spin Physics Symposium (SPIN 2004)*, Triest, Italy, 2004, `hep-ex/0412078`; P. Lenisa *et al.*, in *Proceedings of the 2nd High-Energy Physics Conference in Madagascar (HEP-MAD 04)*, Antananarivo, Madagascar, 2004, eConf **C0409272**, 014 (2004).
GSI-ASSIA Collaboration, R. Bertini (spokesperson) *et al.*, Technical Proposal, `http://www.gsi.de/documents/DOC-2004-Jan-152-1.ps`; GSI-ASSIA Collaboration, M. Maggiora, in *Proceedings of the Conference on Spin and Symmetry*, Prague, 2004, `hep-ex/0505011`.
GSI-PANDA Collaboration, U. Wiedner (spokesperson), Technical Progress Report, `http://www.gsi.de/fair/experiments/hesr-panda/index.html`.

[24] For information on the planned GSI-FAIR facility, see: `http://www.gsi.de/fair`.

[25] GSI-PAX Collaboration, P. Lenisa and F. Rathmann (spokespersons), Technical Proposal, 2005, `hep-ex/0505054`; update of the Technical Proposal, 2006, `http://www.fz-juelich.de/ikp/pax`.

[26] For information on the J-PARC facility, see: `http://j-parc.jp/index-e.html`.

[27] For information concerning the eRHIC/EIC projekt see: `http://www.bnl.gov/eic`.

[28] D. Boer, M. Diehl, R. Milner, R. Venugopalan, W. Vogelsang, *et al.*, *Gluons and the quark sea at high energies: Distributions, polarization, tomography*, `arXiv:1108.1713`.

[29] European Muon Collaboration (EMC), J. Ashman *et al.*, *An investigation of the spin structure of the proton in deep inelastic scattering of polarized muons on polarized protons*, Nucl. Phys. **B328** (1989) 1.

[30] D. de Florian, R. Sassot, M. Stratmann, and W. Vogelsang, *Global Analysis of Helicity Parton Densities and Their Uncertainties*, Phys. Rev. Lett. **101** (2008) 072001, `arXiv:0804.0422`.

[31] D. de Florian, R. Sassot, M. Stratmann, and W. Vogelsang, *Extraction of Spin-Dependent Parton Densities and Their Uncertainties*, Phys. Rev. **D80** (2009) 034030, `arXiv:0904.3821`.

[32] M. Burkardt, A. Miller, and W. D. Nowak, *Spin-polarized high-energy scattering of charged leptons on nucleons*, Rept. Prog. Phys. **73** (2010) 016201, arXiv:0812.2208.

[33] S. E. Kuhn, J. P. Chen, and E. Leader, *Spin Structure of the Nucleon – Status and Recent Results*, Prog. Part. Nucl. Phys. **63** (2009) 1–50, arXiv:0812.3535.

[34] R. L. Jaffe and A. Manohar, *The G_1 Problem: Fact and Fantasy on the Spin of the Proton*, Nucl. Phys. **B337** (1990) 509–546.

[35] M. Burkardt and H. BC, *Angular Momentum Decomposition for an Electron*, Phys. Rev. **D79** (2009) 071501, arXiv:0812.1605.

[36] B. L. G. Bakker, E. Leader, and T. L. Trueman, *A critique of the angular momentum sum rules and a new angular momentum sum rule*, Phys. Rev. **D70** (2004) 114001, arXiv:hep-ph/0406139.

[37] X.-D. Ji, *Gauge invariant decomposition of nucleon spin*, Phys. Rev. Lett. **78** (1997) 610–613, arXiv:hep-ph/9603249.

[38] A. Morreale [PHENIX Collaboration], talk presented at the "18th International Symposium on Spin Physics (SPIN 2008)", University of Virginia, Charlottesville, VA, October 6–11 2008; A. Kocoloski [STAR Collaboration], talk presented at the "18th International Symposium on Spin Physics (SPIN 2008)", University of Virginia, Charlottesville, VA, October 6–11 2008.

[39] PHENIX Collaboration, A. Adare *et al.*, *Inclusive cross section and double helicity asymmetry for π^0 production in $p+p$ collisions at $\sqrt{s} = 200\,GeV$: Implications for the polarized gluon distribution in the proton*, Phys. Rev. **D76** (2007) 051106, arXiv:0704.3599.

[40] PHENIX Collaboration, A. Adare *et al.*, *The polarized gluon contribution to the proton spin from the double helicity asymmetry in inclusive π^0 production in polarized $p+p$ collisions at $\sqrt{s} = 200\ GeV$*, Phys. Rev. Lett. **103** (2009) 012003, arXiv:0810.0694.

[41] STAR Collaboration, B. I. Abelev *et al.*, *Longitudinal double-spin asymmetry for inclusive jet production in $p+p$ collisions at $\sqrt{s} = 200\ GeV$*, Phys. Rev. Lett. **100** (2008) 232003, arXiv:0710.2048.

[42] PHENIX Collaboration, A. Adare *et al.*, *Inclusive cross section and double helicity asymmetry for π^0 production in $p+p$ collisions at $\sqrt{s} = 62.4\ GeV$*, Phys. Rev. **D79** (2009) 012003, arXiv:0810.0701.

[43] STAR Collaboration, C. A. Gagliardi, *Jet Production in Polarized pp Collisions at RHIC*, arXiv:0808.0858.

[44] STAR Collaboration, M. Sarsour, *Constraints on ΔG through Longitudinal Double Spin Asymmetry Measurements of Inclusive Jet Production in Polarized $p+p$ Collisions at 200 GeV*, AIP Conf. Proc. **1149** (2009) 389–392, arXiv:0901.4061.

[45] STAR Collaboration, P. Djawotho, *Gluon polarization measurements with inclusive jets at STAR*, arXiv:1106.5769.

[46] E. Aschenauer, A. Bazilevsky, K. Boyle, K. Eyser, R. Fatemi, *et al.*, *The RHIC Spin Program: Achievements and Future Opportunities*, arXiv:1304.0079, BNL, 2012, http://www.bnl.gov/npp/docs/RHIC-Spin-WriteUp-121105.pdf.

[47] C. Aidala *et al.*, *Research plan for spin physics at RHIC*, BNL formal report BNL-73798-2005 (Feb. 2005).

[48] HERMES Collaboration, P. Liebing, *Extraction of $\Delta g/g$ from HERMES data on inclusive charged hadrons*, AIP Conf. Proc. **915** (2007) 331–334, arXiv:0707.3617.

[49] HERMES Collaboration, A. Airapetian *et al.*, *Measurement of the spin asymmetry in the photoproduction of pairs of high p_T hadrons at HERMES*, Phys. Rev. Lett. **84** (2000) 2584–2588, arXiv:hep-ex/9907020.

[50] COMPASS Collaboration, E. S. Ageev *et al.*, *Gluon polarization in the nucleon from quasi-real photoproduction of high-p_T hadron pairs*, Phys. Lett. **B633** (2006) 25–32, arXiv:hep-ex/0511028.

[51] COMPASS Collaboration, C. Adolph *et al.*, *Leading and Next-to-Leading Order Gluon Polarisation in the Nucleon and Longitudinal Double Spin Asymmetries from Open Charm Muoproduction*, Phys. Rev. **D87** (2013) 052018, arXiv:1211.6849.

[52] C. Hendlmeier, *Polarized Di-Hadron Production in Lepton-Nucleon Collisions at the Next-To-Leading Order of QCD*, doctoral thesis, Universität Regensburg, 2008.

[53] C. Peterson, D. Schlatter, I. Schmitt, and P. M. Zerwas, *Scaling Violations in Inclusive e^+e^- Annihilation Spectra*, Phys. Rev. **D27** (1983) 105.

[54] V. G. Kartvelishvili, A. K. Likhoded, and V. A. Petrov, *On the Fragmentation Functions of Heavy Quarks Into Hadrons*, Phys. Lett. **B78** (1978) 615.

[55] E. Braaten, K. Cheung, S. Fleming, and T. C. Yuan, *Perturbative QCD fragmentation functions as a model for heavy quark fragmentation*, Phys. Rev. **D51** (1995) 4819–4829, arXiv:hep-ph/9409316.

[56] J. Baines *et al.*, *Heavy quarks (Working Group 3): Summary report*, arXiv:hep-ph/0601164.

[57] M. Cacciari, P. Nason, and R. Vogt, *QCD predictions for charm and bottom production at RHIC*, Phys. Rev. Lett. **95** (2005) 122001, arXiv:hep-ph/0502203.

[58] W. Beenakker, W. L. van Neerven, R. Meng, G. A. Schuler, and J. Smith, *QCD corrections to heavy quark production in hadron hadron collisions*, Nucl. Phys. **B351** (1991) 507–560.

[59] W. Beenakker, H. Kuijf, W. L. van Neerven, and J. Smith, *QCD corrections to heavy quark production in $p\bar{p}$-collisions*, Phys. Rev. **D40** (1989) 54–82.

[60] P. Nason, S. Dawson, and R. K. Ellis, *The One Particle Inclusive Differential Cross-Section for Heavy Quark Production in Hadronic Collisions*, Nucl. Phys. **B327** (1989) 49–92 [ERRATUM-ibid.B335:260,1990].

[61] R. K. Ellis and P. Nason, *QCD Radiative Corrections to the Photoproduction of Heavy Quarks*, Nucl. Phys. **B312** (1989) 551.

[62] C. Anastasiou and S. M. Aybat, *The one-loop gluon amplitude for heavy-quark production at NNLO*, Phys. Rev. **D78** (2008) 114006, arXiv:0809.1355.

[63] B. Kniehl, Z. Merebashvili, J. G. Korner, and M. Rogal, *Heavy quark pair production in gluon fusion at next-to-next-to-leading $\mathcal{O}(\alpha_s^4)$ order: One-loop squared contributions*, Phys. Rev. **D78** (2008) 094013, arXiv:0809.3980.

[64] J. G. Korner, Z. Merebashvili, and M. Rogal, *NNLO $\mathcal{O}(\alpha_s^4)$ results for heavy quark pair production in quark-antiquark collisions: The One-loop squared contributions*, Phys. Rev. **D77** (2008) 094011, arXiv:0802.0106.

[65] M. Czakon, *Tops from Light Quarks: Full Mass Dependence at Two-Loops in QCD*, Phys. Lett. **B664** (2008) 307–314, arXiv:0803.1400.

[66] M. Czakon, A. Mitov, and S. Moch, *Heavy-quark production in gluon fusion at two loops in QCD*, Nucl. Phys. **B798** (2008) 210–250, arXiv:0707.4139.

[67] M. Czakon, A. Mitov, and S. Moch, *Heavy-quark production in massless quark scattering at two loops in QCD*, Phys. Lett. **B651** (2007) 147–159, arXiv:0705.1975.

[68] M. Czakon, P. Fiedler, A. Mitov, and J. Rojo, *Further exploration of top pair hadroproduction at NNLO*, arXiv:1305.3892.

[69] M. Czakon, P. Fiedler, and A. Mitov, *The total top quark pair production cross-section at hadron colliders through $\mathcal{O}(\alpha_S^4)$*, Phys. Rev. Lett. **110** (2013) 252004, arXiv:1303.6254.

[70] A. Mitov, *Recent theoretical progress in top quark pair production at hadron colliders*, EPJ Web Conf. **49** (2013) 04002, arXiv:1303.1059.

[71] M. L. Mangano, P. Nason, and G. Ridolfi, *Heavy quark correlations in hadron collisions at next-to-leading order*, Nucl. Phys. **B373** (1992) 295–345.

[72] S. Frixione, M. L. Mangano, P. Nason, and G. Ridolfi, *Heavy quark correlations in photon-hadron collisions*, Nucl. Phys. **B412** (1994) 225–259, arXiv:hep-ph/9306337.

[73] I. Bojak and M. Stratmann, *Next-to-leading order QCD corrections to the polarized hadroproduction of heavy flavors*, Phys. Rev. **D67** (2003) 034010, arXiv:hep-ph/0112276.

[74] I. Bojak, *NLO QCD corrections to the polarized photo- and hadroproduction of heavy quarks*, doctoral thesis, Universität Dortmund, 2000, arXiv:hep-ph/0005120.

[75] I. Bojak and M. Stratmann, *Photoproduction of heavy quarks in next-to-leading order QCD with longitudinally polarized initial states*, Nucl. Phys. **B540** (1999) 345–381, arXiv:hep-ph/9807405.

[76] I. Bojak and M. Stratmann, *Next-to-leading order QCD corrections to the polarized photoproduction of heavy flavors*, Phys. Lett. **B433** (1998) 411–418, arXiv:hep-ph/9804353.

[77] B. Mele and P. Nason, *Next-to-leading QCD calculation of the heavy quark fragmentation function*, Phys. Lett. **B245** (1990) 635–639.

[78] B. Mele and P. Nason, *The Fragmentation function for heavy quarks in QCD*, Nucl. Phys. **B361** (1991) 626–644.

[79] M. Cacciari and M. Greco, *Large p_T hadroproduction of heavy quarks*, Nucl. Phys. **B421** (1994) 530–544, arXiv:hep-ph/9311260.

[80] M. Cacciari, M. Greco, S. Rolli, and A. Tanzini, *Charmed mesons fragmentation functions*, Phys. Rev. **D55** (1997) 2736–2740, arXiv:hep-ph/9608213.

[81] M. Cacciari, M. Greco, and P. Nason, *The p_T spectrum in heavy-flavour hadroproduction*, JHEP **05** (1998) 007, arXiv:hep-ph/9803400.

[82] M. Cacciari, S. Frixione, and P. Nason, *The p_T spectrum in heavy-flavor photoproduction*, JHEP **03** (2001) 006, arXiv:hep-ph/0102134.

[83] J. H. Kühn and G. Rodrigo, *Charge asymmetry in hadroproduction of heavy quarks*, Phys. Rev. Lett. **81** (1998) 49–52, arXiv:hep-ph/9802268.

[84] J. H. Kühn and G. Rodrigo, *Charge asymmetry of heavy quarks at hadron colliders*, Phys. Rev. **D59** (1999) 054017, arXiv:hep-ph/9807420.

[85] L. G. Almeida, G. Sterman, and W. Vogelsang, *Threshold Resummation for the Top Quark Charge Asymmetry*, Phys. Rev. **D78** (2008) 014008, arXiv:0805.1885.

[86] J. Riedl, *Produktion schwerer Quarks in hochenergetischen Prozessen*, diploma thesis, Universität Regensburg, 2005.

[87] J. Riedl, A. Schäfer, and M. Stratmann, *Prospects of Open Charm Production at GSI-FAIR and J-PARC*, Eur. Phys. J. **C52** (2007) 987–997, arXiv:0708.3010.

[88] PHENIX Collaboration, A. Adare *et al.*, *Double Spin Asymmetry of Electrons from Heavy Flavor Decays in $p+p$ Collisions at $\sqrt{s} = 200$ GeV*, Phys. Rev. **D87** (2013) 012011, arXiv:1209.3278.

[89] C. Franco, *New Results on Gluon Polarisation from COMPASS*, Proceedings of DIS 2009.

[90] J. Riedl, A. Schäfer, and M. Stratmann, *Next-to-Leading Order QCD Corrections to Heavy Quark Correlations in Longitudinally Polarized Hadron-Hadron Collisions*, Phys. Rev. **D80** (2009) 114020, arXiv:0911.2146.

[91] J. Riedl, M. Stratmann, and A. Schäfer, *Longitudinally Polarized Photoproduction of Heavy Flavors at Next-to-Leading Order of QCD*, Eur. Phys. J. **C73** (2013) 2360, arXiv:1212.1319.

[92] S. Gadret, *Etude de la production de charme ouvert et de Drell-Yan dans les collisions p+p à 200 GeV avec le détecteur PHENIX à RHIC*, doctoral thesis, Université Blaise Pascal, 2005.

[93] F. Mahmoudi, *Chromodynamique Quantique aux collisionneurs hadroniques : Vers une automatisation du calcul des processus multi-particules à l'ordre d'une boucle. Application à la production de deux photons et d'un jet*, doctoral thesis, Université de Savoie, LAPTH, 2004.

[94] B. Jäger, *Studies of Hadronic Spin Structure in Hard Scattering Processes at the Next-to-Leading Order of QCD*, doctoral thesis, Universität Regensburg, 2004.

[95] M. E. Peskin and D. V. Schroeder, *An Introduction to Quantum Field Theory*. Westview Press, 1995.

[96] P. Pascuale and R. Tarrach, *QCD: Renormalization for the Practitioner*. Springer, 1984.

[97] CTEQ, R. Brock *et al.*, *Handbook of perturbative QCD; Version 1.1: September 1994*, FERMILAB-PUB-94-316.

[98] F. Halzen and A. Martin, *Quarks & Leptons: An Introductory Course In Modern Particle Physics*. John Willy & Sons, 1984.

[99] R. P. Feynman, *Space-time approach to nonrelativistic quantum mechanics*, Rev. Mod. Phys. **20** (1948) 367–387.

[100] L. D. Faddeev and V. N. Popov, *Feynman diagrams for the Yang-Mills field*, Phys. Lett. **B25** (1967) 29.

[101] S. Bethke, *The 2009 World Average of* $\alpha_s(M_Z)$, Eur. Phys. J. **C64** (2009) 689–703, `arXiv:0908.1135`.

[102] G. 't Hooft and M. J. G. Veltman, *Regularization and renormalization of gauge fields*, Nucl. Phys. **B44** (1972) 189.

[103] F. Bloch and A. Nordsieck, *Note on the radiation field of the electron*, Phys. Rev. **52** (1937) 54–59.

[104] W. A. Bardeen, A. J. Buras, D. W. Duke, and T. Muta, *Deep Inelastic Scattering Beyond the Leading Order in Asymptotically Free Gauge Theories*, Phys. Rev. **D18** (1978) 3998.

[105] S. B. Libby and G. Sterman, *Jet and lepton pair production in high-energy lepton-hadron and hadron-hadron scattering*, Phys. Rev. **D18** (1978) 3252.

[106] R. K. Ellis, H. Georgi, M. Machacek, H. D. Politzer, and G. G. Ross, *Factorization and the parton model in QCD*, Phys. Lett. **B78** (1978) 281.

[107] R. K. Ellis, H. Georgi, M. Machacek, H. D. Politzer, and G. G. Ross, *Perturbation theory and the parton model in QCD*, Nucl. Phys. **B152** (1979) 285.

[108] D. Amati, R. Petronzio, and G. Veneziano, *Relating hard QCD processes through universality of mass singularities*, Nucl. Phys. **B140** (1978) 54.

[109] D. Amati, R. Petronzio, and G. Veneziano, *Relating hard QCD processes through universality of mass singularities. 2*, Nucl. Phys. **B146** (1978) 29–49.

[110] G. Curci, W. Furmanski, and R. Petronzio, *Evolution of parton densities beyond leading order: the nonsinglet case*, Nucl. Phys. **B175** (1980) 27.

[111] J. C. Collins, D. E. Soper, and G. Sterman, *Factorization for short distance hadron-hadron scattering*, Nucl. Phys. **B261** (1985) 104.

[112] J. C. Collins, D. E. Soper, and G. Sterman, *All order factorization for Drell-Yan cross sections*, Phys. Lett. **B134** (1984) 263.

[113] J. C. Collins, *Hard scattering in QCD with polarized beams*, Nucl. Phys. **B394** (1993) 169–199, arXiv:hep-ph/9207265.

[114] S. Kretzer, *Fragmentation functions from flavour-inclusive and flavour-tagged e^+e^- annihilations*, Phys. Rev. **D62** (2000) 054001, arXiv:hep-ph/0003177.

[115] D. de Florian, R. Sassot, and M. Stratmann, *Global analysis of fragmentation functions for pions and kaons and their uncertainties*, Phys. Rev. **D75** (2007) 114010, arXiv:hep-ph/0703242.

[116] D. de Florian, R. Sassot, and M. Stratmann, *Global analysis of fragmentation functions for protons and charged hadrons*, Phys. Rev. **D76** (2007) 074033, arXiv:0707.1506.

[117] G. Altarelli and G. Parisi, *Asymptotic Freedom in Parton Language*, Nucl. Phys. **B126** (1977) 298.

[118] V. N. Gribov and L. N. Lipatov, *Deep inelastic e p scattering in perturbation theory*, Sov. J. Nucl. Phys. **15** (1972) 438–450 [Yad.Fiz.15:781-807,1972].

[119] Y. L. Dokshitzer, *Calculation of the Structure Functions for Deep Inelastic Scattering and e^+e^- Annihilation by Perturbation Theory in Quantum Chromodynamics*, Sov. Phys. JETP **46** (1977) 641–653 [Zh.Eksp.Teor.Fiz.73:1216-1240,1977].

[120] W. Vogelsang, *A Rederivation of the Spin-dependent Next-to-leading Order Splitting Functions*, Phys. Rev. **D54** (1996) 2023, arXiv:hep-ph/9512218.

[121] W. Vogelsang, *The spin-dependent two-loop splitting functions*, Nucl. Phys. **B475** (1996) 47, arXiv:hep-ph/9603366.

[122] CTEQ, H. L. Lai *et al.*, *Global QCD analysis of parton structure of the nucleon: CTEQ5 parton distributions*, Eur. Phys. J. **C12** (2000) 375, arXiv:hep-ph/9903282.

[123] A. D. Martin, R. G. Roberts, W. J. Stirling, and R. S. Thorne, *MRST2001: Partons and α_s from precise deep inelastic scattering and Tevatron jet data*, Eur. Phys. J. **C23** (2002) 73, arXiv:hep-ph/0110215.

[124] J. Pumplin *et al.*, *New generation of parton distributions with uncertainties from global QCD analysis*, JHEP **07** (2002) 012, arXiv:hep-ph/0201195.

[125] P. M. Nadolsky *et al.*, *Implications of CTEQ global analysis for collider observables*, Phys. Rev. **D78** (2008) 013004, arXiv:0802.0007.

[126] A. D. Martin, W. J. Stirling, R. S. Thorne, and G. Watt, *Uncertainties on α_S in global PDF analyses*, Eur. Phys. J. **C64** (2009) 653–680, arXiv:0905.3531.

[127] J. Owens, A. Accardi, and W. Melnitchouk, *Global parton distributions with nuclear and finite-Q^2 corrections*, Phys. Rev. **D87** (2013) 094012, arXiv:1212.1702.

[128] A. D. Martin, W. J. Stirling, R. S. Thorne, and G. Watt, *Parton distributions for the LHC*, Eur. Phys. J. **C63** (2009) 189–285, arXiv:0901.0002.

[129] M. Glück, E. Reya, M. Stratmann, and W. Vogelsang, *Models for the polarized parton distributions of the nucleon*, Phys. Rev. **D63** (2001) 094005, arXiv:hep-ph/0011215.

[130] D. de Florian, G. A. Navarro, and R. Sassot, *Sea quark and gluon polarization in the nucleon at NLO accuracy*, Phys. Rev. **D71** (2005) 094018, arXiv:hep-ph/0504155.

[131] B. Jäger, A. Schäfer, M. Stratmann, and W. Vogelsang, *Next-to-leading order QCD corrections to high-p_T pion production in longitudinally polarized pp collisions*, Phys. Rev. **D67** (2003) 054005, arXiv:hep-ph/0211007.

[132] B. Jäger, M. Stratmann, and W. Vogelsang, *Single inclusive jet production in polarized pp collisions at $O(\alpha_s^3)$*, Phys. Rev. **D70** (2004) 034010, arXiv:hep-ph/0404057.

[133] D. de Florian, R. Sassot, M. Stratmann, and W. Vogelsang, *Global analysis of helicity PDFs: Past – present – future*, arXiv:1108.3955.

[134] Asymmetry Analysis Collaboration (AAC), M. Hirai, S. Kumano, and N. Saito, *Determination of polarized parton distribution functions and their uncertainties*, Phys. Rev. **D69** (2004) 054021, arXiv:hep-ph/0312112.

[135] Asymmetry Analysis Collaboration, M. Hirai and S. Kumano, *Determination of gluon polarization from deep inelastic scattering and collider data*, Nucl. Phys. **B813** (2009) 106–122, arXiv:0808.0413.

[136] E. Leader, A. V. Sidorov, and D. B. Stamenov, *Determination of Polarized PDFs from a QCD Analysis of Inclusive and Semi-inclusive Deep Inelastic Scattering Data*, Phys. Rev. **D82** (2010) 114018, arXiv:1010.0574.

[137] COMPASS Collaboration, C. Adolph *et al.*, *Leading order determination of the gluon polarisation from DIS events with high-p_T hadron pairs*, Phys. Lett. **B718** (2013) 922–930, arXiv:1202.4064.

[138] QCDSF, M. Göckeler *et al.*, *Generalized parton distributions from lattice QCD*, Phys. Rev. Lett. **92** (2004) 042002, arXiv:hep-ph/0304249.

[139] C. von Weizsäcker, *Radiation emitted in collisions of very fast electrons*, Z. Phys. **88** (1934) 612–625.

[140] E. Williams, *Nature of the high-energy particles of penetrating radiation and status of ionization and radiation formulae*, Phys. Rev. **45** (1934) 729–730.

[141] S. Frixione, M. L. Mangano, P. Nason, and G. Ridolfi, *Improving the Weizsäcker-Williams approximation in electron-proton collisions*, Phys. Lett. **B319** (1993) 339–345, arXiv:hep-ph/9310350.

[142] V. Budnev, I. Ginzburg, G. Meledin, and V. Serbo, *The Two photon particle production mechanism. Physical problems. Applications. Equivalent photon approximation*, Phys. Rept. **15** (1975) 181–281.

[143] H. A. Olsen, *Improved Weizsäcker-Williams method*, Phys. Rev. **D19** (1979) 100.

[144] M. Glück, E. Reya, and A. Vogt, *Photonic parton distributions*, Phys. Rev. **D46** (1992) 1973.

[145] M. Stratmann and W. Vogelsang, *Spin-dependent parton distributions of the longitudinally polarized photon beyond the leading order*, Phys. Lett. **B386** (1996) 370, arXiv:hep-ph/9606346.

[146] M. Cacciari and P. Nason, *Is there a significant excess in bottom hadroproduction at the Tevatron?*, Phys. Rev. Lett. **89** (2002) 122003, arXiv:hep-ph/0204025.

[147] M. Cacciari, S. Frixione, M. L. Mangano, P. Nason, and G. Ridolfi, *QCD analysis of first b cross-section data at 1.96 TeV*, JHEP **07** (2004) 033, arXiv:hep-ph/0312132.

[148] Particle Data Group, C. Amsler *et al.*, *Review of particle physics*, Phys. Lett. **B667** (2008) 1–1340.

[149] R. Vogt, private communication.

[150] CLEO, A. H. Mahmood *et al.*, *Measurement of the B-meson inclusive semileptonic branching fraction and electron energy moments*, Phys. Rev. **D70** (2004) 032003, arXiv:hep-ex/0403053.

[151] BABAR, B. Aubert *et al.*, *Measurement of the electron energy spectrum and its moments in inclusive $B \to Xe\nu$ decays*, Phys. Rev. **D69** (2004) 111104, arXiv:hep-ex/0403030.

[152] J. Wiss, *Recent results on fully leptonic and semileptonic charm decays*, eConf **C060409** (2006) 025, arXiv:hep-ex/0605030.

[153] M. Luszczak, R. Maciula, and A. Szczurek, *Nonphotonic electrons at RHIC within k_t-factorization approach and with experimental semileptonic decay functions*, Phys. Rev. **D79** (2009) 034009, arXiv:0807.5044.

[154] P. Breitenlohner and D. Maison, *Dimensional renormalization and the action principle*, Commun. Math. Phys. **52** (1977) 11.

[155] A. Weber, *Soft gluon resummations in polarized space-like and time-like processes*, doctoral thesis, Universität Dortmund, 1992.

[156] G. Passarino and M. J. G. Veltman, *One Loop Corrections for e^+e^--Annihilation into $\mu^+\mu^-$ in the Weinberg Model*, Nucl. Phys. **B160** (1979) 151.

[157] Z. Kunszt and D. E. Soper, *Calculation of jet cross-sections in hadron collisions at order α_s^3*, Phys. Rev. **D46** (1992) 192–221.

[158] B. Harris and J. Owens, *The Two cutoff phase space slicing method*, Phys. Rev. **D65** (2002) 094032, arXiv:hep-ph/0102128.

[159] A. Nordsieck, *The Low Frequency Radiation of a Scattered Electron*, Phys. Rev. **52** (1937) 59–62.

[160] T. D. Lee and M. Nauenberg, *Degenerate Systems and Mass Singularities*, Phys. Rev. **133** (1964) B1549–B1562.

[161] T. Kinoshita, *Mass singularities of Feynman amplitudes*, J. Math. Phys. **3** (1962) 650–677.

[162] G. P. Lepage, *A New Algorithm for Adaptive Multidimensional Integration*, J. Comput. Phys. **27** (1978) 192.

[163] G. P. Lepage, *Vegas: an adaptive multidimensional integration program*, Cornell preprint CLNS 80-447 (1980).

[164] M. Jamin and M. E. Lautenbacher, *Tracer: Version 1.1: A Mathematica package for gamma algebra in arbitrary dimensions*, Comput. Phys. Commun. **74** (1993) 265.

[165] S. Wolfram, *Mathematica*, see also: `www.wri.com`.

[166] R. Mertig, M. Böhm, and A. Denner, *FEYN CALC: Computer algebraic calculation of Feynman amplitudes*, Comput. Phys. Commun. **64** (1991) 345–359.

[167] R. W. Brown, D. Sahdev, and K. O. Mikaelian, *Probing higher order QCD: charge conjugation asymmetries from two gluon exchange*, Phys. Rev. Lett. **43** (1979) 1069.

[168] F. Halzen, P. Hoyer, and C. S. Kim, *Forward-backward asymmetry of hadroproduced heavy quarks in QCD*, Phys. Lett. **B195** (1987) 74.

[169] M. T. Bowen, S. D. Ellis, and D. Rainwater, *Standard model top quark asymmetry at the Fermilab Tevatron*, Phys. Rev. **D73** (2006) 014008, `arXiv:hep-ph/0509267`.

[170] S. Dittmaier, P. Uwer, and S. Weinzierl, *NLO QCD corrections to $t\bar{t}+jet$ production at hadron colliders*, Phys. Rev. Lett. **98** (2007) 262002, `arXiv:hep-ph/0703120`.

[171] J. Weinelt, Masters Thesis, *Measurement of the charge asymmetry in top-antitop quark production with the CDF II experiment*, FERMILAB-MASTERS-2006-05, 2006.

[172] D0 Collaboration, V. Abazov *et al.*, *First measurement of the forward-backward charge asymmetry in top quark pair production*, Phys. Rev. Lett. **100** (2008) 142002, `arXiv:0712.0851`.

[173] CDF Collaboration, T. Aaltonen *et al.*, *Forward-Backward Asymmetry in Top Quark Production in $p\bar{p}$ Collisions at $\sqrt{s} = 1.96$ TeV*, Phys. Rev. Lett. **101** (2008) 202001, `arXiv:0806.2472`.

[174] CDF Collaboration, T. Aaltonen *et al.*, *Evidence for a Mass Dependent Forward-Backward Asymmetry in Top Quark Pair Production*, Phys. Rev. **D83** (2011) 112003, `arXiv:1101.0034`.

[175] D0 Collaboration, V. M. Abazov *et al.*, *Forward-backward asymmetry in top quark-antiquark production*, Phys. Rev. **D84** (2011) 112005, `arXiv:1107.4995`.

[176] ATLAS Collaboration, G. Aad *et al.*, *Measurement of the charge asymmetry in top quark pair production in pp collisions at $\sqrt{s} = 7$ TeV using the ATLAS detector*, Eur. Phys. J. **C72** (2012) 2039, `arXiv:1203.4211`.

[177] U. De Sanctis, *Measurements of the top quark charge asymmetry at the LHC*, `arXiv:1211.5991`.

[178] F. Kohn, *Measurement of the charge asymmetry in top quark pair production in pp collision data at $\sqrt{s} = 7$ TeV using the ATLAS detector*, doctoral thesis, Universität Göttingen, 2012.

[179] P. Nason, S. Dawson, and R. K. Ellis, *The Total Cross-Section for the Production of Heavy Quarks in Hadronic Collisions*, Nucl. Phys. **B303** (1988) 607.

[180] F. A. Berends, K. J. F. Gaemers, and R. Gastmans, *α^3 contribution to the angular asymmetry in $e^+e^- \to \mu^+\mu^-$*, Nucl. Phys. **B63** (1973) 381–397.

[181] F. A. Berends, K. J. F. Gaemers, and R. Gastmans, *Hard photon corrections for Bhabha scattering*, Nucl. Phys. **B68** (1974) 541–550.

[182] F. A. Berends, R. Kleiss, S. Jadach, and Z. Was, *QED radiative corrections to electron-positron annihilation into heavy fermions*, Acta Phys. Polon. **B14** (1983) 413.

[183] S. Catani, D. de Florian, G. Rodrigo, and W. Vogelsang, *Perturbative generation of a strange-quark asymmetry in the nucleon*, Phys. Rev. Lett. **93** (2004) 152003, arXiv:hep-ph/0404240.

[184] J. Riedl, *Longitudinally polarized hadro- and photoproduction of heavy quarks*, Mod. Phys. Lett. **A24** (2009) 3045–3051.

[185] J. Riedl, A. Schäfer, and M. Stratmann, *Longitudinally polarized hadroproduction of heavy quarks*, AIP Conf. Proc. **1149** (2009) 373–376.

[186] C. Lourenco and H. K. Wohri, *Heavy flavour hadro-production from fixed-target to collider energies*, Phys. Rept. **433** (2006) 127–180, arXiv:hep-ph/0609101.

[187] Marco Contalbrigo, private communication.

[188] B. Jäger, M. Stratmann, and W. Vogelsang, *Longitudinally polarized photoproduction of inclusive hadrons at fixed-target experiments*, Eur. Phys. J. **C44** (2005) 533–543, arXiv:hep-ph/0505157.

[189] PHENIX Collaboration, A. Adare *et al.*, *Measurement of Bottom versus Charm as a Function of Transverse Momentum with Electron-Hadron Correlations in $p+p$ Collisions at $\sqrt{s} = 200$ GeV*, Phys. Rev. Lett. **103** (2009) 082002, arXiv:0903.4851.

[190] PHENIX Collaboration, A. Adare *et al.*, *Measurement of high-p_T single electrons from heavy-flavor decays in $p+p$ collisions at $\sqrt{s} = 200$ GeV*, Phys. Rev. Lett. **97** (2006) 252002, arXiv:hep-ex/0609010.

[191] PHENIX Collaboration, A. Adare *et al.*, *Dilepton mass spectra in $p+p$ collisions at $\sqrt{s} = 200$ GeV and the contribution from open charm*, Phys. Lett. **B670** (2009) 313–320, arXiv:0802.0050.

[192] PHENIX Collaboration, S. S. Adler *et al.*, *Measurement of single muons at forward rapidity in $p+p$ collisions at $\sqrt{s} = 200$ GeV and implications for charm production*, Phys. Rev. **D76** (2007) 092002, arXiv:hep-ex/0609032.

[193] STAR Collaboration, J. Adams *et al.*, *Open charm yields in $d+Au$ collisions at $\sqrt{s_{NN}} = 200$ GeV*, Phys. Rev. Lett. **94** (2005) 062301, arXiv:nucl-ex/0407006.

[194] STAR Collaboration, B. I. Abelev *et al.*, *Erratum: Transverse momentum and centrality dependence of high-p_t non-photonic electron suppression in $Au+Au$ collisions at $\sqrt{s_{NN}} = 200$ GeV*, Phys. Rev. Lett. **98** (2007) 192301, arXiv:nucl-ex/0607012 [Erratum-ibid.106:159902,2011].

[195] STAR Collaboration, B. I. Abelev *et al.*, *Measurement of D* Mesons in Jets from $p+p$ Collisions at $\sqrt{s} = 200$ GeV*, Phys. Rev. **D79** (2009) 112006, arXiv:0901.0740.

[196] PHENIX Collaboration, A. Adare *et al.*, *Heavy Quark Production in $p+p$ and Energy Loss and Flow of Heavy Quarks in Au+Au Collisions at $\sqrt{s_{NN}} = 200$ GeV*, Phys. Rev. **C84** (2011) 044905, arXiv:1005.1627.

[197] PHENIX Collaboration, S. S. Adler *et al.*, *Double helicity asymmetry in inclusive mid-rapidity π^0 production for polarized $p+p$ collisions at $\sqrt{s} = 200$ GeV*, Phys. Rev. Lett. **93** (2004) 202002, arXiv:hep-ex/0404027.

[198] PHENIX Collaboration, S. S. Adler *et al.*, *Improved measurement of double helicity asymmetry in inclusive midrapidity π^0 production for polarized $p+p$ collisions at $\sqrt{s} = 1200$ GeV*, Phys. Rev. **D73** (2006) 091102, arXiv:hep-ex/0602004.

[199] STAR Collaboration, B. I. Abelev *et al.*, *Longitudinal double-spin asymmetry and cross section for inclusive jet production in polarized proton collisions at $\sqrt{s} = 200$ GeV*, Phys. Rev. Lett. **97** (2006) 252001, arXiv:hep-ex/0608030.

[200] D. de Florian, *Next-to-leading order QCD corrections to one hadron production in polarized pp collisions at RHIC*, Phys. Rev. **D67** (2003) 054004, arXiv:hep-ph/0210442.

[201] R. Mertig and W. L. van Neerven, *The Calculation of the two loop spin splitting functions $P_{ij}(x)$*, Z. Phys. **C70** (1996) 637, arXiv:hep-ph/9506451.

[202] G. Bunce *et al.*, *Plans for the RHIC Spin Physics Program*, June 2008, http://spin.riken.bnl.gov/rsc/.

[203] C. Hendlmeier, A. Schäfer, and M. Stratmann, *Next-to-leading order QCD corrections to spin-dependent hadron-pair photoproduction*, Eur. Phys. J. **C55** (2008) 597–605, arXiv:0803.1940.

[204] Spin Muon Collaboration (SMC), B. Adeva *et al.*, *Spin asymmetries for events with high p_T hadrons in DIS and an evaluation of the gluon polarization*, Phys. Rev. **D70** (2004) 012002, arXiv:hep-ex/0402010.

[205] F. Robinet, *Mesure de la polarisation des gluon dans le nucléon par la muo-production de mésons charmés à COMPASS*, doctoral thesis, UFR de Physique, Université Paris Diderot (Paris 7), 2008.

[206] S. Koblitz, *Determination of the Gluon Polarisation from Open Charm Production at COMPASS*, doctoral thesis, Universität Mainz, 2008.

[207] C. Franco, *Measurement of the Gluon Polarisation from Open-Charm Production at COMPASS*, doctoral thesis, Universidade Técnica de Lisboa, 2011.

[208] K. Kurek, *Understanding the Nucleon's Spin Structure – The Direct Gluon Polarisation Measurement at the COMPASS Experiment*, habilitation thesis, National Centre of Nuclear Research, Świerk, 2011.

[209] M. Glück, E. Reya, and M. Stratmann, *Probing the parton densities of virtual photons at e p colliders*, Phys. Rev. **D54** (1996) 5515–5522, arXiv:hep-ph/9605297.

[210] A. Watson, *Spin spin asymmetries in inclusive muon proton charm production*, Z. Phys. **C12** (1982) 123.

[211] S. Frixione and G. Ridolfi, *Jet photoproduction at HERA*, Nucl. Phys. **B507** (1997) 315–333, arXiv:hep-ph/9707345.

[212] A. Accardi, J. Albacete, M. Anselmino, N. Armesto, E. Aschenauer, *et al.*, *Electron Ion Collider: The Next QCD Frontier - Understanding the glue that binds us all*, arXiv:1212.1701.

[213] N. Craigie, K. Hidaka, M. Jacob, and F. Renard, *Spin Physics at Short Distances*, Phys. Rept. **99** (1983) 69–236.

[214] E. Heindl, C. Kefes, M. Soda, J. Vancea, and C. H. Back, *Hot electron spin attenuation lengths of bcc $Fe_{34}Co_{66}$—Room temperature Magnetocurent of 1200%*, Journal of Magnetism and Magnetic Materials **321** (2009) 3693–3697.

Acknowledgements

This work would not have been possible without the help of several people. Here I will take the chance to thank them.

I am grateful to Prof. Schäfer who gave me the possibility of working in this interesting field. In weekly meetings we, i.e., all students working at his chair on pQCD, could discuss all issues of perturbative QCD. Furthermore, he took care of the financial support for this thesis. I express also my gratitude to him because he gave me the chance to present my results on (international) conferences. Moreover, I am grateful to all financiers of this PhD thesis, especially to the Bischöfliche Studienförderung of the Cusanuswerk, Bonn, Germany, of whom I received a grant.

Marco Stratmann introduced me patiently into the sophisticated details of perturbative QCD. I could discuss with him all technical details of the calculation. This collaboration worked fine all the time despite being mostly restricted to email. Special thanks is due to him for proofreading the manuscript of this thesis and for useful annotations. He also advised me, which observables are of special relevance for the phenomenological sections both for this thesis and for my diploma thesis [86] and our papers [87, 90, 91, 184, 185].

I also want to mention the useful discussions with the other doctoral students working on perturbative QCD, especially with Christof Hendlmeier.

Moreover, I am grateful to Alexander Lenz, Jürgen Rohrwild and Markus Bobrowski for our pleasant work [12–14] on the CKM matrix and a possible 4th family in the standard model.

I want to mention also Emanuel Heindl with whom I often spent lunchtime discussing amongst others physical problems, see, e.g., the acknowledgements of [214].

Furthermore, I am grateful to my officemates at the University of Regensburg, Simone Gutzwiller, Arifa Ali Khan, Martin Gürtler, and Jürgen Rohrwild, for the great time and the pleasant atmosphere.

My thanks go especially to Simone Gutzwiller and Sabine Rygol for proofreading this manuscript.

Last, but not least, I want to mention all my friends and my parents who were supporting me all the time on my way.